AFRL-RX-WP-TR-2013-0069

SAFER NANOMATERIALS AND NANOMANUFACTURING

James E. Hutchison, Eric Johnson, Karen Guillemin, John Postlethwait, Mark Lonergan, Andy Berglund, Steve Kevan, Richard Taylor and Dave Johnson
University of Oregon

FEBRUARY 2013
Final Report

STINFO COPY

AIR FORCE RESEARCH LABORATORY
MATERIALS AND MANUFACTURING DIRECTORATE
WRIGHT-PATTERSON AIR FORCE BASE, OH 45433-7750
AIR FORCE MATERIEL COMMAND
UNITED STATES AIR FORCE

NOTICE AND SIGNATURE PAGE

Using Government drawings, specifications, or other data included in this document for any purpose other than Government procurement does not in any way obligate the U.S. Government. The fact that the Government formulated or supplied the drawings, specifications, or other data does not license the holder or any other person or corporation; or convey any rights or permission to manufacture, use, or sell any patented invention that may relate to them.

Qualified requestors may obtain copies of this report from the Defense Technical Information Center (DTIC) (http://www.dtic.mil)

AFRL-RX-WP-TR-2013-0069 HAS BEEN REVIEWED AND IS APPROVED FOR PUBLICATION IN ACCORDANCE WITH ASSIGNED DISTRIBUTION STATEMENT.

____//SIGNATURE//_____
PETER A. MIRAU, Program Manager
Soft Matter Materials Branch
Functional Materials Division

____//SIGNATURE//_____
KATIE E. THORP, Chief
Soft Matter Materials Branch
Functional Materials Division

____//SIGNATURE//_____
KAREN R. OLSON, Deputy Chief
Functional Materials Division
Materials & Manufacturing Directorate

This report is published in the interest of scientific and technical information exchange and its publication does not constitute the Government's approval or disapproval of its ideas or findings.

REPORT DOCUMENTATION PAGE

The public reporting burden for this collection of information is estimated to average 1 hour per response, including the time for reviewing instructions, searching existing data sources, gathering and maintaining the data needed, and completing and reviewing the collection of information. Send comments regarding this burden estimate or any other aspect of this collection of information, including suggestions for reducing this burden, to Department of Defense, Washington Headquarters Services, Directorate for Information Operations and Reports (0704-0188), 1215 Jefferson Davis Highway, Suite 1204, Arlington, VA 22202-4302. Respondents should be aware that notwithstanding any other provision of law, no person shall be subject to any penalty for failing to comply with a collection of information if it does not display a currently valid OMB control number. **PLEASE DO NOT RETURN YOUR FORM TO THE ABOVE ADDRESS**.

1. REPORT DATE *(DD-MM-YY)* February 2013	2. REPORT TYPE Final	3. DATES COVERED *(From - To)* 18 October 2005 – 18 January 2013

4. TITLE AND SUBTITLE SAFER NANOMATERIALS AND NANOMANUFACTURING	5a. CONTRACT NUMBER FA8650-05-1-5041
	5b. GRANT NUMBER
	5c. PROGRAM ELEMENT NUMBER 62102F
6. AUTHOR(S) Prof. James E. Hutchison, Eric Johnson, Karen Guillemin, John Postlethwait, Mark Lonergan, Andy Berglund, Steve Kevan, Richard Taylor and Dave Johnson (University of Oregon)	5d. PROJECT NUMBER 4347
	5e. TASK NUMBER 11
	5f. WORK UNIT NUMBER X02W (11502702)

7. PERFORMING ORGANIZATION NAME(S) AND ADDRESS(ES) University of Oregon 1226 University of Oregon Eugene, OR 97403-1226	8. PERFORMING ORGANIZATION REPORT NUMBER

9. SPONSORING/MONITORING AGENCY NAME(S) AND ADDRESS(ES) Air Force Research Laboratory Materials and Manufacturing Directorate Wright-Patterson Air Force Base, OH 45433-7750 Air Force Materiel Command United States Air Force	10. SPONSORING/MONITORING AGENCY ACRONYM(S) AFRL/RXAS
	11. SPONSORING/MONITORING AGENCY REPORT NUMBER(S) AFRL-RX-WP-TR-2013-0069

12. DISTRIBUTION/AVAILABILITY STATEMENT
Approved for public release; distribution is unlimited.

13. SUPPLEMENTARY NOTES
Approved by 88ABW Public Affairs Office: Case number 88ABW-2013-2262 on 10 MAY 2013. Report contains color.

14. ABSTRACT
The ultimate objective of this initiative was the rational design of safe, yet high performance nanoscale materials, efficient and inexpensive manufacture of these materials, and the incorporation of the nanoscale materials into high-performance microscale or larger devices. This approach was will simultaneously meet the Air Force's need for high performance materials while also addressing its concern for protecting human health and minimizing harm to the environment.

15. SUBJECT TERMS
nanomaterials, nanomanufacturing, nanoparticles

16. SECURITY CLASSIFICATION OF:			17. LIMITATION OF ABSTRACT: SAR	18. NUMBER OF PAGES 176	19a. NAME OF RESPONSIBLE PERSON (Monitor) Peter A. Mirau
a. REPORT Unclassified	b. ABSTRACT Unclassified	c. THIS PAGE Unclassified			19b. TELEPHONE NUMBER *(Include Area Code)* (937) 255-9155

REPORT DOCUMENTATION PAGE Cont'd

6. AUTHOR(S)

Robert Tanguay, Stacey Harper, Bettye L. S. Maddux, Brian Paul, Chih-Hung Chang, Vincent Remcho, R. T. Miller, Sundar V. Atre, Shoichi Kimura, Vinod Narayanan, Greg Rorrer, Doug Keszler, Mas Subramanian, Jeff Nason, Lewis Semprini and Tyler Radniecki (Oregon State University)

Galya Orr, D. R. Palo, S. Ramprasad, Shane Addleman, Marvin Warner, Mark Jones and Glen E. Fryxell (Pacific Northwest National Laboratory)

Mingdi Yan, Jun Jiao, Bin Jiang, Carl C. Wamser, Rolf Koenenkamp and Scott Reed (Portland State University)

7. PERFORMING ORGANIZATION NAME(S) AND ADDRESS(ES)

Oregon State University
104 Kerr Administration Building
Corvallis, OR 97331

Pacific Northwest National Laboratory
P. O. Box 999
Richland, WA 99352

Portland State University
1719 SW 10th Ave
Portland, OR 97201

TABLE OF CONTENTS

Approved for public release; distribution is unlimited.

LIST OF FIGURES

LIST OF TABLES

SUMMARY

The Oregon Nanoscience and Microtechnologies Institute (ONAMI) is Oregon's first Signature Research Center.[4] ONAMI accelerates research and commercialization of materials science and related device and system technologies in the Pacific Northwest through a deep collaboration among Oregon universities, the Pacific Northwest National Laboratory, industry, and the investment community. It has become an internationally recognized leader in nanotechnology. The Safer Nanomaterials and Nanomanufacturing Initiative (SNNI) is the largest and most successful research thrust within the ONAMI.[5] SNNI strives to address four fundamental questions that are central to the development of nanotechnology as a responsible and publicly accepted technology. What are the biological impacts related to nanoparticles? What are the best strategies to developing nanoparticle materials that retain full function, yet pose no threat to health or the environment? With the tools that we have developed, can we develop chemistries for a broader range of nanoparticles in large scale? How can the properties of individual and ensembles of nanoparticles be harnessed through interfaces with other nanoparticles, microstructures and macroscale systems?

The ONAMI collaborative addresses these key questions through three research thrusts that bring innovative approaches and unparalleled talent and resources to the project. At the heart of the effort is the merger between green chemistry and nanoscience, a concept pioneered at the University of Oregon. By bringing together key scientists in the life sciences, materials science, chemistry, physics and engineering, we have designed an effort merging fundamental and applied research at the forefront of the research within each thrust.

In the first thrust group, we focus on nanoparticle design and their biological impacts. We conduct studies on a large, diverse library of well-defined nanoparticles to identify the structure/property relationships that dictate the biological impacts of nanoparticles and use these relationships to design and produce safer nanoparticles that still possess the desired physical properties. This thrust group directly addresses AFRL's concern regarding the safety of nanomaterials. Key collaborations with AFRL have grown from this research area.

In the second thrust group, we focus on nanoparticle synthesis and production with the aim of producing precision-engineered nanoparticles with precisely controlled composition and structure. We design, develop and test new chemistries and reactor formats for nanoparticle manufacturing in an effort to produce higher quality nanoparticles, at higher throughput and with less waste.

In the third thrust group, we address a topic that is critical to successful deployment of nanoparticles in high-performance devices such as sensors, electronics, or optics and that is interfacing nanoparticles with nano-, micro- and macro-scopic devices - utilizing environmentally benign approaches. In the past few years, we have focused on nanodevice applications for energy and energy storage.

Background and program objectives

Nanoscience and nanotechnology promise to revolutionize many areas within science and technology ranging from electronics to medicine because unprecedented size-dependent material properties are being discovered in nanoscale materials. These properties can be harnessed to produce entirely new materials and devices of interest to the Air Force, including sensors, electronic and optical materials, adaptive materials and nanocomposites. Given the predicted widespread use of nanomaterials, concerns have arisen about the biological and environmental impact of the materials and the processes used to manufacture them. Indeed, the National Nanotechnology Initiative (NNI) recently published its 2011 strategy to establish guidelines and research needs on the environmental, health and safety for engineered nanoscale materials[6]. Within NNI, several organizations (e.g. EPA, FDA, NIST) are working to determine methods to measure and catalog nanoscale materials due to increased interest to understand the toxicity of nanoparticles. The Strategy guide specifically addresses the need to develop a database or federated databases of nanomaterial properties and biological/ecological effects. SNNI works with these organizations in ongoing efforts to establish standards, testing strategies, and database development to address these significant issues. Some of our efforts are outlined below under program integration and policy guidance. The ultimate objective of this initiative however is the rational design of safe, yet high performance nanoscale materials, efficient and inexpensive manufacture of these materials, and the incorporation of the nanoscale materials into high-performance microscale or larger devices. This approach will simultaneously meet the Air Force's need for high performance materials while also addressing its concern for protecting human health and minimizing harm to the environment.

Program integration, policy guidance and characterization research (Task 0): SNNI's approach to managing a successful and growing research Initiative involved three key foci: program integration, policy guidance and supporting research efforts in developing methods and tools for nanomaterial characterization.

Program integration: SNNI supports and manages the research thrusts of the Initiative through (i) it's Greener Nano (GN) Conference Series, (ii) participation in academic, government and industrial conferences or workshops as plenary or keynote speakers and as an exhibitor, (iii) regular group meetings, and (iv) quarterly reporting.

The GN conferences bring national and international attention to SNNI. The GN series also served to strengthen collaborations within SNNI research staff, with key collaborations with AFRL researchers, other governmental agencies (e.g. NIST), other academic institutions (e.g. CEIN-UCLA, CEINT-Duke) and industrial partners (e.g. Life Technologies, Sony, HP). Indeed, most of the GN Conferences have been held on industry campuses (e.g. Life Technologies, HP).

SNNI researchers have participated in conferences and workshops as invited or plenary speakers, session chairs, co-conference organizers, poster presenters, or exhibitors. Some examples include, the American Chemical Society, Materials Research Symposium, American Physical Society, the Society for Toxicology, The SETAC World Congress Conference, The Nanotechnology for Defense (NT4D), the National Nanotechnology Initiative's (NNI) public meetings to establish strategy for EHS, IEEE Nano, Nanotechnology Health and Safety Forum, Organisation for Economic Co-operation and Development (OECD) conference on Nanotechnology, and NIST Workshop on developing reference materials for nanotechnology. Over the past six years, key researchers have held regular group meeting between participants, which have led to successful collaborations and external funding that continue today. For example, Thrust Group 1 has collectively published over 50 manuscripts and is currently working on Center funding, Thrust Group 3 resulted in the successful spin off of a NSF funded Center for Chemical Innovation, the Center for Sustainable Materials Chemistry (CSMC).[7] Cumulatively, researchers in SNNI have published >200 publications and successfully won >$56M in external awards as a result of the seed funding they received from SNNI (see Figure 1). These results have been previously reported in our quarterly reports submitted to AFRL.
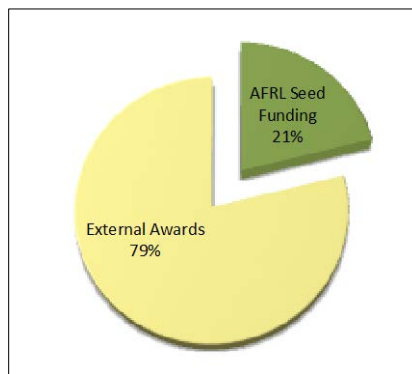
Figure 1. Total awards: AFRL = $15,263,377, External funding that resulted from AFRL grant = $56,950,782

Approved for public release; distribution is unlimited.

Policy guidance: ONAMI and SNNI have participated in several areas to guide the development of safer nanotechnologies. We have worked with several agencies over the years to guide policy and participate in developing strategies for defining the guiding principles and developing EHS standards for nanotechnology (NIOSH, EPA, NIST, NNI, ISO, NRC). For example, we

- Served as a committee member for National Research Council Committee on Research Strategy for Nanomaterials Environmental Health and Safety[8]

- Served as members of the Scientific Advisory Boards for both the University of California Center for the Environmental Implications of Nanotechnology and the Duke Center for the Environmental Implications of Nanotechnology

- Serve on the Scientific Advisory Board for the Nanosafety Consortium for Carbon[9]

- Participated in several NNI workshops, including the development of the 2011 Research Strategy for EHS[6]

- Collaborated with our neighbors, the State of Washington to develop a roadmap for adopting green chemistry practices in the state[10]

- Contributed to the development of the 2011 Laboratory Waste Management Guide for The Local Hazardous Waste Management Program in King County, Washington[11]

- Participated in the President's Council of Advisors on Science and Technology (PCAST) public meetings on nanotechnology focus areas and strategic plan for NNI

- Assisted our legislative office in drafting the Reauthorization Act of 2009[12, 13]

- Served as U.S. delegates to the International Standards Organization (ISO) Technical Committee (TC) 229 for Nanotechnologies and drafted several U.S. positions in terminology and nomenclature and standards for Environmental Health and Safety of nanomaterials

- Participated in the development of the Nanoinformatics 2020 Roadmap[14]

- Published guidelines on the use of extensive characterization during discovery, manufacture and testing of nanoparticles. This paper provides the framework to help guide characterization of nanomaterials for reproducible applications and for toxicological and biological applications. It serves as a framework to establish funding for federal research priorities.[15]

These efforts resonate in official strategy documents from the workshops in which we participated, such as the 2011 NNI EHS Research Strategy document[6], The National Research Council's Strategy for Environmental, Health, and Safety (EHS) Aspects of Engineered Nanomaterials[8], The Nanoinformatics 2020 Roadmap[14].

Additionally, the GN Conference series have held sessions dedicated to developing the guiding principles and iterative design schemes (or 'design rules') for inherently safer nanomaterials. The GN10 program yielded a joint report with the American Chemical Society, Green Chemistry Institute, "Green Nanotechnology, Challenges and Opportunities".[16] Our pioneering efforts to develop 'precision-engineered' nanoparticles, 'precisely-characterized' nanoparticles and 'design rules' for greener safer nanomaterials have become popular descriptors of efforts throughout the nanotechnology community both the U.S. and abroad in government, academic and industrial institutions.

Characterization research support: Understanding the material properties and structure of nanoparticles is an integral component to developing responsible nanomaterials. Many of the tools to characterize nanomaterials (e.g. TEM, SEM, NMR, etc.) are insufficient to fully understand how nanoparticles change in varying conditions; biological systems and environmental conditions. We develop minimum characterization standards tailored toward the particle of interest.[15] We are currently collaborating with NIST to address the challenges of characterization at the bio-nano interface. We are also partnering with small companies such as Hummingbird Scientific, Nanocomposix and Dune Sciences to advance methods and reference materials need to support characterization efforts.

We have also developed some novel uses for current technologies to measure in situ nanoparticle growth.[17] We purchased a tabletop SAXS and have analyzed time resolved SAXS measurements of gold (Au) nanoparticles (NP) in solvents with varying ionic strength and SAXS measurements of GaO clusters in multiple solvents.[18]

Research objectives
To address the challenges in establishing environmentally-benign approaches to the incorporation of nanomaterials into high-performance materials and devices, we blend the guiding principles of green chemistry, state-of-the-art nanoparticle synthesis and functionalization, detailed biological investigations of nanoparticle toxicity, high-performance microreactor development for nanoparticle production, efficient and benign assembly strategies for bulk materials and devices and detailed physical characterization of these materials and devices. To this end, three interrelated objectives guide the work of the initiative. These objectives form the basis for three *research thrusts* of the initiative.

Thrust group 1. Designing greener nanoparticles: Understanding the biological effects of well-defined nanoparticle samples, using this knowledge to design safer nanoparticles for nanodevices and consolidating all existing data.

Thrust group 2. Developing greener nanomanufacturing of engineered nanoparticles: Development of microreactor platforms for efficient production of functionalized nanoparticles that reduce material consumption and waste production while providing needed quantities of structurally-defined materials.

Thrust group 3. Interfacing nanoparticles and nanostructures for device applications: Identify environmentally-benign chemical strategies to incorporate nanoparticles and nanostructures into extended arrays of devices that preserve, or enhance, the properties of the nanoparticles in applications such as electronics, optics and sensing. In recent years, we have focused on energy and energy storage applications.
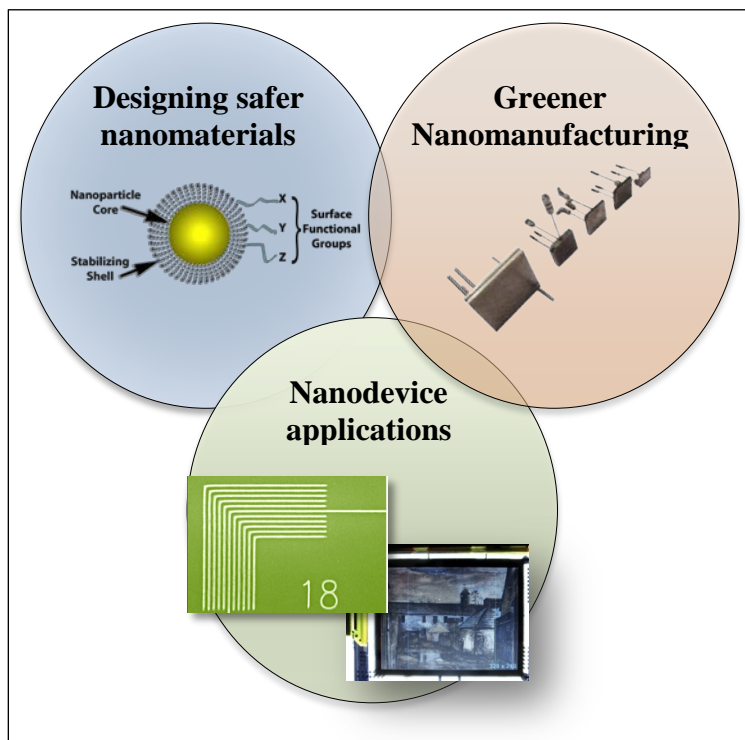
Figure 2. Graphical representation of Thrust Groups.

Thrust Group 1: Designing Greener Nanomaterials
The overarching goal of this thrust group is to formulate structure-property relationships for the biological impact of engineered nanoparticles and to apply these relationships to the design of new materials with tailored properties. By studying the potential toxicological effects of nanoparticles before they are incorporated into technologies we can minimize negative consequences of a growing nanotechnology and promote sustainability. Because nanoparticles are key building blocks for applications such as in chemical/biological sensing, nanoelectronics, quantum computing, and nanophotonics they are likely to be widely distributed throughout the environment. By using a library of structurally and compositionally well-defined nanoparticles in conjunction with biological assays that examine multiple aspects of cellular and organismal health, it will be possible to identify those that cause harm and develop structure-property relationships to feed back into product design. *Research tasks under this research thrust to meet this goal are:*

Task 1: Probe the biological impacts of functionalized nanoparticles (K. Guillemin, J. Hutchison, E, Johnson, R. Tanguay, G. Orr, M. Warner, M. Lonergan, L. Semprini, J. Nason, T. Radniecki): Biological assays have been established to link the physical, chemical, and geometric properties of structurally well-defined functionalized nanoparticles to their function in biological systems. The biological assays give information on nanoparticle movement and tissue accumulation, changes in gene expression in response to nanoparticle interaction with the cellular environment, and subsequent alterations to organismal viability and development. We have developed a whole-animal, high-content screening system using embryonic zebrafish and augment these studies in other biological systems *in vitro* (cultured cells, bacteria, yeast) and *in vivo* (zebrafish, *Drosophila*).

Task 2: Expanded libraries of precisely engineered nanoparticles (J. Hutchison, M. Lonergan, A. Berglund, S. Reed, M. Yan): This task involves the design of new routes to nanomaterials using feedback from Task 1 to reduce their toxicity and proposes to expand the current library of nanoparticles for investigation of biological interactions to; (a) develop a diverse array of functionalized gold nanoparticles with core sizes in the range of 2-20 nm, (b) develop precise libraries of compound semiconductor nanoparticles (specifically PbS and CdSe) and purification methods, (c) exploration of the use of naturally occurring lipids and RNA aptmers to control nanoparticle shape and size and (d) modification of the surface functionalization of nanoparticles.

Task 3: Computational and analytic tools to support the development of environmentally-benign nanomaterials (Harper, R. Tanguay): There is a paucity of data on nanoparticle characterization and toxicity or a means for disseminating new data. Many government agencies have called for a method to catalog the anticipated accumulation of data on nanoparticles into a relatively easy searchable database.[14] This task aims to develop such a collaborative knowledgebase of Nanomaterial-Biological Interactions (NBI) that is systematically linked to related data/knowledgebases. NBI will serve as a repository for annotated data on nanomaterial-biological interactions. Relevant computational, analytic and data mining tools will be integrated and/or developed to extract useful knowledge from diverse datasets on nanomaterial characterization, synthesis methods and nanomaterial-biological interactions defined at multiple levels of biological organizations.

Probing the biological impacts of functionalized nanoparticles
In vitro investigations of gold nanoparticles in biological systems
Project Investigators: Eric Johnson, Karen Guillemin, Jim Hutchison, John Postlethwait
(University of Oregon)
Our research groups focused on the tracking and effects of gold nanoparticles (AuNPs) within biological systems. Most of the research was conducted in *Drosophila*, though one zebrafish study was done as well.

Visualization and tracking of AuNPs in biological systems
The visualization and tracking part of this project proved to be extremely difficult. Traditionally, tracking in biological systems is achieved by attaching a fluorescent marker to the nanomaterial, and using confocal microscopy to identify and determine the localization of the nanomaterial. However, these AuNPs have the ability to "quench" the fluorescence from any tag, so that route had to be abandoned. Many hours and resources were also committed to determining localization via TEM, but this suffered from issues with dosing, contrast, and differentiating AuNPs from uranium-stained sub-cellular structures, such as ribosomes, and was also abandoned as not being cost or time effective.

We were successful in visualizing some of the cellular repercussions of exposure to AuNPs, as described in Figure 3. One of the common malformations found in the embryonic zebrafish screen was a mass on the trunk, which detailed histology and microscopy revealed to be due to an increase in cell proliferation.
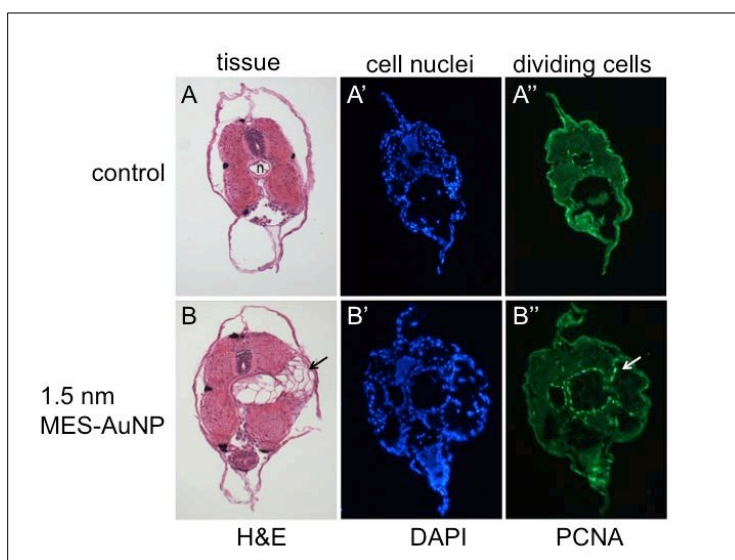
Figure 3. Exposure of zebrafish to 1.5 nm MES-AuNPs induces abnormal cell masses and cell proliferation

Zebrafish were exposed to 1.5 nm MES-AuNPs from 8-120 hpf, at which point they were euthanized, and tissue was fixed, sectioned, and processed for histology and immunohistochemistry. Transverse section through the trunk of a control (A) and treated (B) larva are shown. Hemolysin and eosin (H&E) staining revealed an abnormal cell mass (arrow in B), which appeared similar in cellular structure to the notochord (n, in A). Staining for all nuclei

(DAPI, in blue) and a marker of proliferating cells (PCNA, in green) revealed a concentration of cell proliferation surrounding the abnormal cell mass in the MES-AuNP treated fish (white arrow in B'').

In vitro investigations of AuNP effects on Drosophila Kc cells
Kc cells were assessed for cell viability and cell metabolism across a range of concentrations, and microarray experiments were performed to investigate changes in gene expression as a result of AuNP exposure. As shown in Figure 4, the results of our cytotoxicity and metabolism assays indicate the importance of AuNP size in determining toxicity, but also show differential toxicity of AuNPs with the same core size but different surface functionalizations. These studies were also conducted using flow cytometry to correlate bulk fluorescence measurements with single-cell measurements. The effect of ligand alone was also tested using flow cytometry and was found to not have any effect, even at very high concentrations (data not shown), indicating the it is the combination of ligand attached to the AuNPs that mediates the effect.
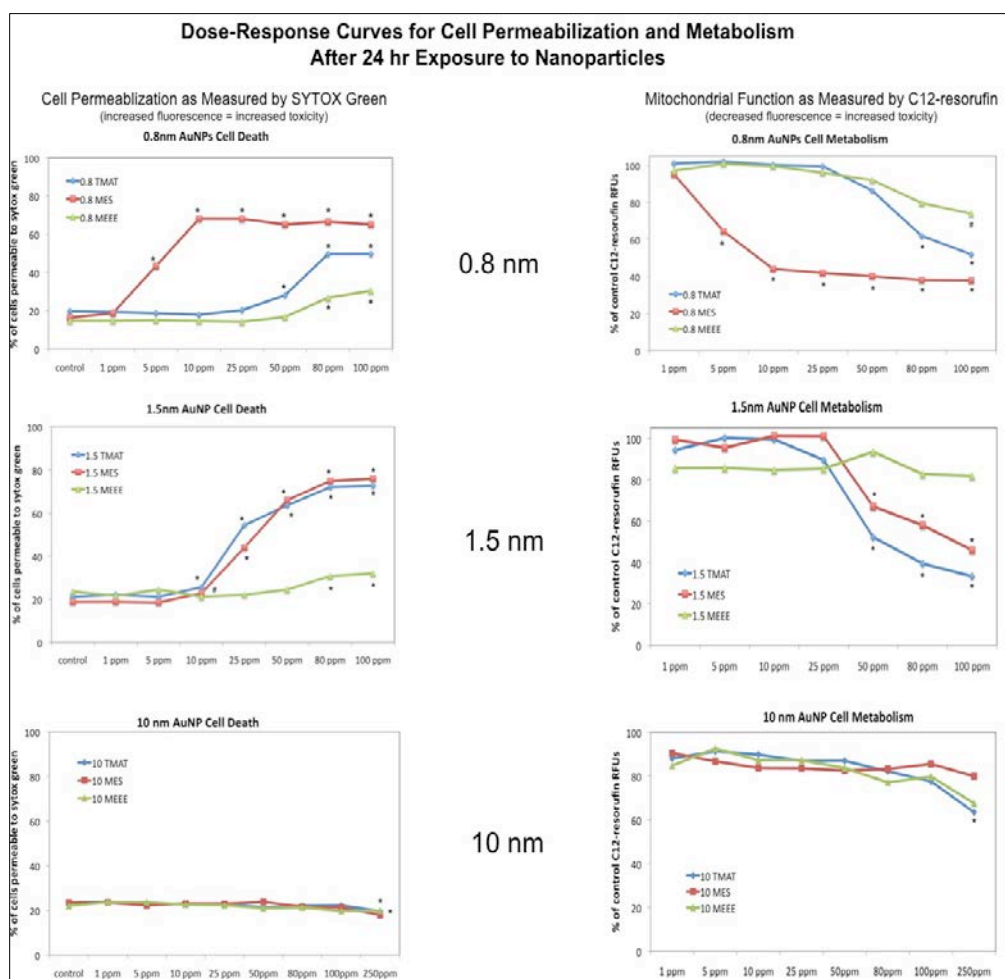
Figure 4. Results of cell viability and metabolism assays conducted on Kc cells exposed to AuNPs covered with TMAT (cationic), MES (anionic), or MEEE (neutral) for 24 hrs.

Data points significantly different than controls are designated by # ($p<0.05$) or * ($p<0.01$). Dose-response curves for AuNPs effects on cell viability and metabolism were determined via

bulk fluorescence readings using a Spectramax M5e (Molecular Devices) in a 96-well format with 8 biological replicates. The results clearly show cases of both size- and charge-dependent toxicity. Anionic, cationic, and neutral, 10 nm AuNPs were non-toxic, but the smaller gold nanoparticles (0.8 &1.5 nm) show differential toxicity depending on surface chemistry. Both TMAT and MES showed toxicity at quite low concentrations, while the neutral MEEE particles did not show significant difference from controls until the highest exposure concentrations, and even then, the magnitude of the effect is much smaller.

The effect of AuNP exposure on the gene expression of *Kc* cells was also investigated to try and elucidate potential biological pathways involved in the response or a potential "mode of action" for AuNP toxicity. *Kc* cells were exposed to 50 ppm of various AuNPs for 24 hours, and then RNA was extracted, labeled, and hybridized on cDNA microarrays to assess relative transcript abundance. The data was analyzed with a variety of strategies, but the most fruitful and informative appears to be to select genes above a certain cut-off value for enrichment (2-fold or 1.4-fold up-regulation compared to control) and compare the representation of "gene ontology families" in the enriched list of genes versus the total list of genes found to be expressed in *Kc* cells. This is called Gene Ontology analysis and some example results are shown in Figure 5.

Approved for public release; distribution is unlimited.
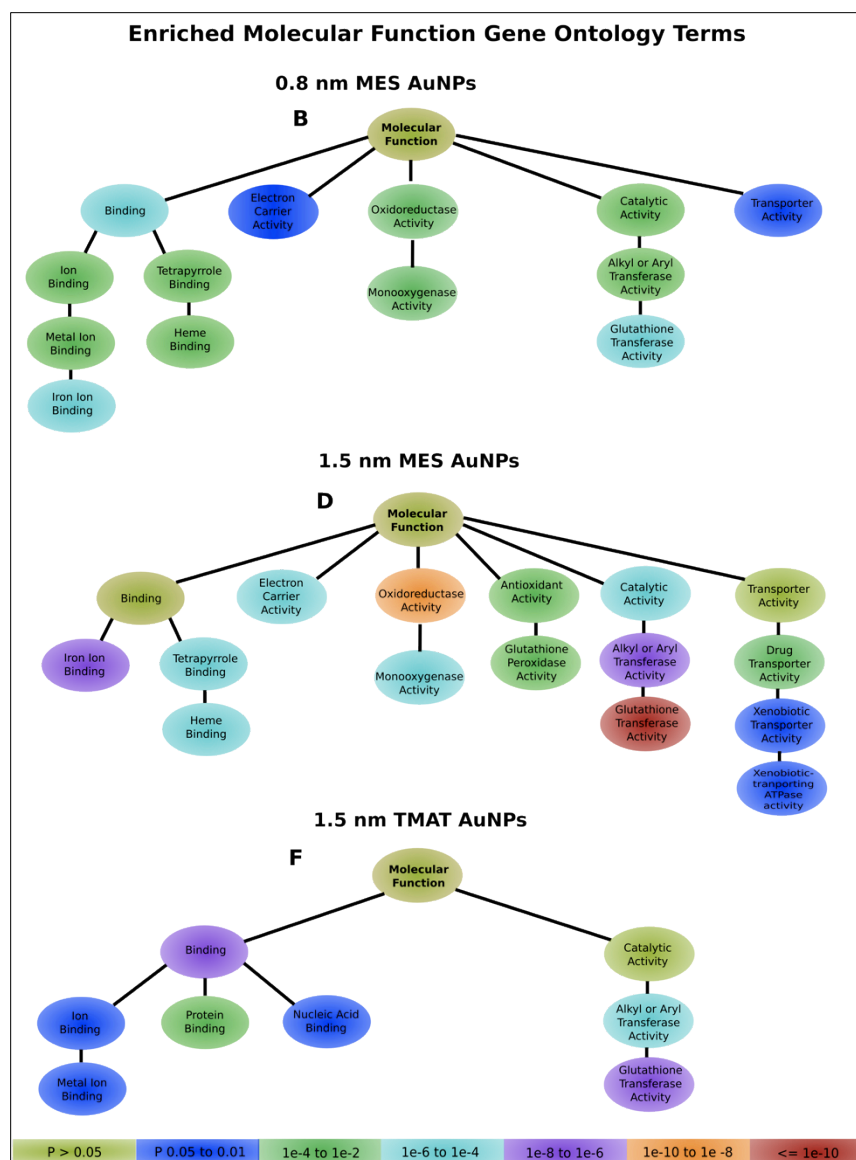
Figure 5. Visual representations of the hierarchy of molecular function GO families found to be significantly enriched after 24-hour exposures to 50 ppm AuNPs.

The arrangement of the hierarchies across different AuNPs follows a similar pattern to facilitate comparison between the particle types. The key to the significance levels associated with the differently colored GO terms is given at the bottom of the figure.

We used this information on candidate genes (including HSP's, GST's, and metallothionenes, to name a few) involved in the response to AuNP exposure to develop a series of reporter constructs that we hoped could serve as reporters for a *luciferase*-based assay to rapidly screen an RNAi knockout library for other genes that might be involved in the AuNP response. The pilot phase of this project worked well, with transient transfection of the construct into *Kc* cells, but the data was highly variable from experiment to experiment, and we were unable to stably transfect the *Kc* cells to establish permanent reporter cell lines that could have brought more consistency to the data. Eventually this RNAi-screening project was abandoned due to the high

variability and inconsistency of the results, and we decided to shift our focus away from *in vitro* assays, towards studying the effect of AuNPs on adult *Drosophila in vivo*.

In vivo investigations of AuNP effects on adult Drosophila melanogaster
In vivo effects of AuNPs on adult flies were tested for two routes of exposure, injection into the abdomen and oral exposure.   Mortality results for these experiments are given in Figure 6. We also began experiments to quantify the AuNP exposure using inductively coupled plasma mass spectrometry. Results for the injected exposure are shown in figure 7 and suggest that adult flies are able to clear 1.5 TMAT AuNPs out of their systems quite rapidly.
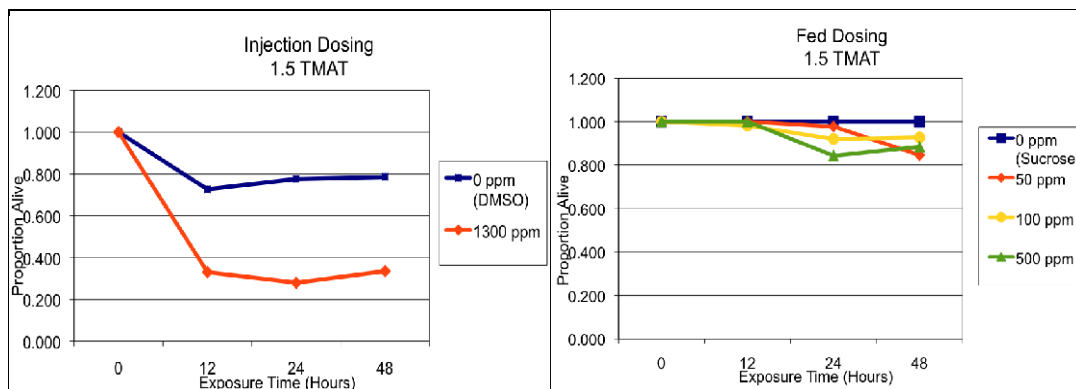
Figure 6. Effect of 1.5 nm TMAT exposure via injection (left panel) or oral exposure (right panel).

The amount injected was calculated to approximate a final concentration of 50 ppm in the fly hemolymph. The oral exposure was done by starving the flies and then feeding them either sucrose or sucrose laced with varying concentrations of 1.5 nm TMAT AuNPs.
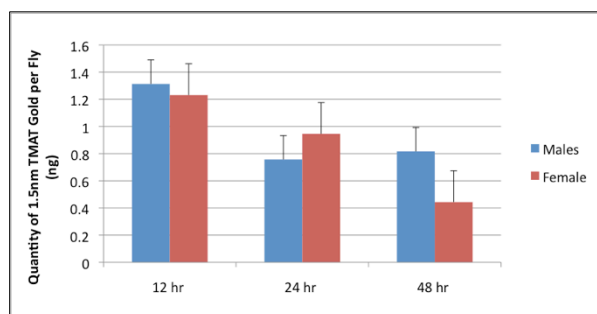
Figure 7. Preliminary ICP-MS data from flies injected with 1.5 nm TMAT AuNP shows rapid clearance of these particles after injection.

More data is needed, especially at the 0 hr after injection time point, as the theoretical injected amount was 42 ng, and only 1.2 ng is detected just 12 hrs later.

We have also conducted a preliminary time-course investigation into the changes in gene expression for adult flies upon exposure to 1.5 nm TMAT AuNPs. For these experiments we chose to quantify transcript abundance in absolute terms using mRNA-seq and next-generation sequencing techniques, which is rapidly replacing microarrays & quantitative PCR as the "gold

standard" for analysis of gene expression. Again the results are far too complex to be conveyed here, but gene ontology analysis suggested that many of the same biological pathways and systems that were adversely effected by 1.5 nm TMAT AuNP exposure in the *in vitro* system were also negatively impacted in a whole animal exposure scenario.

In conclusion, we have established dose-response curves for *in vitro* exposures to all of the nanomaterials supplied to us by the Hutchison group, and have collected useful data sets on gene expression for those materials shown to exhibit toxicity in both *in vitro* and *in vivo* systems.

Identifying the Inhibition and Expression of Sentinel Genes of the Bacteria Nitrosomonas europaea Upon Exposure to Metal Nanoparticles
Project Investigators: Lewis Semprini, Jeff Nason (Oregon State University), Tyler Radniecki (now at San Diego State University)

The objective of this work was to generate crucial ecotoxicological data of metal nanoparticles (NPs) on the environmentally ubiquitous ammonia oxidizing bacteria (AOB), *Nitrosomonas europaea (N. europaea)*. AOB play a key role in the nitrogen cycle and the removal of nitrogen from wastewater treatment plants. However, AOB are widely considered among the most sensitive fauna in the environment being readily inhibited by a wide range of compounds at levels often orders of magnitude below EPA standards[19]. This sensitivity makes AOB an ideal candidate to be an early warning indicator species of environmental toxicity to NPs[20]. The proposed work evaluated inhibition, potential toxicity, and gene expression in response of exposure of *N. europaea* to metal NPs. Specifically, silver nanoparticles (Ag-NP) were investigated. Specific objectives were to:

1. Develop a protocol to investigate the inhibition and potential toxicity to Ag-NP using *N. europaea* as a model bacteria,

2. Use the protocol to determine the inhibition and toxicity of Ag-NPs that vary with respect to size, surface charge and functional,

3. Evaluate whether sentinel genes that have been previously identified in our research with heavy metals respond to the exposure the Ag-NPs,

4. Identify new sentinel genes that result upon exposure Ag-NPs. In our second year of funding we extended these tasks to include the development of a high-throughput screening assay for a variety of functionalized Ag-NP.

Additional Specific objectives were to:

5. Develop a high-throughput screening assay to determine NP toxicity to *N. europaea*,

6. Characterize and investigate the physical/chemical properties of Ag-NP in relevant aquatic systems,

7. Use the developed high-throughput screening assay to measure the toxicity of functionalized Ag-NP with different aquatic chemistries.

We chose to focus our research efforts on Ag-NP. Recent advances in nanotechnology have enhanced the use of silver even further through the creation of Ag-NPs, particles of elemental silver with a diameter of 100 nm or less. Because of their anti-microbial properties, Ag-NPs are the most widely used engineered nanomaterials in consumer products (259 out of 483 nanoproducts surveyed in and are used in a wide variety of materials including nanotextiles, food

containers, clothes washers and dishwashers).[21, 22] *N. europaea*, the model AOB, is an obligate chemolithoautotroph deriving its energy for growth and activity from the oxidation of ammonia (NH_3) to nitrite (NO_2^-). Utilizing a two-step process in which the ammonia monooxygenase enzyme (AMO) oxidizes NH_3 to hydroxylamine (NH_2OH), which is further oxidized to NO_2^- via the hydroxylamine oxidoreductase enzyme (HAO).[20] *N. europaea* is an excellent system to examine the potential ecotoxicity of Ag-NP due to its well defined biochemistry, ability to asses activity it a multitude of ways (*e.g.* NO_2^- production, AMO and HAO activity, oxygen uptake, cell growth and membrane stability) and its ability to be examined in a variety of test media ranging from simple buffer and $(NH_4)_2SO_4$ solutions to complex wastewater matrices.

Objective 1. Develop a protocol to investigate the inhibition and potential toxicity to metal NPs using N. europaea as a model bacterium.

The manner in which Ag-NP were added to the test media had a profound influence on the stability of the Ag-NP suspension, the sensitivity of *N. europaea* to the Ag-NP exposure and the repeatability of the dosing (Figure 8). The addition of a high concentration Ag-NP stock solution (3,630 ppm) directly to a high ionic strength test media consisting only of 30 mM HEPES (pH 7.8) and 2.5 mM $(NH_4)_2SO_4$ (Method 1) resulted in highly variable inhibition responses ($R^2 = 0.09$, Figure 8A) caused by a rapid aggregation and increase in Ag-NP size, in the absence of cells (Figure 8C). Conversely, the dilution of a high concentration Ag-NP stock solution (3,630 ppm) to a concentration of 0.25-1.0 ppm in DDI H_2O, before the addition of the HEPES and $(NH_4)_2SO_4$ (Method 2) resulted in a strong dose-dependent inhibition curve ($R^2 = 0.93$, Figure 8B), increased sensitivity and a stable Ag-NP suspension with minimal increases in particle size (Figure 8C). The increased stability of Ag-NP added using Method 2 can be explained by colloidal collision theory. When particles are added to media of high ionic strength they tend to rapid aggregate due to their having a high collision efficiency function, while when added to DI water the collision efficiency function approaches zero, and little aggregation occurs.
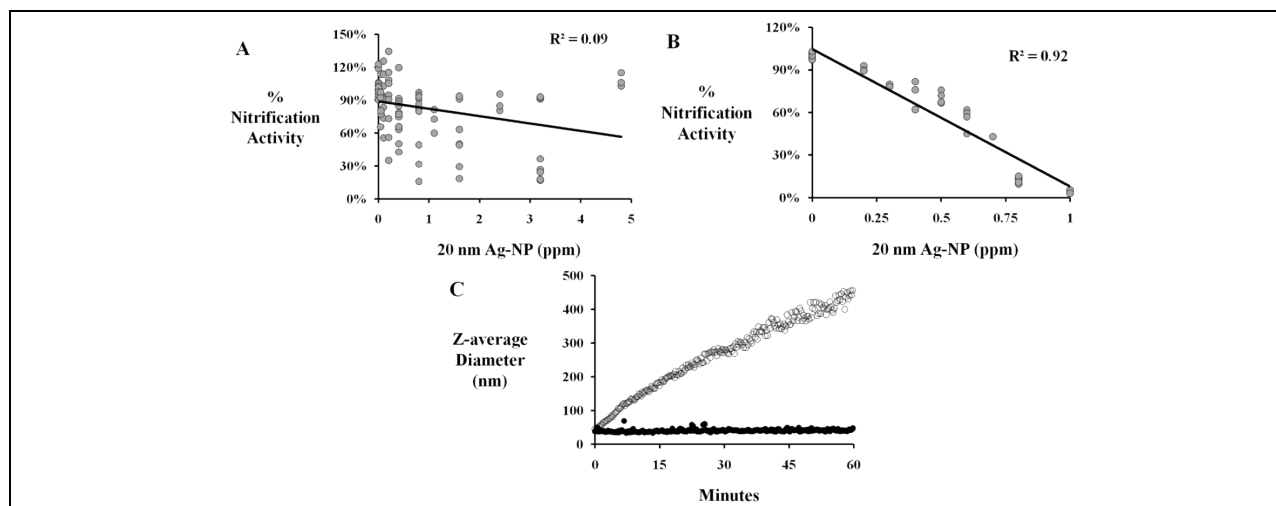
Figure 8. Nitrification activity of N. europaea cells exposed to 20 nm Ag-NP added to the test media either via Method 1 (A) or Method 2 (B). (C) The z-average diameter of 20 nm Ag-NP added to the test media either via Method 1 (○) or Method 2 (●).

Objective 2. Use the protocol to determine the inhibition and toxicity of metal NPs that vary with respect to size, surface charge and functional groups.

Once stable Ag-NP test solutions were created using Method 2, a series of 3-hr batch assays were conducted in which *N. europaea* cells were exposed to various concentrations of either Ag^+ (added as $AgNO_3$), 20 nm Ag-NPs or 80 nm Ag-NPs. *N. europaea* cells demonstrated a high sensitivity to both Ag^+ and the Ag-NPs with the order of sensitivity being as follows (EC_{50}'s - effective concentration resulting in a 50% decrease in nitrification activity, are in parenthesis): Ag^+ (0.08 ppm) > 20 nm Ag-NP (0.47 ppm) > 80 nm Ag-NP (1.44 ppm) (Figure 9a). These reported EC_{50}'s of pure cultures of *N. europaea* to Ag+ and Ag-NP are 1-2 orders of magnitude lower than those reported for mixed nitrifying activated sludge and heterotrophic bacteria, such as *Escherichia coli*[23]. Other studies have reported similar orders of sensitivity with bacteria being more sensitive to smaller Ag-NP and even more sensitive yet to Ag^+[24].

Several studies have suggested that the toxicity of the Ag-NP may be due to the release of dissolved dAg[25]. To determine whether dAg was playing a role in the observed toxicity of Ag-NP to *N. europaea* cells, separate abiotic experiments were conducted in which Ag-NP were placed in the test solution under identical conditions to the biotic experiments. While it is true that the presence of cells may alter the conditions the Ag-NP experience (e.g., altered aggregation state, binding to outer-membrane, etc.), it is not possible to conduct this experiment with the cells present. This is due to the high affinity of Ag^+ to the thiols located on the outer-membrane of the cells which, in turn, would prevent the dAg from being removed via filtration.

At the end of the 3 hr abiotic experiment, the media was filtered using ultra-filtration to remove the Ag-NPs and the filtrate was monitored for total silver. The results of these studies demonstrated that a relatively large fraction of the Ag-NPs, by mass, was being liberated with an observed 30% release, by mass, from 20 nm Ag-NPs and a 5% release, by mass, from 80 nm Ag-NPs (Figure 9b). The higher dissolution rates of the 20 nm Ag-NP are likely due to a higher surface area to volume ratio per mass and thus a larger reaction area for which dAg dissolution can occur. Control studies using Ag-NP in DI water showed no liberation of dAg (data not shown), suggesting that the liberation was catalyzed by the test media conditions and was not simply a transfer of Ag+ from the Ag-NP stock solutions.

A plot of the measured activity of *N. europaea* cells exposed to either Ag^+ or Ag-NP (from Figure 9a) against the predicted dAg from the Ag-NP (from Figure 9b) yields a plot in which the dose-inhibition curve of Ag^+, 20 nm Ag-NP and 80 nm Ag-NP lie directly on top of one another (Figure 9c). This strongly suggests that it is the released Ag^+ that is responsible for the observed Ag-NP toxicity and limits the likelihood of a nanoparticle-specific effect. Thus, the increased toxicity of 20 nm Ag-NP versus 80 nm Ag-NP, as well as the increased sensitivity of *N. europaea* to non-aggregated Ag-NPs, can be credited to the increased rate of Ag^+ dissolution on a mass basis due to a higher surface area to volume ratio.
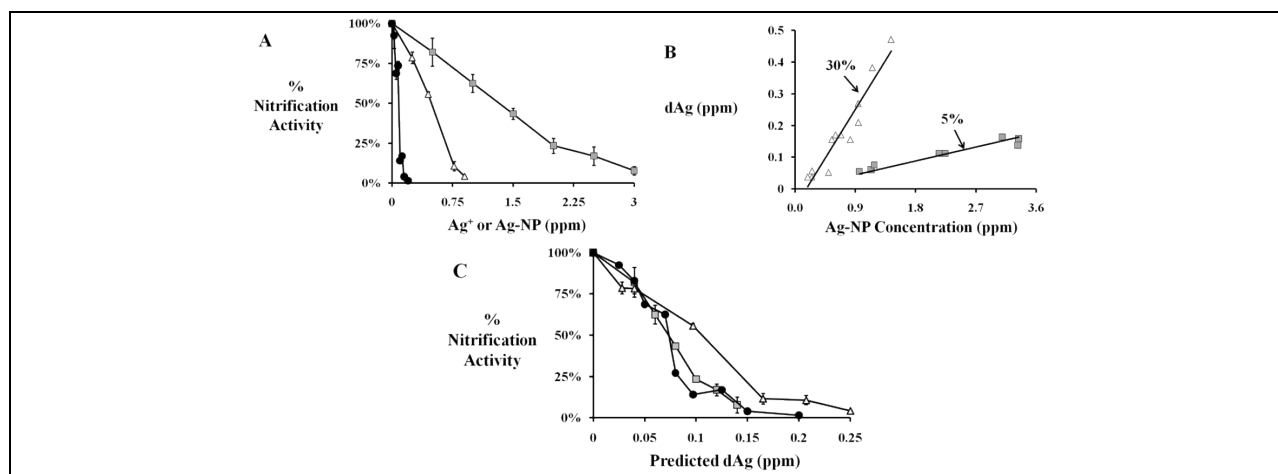
Figure 9. (A) Nitrification activity of N. europaea cells exposed to Ag+ (●), 20 nm Ag-NP (Δ) and 80 nm Ag-NP (■). (B) The abiotic dissolution of dAg, as measured by ultrafiltration, from 20 nm Ag-NP (Δ) and 80 nm Ag-NP (■) after 3 h in the test media. (C) Nitrification activity of N. europaea cells versus the predicted concentration of dAg in the test media for Ag+ (●), 20 nm Ag-NP (Δ) and 80 nm Ag-NP (■). Error bars represent 95% confidence intervals.

The inhibition exerted by both Ag$^+$ and 20 nm Ag-NP were found to be irreversible as activity of the *N. europaea* cells did not increase after several washes to remove the Ag$^+$ or Ag-NP. In the case of Ag$^+$, the activity of the cells continued to decrease after the cells were washed. A closer examination of the washed cells revealed that this lack of reversibility may be due to the failure to remove the tightly-bound Ag from the cells, as the nitrification activity of the washed cells was highly dependent on the quantity of Ag still found associated with the cells (Figure 10).
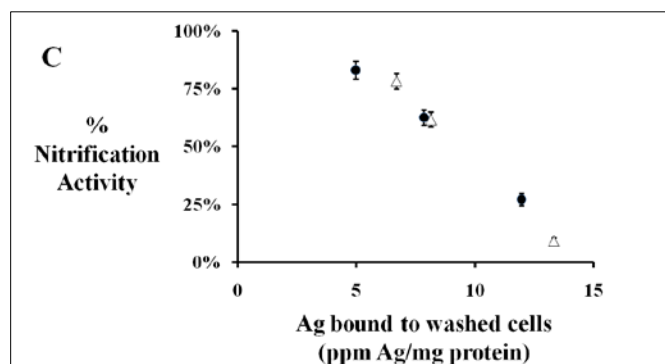
Figure 10. The nitrification activity of the washed N. europaea cells that were originally exposed to various concentration of either Ag+ (●) or 20 nm Ag-NP (Δ) versus the amount of Ag that remained associated with the washed N. europaea cells. Error bars represent 95% confidence intervals.

Interestingly, the level of total Ag found associated with Ag-NP exposed cells was the same as the concentration of total Ag found associated with Ag$^+$ exposed cells even though the Ag-NP exposed cells were exposed to total Ag concentrations 5 times greater, on a per mass basis, than the Ag$^+$ exposed cells. This further supports our hypothesis that liberated dAg is responsible for

Ag-NP toxicity and suggests that only the liberated dAg remained tightly bound to the cells as the majority of the Ag, presumably the Ag-NP, were effectively removed via washing.

Objective 3. Evaluate whether sentinel genes that have been previously identified in our research with heavy metals respond to the exposure the NPs.
In past studies with the heavy metals, Zn^{++} and Cd^{++}, we found that the expression of *merA*, a mercury resistance protein, was highly up-regulated in batch tests and chemostat tests with *N. europaea* [26] upon exposure to Zn^{++} and Cd^{++}. Using Real Time-PCR analysis we performed preliminary studies to determine if *merA* was also up-regulated upon exposure to Ag^+. We could not draw strong conclusions from these tests as to whether up-regulation of *merA* was achieved upon exposure to Ag^+.

Objective 4. Identify new sentinel genes that result upon exposure to metal NPs.
We attempted to determine whether specific genes of *N. europaea* were up-regulated in response to the exposure of Ag^+ and Ag-NP. Gene expression tests were performed with Affymetrix microarrays that contain the genes for the complete genome of *N. europaea.* We could not identify any genes that were up-regulated or down-regulated upon Ag^+ and Ag-NP compared to the controls. Due to the expense of these microarrays, and our obtaining an NSF grant on this topic, we did not proceed with additional gene expression studies with SNNI funding.

Objective 5. Develop a high-throughput screening assay to determine NP toxicity to N. europaea.
Using the same methods as the as large bottle format, 35-ml cell cultures tests, used to generate data shown in Figures 8 and 9, we decreased the assay size to 1-ml. This permitted the use of a 96-well plate to run the inhibition assays with *N. europaea.* The standard assay, the production of nitrite could also be measured using a 96-well plate reader. The method development required analysis of the effective means of adding and mixing microliter volumes of needed components to the 96-well plates and to achieve effective mixing during cell incubations. We achieved effective mixing using 2-ml wells and 1 ml total liquid volume. Presented in Figure 11 are the results of a comparison test of the large bottle format and the 96 well-plate format for the exposure to 20 nm citrate Ag-NPs. The results show excellent agreement between the large bottle format and the 96-well plate format.
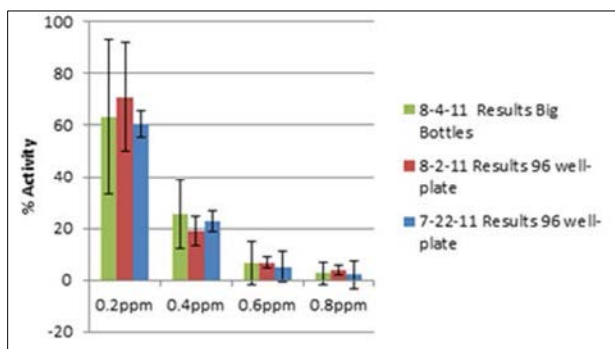
Figure 11. 3hr exposure assay upon exposure to 20nm citrate Ag-NP using the traditional Big Bottle format and the 96-well plate method. % Activity is based on the rate of nitrite production of exposed cells compared to the non-exposed control cells.

Objective 6. Characterize and investigate the physical/chemical properties of Ag-NP in relevant aquatic systems and Objective 7. Use the developed high-throughput screening assay to measure the toxicity of functionalized Ag-NP in a variety of relevant aquatic chemistries.

We have begun to use the 96-well plate method to evaluate the effect of physical/chemical properties on Ag-NP inhibition. We have performed preliminary studies on the effect of humic acids on Ag-NP inhibition as well as well as the stage of growth of *N. europaea*. We have found that cells that are growing more slowly are less inhibited by Ag^+ and Ag-NP then cells that are growing more rapidly. We have also found that in the presence of Suwanne River Humic Acid (SRHA) protected *N. europaea* from Ag-NP inhibition as shown in Figure 12. However, when *N. europaea* was exposed to Ag^+ and SRHA no protection was observed (data not shown). The results indicate that SRHA likely inhibits the release of Ag^+ from the Ag-NP.
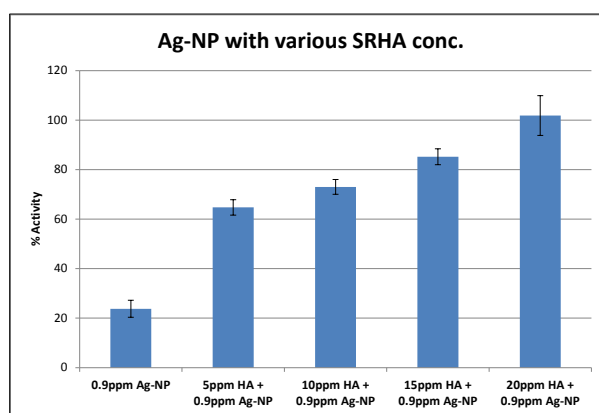
Figure 12. Activity of N. europea in the presence of Ag-NP and Suwannee River Humic Acid (SRHA).

SNNI seed funding and the collaborations that grew within the thrust group facilitated the development of several side projects related to examining the stability of engineered nanoparticles in various relevant aquatic media used for toxicity testing. Throughout the project period, we worked with Dr. Tanguay, Dr. Harper, and Dr. Lonergan and their students on better understanding the colloidal stability of the engineered nanoparticles they were utilizing in their toxicity testing. In all cases, we worked to develop protocols for characterizing the physico-chemical properties of nanomaterials before, during and after toxicity assays (Y5 Objective 1 and Y6 Objective 2) this was done primarily by focusing on the aggregation state of the NPs in the relevant aquatic media using UV-Vis spectroscopy, dynamic light scattering (DLS), and transmission electron microscopy (TEM). We demonstrated, for example, that order of additions in the preparation of exposure media containing Ag-NPs was critical to obtaining repeatable results. Our work with AgNPs and *N. eurpoaea* has made clear the importance of characterizing physico-chemical properties and behavior and their relation to toxicity. In related work, we have explored interactions between SRHA and gold nanoparticles (AuNPs) with different organic capping agents. The AuNPs, obtained from the Hutchison Lab at UO and NanoComposix, serve as a useful model system to examine the influences of organic capping agents on nanoparticle colloidal stability. One advantage of working with gold for the colloidal stability studies is that the AuNPs do not dissolve under environmentally relevant conditions. It is our hope that these findings can be extended to other classes of NPs, including silver. SRHA appeared to adsorb to

each class of AuNP, regardless of capping agent. In the presence of monovalent electrolytes, the presence of SRHA stabilized the AuNPs with respect to aggregation due to electrostatic and steric interactions between SRHA coated particles. In the presence of SRHA and divalent cations, enhanced aggregation was observed and attributed to divalent cation bridging between SRHA molecules adsorbed to adjacent NPs. The results of these studies have been published. [27, 28]

In recent work, we have examined the influence of different organic matter fractions on this same type of behavior. With 10 nm citrate-capped gold nanoparticles, four different classes of NOM (Suwannee River Humic Acid, Suwannee River Fulvic Acid, Suwannee River Natural Organic Matter, and Pony Lake Fulvic Acid) were shown to stabilize the NPs with respect to aggregation.   Figure 13 shows the aggregation profiles of citrate capped gold nanoparticles in the presence of 1 mg/L of each of the four NOM isolates at an ionic strength of 80 mM. In trials with varying NOM concentrations, only low concentrations (< 1 mg C/L) of higher molecular weight and more hydrophobic NOM isolates (SRHA and PLFA) were necessary to stabilize the NPs. However, larger concentrations (> 1-2 mg C/L) of smaller molecular weight fractions were necessary to provide the same stabilizing effect.
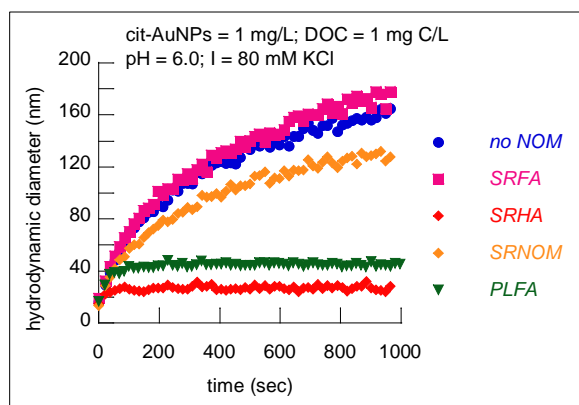
Figure 13. Time resolved dynamic light scattering data characterizing the change in hydrodynamic diameter of 10 nm gold nanoparticles in the presence of an electrolyte (KCl) and several different natural organic matter fractions.

Rapid Throughput Whole Animal Platform To Define Nanoparticle/Biological Interactions: A Path To Safer Nanomaterial Design
Project Investigators: Robert Tanguay (Oregon State University), Jim Hutchison (University of Oregon)
The purpose of this project is to expand and automate a whole animal assay to help define specific nanomaterial properties that influence biological interactions and responses. Dr. Tanguay served as the group leader. We have exploited the advantages of zebrafish as an *in vivo* platform to assess the impact of chemical exposures on early development for over 10 years. Our dynamic group uses embryonic and larval zebrafish to define the mechanisms by which pharmaceuticals, novel small molecules, and environmental chemicals interact with molecular targets to alter complex biological process such as organogenesis, central nervous system development, tissue regeneration, and signal transduction pathways. We have now established the embryonic zebrafish experimental platform as a rapid whole animal model for assessing

Approved for public release; distribution is unlimited.

nanomaterial biological interactions and response. To maximize the impact of this whole animal approach for safer nanomaterial design, it was necessary to fully automate the assay. As part of this effort, our group has developed the tools to incorporate high-throughput toxicological screening of nanomaterials during early-stages nanomaterial design. For high through-put testing, our expanded specific pathogen free zebrafish facility now produces sufficient high-quality disease-free embryos for rapid throughput studies, has streamlined embryo transfer methods, has defined easily quantifiable endpoints, has completed automated image acquisition and analysis methods. In addition automated behavioral analysis platforms have been built and demonstrated to be robust and sensitive. The primary objectives of this project were to fully implement our high-throughput methods for nanomaterial toxicological screening using embryonic zebrafish and to investigate larger nanoparticle (NP) libraries.

Objective 1: Screening level evaluations using embryonic zebrafish
Deliverables: In vivo nanomaterial responses will be defined for additional SNNI-generated and external nanoparticles.
The screening level evaluating embryonic toxicity to zebrafish has been refined to test *in vivo* biological responses to nanomaterials in a high throughput manner. Our screening approach has helped define biological activity and toxic potential of nanomaterials, while using small amounts of highly-pure functionalized nanoparticles obtained from both SNNI investigators and external sources. We have streamlined the evaluation of toxicity from 6 – 120 hours post fertilization (hpf) to assess 16 animals at each standard concentrations (0.4, 2, 10, 50 µg/mL, five-fold serial dilution) of nanomaterials, with two sets of controls (positive: to ensure animals are sensitive to stressors, and a negative control: to ensure the animals were of good quality). Previously, for our biological assay, we manually removed the chorion, a cellular barrier, in batches of 1000 using an enzyme, and place them into 96-well plates filled with 100 µL of nanomaterial solutions [29]. Conducting all the screening manually, created a bottleneck, so we implemented automated liquid handling into the screening process to improve efficiency and accuracy of nanomaterial delivery. Additionally, we collaborated with engineers and developed a semi-automated device (Figure 14a) to dechorionate the embryos in mass (up to 5,000 in 30 minutes) and an automated embryo handler to deposit dechorionated embryos into 96-wells plate within 8 minutes with less than 5% error rate (Figure 14b) [30]. With this ability to screen in a high through-put manner, we developed and implemented a custom in-house analysis and assessment program, Zebrafish Assessment and Analysis Program (ZAAP), that allowed evaluators to assess for 18 adverse effects (both behavioral and morphological) in real time and the data be stored in a database. With the data stored in a database, we are able to data-share with the Nanomaterial-Biological Interaction Knowledgebase (NBI).

Figure 14. Automated (a) dechorionator and (b) embryo handler.

At present, our lab has assessed over 150 different 'types' of nanomaterials using this high through-put zebrafish screening assay. These nanomaterials include a seventeen member gold library, copper and cobalt coated nanoparticles, a series of dendrimers, single-walled and multi-walled carbon nanotubes, 11 commercially available silver nanoparticles, PbS semiconductor nanoparticles, various zinc oxide, carboxylated and sulfonated nanocellulose nanotubes, a series of titanium oxide nanotubes, and various surface coated silver, carbon based fullerenes C_{60} and titanium dioxide nanoparticles. Figure 15 is a visual representative of the data generated from a subset of the gold library nanoparticles synthesized by SNNI investigator, Dr. James Hutchison. This figure illustrates how the manipulation of only one feature (size or surface functional group) on an otherwise similar nanoparticle results in various degrees of biological response.
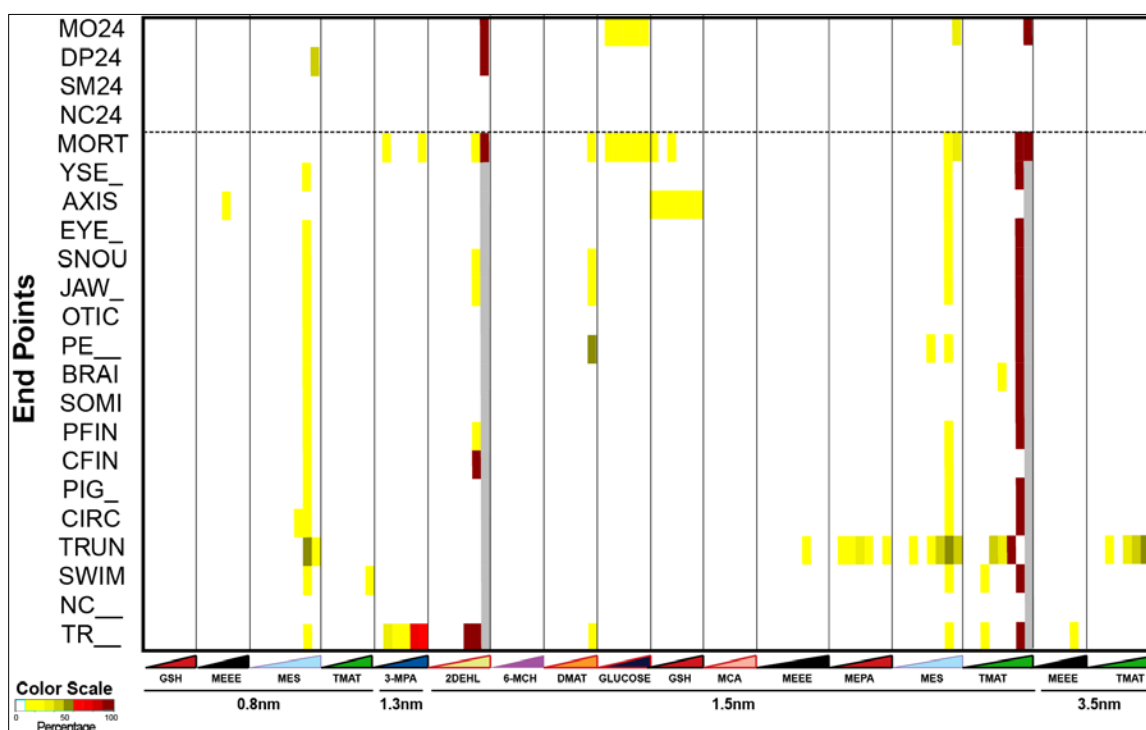
Figure 15. Heatmap depicting the biological response of 17 gold nanoparticles synthesized by Dr. James Hutchison's lab in size ranging from 0.8 – 3.5nm.

When 100% mortality was observed, the endpoints were grayed out to illustrate there were no survivors at that concentration. Surface functionalities influenced the toxicity of the cellulose nanocrystals. Endpoint evaluated are defined as follows: MO24 = mortality observed at 24 hpf; DP24 = developmental progression at 24 hpf; SM24 = spontaneous movement at 24 hpf; NC24 = notochord malformation at 24 hpf. Endpoints evaluated at 120 hpf were: MORT = cumulative mortality; YSE = yolk sac edema; AXIS = axis defects; EYE = eye defects; SNOU = snout defect; JAW = jaw defect, OTIC = otic (ear) defect; PE = pericardial edema; BRAI = brain defect; SOMI = somite defect; PFIN and CFIN = pectoral and cadual fin defect; PIG = pigmentation abnormalities; CIRC = circulation defects; TRUN = trunk defect; SWIM = swim bladder abnormalities; NC = notochord defect at 120 hpf and TR = touch response abnormality.

Objective 2: Define behavioral consequences following NP exposures
Deliverables: 1) Identification of the nanoparticle functional properties that interact with the developing central nervous system. 2) Identification of the neuronal populations that are targeted by nanoparticles.

In addition to the morphology toxicity screening level of nanomaterials, we developed assays to evaluate behavioral responses following nanoparticle exposures. This assessment measures motor activity levels induced by a change in lighting. Prior to evaluation, embryos are acclimated to the dark for 20 minutes, after which the lights are turned on (light period) for 10 minutes, and then off for ten minutes (dark period), and this alternation of light and dark is cycled 3 times. The total distance moved and their speed is recorded in a Viewpoint LifeSciences Zebrabox, a commercially available system. The raw output data files are processed using a custom perl script designed to compute the average total movement in either the light or the dark period. We have scaled this assay to measure up to 500 animals simultaneously. With a system in place, we identified behavioral abnormalities in embryonic zebrafish statically exposed from 6-120 hpf to a 1.5nm gold nanoparticle (AuNP) functionalized with N,N,N-trimethylammoniumethanethiol (TMAT), and 2-mercaptoethanesulfonic acid (MES), but not with 2-(2-(2-mercaptoethoxy)ethoxy)ethanol (MEEE). As Figure 16a illustrates, the total distance moved in the dark for embryos exposed to 50 µg/mL of MES- AuNPs and 10 µg/mL TMAT-AuNPs was significantly less than the control and 1.5nm MEEE-AuNPs. When analyzing the total distance traveled during the dark cycles for the three consecutive cycles, both MES-and TMAT-AuNPs induced hypomotor activity (Figure 16b). [31] With the numerous neuronal transgenic zebrafish lines available, we are positioned to identify which neuronal populations are being targeted by these nanoparticles in the near future.
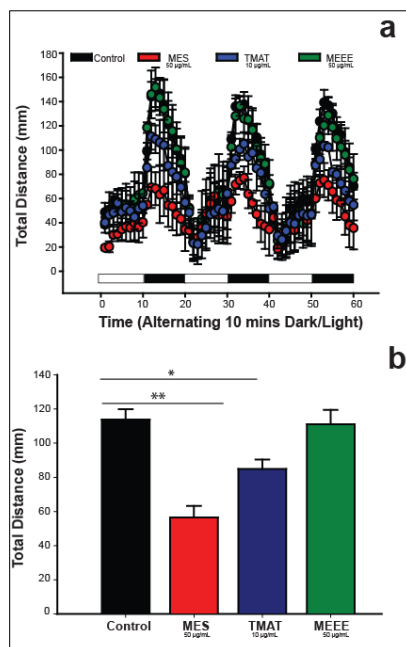
Figure 16. AuNP exposure results in abnormal behavior at 120 hpf.

Objective 3: Define cellular-level effects of nanoparticles in whole organisms
Deliverables: 1) Identification of cellular-level responses in whole animal model 2)
Localization of tissues/cell types affected by nanomaterial exposure
The zebrafish model can be effectively used to identify NPs that alter *in vivo* cellular death. We took advantage of this model by asking whether nanomaterials caused an increase in cellular death. Embryos were exposed to the nanomaterials, and then incubated with acridine orange, which is a dye, that penetrates weak cell membranes and when bound to DNA, fluoresces to signify cellular death. After an incubation period, the embryos are immediately euthanized and are imaged using a motorized microscope, which is time-consuming, as it can take up to 30 minutes to analyze a single animal. To overcome this laborious task, we developed and optimized a fluorescent plate reader-based assay. This plate-based approach makes the assay scalable to rapid through-put experiments where 96 animals can be analyzed simultaneously in less than 20 minutes. Although the plate-based assay does not allow localization of cell types affected by nanomaterial exposure, we have the ability to conduct the single animal imaging approach once we identify nanomaterials that causes cellular-level responses. By applying this concept to assessing nanomaterials, we assessed more materials and minimize the number of animals used. With these assays in place, we are equipped to investigate and localize the cellular-level responses.

Objective 4: Uptake and elimination profiles of newly synthesized gold NPs (AuNPs).
Deliverables: Whole animal body burdens of functionalized gold nanoparticles will be quantitatively determined using INAA.
We recognize that in general, nanomaterials can have differential uptake rates despite identical exposure conditions. With this knowledge, we took the approach to measure body burden of nanomaterials in zebrafish at certain times after exposure. Previously, we utilized instrument neutron activation analysis (INAA); however, due to its inability to measure metals without gamma radioactive isotopes (such as lead), the requirement of a radiation center and the relatively high cost of the analysis, it was difficult to routinely use INAA. As an alternative, we focused on determining the level of detection using Inductively Coupled Plasma – Mass Spectrometry (ICP-MS). As a proof of concept, we measured both gold and lead using ICP-MS.[29] ICP-MS can detect these metals in the 10 ppt range for gold and 20 ppt for lead, both are with a 5% accuracy. This method has been applied to estimate total embryonic NP load following exposure to a series of metal-cored NPs. We have also utilized ICP-MS to estimate the body burden of embryonic zebrafish exposed to 1.5nm MES-, TMAT- and MEEE-AuNPs. [29, 32]

Objective 5: Biodistribution analysis
Deliverables: Although we have NP structure and embryonic response data, to date we have not yet identified target tissues. These studies will identify potential target tissues for mechanistic-based studies.
Understanding the biodistribution of nanomaterials in a whole organism is currently the most difficult task at hand. If the nanomaterial is not synthesized with fluorescent material (ie: quantum dots), it is not trivial to visualize biodistribution, even in a small organism like the zebrafish, which is ~8 mm by the end of the toxicity assay (5 dpf). We have purchased and used numerous instrumentations in an attempt to identify potential target tissues. In collaboration with Dr. Stacey Harper (OSU), we purchased a Cytoviva Hyperspectral microscope in hopes to identify <2 nm nanomaterials, however there were many technical difficulties with this

Approved for public release; distribution is unlimited.

instrumentation when used for whole organisms although it has been demonstrated effective in cell culture.

Our next approach was to utilize electron microscopy on slices of embryonic zebrafish exposed to <2 nm gold nanoparticles. However, this task was laborious and calculated to take over 100 hours for a single fish. We conduct high-resolution microtomography (micro-CT) on exposed embryos and identified potential locations, but the cycle time and reproducibility was not ideal. Additionally, we have collaborated with Dr. Galya Orr (PNNL), to use their high power microscopes that are able to non-invasively image through live organisms. These microscopes were successful when using fluorescently labeled materials, but ineffective for <2 nm gold nanomaterials. We are currently working with Dr. James Hutchison's group (UO) to synthesize gold nanomaterials that are fluorescently labeled to overcome this important barrier.

Objective 6: Define the long lasting consequences following nanoparticle exposure. Deliverables: We will identify if specific nanomaterials properties that produce long lasting effects on vertebrate viability or function.
Previously, we identified that 1.5nm MES- and TMAT-AuNPs were developmentally toxic, while 1.5nm MEEE-AuNPs were not. To understand whether exposure only during development produced long lasting effects, we allowed embryos to be exposed from 0-5 days to embryo media, 10 µg/mL TMAT-AuNPs, and 50 µg/mL MES-AuNPs, and then washed and allowed to grow up to 122 days (which is when a zebrafish reaches adulthood). The concentrations selected did not produce any developmental effects during the 0-5 day assay. At 4 months of age, the number of adult zebrafish survivorship, length, weight and health condition was measured and calculated (Table 1). Condition factor (K) indices were calculated for each treatment to quantify the condition of the fish [K=mass (g)×100/length3 (mm)] and to account for the different number of survivors per treatment. In this study, we found that the different nanoparticles lead to an increase in both the weight and length of adult zebrafish, and that acute exposure to 1.5nm MES-AuNPs decreased the number of survivors into adulthood (Figure 17).[33] Additionally, we also found that the acute, developmental exposure to gold nanoparticles that only differed in their functional group, resulted in behavioral effects persisting into adulthood.

Table 1. Mean growth, survival and condition factor indices (±SEM) of adult zebrafish exposed to embryo media, MES- or TMAT–AuNP.

Exposure	Survival (%)	Length (mm)	Weight (g)	Condition factor (K)
Embryo media	80	34.78 (0.22)	0.50 (0.011)	0.97 (0.049)
MES-AuNPs	52	38.25 (0.32)[a]	0.63 (0.021)[b]	1.12 (0.032)
TMAT-AuNPs	78	36.27 (0.31)[a]	0.54 (0.016)	1.12 (0.022)

Means with different superscript letter designations within columns are statistically significantly different from the embryo media control (p<0.05).
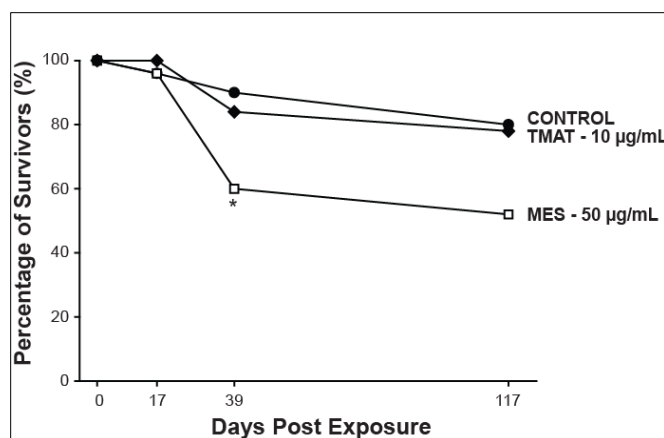
Figure 17. AuNPs effect on development into adulthood.

Percent of adult survivorship of embryos exposed to 1.5 nm MES- or TMAT–AuNPs, or embryo media control from 0 to 5 days post fertilization (dpf), and rinsed prior to being raised in fresh water until 122 dpf. Statistical significance was determined using a Fisher exact test. *p<0.05.

Interactions and fate of engineered nanomaterials in living cells and the zebrafish embryo
Galya Orr, Pacific Northwest National Laboratory
Investigate the response of lung epithelial cells to aerosolized nanoparticles at the air-liquid interface
The focus of this project was to delineate relationships between distinct properties of airborne engineered nanoparticles (NPs) and their cellular interactions, fate and response in alveolar epithelial cells at the air-liquid interface. The majority of *in vitro* studies characterizing the impact of NPs on cells that line the respiratory tract have been conducted in cells exposed to NPs in suspension. This approach introduces processes that are unlikely to occur during inhaled NP exposures *in vivo*, such as the formation of large agglomerates that no longer carry the properties of nanomaterial, the formation of coronas of proteins and small molecules found in the growth medium but not in the lung, and the shedding of toxic doses of dissolved ions into the growth medium, which is unlikely to occur during airborne exposures. These key differences limit the ability to extrapolate results from *in vitro* studies to pulmonary toxicity in animals or humans. To more closely mimic *in vivo* exposures to airborne NPs, we established the exposure of alveolar epithelial cells to aerosolized NPs at the air-liquid interface (ALI)[3]. This approach enabled us to delineate accurate relationships between properties of airborne NPs and cellular mechanisms and response that are relevant to inhaled NP exposures *in vivo*.

Our effort was initially focused on ZnO NPs, which are used extensively in multiple applications and pose a significant source for human exposure. ZnO NPs are readily dissolved in growth media, producing toxic doses of Zn^{2+} that might have been the cause for the confusion that still exists about ZnO NP toxicity. Exposures to airborne ZnO NPs can induce adverse effects, but the relevance of the dissolved Zn^{2+} to the observed effects *in vivo* is still unclear. Our goal was to mimic *in vivo* exposures to airborne NPs and decipher the contribution of the intact NP from the contribution of the dissolved ions to airborne ZnO NP toxicity. We established the exposure of alveolar type II epithelial cells to aerosolized NPs at the ALI, and compared the impact of aerosolized ZnO NPs and NPs in suspension at the same cellular doses, measured as the number of particles per cell. By evaluating membrane integrity and cell viability 6 and 24 hours post

25

exposure we found that aerosolized NPs induced toxicity at the ALI at doses that were in the same order of magnitude as those required to induce toxicity in submersed cultures. These observations unraveled the ability of airborne ZnO NPs to induce toxicity without the contribution of dissolved Zn^{2+} and suggested distinct mechanisms at the ALI and in submersed cultures[3]. While toxicity in submersed cultures might be dominated by the dissolved ions, toxicity at the ALI might be driven by direct interactions of cellular structures with the intact NP or with locally dissolved Zn^{2+} at the contact site of the NP with the cell, rather than from global dissolution. The work cleared the confusion created by *in vitro* exposures in submersed cultures by showing that ZnO NP toxicity is not dependent on the massive dissolution of the particles and the production of toxic doses of Zn^{2+}, unraveling the potency of exposures to the intact NPs.

To better understand the underlying mechanisms we quantified oxidative stress in cells exposed to aerosolized ZnO NPs at the ALI and in cells exposed to NPs in suspension. A fluorescent probe (DCF) was used to detect intracellular ROS generation and quantify their level over time using flow-cytometry. As shown in Figure 18, a significant increase in oxidative stress was detected at the ALI 6 hours post exposure ($p < 0.0001$) to a toxic NP dose, which decayed back to baseline 8-10 hours post exposure. Assessing membrane integrity in these cells by LDH release (*Figure 7B in* Xie et al[3]) showed a significant decrease in membrane integrity as early as 6 hours post exposure ($p = 0.0259$), which was correlated with the peak in oxidative stress. In contrast, a robust increase in oxidative stress of more than 10 fold was observed in submersed cultures as early as 2 hours post exposure ($p < 0.01$), which decayed back to baseline 8-10 hours post exposure. Despite the difference in the patterns of oxidative stress at the ALI and in submersed conditions, the pattern of membrane damage was similar in both conditions (*Figure 7D in* Xie et al[3]), showing a significant increase in LDH release as early as 6 hours post exposure.
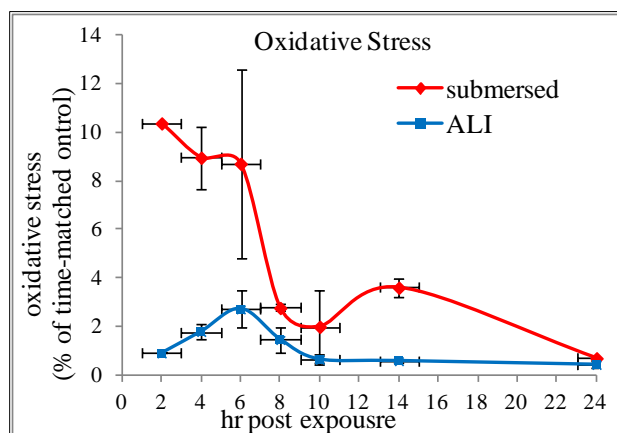
Figure 18: Oxidative stress response measured in alveolar epithelial cells exposed to aerosolized NPs at the ALI (blue) is fundamentally different than the response of cells exposed in submersed cultures (red) to the same cellular dose (measured as number of particles per cell).

A robust and immediate response is observed in submersed cultures where Zn ions are shed into the growth medium (*modified from Xie et al[3]*).

To test the hypothesis that toxicity in submersed cultures is largely due to readily available zinc ions that are shed into the growth medium, while toxicity at the ALI is due, at least in part, to the

intact NP, we quantified and compared intracellular Zn^{2+} concentrations in the two exposure systems. Using FluoZin™-3, a fluorescent indictor for Zn^{2+}, we quantified and compared intracellular Zn^{2+} in cells exposed to aerosolized NPs at the ALI and in cells exposed to NPs in solution using flow-cytometry. Figure 19 demonstrates the use of FluoZin™-3, showing increase in intracellular Zn^{2+} (green) in cells exposed to a toxic dose of aerosolized particles.
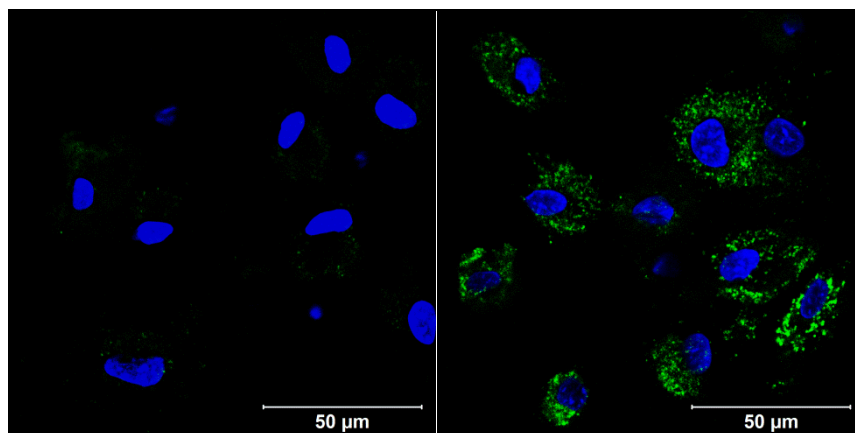
Figure 19: FluoZin-3 (Green) is used to detect and quantify intracellular Zn^{2+}, and Hoechst (Blue) is used to outline the nuclei in control cells (left) and in cells exposed to a toxic dose of aerosolized NPs right) (*modified from Mihai et al*[1]).

Using flow-cytometry, the fluorescence intensity of FluoZin-3 was measured in cells exposed to increasing NP doses in the two exposure systems. The average intensity of 30 thousand cells per exposure was calculated and plotted in Figure 20. A striking difference was found in cellular Zn^{2+} at the lowest toxic dose in submersed and ALI cultures. The levels of intracellular Zn^{2+} observed at the ALI were far below the levels observed in submersed cultures at toxic NP doses, suggesting that processes originating from the intact NP are involved in toxicity at the ALI[3].
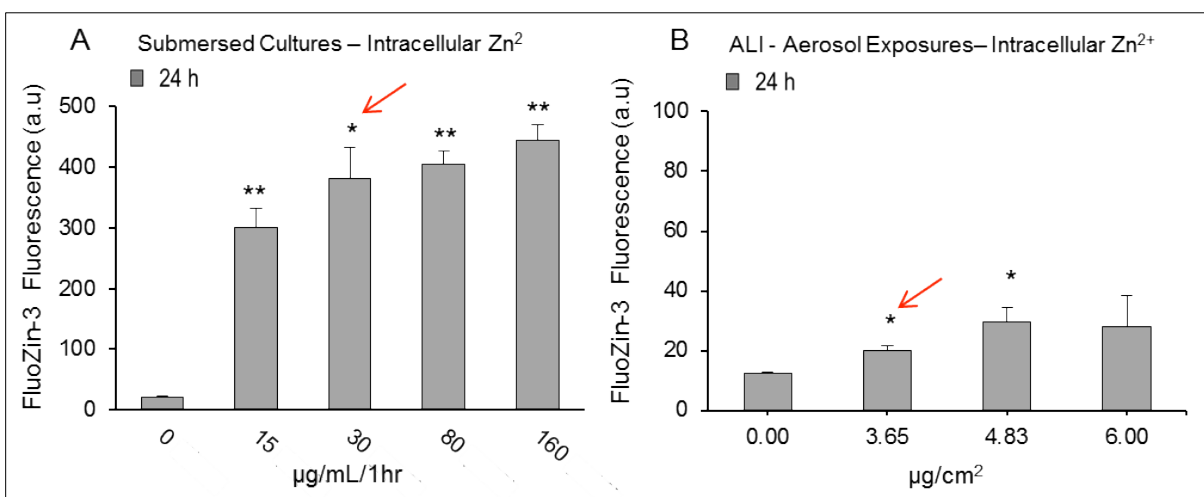
Figure 20: Intracellular Zn^{2+} was measured using FluoZin-3 in cells exposed to ZnO NPs in solution (A) and in cells exposed to aerosolized NPs at the ALI (B) 24 hours post exposure.

The lowest dose that initiates toxicity in each system is marked by the arrow. The level of intracellular Zn^{2+} at the toxic dose is nearly 20 folds higher in submersed cultures when compared with Zn^{2+} levels at the ALI, indicating that toxicity at the ALI is induced, in part, by the intact NP.

By measuring intracellular Zn^{2+} over time in cells exposed at the ALI to a toxic dose of aerosolized ZnO NPs we found that Zn^{2+} levels peak 3 hours post exposure (Figure 21), preceding the peak in oxidative stress by 3 hours. These observations suggest that a local dissolution of the internalized NPs inside the cell might contribute to oxidative stress and toxicity.
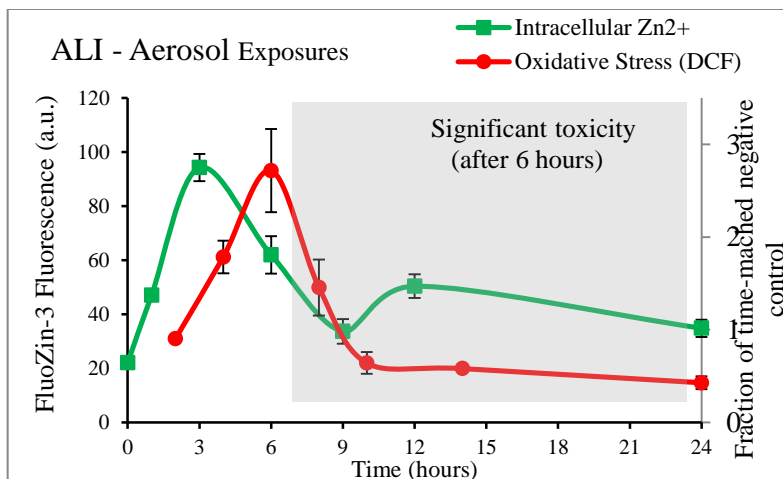
Figure 21: The level of intracellular Zn^{2+} (green) peaks 3 hours post exposure, preceding the peak in oxidative stress (red) by 3 hours, in cells exposed at the ALI to a toxic dose of aerosolized NPs. Intracellular Zn^{2+} decays over time but is kept above normal for at least 24 hours post exposure (*taken from Mihai et al*[1]).

Investigate the fate of NPs with distinct properties in developing zebrafish embryos over time

In collaboration with Dr. Tanguay and his group (OSU) we established different fluorescence imaging techniques to identify the fate of nanomaterial within zebrafish embryos and evaluate the impact of the exposures on the embryo's development. In addition to time-lapse wide-field fluorescence imaging, we used multi-photon confocal fluorescence microscopy incorporating NIR excitation, which provides deep penetration of the laser light with minimal damage to living tissues, to achieve 3D imaging of the NPs within the developing embryos over time. The fate of the particles was correlated with the development and survival of the embryos to identify toxic or biocompatible particle properties and underlying mechanisms.

Figure 22 demonstrates the use of the multi-photon confocal fluorescence microscope to detect the accumulation of quantum dots (red) within the developing embryo. The heartbeat (in the area marked by the yellow line) was observed all through the imaging session, indicating viability of the embryo. These quantum dots (CdTe) were toxic to the organism at 50 ppm and their accumulation within distinct tissues or organs could shed light on the underlying mechanism.

28
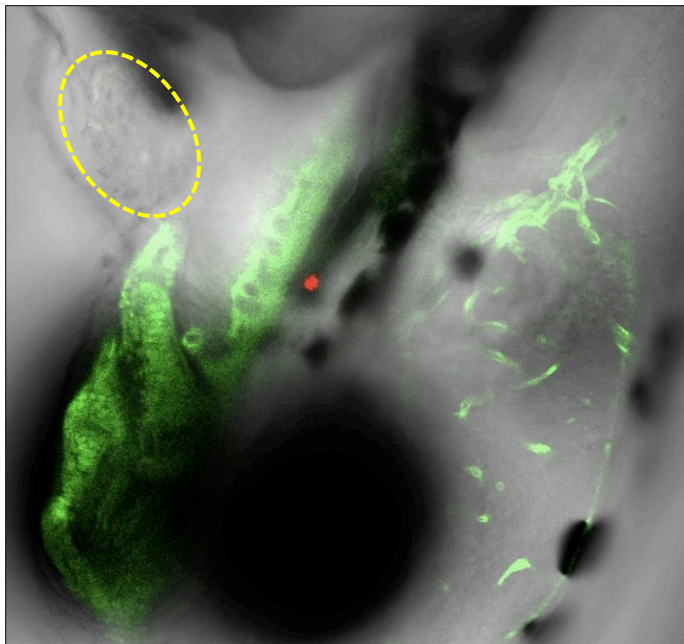
Figure 22: CdTe quantum dots (red), provided by AFRL, were used to expose transgenic embryos expressing FLI-GFP, a marker for vascular endothelial cells (green).

The quantum dots largely accumulated in the intestine (Figure 23), suggesting that their toxicity originates from interactions with cells and structures in the intestinal tract. Our effort established the techniques and protocols for further studies that will continue under the user program in EMSL to provide a better understanding of the processes leading to toxicity of these quantum dots.
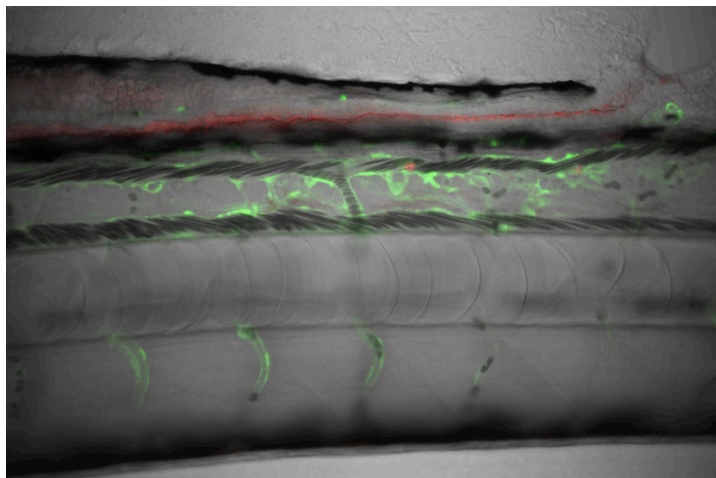
Figure 23: Image of a Zebrafish embryo exposed to CdTe quantum dots (red), showing the accumulation of the NPs within the intestine. The endothelial cells are marked by FLI-GFP (green).

Expanded libraries of precisely engineered nanoparticles
Libraries of precisely engineered nanoparticles for biological investigation
Jim Hutchison and Mark Lonergan (University of Oregon)
The objective of this Task was to produce well-defined reference materials needed for toxicological and biological investigations in partnership with researchers with the toxicologists, biologists and environmental scientists studying impacts (Task 1, see above) and the nanomaterials characterization specialist (Task 0). The task involved the production of materials with precisely controlled size, shape, composition, surface function and purity so that the influence of each structural feature on the biological impact may be determined. We developed new methods of synthesis and purification to access nanoparticles with new structural or chemical features and carefully characterized the materials to ensure strong correlations between nanoparticle structure/composition and the observed biological effect.

Preparation of new and reference materials needed to investigate the role of nanoparticle size, composition and surface function on toxicity and biological response
We developed new synthetic approaches and prepared new nanoparticles in support of a variety of toxicological, biological and environmental studies described in Task 1 of this report. The library of gold nanoparticles was expanded and refined to support the zebrafish assays conducted in Tanguay's laboratory[29, 31-33] and the studies on nanoparticle interactions with natural organic matter in Nason's group.[34] In addition, we examined the role of the inorganic core by preparing PbS nanoparticles with different surface coatings.[35]

More than a dozen new or refined thiol-stabilized gold nanoparticles were prepared. In each case, refinements to the synthetic procedures were required to gain even greater control over the nanoparticle structural definition and to establish that structure rigorously. To support these efforts we developed new synthetic methods for triphenylphosphine-stabilized undecagold, developed methods to prepare water-soluble, ligand stabilized nanoparticles with larger core diameters and extended our characterization of the nanoparticles to include characterization in the exposure media.

We used *diafiltration*, a continuous-flow nanoporous membrane separation technique used in biotechnology applications as a primary approach to remove small molecule impurities from nanoparticles. In certain cases where diafiltration was not effective, for example with nanoparticles that were not soluble in water, we developed several chromatographic purification strategies.

In order to establish the relationship between nanoparticle structure and biological response, it is necessary to thoroughly characterize the structural parameters in each nanoparticle material. Two key innovations developed in this area include rapid analyses of particle core size and size distribution using transmission electron microscopy and our SMART TEM Grids and the use of laboratory-based SAXS as a routine tool for rapid nanoparticle size and distribution characterization. We reviewed our approach to successful nanoparticle characterization in a recently published perspective article in ACS Nano.[15]

Environmental transformations of nanoparticles
We used the SMART TEM Grids to monitor the effects of environment on nanoparticles by tethering the nanoparticles to the grid, exposing them to different environments and examining the changes by transmission electron microscopy.[36] The key results of these studies were: 1. TEM images of silver nanoparticles five weeks showing the degradation of the parent particles and the generation of new nanoparticles when held in 100% humidity on surfaces. In solution these particles are stable on the order of months; 2. TEM images showing the generation of nanoparticles from silver wire, a silver earring, silverware, and a copper wire showing the presence of a previously undetected source of nanomaterials. These results improved our understanding of the fundamental transformations of nanoparticles that are important for developing a realistic picture of how materials will change when "released" into natural environments. Our work on silver nanoparticles should influence the regulation of silver nanoparticles in consumer products and help to further develop metrics for silver release from both large and small objects.

Develop precise libraries of oxide and compound semiconductor nanoparticles and purification methods for investigation of biological interactions.
The libraries of gold nanoparticles are precision probes to examine the influence of surface modification and nanoparticle dimensions on the biological or environmental activity of the nanoparticles. What is missing are analogous libraries of nanoparticles that make it possible to probe the influence of the nanoparticle core material. Within this task we took some important steps toward developing such libraries and overcame two significant challenges associated with these materials.

Typical metal oxide or chalcogenide nanoparticle syntheses involve the production of the nanoparticle in the presence of oleic acid or some other stabilizer that can prevent introduction of water-solubilizing surface ligands. One needs to find ways to conduct ligand exchange reactions that introduce the desired ligand. We chose to examine these reactions for PbS nanoparticles because these are technologically important and to examine how a nanoparticle with a heavy metal in the core would influence the toxicity of the nanoparticles. We were able to replace oleic acid ligand on the PbS with a thiol-containing ligand. This solution was suboptimal because the photoactivity of the lead sulfide caused the sulfur-binding group to oxidize, making the thiol ligands unstable.[37] Thus, we developed a way to attach a chelating ligand with two binding groups to the PbS core. This ligand remains stable in the presence of light. It also diminishes or eliminates the toxicity associated with lead exposed on the surface.

The other problem that we recently overcame is gaining reliable access to metal oxide nanoparticles. These nanoparticles are typically produced at temperatures in excess of 300 °C, requiring sophisticated control over the reaction conditions. As a consequence, there can be variability in the size, size distribution and crystallinity of the material. Furthermore, the high temperatures prohibit the use of more sensitive stabilizing agents. We recently discovered a new general approach to the production of a wide range of metal oxide nanoparticles that allows rapid access to these nanoparticles under mild conditions. Investigations are underway to examine how ligand exchange can be used to introduce water-solubilizing ligands and produce metal oxide nanoparticle libraries to complement the gold nanoparticle libraries.

Exploration of the use of naturally occurring lipids to control nanoparticle shape and size
Scott Reed (formerly at Portland State University, now at the University of Colorado, Denver)
The primary outcomes from this project are categorized in the following three sub-projects: 1) Use of lipids as benign ligands for nanoparticle synthesis 2) control of nanoparticle shape using lipids, and 3) minimization of toxic reducing agents (formaldehyde) in the synthesis of nanomaterials. The first and second sub-projects originated from the original Statement of Work for this project and were the focus of most of our effort. The second goal is the thesis work of a graduate student that has not yet defended his thesis and more results are anticipated as this project is wrapped up. The third sub-project arose from a serendipitous discovery during our work.

Sub-project 1: Use of lipids as a benign ligand for nanoparticle synthesis
We have developed techniques to prepare gold and silver nanoparticles using lipids as capping ligands. We have published our results using gold nanoparticles and phosphatidylcholine (PC) lipid.[38] Many nanoparticle properties can be tuned using this approach including metal core size and solubility. In particular, an unprecedented solubility conversion was observed that allows for new methods for preparing and modifying functional nanostructures in benign solvents. Preparation of nanoparticles in organic solvents (*e.g.* dichloromethane, chloroform, or toluene) provide for an optimal narrow core dispersity. Transfer from organic solubility to water solubility occurs by the formation of a lipid bilayer structure. The particles were found to retain their spherical shape and average core diameter of 7 nm during multiple solvent transfer events. Figure 24 is a representative sample of gold nanoparticles prepared from PC in a biphasic solvent system with sodium borohydride reducing agent. By performing the synthesis in organic solvent and then transferring to water, a much narrower dispersity is achieved.

Samples of these PC-stabilized gold nanoparticle were sent to Stacey Harper (OSU) for toxicity analysis and are included in the SNNI database. Substantial progress has been made in characterization of lipid-stabilized nanoparticles prepared by a number of different synthetic routes. The routes including aqueous, organic, and biphasic synthesis that involve a phase transfer of nanoparticles.
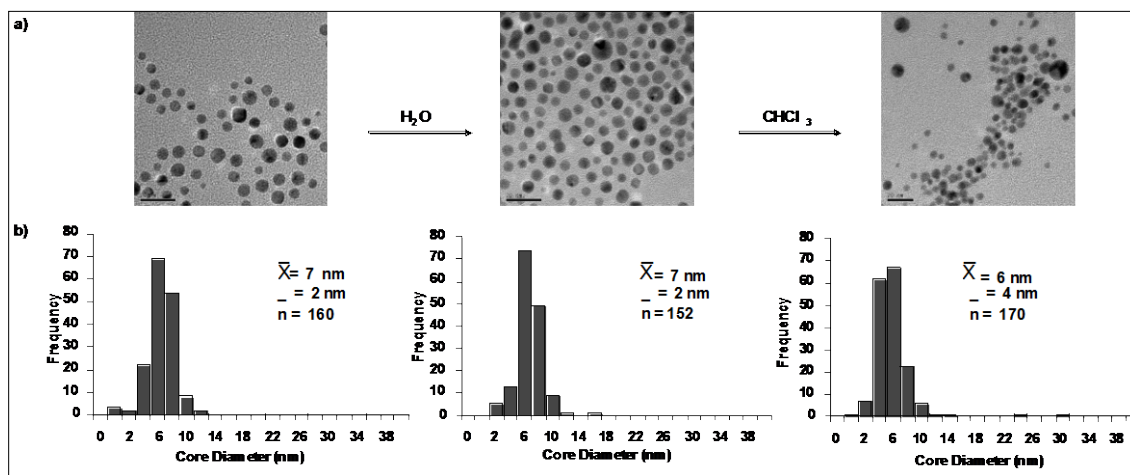
Figure 24. TEM micrographs of Au-Soy$_{95}$PC nanoparticles as synthesized in H$_2$O/CHCl$_3$, with NaBH$_4$ (Left) after transfer to H$_2$O (center), and after re-suspension in CHCl$_3$ (right). Scale bars = 20 nm. n = total number of particles counted.[38]

We have also designed a two-step synthetic approach that provides a route to asymmetric bilayer coating of metal nanoparticles. The TEM shown in figure 25 was prepared from a stepwise addition of Soy$_{95}$PC to precursor monolayer coated nanoparticles. Transfer from organic solubility to water solubility occurs with the formation of a bilayer structure. The particles were found to be spherical of with an average core diameter of 11 nm. These nanoparticles were ~3 nm smaller than observed in the monolayer coated nanoparticle.
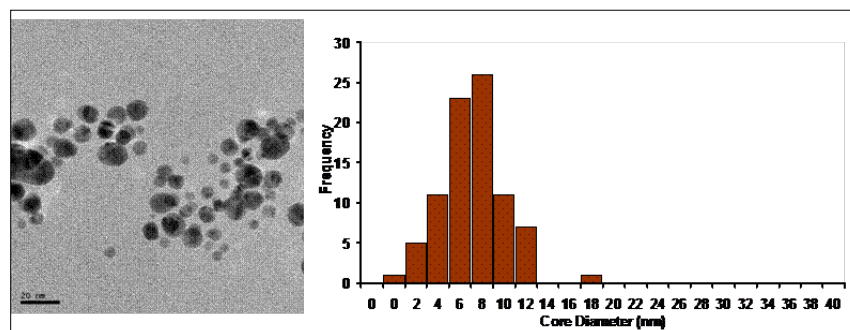
Figure 25. TEM micrograph of a representative sample of the bilayer Au-[Soy$_{95}$PC][Soy$_{95}$PC] nanoparticles in H$_2$O.

Using water-soluble PC nanoparticles we have explored the interaction of porphyrin dyes with the gold in order to better understand and control the quenching ability of the gold. Water-soluble lecithin stabilized gold nanoparticles were synthesized as described previously and ligand exchange was performed with mercaptopropanesulfonate. These samples were then mixed at various concentrations with tetrapyridyl porphyrin to investigate quenching interactions. On-going work will explore the use of these nanoparticle-fluorophore conjugates as biocompatible probes.

We next developed hybrid bilayer nanoparticles (HBNs) using thiols in combination with lipids that provides a strong protective coating for the nanoparticles. Addition of a sub-monolayer quantity of hydrophobic alkanethiol provided an anchor that hold the lipids close to the metal core resulting in nanoparticles that are stable to temperature, acid, and high concentrations of cyanide. This is the first report ever of hybrid bilayers supported on gold nanoparticles.[39] These materials will provide insight into how endocytosis and exocytosis occur and will contribute to our understanding of how synthetic nanostructures can be used for drug delivery. While previous papers have reported stability of gold nanoparticles to cyanide for hours or days, we have stored samples in cyanide etch for months without measurable loss. We are aware of no other ligand system with comparable stability. This will be of utility for lithography, sensors, and many other applications. These materials may also provide insight into the environmental fate of synthetic nanomaterials.

To further establish the applicability of these green nanoparticles as useful probes and models, we explored the use of the nanoparticles as low-density lipoprotein (LDL) mimics for detection of C-reactive protein (CRP). This involved the development of a synthesis using sodium oleate to facilitate curvature of lipids around gold nanoparticles prior to lipid coating.[40] We established technique for controllable clustering of nanoparticles using biocompatible combination of

phospholipid and sodium oleate (TEM of CRP induced clustered gold nanoparticles in Figure 26 below).

We described a novel bio-mimetic system that mimics the exterior lipid coating of LDL. We reported on the use of this system to study how CRP recognizes nanoscale curvature in lipid membranes. CRP levels are used to identify patients for statin therapy, however, much remains unknown about how CRP recognizes damaged membranes and lipoproteins. Our discovery sheds light on the role of CRP and how membrane shape may be an important part of how apoptotic cells are recognized and removed from the body. This work will have an impact on research on nanomaterials, atherosclerosis, and the design of protein diagnostics. We determined that CRP causes clustering of PC coated gold nanoparticles (Figure 26).
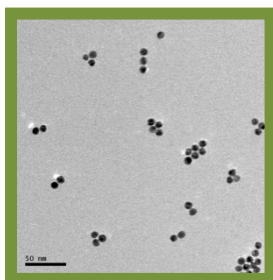
Figure 26. CRP induced clustering.

Sub-project 2: control of nanoparticle shape using lipids
We have successfully expanded our lecithin-based green synthetic routes to include the synthesis of silver nanoparticles, gold prisms, and silver-gold core-shell nanomaterials. In the process of finding a substitute for CTAB in gold nanorod (GNR) growth, we chose L-α-Phosphatidylcholine because of its similar trimethylammonium head group and its abundance in soybeans. However, no asymmetric growth was seen when using PC with $HAuCl_4$. Upon adding CTAB to $HAuCl_4$ the Au^{III} solution is a bright yellow and changes to an orange color which led us to believe there was an exchange of Cl^- for Br^-. Upon addition of KBr to the Au^{III} solution, the solution turns a dark orange color. Particle growth using this Au^{III} source with bromide gives a second plasmon in the near-infrared (NIR). The increasing amounts of bromide give longer wavelength shifts in the red shifted plasmon.

This however, did not give reproducible results in regards to the intensity of the red-shifted plasmon and investigations are under way to determine the mechanism responsible for this anisotropic growth. A NIR SPR was obtained using 30 % purity soy lecithin. When 95% purity PC was used scattering and precipitation resulted. This led us to believe there are other ligands in 30% soy lecithin that help to stabilize the particles and may contribute to asymmetric growth.

For control of aspect ratio, it is shown that the amount of ascorbic acid added can control the length of the rods. There is a lower limit to the amount of ascorbic acid used as shown when concentration falls below 100 mM. Coarse tuning of the plasmon from 700 nm up to 1050 nm is possible. In order to fine tune the NIR region, we found that the amount of seed added can easily control the plasmon to within ~50 nm.

The main controlling feature we have found in particle growth is the seed. Multiple seed sources and seed preparations have been utilized in the growth of GNPs and we have found that the source of the seed is important for anisotropic growth.

Purification of GNRs in solution was achieved by centrifugation of a prepared solution at 4000 rpm (~1900 g). After 1 hour, the supernatant retains some of its red color and upon inspection of the pellet (after being re-dissolved in water), it is seen that the red-shifted plasmon increases in intensity as compared to the blue shifted plasmon. TEM spectra of these particles show an increased amount of rod shaped nanoparticles of differing aspect ratios and prisms.

Sub-project 3: minimization of toxic reducing agents (formaldehyde) in the synthesis of nanomaterials.
We asked ourselves why metal nanoshell and core shell syntheses were being performed with a 1000-fold excess of the toxic reagent formaldehyde and found some interesting answers. All prior reports overlooked the fact that ammonia and formaldehyde react to form a polymer. And it is this polymer that is responsible for asymmetric deposition of silver coatings. We discovered that 1) The polymer formed by formaldehyde and ammonia is critical to obtaining near-infrared absorbing gold-silver core-shell nanoparticles and 2) formaldehyde can be cut 100-fold by understanding this additional role of formaldehyde.[41]

Core-shell structures were clearly identified in TEM images and the EDX analysis showed that the inner core is Au and the outer shell is Ag. These gold-core / silver-shell nanoparticles structures have potential applications in biomedical research. Initial reduction results in spherical silver nanoparticles, followed by the gradual formation of the core-shell materials. The gradual asymmetric growth is visually striking: the yellow solution gradually turns into a green solution within a period of one hour. The UV spectra show the gradual asymmetric growth at the cost of spherical silver nanoparticles evidenced by the gradual decrease in the intensity 400 nm region.
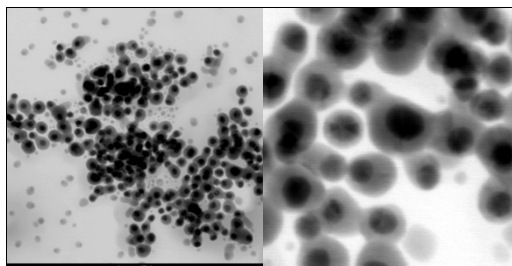
Figure 27. Representative TEM of gold-core / silver-shell nanoparticles.

As nanomaterials become adopted for larger-scale applications it is important to optimize their syntheses to reduce the potential environmental impact of their production. The persistent use of high concentrations of formaldehyde since Zsigmondy's original synthesis suggests that the properties of this polymer or similar polymers could favorably influence the metal coating process. Therefore, finding a suitable replacement for this polymer could help to minimize the use of formaldehyde and allow a switch to more benign reducing agents.

Nucleic Acid Functionalized Gold Nanoparticles for Biological Sensing and Therapeutic Applications
Andy Berglund, Jim Hutchison (University of Oregon)
Study of Nucleic Acid-Au Surface Interactions
The goal of our project was to identify ssDNA/RNA sequences that have exquisite binding specificity and/or high affinity for the surface of nanoparticles (NPs) of interest and to use them to mediate nanoparticle growth. Based on the exciting properties and potential applications of gold nanorods (AuNRs) in therapeutics, we selected them as our first target.

Our initial approach was to use SELEX (Systematic Evolution of Ligands by Exponential enrichment) to identify aptamers that bound Au surfaces with high affinity (Figure 28). SELEX is a powerful methodology that isolates and amplifies rare ssDNA or RNA sequences with unique characteristics from the large pool of random molecules (10^{14}).
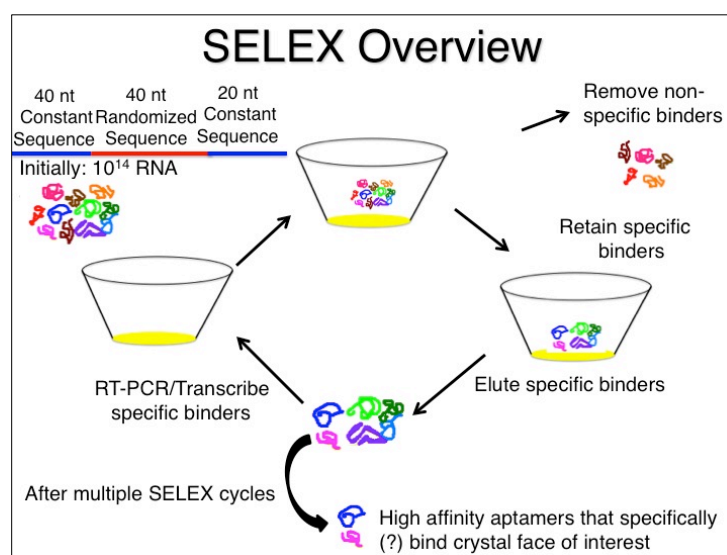
Figure 28: SELEX overview. Au(111) crystal face is prepared by evaporation.

Randomized DNA sequences are transcribed into RNA, which forms the initial pool of aptamers. This pool is incubated with the surface, and non-specific binders are rinsed away. Specific binders are then eluted. These binders undergo RT-PCR, which converts them to cDNA. They are then amplified by PCR. The cDNA is transcribed to form the RNA pool for the next round of SELEX.

To isolate aptamers that bind to specific gold surfaces, we designed and constructed a microreactor that we dubbed *in vitro* selection on surfaces (ISOS). ISOS allows for the selection of RNA aptamers for virtually any planar substrate (Figure 29). While we initially focused on the Au(111) surface, the ability to select aptamers for any surface could have numerous applications in nanotechnology and surface science. ISOS allowed us to precisely control the surface area of Au(111) exposed, the volume and concentration of RNA in the experiment and the temperature.
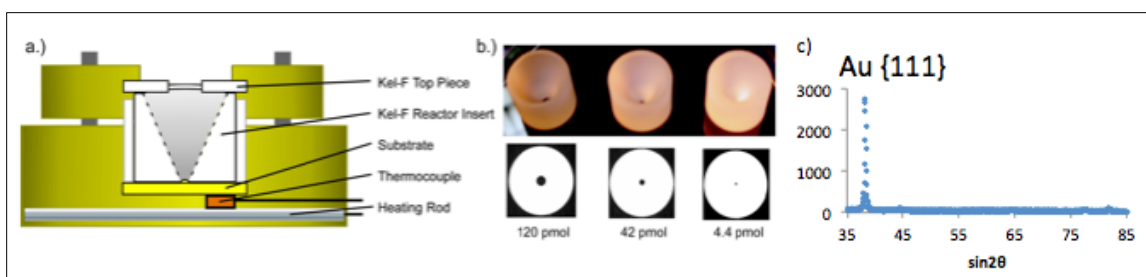
Figure 29: ISOS microreactor used in our SELEX a) Cutaway view of ISOS b) three inserts used to control the concentration of Au during the SELEX experiment c) XRD performed on evaporated Au surface

In our SELEX experiment, we performed six rounds of selection, increasing the stringency of the selection with each step by either decreasing the surface area of gold available, increasing the concentration of competitor tRNA or increasing the temperature. This resulted in the isolation of ~1000 high affinity sequences out of an initial pool of 10^{14} sequences. Interestingly, the isolated sequences were comparatively purine rich (Figure 30). We hypothesize that the adenine residues interact more strongly with the surface than the other nucleobases, as described previously.[42]
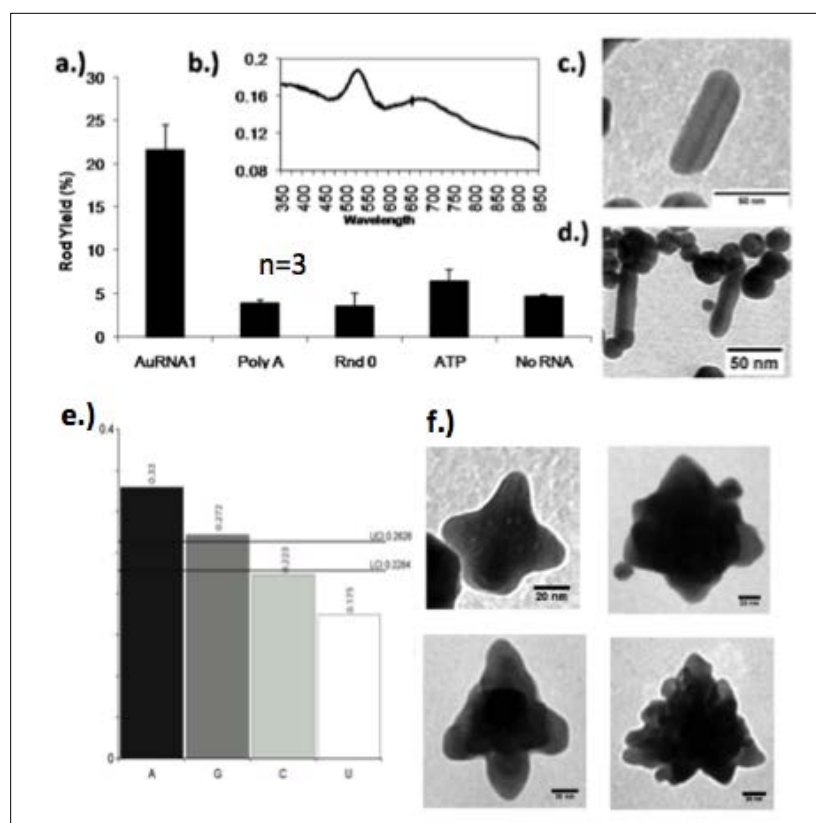
Figure 30: Preliminary Results of the SELEX performed on evaporated Au {111} a.) Percent yield of gold nanorods for NPs produced using different sequences b.) UV-Visible absorbance of NPs produced using AuRNA1 c.&d.) Images of gold nanorods produced using AuRNA1 e.) % of each base in final pool aptamers f.) Shapes produced using AuRNA2.

We screened the isolated aptamers for their ability to mediate NP growth. Initially, we found two promising sequences that appeared to dictate NP growth and dubbed them AuRNA1 and AuRNA2 (Figure 30). AuRNA1 seemed to promote growth of AuNRs, whereas AuRNA2 seemed to promote growth of Au tripods. Unfortunately, the apparent influence of these aptamers upon growth of the nanoparticles was not robust. When we had only performed a few trials (n=3), it appeared that AuRNA1 produced AuNRs in 22% yield. As the number of synthetic trials increased, it was clear that statistically, the aptamers were having no effect on NP formation.

We were concerned that we may have inadvertently selected for aptamers that would predominantly bind spherical Au, the surface of which is known to be mainly Au(111). We began work on some AuNR assemblies and planned to perform a new SELEX experiment on the actual substrate of interest. We first decided it was necessary to test our assumption that our SELEX conditions were conducive to competition for the Au surface between individual aptamers. Therefore, we developed a binding assay appropriate for testing the binding affinity of the sequences.

For our binding affinity assay, we employed Whatman's minifold dot blot array to separate an evaporated gold surfaces into individual $2mm^2$ areas. Our plan was to saturate the gold surface with a radiolabelled competitor and then add an unradiolabelled competitor to compete with it to bind the Au (Figure 31). We planned to characterize the relative binding ability of each sequence according to what concentration of it was required to remove half of dA_{15} bound to the surface.
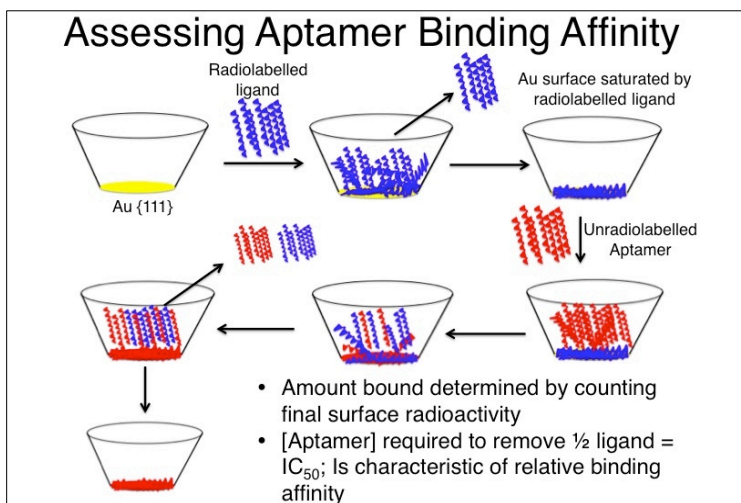
Figure 31: Assay for Assessing Aptamer Binding Affinity.

The Au (111) surface is prepared by evaporation. A microdot blot array separates the gold surface into a series of $2mm^2$ surface areas. Radiolabelled ligand is added to the surface and incubated. Excess ligand is removed. Unradiolabelled aptamer is added to compete with the ligand for the surface. Scintillation counting is used to measure the final amount of ligand bound after the competition.

Approved for public release; distribution is unlimited.

First, we determined that 50-100 pmoles of dA_{15} (Figure 32) or dC_{15} (data not shown) was sufficient to saturate each $2mm^2$ gold area. Then we ran a series of experiments in which we pre-bound the Au surface with one radiolabelled sequence and tried to remove it using a large excess of unradiolabelled competitor (Figure 32). This did not work, even when there was over $1x10^6$ times more competitor than original binder. Extending the competition time to up to 24 hours also had no influence on the ability of either oligonucleotide to remove the other from the surface of the gold. This means that SELEX is an inappropriate way to identify/isolate nucleic acid sequences with a high binding affinity to a Au surface.
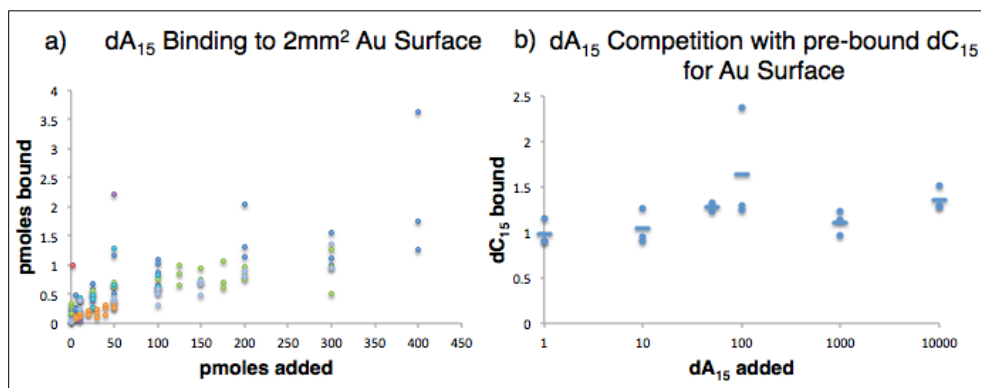
Figure 32: Binding assays. a) Sample binding curve used to determine how much of each oligonucleotide saturated the Au surface b) Competition assay in which dA_{15} was used to try and remove radiolabelled dC_{15} previously bound to the Au surface.

Conclusions from this study

- ISOS is a promising way to isolate sequences of DNA/RNA that bind surfaces of interest
- A new method for evaluating relative binding affinities of labeled molecules to surfaces has been developed
- Single-stranded DNA interacts strongly with Au surfaces. Once a sequence is bound, other sequences of DNA are unable to displace it effectively from the surface. This means SELEX is not a good way to identify sequences that can influence NP formation, since it relies on competition between sequences during a series of binding events.
- Decreasing DNA chain length did not permit displacement of bound nucleic acids (data not shown), suggesting electrostatic repulsion may play a more important role than steric hindrance.

Future work: We are in the process of testing the relative affinity of single-stranded DNA sequences for Pd surfaces. We are interested in determining whether individual sequences can displace other sequences bound to the surface.

Aptamer-based Colorimetric Nanoparticle Sensors

The long-term goal of this project is to design/synthesize colorimetric nanoparticle aptasensors that rapidly and reproducibly detect environmental pathogens and/or contaminants with high selectivity and sensitivity.

Detection of allergens, pathogens, pharmaceutical compounds and environmental pollutants by aptamer-based sensors is typically based on fluorescence[43], enzymatic cleavage[44], PCR[45, 46], electrochemical[47] or colorimetric nanoparticle methods.[48] From a personal or commercial detection standpoint, colorimetric sensing has a huge practical advantage over other detection methods because the process is rapid and requires no specialized equipment or technical expertise.

In typical aptamer-based colorimetric sensing, DNA-functionalized nanoparticles are first assembled into aggregates based on interactions between complementary DNA sequences, causing them to appear blue (Figure 33). After analyte addition, the nanoparticles disassemble, causing the solution to turn pink (Figure 33).
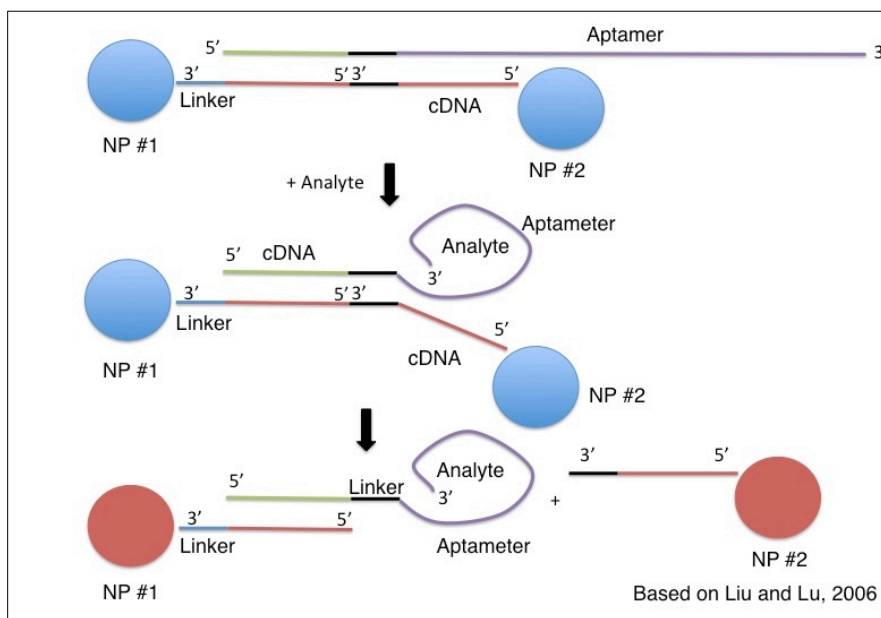
Figure 33: Aptamer-based Colorimetric Sensing Scheme.

In the absence of analyte, NPs assemble into aggregates and their plasmons interact. When analyte is added, the interaction is disrupted, resulting in a colour change.

A key problem with existing colorimetric nanoparticle sensors is that that they fail to respond to biologically relevant analyte concentrations. An existing adenosine sensor[49] employs an aptamer whose L.O.D. is in the 1-10 μM range.[50] The average adenosine concentration in cells is 1.5 uM[51] and it spikes in response to nearby tissue injury. The nanoparticle assemblies only react ≥ 300 μM[48, 49]. In our work, we hope to increase the range of analyte detection to include biologically relevant concentrations.

Our approach consists of attaching DNA aptamer sequences to glutathione(GSH)-stabilized nanoparticles via the use of a novel NHS ester-maleimide linkage (Figure 34), and optimizing the attachment conditions to produce NPs with very few DNA sequences attached to them. We hypothesize that decreasing the number of sequences attached to each particle will reduce the size of nanoparticle aggregates, eliminating steric hindrance that prevents interaction of the aptamer with the analyte, thus increasing the sensor's response range.
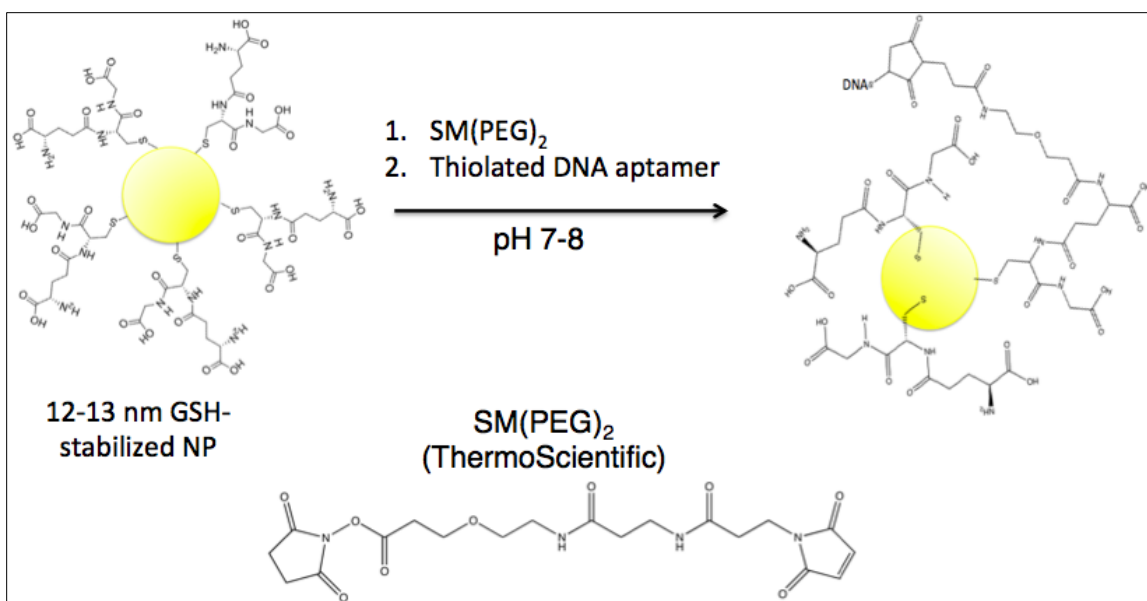
Figure 34: Approach to Functionalizing GSH-stabilized NPs with aptamers.

A solution of GSH-stabilized NPs in sodium phosphate buffer is incubated with SM(PEG)$_2$, then thiolated DNA. The NHS-ester of SM(PEG)$_2$ reacts with GSH's primary amine, and then the maleiimide groups reacts with the thiol group on the DNA. The product is purified by diafiltration.

Initially, we have focused on performing ligand exchange on citrate-formed NPs to produce GSH-stabilized NPs. We found that adding HAuCl$_4$ to citrate solution at reflux produced a well-defined product (Figure 35). We used transmission electron microscopy (TEM) to verify that the particles were spherical, and small angle x-ray scattering (SAXS) to determine that the size distribution was 13.7 ± 1.8 nm (data not shown). X-ray photoelectron spectroscopy (XPS) confirmed that a thiol was bound to the surface of the NPs.
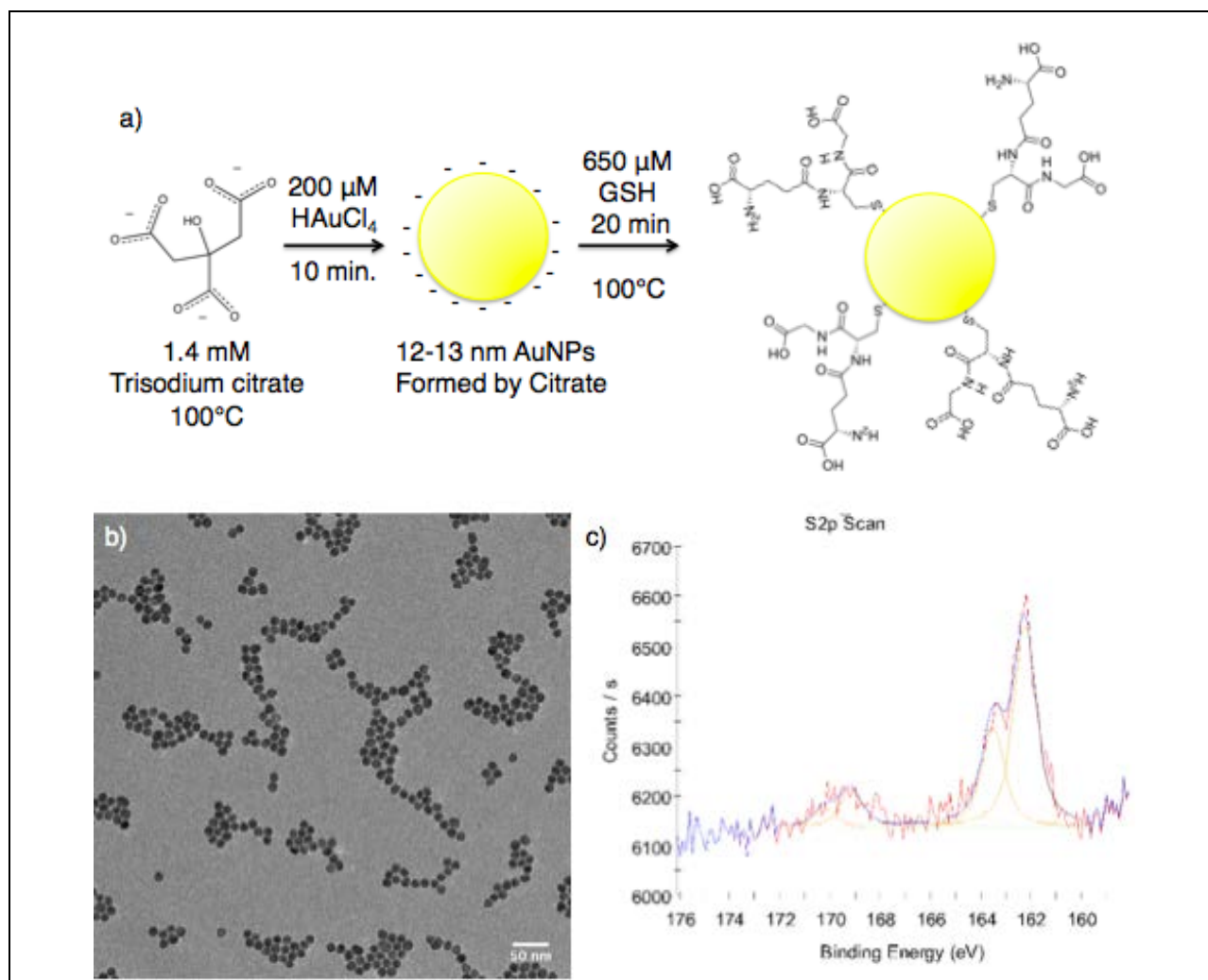
Figure 35: a) Preparation of GSH-functionalized NPs. Citrate-stabilized NPs are prepared by adding HAuCl₄ to citrate solution at reflux. After 10 minutes, GSH is added while still at elevated temperature. The solution refluxes 20 minutes and is then removed from heat and left to stir overnight. NPs are purified by diafiltration. b) TEM shows NPs are spherical c) XPS demonstrates thiol bound to NPs.

We then tested the salt stability of the GSH-stabilized NPs. Salt stability is crucial, since physiological concentrations of NaCl are around 150mM and hybridization of DNA-functionalized NPs is typically performed at 300mM.[48, 52] We found that the purified GSH-functionalized NPs were completely stable in up to125 mM NaCl solution, a large improvement over the <50mM NaCl salt stability of the citrate NPs themselves (Figure 36). We also found that backfilling the GSH ligand shell with a thiolated PEG8 chain further increased the upward limit of salt stability to 200-250 mM.

Figure 36: Salt stability of NPs as a function of ligand shell.

Citrate and GSH stabilized NPs were prepared as before (Figure 7) and then purified by diafiltration. Purified GSH NPs were incubated with 3 μM OEG and then diafiltered. Each nanoparticle solution is buffered to pH 7.8 in 0.01 M sodium phosphate prior to incubating it in a solution containing the appropriate NaCl concentration.

Conclusions from this study

• 12-13 nm AuNPs are readily functionalized with glutathione (GSH)

• GSH-stabilized NPs are more stable in salt solutions than citrate-stabilized AuNPs or AuNPs functionalized with small amounts of DNA

• GSH-functionalized NP stability is further increased by back-filling the ligand shell using OEG

Future Work

• Employ SM(PEG)$_2$ to anchor DNA aptamer sequences of interest to the NPs

• Assess effect of decreasing amount of DNA sequences attached to the NPs on their sensing performance

• Optimize NP assembly configuration for increased range of sensor response

Modify the surface functionalization of nanoparticles
Mingdi Yan (Portland State University)
The goal of this project is to develop methods of introducing surface functionality to interface nanoparticles with other materials while maintaining a reduced toxicity. Functional nanomaterials must be capable of interfacing with a wide array of other materials. The use of ligand exchange reactions to introduce surface functional groups will be extended by introducing new ligands that can be easily conjugated to a wide range of materials after the exchange. This method allows conjugation to nearly any carbon-based material regardless of chemical functionality. There is no need to introduce specific functional groups onto the material that will be conjugated. The functional group to be introduced on nanoparticles is the perfluorophenyl azido (PFPA) group. Upon photochemical or thermal activation, the PFPA group undergoes insertion reactions with neighboring molecules. This conjugation chemistry does not require the attached molecules to possess reactive functional groups and is therefore universal. We will synthesize PFPA-functionalized metal and silica nanoparticles that can then be used to immobilize a variety of molecules and materials.

Nanoparticles functionalized with photoactive cross-linking moieties.
Silica and gold nanoparticles including nanorods will be functionalized PFPAs containing a silane or a thiol group will be used to functionalize silica or Au nanoparticles. A PFPA-disulfide and a silane-containing analog will be used to functionalize gold and silica nanoparticles respectively.

Techniques for photoactive cross-linking of nanoparticles to surfaces.
The first class of materials to be tested will be synthetic polymers. To immobilize the polymer, PFPA-functionalized nanoparticles will be dispersed in a polymer solution. Thermal or photochemical cross-linking reactions will be used to link nanoparticles to surfaces followed by purifications to remove the unattached polymer.

This new technique relies on the photochemistry of perfluorophenylazides (PFPAs). Irradiation of PFPAs generates highly reactive singlet perfluorophenylnitrenes that can subsequently undergo C-H, N-H insertion and C=C addition reactions with the neighboring molecules (Scheme 1). The functional group R serves as the anchoring point to the nanoparticle whereas the azido groups form covalent bonds to the polymer upon UV activation. The functionalized PFPA therefore acts as a coupling agent attaching polymers to nanoparticles surfaces. The F atoms on the phenyl group increase the life-time of the perfluorophenyl nitrene that subsequently undergoes insertion reactions. Without F, the photogenerated singlet nitrene quickly rearranges to the corresponding 7-membered ketenimine which reacts with amines to give azepinamines, or produces polymer tars in the absence of a nucleophile. An advantage of this technique is the possibility to immobilize a wide variety of molecules because no special functional groups are necessary for the attachment. In addition, the R group can be selected depending on the chemical composition of the nanoparticle. This approach is therefore general with respect to both the molecule to be attached and the type of the nanoparticle material.

Approved for public release; distribution is unlimited.
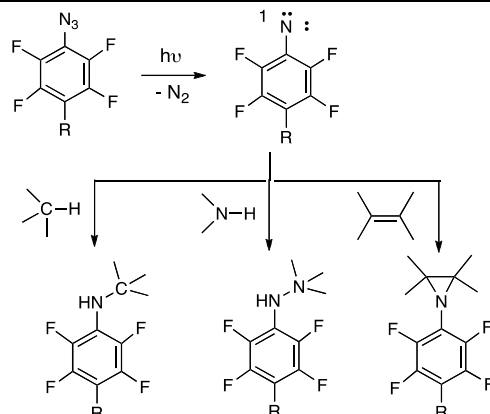
Scheme 1. Simplified schematic of the photochemical reactions of perfluorophenylazides.

Silica Nanoparticles

We conducted extensive studies on silica nanoparticles and demonstrated the successful immobilization of polymers on silica nanoparticles using PFPA as the coupling agent. Results from this study has just been published.[53]

The key step is the preparation of PFPA-functionalized nanoparticles that can be used to attach a variety of molecules and materials. To achieve this, a simple one-pot procedure was developed for the synthesis and the subsequent functionalization of silica nanoparticles. The widely adopted Stöber method was employed to prepare monodisperse silica nanoparticles from $Si(OEt)_4$ by way of a hydrolysis and condensation reaction. The prepared nanoparticles were then functionalized in situ by subsequently adding PFPA-silane directly into the Stöber solution, reacting at room temperature overnight followed by refluxing (Scheme 2). The IR spectrum of obtained nanoparticles showed the typical absorption of the azido group at 2126 cm^{-1}, indicating the successful functionalization of the nanoparticles with PFPA. Polymer immobilization was carried out by irradiating PFPA-functionalized nanoparticles suspended in the polymer solution while stirring (Scheme 2).
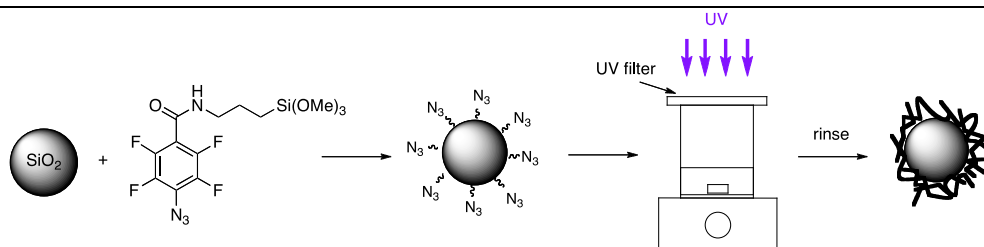
Scheme 2. Functionalization of silica nanoparticles with PFPA-silane and subsequent polymer immobilization.

Excess polymer was removed by repetitive extraction of the nanoparticles with the solvent. The presence of polymers attached to SiO_2 nanoparticles was confirmed by ^{1}H NMR. Nanoparticles coated with polystyrene (Figure 37b) showed peaks that corresponded to those of the polymer itself (Figure 37a). This immobilization procedure was also applied to poly(2-ethyl-2-oxazoline), a hydrophilic polymer, and poly(4-vinyl pyridine), a basic polymer. ^{1}H NMR spectra confirmed that both polymers were successfully attached to the PFPA-functionalized nanoparticles.
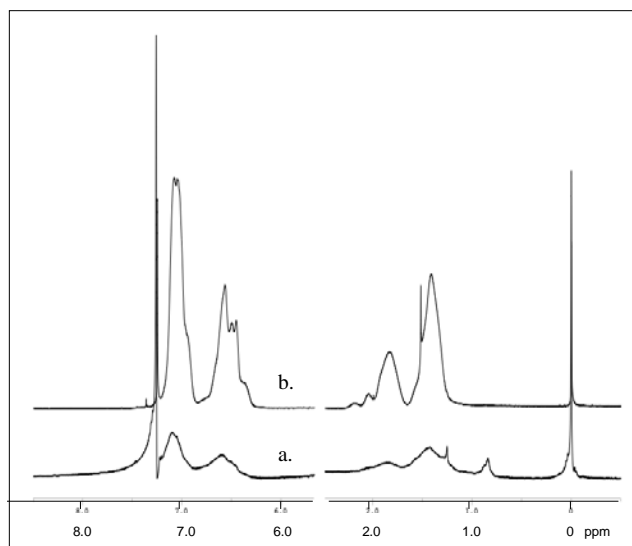
Figure 37. ^{1}H NMR spectra of (a) PS-coated silica nanoparticles and (b) PS in CDCl$_3$.

To establish that the polymer was indeed covalently bonded to the surface of the silica nanoparticles rather than just physisorbed, control experiments were carried out in which the Stöber nanoparticles were functionalized with octadecyltrimethoxysilane (ODTMS) instead of PFPA-silane. The ODTMS-coated nanoparticles were subjected to the same procedure as PFPA-coated nanoparticles to attach PS, PEOX, or P4VP. In all cases, the ^{1}H NMR spectrum of the resulting nanoparticles did not show peaks in common with the respective polymer but instead contained only peaks corresponding to ODTMS. In another experiment, freshly prepared Stöber nanoparticles were irradiated in the presence of a solution of polystyrene in chloroform. After the resulting nanoparticles were washed with the solvent, no polystyrene molecules were detected in ^{1}H NMR. These results confirmed that the surface azido groups were responsible for the successful attachment of polymers.

The amount of polymers immobilized on the nanoparticles was determined thermogravimetrically using TGA. The weight of the coupling agent PFPA on the nanoparticles is subtracted from the total weight loss to obtain the weigh of the immobilized polymer only. The polymer grafting density per unit area (mg/m^2) was calculated using the following equation,

$$\frac{\Delta W_p - \Delta W_{PFPA}(W_p / W_{PFPA})}{[W_p /(\frac{4}{3} \pi r^3 \times d)] \times 4\pi r^2}$$

(1)

where ΔW_p is the change in the sample weight upon heating from 120 to 940 °C, ΔW_{PFPA} is the weight change of PFPA-functionalized nanoparticles at 120-940 °C, W_p and W_{PFPA} are the weights of the polymer-coated and PFPA-functionalized nanoparticles at 940 °C, respectively, d is the density of the nanoparticles which is 2.0 g/cm^3 or 2.0 x 10^9 mg/m^3, and r is the radius of the nanoparticles (averaged at 46.5 nm measured by SEM).

The grafting densities, in the range of several mg/m^2, are comparable to those reported in the literature for polymers attached to nanoparticles by the graft-to approach, demonstrating good coupling efficiencies under the current experimental conditions. For the immobilization to take

place, polymer molecules must be in close proximity with the surface azido groups. In our studies, the coupling reaction was carried out where the PFPA-functionalized nanoparticles were suspended in the polymer solution. The immobilization was likely achieved where the polymer molecules were first adsorbed from solution to the nanoparticle surface and were then covalently attached upon UV activation of the azido groups. For homopolymers, the amount of polymers adsorbed depends on several parameters including polymer concentration, solvency, and molecular weight. Higher solution concentrations usually give increased amounts of adsorbed polymers, thus higher grafting density. This was observed in the present studies in which the grafting density increased with increasing polymer concentration (Figure 38). In addition, higher grafting densities were observed for PEOX and P4VP whereas PS gave lower values. This could be attributed to the solvent effect where chloroform is a better solvent for PS than for PEOX or P4VP. Generally, in the absence of strong solvent-substrate interactions, more polymer will be adsorbed to substrates from poor solvents than from good solvents.[54] In a good solvent, the polymer is well solvated. The repulsion between segments of adsorbed polymers is greater and thus the amount of surface-adsorbed polymer is lower. Polymer adsorption generally increases in a poor or the theta solvent.
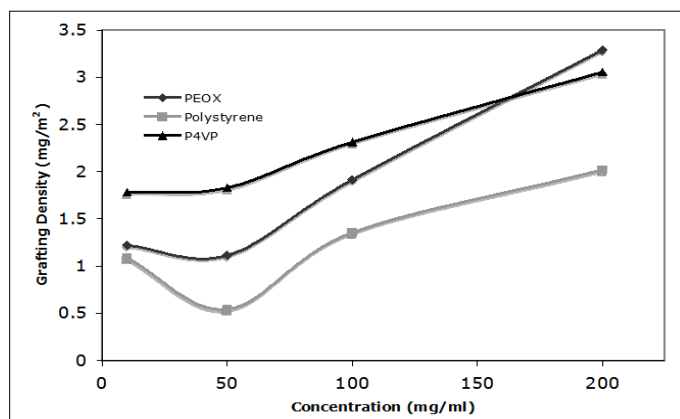
Figure 38. Grafting density of polymer on silica nanoparticles at various polymer concentrations.

The effect of molecular weight on the polymer grafting density was investigated using PS and PEOX of different molecular weights. For PS, the grafting density increased with increasing molecular weight (Figure 39). Assuming that a polymer adsorption process precedes the photochemical immobilization, this result implies that more polymers were adsorbed on the functionalized nanoparticles as the size of the polymer increased. For PEOX, however, the grafting density was more or less similar for all 3 molecular weights (Figure 39). The result can be explained by assuming that the surface was fully covered with PEOX molecules. In this case a unit surface area can accommodate a smaller number of larger polymers and a higher number of smaller polymers. The size and the number of polymers offset each other, yielding similar amounts of polymer on the surface.

Approved for public release; distribution is unlimited.
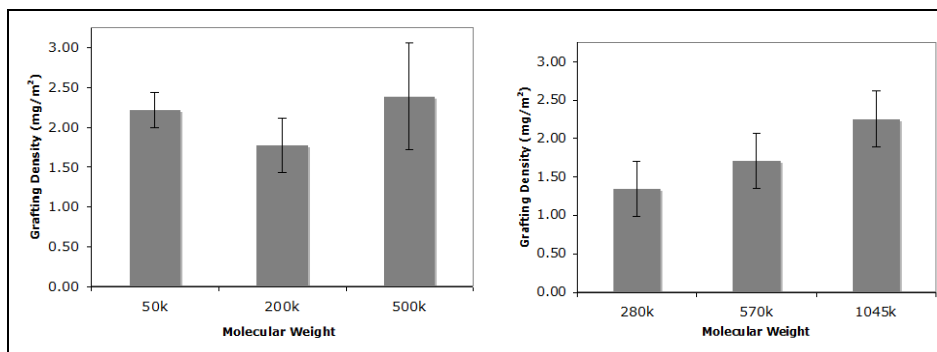
Figure 39. Grafting density vs. molecular weight for PS (left) and PEOX (right).

The immobilization was carried out by irradiating a suspension of PFPA-functionalized nanoparticles in 100 mg/mL solution of the polymer in $CHCl_3$. Each data was the average of 3 samples.

Au and Ag Nanoparticles

The same surface functionalization chemistry has been applied to metallic nanoparticles of Au and Ag. Towards this end, we synthesized the PFPA disulfide and subsequently used it to functionalize Au and Ag nanoparticles (Figure 40). In collaboration with Professor Walter Caseri of ETH Zurich, we used PFPA-functionalized Au nanoparticles to prepare polymer nanocomposite materials for dichroic properties.[55]
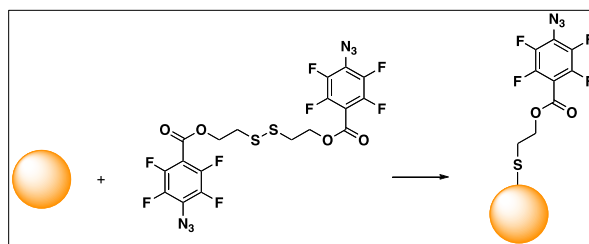
Figure 40. Surface functionalization of Au and Au nanoparticles with PFPA disulfide.

Computational and analytic tools to support the development of environmentally-benign nanomaterials
Stacey Harper (Oregon State University), Bettye L.S. Maddux (University of Oregon and Oregon State University)

Research under this SNNI sub-award has focused on the development of *rapid assays* to quickly determine the toxic potential of nanomaterials, the *investigation and development of tools* to evaluate nanomaterial physicochemical properties, and the *informatics infrastructure* to identify the specific features of a nanomaterial that govern its environmental behavior and biological interactions. This work aims to fill data gaps regarding the risks associated with nanomaterial exposure, and the principal characteristics that may be predictive of nanomaterial interactions with biological systems. Our group has been developing rapid testing strategies to identify the specific features of nanomaterials that result in toxicity. Informatics and computational approaches are applied to define structure-property relationships that govern nanomaterial-biological interactions and identify key drivers for nanomaterial toxicity.

Rapid Assays
Our group aims to develop rapid assays that offer some predictive power for how nanomaterials might interact with biological systems, yet are simple enough to be reproducible and reliable. We leverage a dynamic whole animal (*in vivo*) assay to reveal whether a nanomaterial is potentially toxic at multiple levels of biological organization (i.e. molecular, cellular, systems, organismal). Early developmental life stages are often uniquely sensitive to environmental insult, due in part to the enormous changes in cellular differentiation, proliferation and migration required to form the required cell types, tissues and organs. Molecular signaling underlies all of these processes. Most toxic responses result from disruption of proper molecular signaling, thus, early developmental life stages are perhaps the ideal life stage to determine if chemicals or nanomaterials are toxic. The embryonic zebrafish model was chosen to investigate nanomaterial biological activity and toxic potential. Investigations using this model system can reveal subtle interactions so we have developed an 'EZ' (embryonic zebrafish) Metric for nanomaterial toxicity' (EZ Metric) that takes into account the types and frequency of sublethal effects in addition to overt mortality. The EZ Metric is calculated using a weighted approach in which the severity of the impact on organismal survival is taken into account; more detrimental effects are weighted more heavily in this instance. We also provide an additive EZ Metric value that can be used to compare the number of impact incidences independent on the severity or lethality. The EZ Metric has been used to compare morbidity and mortality elicited from exposure to engineered nanomaterials through the Nanomaterial-Biological Interactions (NBI) knowledgebase at Oregon State University.

Natural phytochelatin (PC) cysteine-rich peptides found in certain plants, present extremely high metal uptake, tolerance and specificity. These advantages led to the development of a new class of gold-based nanomaterials with PC peptides, which have the potential to serve as chelating and stabilizing ligands. To assess the biocompatibility of such chelators, a zebrafish embryo-larval test was used to assess the toxicity of nanoparticle suspensions. The objectives were to determine concentration-response scenarios for AuGSH-His2 and AuGSH-Trp2, quantify the uptake of AuGSH-His and AuGSH-Trp2 in embryos over time, and to determine the particle size distribution of AuGSH-His2 and AuGSH-Trp2 in solution over time. Tenfold serial dilutions (0-200 ppm) were prepared in particle-free exposure media. At the 7.0± nm particle core size, virtually no aggregates observed by TEM differed from the average diameter calculated by dynamic light scattering in the serial dilutions. The average diameter of nanoparticles in suspension at higher concentrations remained constant in exposure media over the course of experiments, while, at lower concentrations the average diameter was increased. The uptake of the nanomaterial was determined via INAA (instrumental neutron activation analysis) for the total of gold present in individual embryo at 24 and 120 hpf. Results showed acute toxic responses at the highest concentrations for both AuGSH–His2 and –Trp2 (Figure 41). The uptake for both nanomaterials correlated well with the amount of gold available in solution.
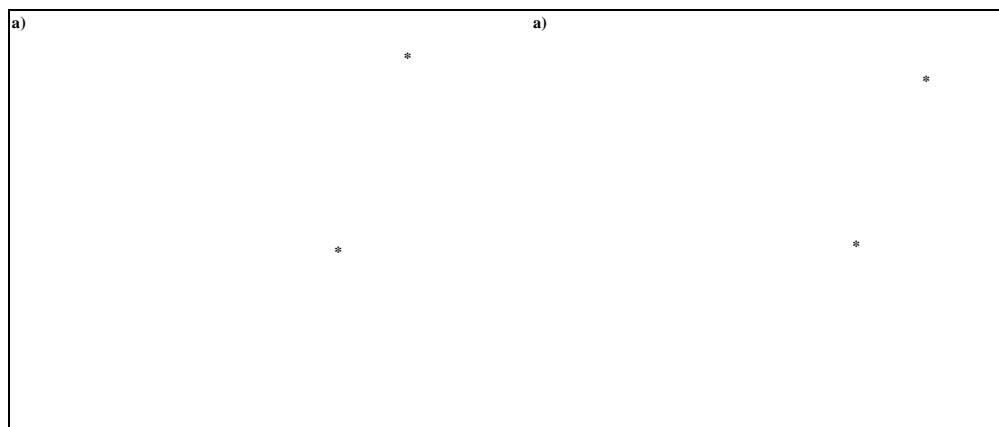
Figure 41. Acute toxicity observed in dechorionated zebrafish embryos exposed to AuGSH-His2 (upper) and AuGSH-Trp2 (lower). Asterisks indicate results are statistically different from controls.

In this study, stability/aggregation of 10 and 100 nm citrate-stabilized AgNPs, which are supplied by the manufacture, were evaluated with dynamic light scattering (DLS) for 7 days in different dilutions of embryo culture media of zebrafish (Instant Ocean Salts). Both 10 nm sized- and 100 nm sized-AgNPs are significantly aggregated in non-diluted 100 % embryo media, and the aggregates of 10 nm sized-AgNPs were bigger than those of 100 nm sized-AgNPs. When AgNPs were suspended in the media diluted with deionized water to make low salt solution, the aggregation was decreased. It was found that AgNPs were stable in media diluted up to 10-fold (10 % media) during the whole test period of 7 days. The aggregation was also influenced by the test concentration of AgNPs and the aggregated particles were precipitated in non-diluted media, which is critical to identify the toxic concentration of nanoparticles. Diluted 10 % media without AgNPs did not induce any physiological adverse effects on the embryo development determined by mortality, hatching, deformity, spontaneous tail movement, and heartbeat. Toxicity of AgNPs in different size and media types were investigated and AgNPs showed more toxicity in diluted media, in which the nano-sized particles were more stable. This suggested that AgNPs are toxic to the developmental process of embryos and the embryo culture media may be diluted up to 10-fold to keep the citrate-coated AgNPs more stable for the toxicity tests.

In order to fill important gaps with regard to nanoparticles by defining the relationships between their physiochemical properties and the biological responses to their exposure, we have recently begun a project to concurrently use nanocrystalline cellulose (NCC) as a nanomaterial platform and at the same time reduce uncertainty of the risks posed by NCC. We aim to determine *in vivo* dose-responses from exposure to a series of NCC formulations using embryonic zebrafish, elucidate the molecular mechanism of NCC toxicity, and identify physical and chemical modifications of NCC that alters its toxic potential. Our preliminary results, thus far, indicate that NCC is an ideal, non-toxic platform (Figure 42) on which to discretely test the specific hypotheses that we have generated using the NBI knowledgebase.

Approved for public release; distribution is unlimited.
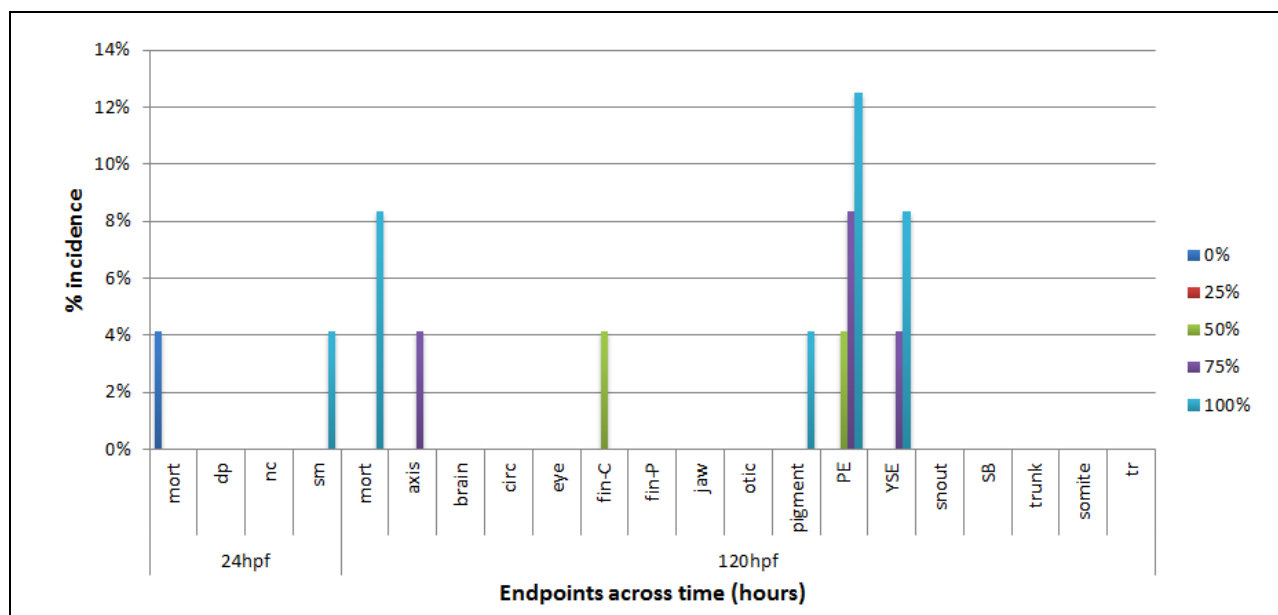
Figure 42. Incidence of morbidity and mortality in embryonic zebrafish exposed to NCC.

We have developed a rapid, flexible, and inexpensive screen to categorize the oxidative capacity of nanomaterials from the extension of existing fluorometric oxygen radical absorbance methods. Oxidative injury is a particular area of concern for nanomaterials and many techniques fail to identify the physicochemical properties responsible for a material's redox behavior. In our assay, we hypothesize that the anti- and pro- oxidative capacity of nanomaterials can be assayed by systematically examining their effects on redox sensitive fluorophores, antioxi-dants, and pro-oxidants (Figure 43).
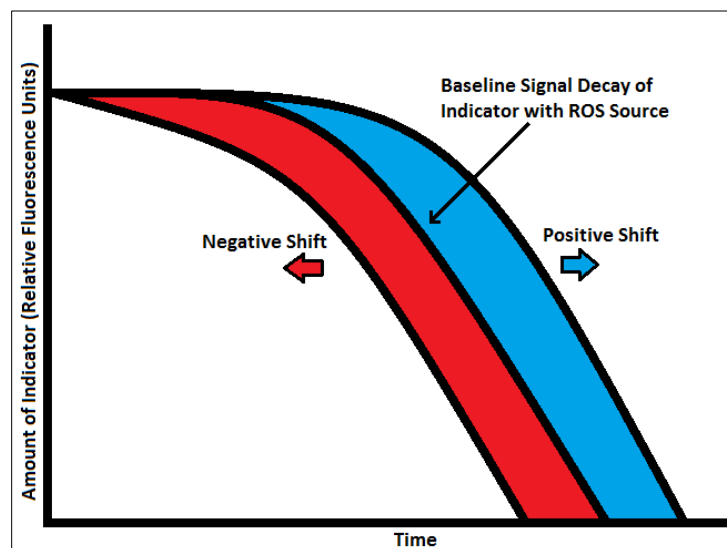
Figure 43. Conceptual overview of the oxidative potential assay.

Shift toward the left is indicative of oxidant behavior while a shift to the right is indicative of anti-oxidant behavior.

Approved for public release; distribution is unlimited.

We predict that antioxidant nanomaterials will lead to positive shifts (increases) in the relative signal of the fluorophore when a ROS source is present. We predict that pro-oxidant nanomaterials will lead to negative shifts (decreases) in the relative signal of the fluorophore when a ROS source is present and/or upon direct exposure to the indicator. In this study, small molecules and nanomaterials were challenged with known concentrations of anti-oxidants (AO), trolox or melatonin, to observe how the test material changed the AO's ability to protect a fluorophore, fluorescein and/or melatonin, from 2, 2'-azobis-2-methyl-propanimidamide dihydrochloride (AAPH), a peroxyl radical producing azo-initiator. This method was tested against small molecules with known oxidative capacities including: EDTA (weak AO), alpha-lipoic acid (AO), ranitidine HCl (non-oxidant), ammonium persulfate (strong oxidant), and potassium permanganate (oxidant). Additionally, the following nanomaterials were tested and acted as follows: C_{60} as a weak AO, hydroxylated C_{60} ($C_{60}(OH)_{24}$) as an AO, custom gold-cored glutathione conjugated nanoparticles as an AO, and erbium(IV)oxide nanoparticles as a non-oxidant. Strategically testing families of nanomaterials will allow us to glean potential nanomaterial structure activity relationships that could empower toxin/therapeutic identification and design.

Informatics Infrastructure
Dr. Harper has been working extensively with researchers in the nanoinformatics community. Results of these interactions and activities include: Nanoinformatics 2020 Roadmap[14], an invited talk to the Nanotechnology Environmental Health Implications (NEHI) working group entitled "Nanoinformatics: A grassroots effort to support an interoperable infrastructure". During this presentation, Dr. Harper presented updates on the Nanomaterial-Biological Interactions (NBI) knowledgebase as well as the broader nanoinformatics vision for interoperability among data resources. The NBI is intended as a platform for consolidating and integrating data of nanomaterial effects in experimental animal models (including humans) and evaluate biological effects from a variety of research platforms (i.e. *in vivo* and *in vitro* approaches). The NBI serves as a repository for annotated data on the interactions of nanomaterials with biological systems and function as an expert system to identify unifying principles and determine the relative importance of specific structural characteristics for desired functionality. Dr. Harper has given numerous invited presentations including: "Nanomaterial-Biological Interactions Knowledgebase" to the Integrative Cancer Research Nanotechnology Working Group in July 2010; "Risk Characterization Information" at the Capstone Meeting: Risk Management Methods & Ethical, Legal, and Societal Implications of Nanotechnology, National Nanotechnology Initiative Workshop in DC on March 30, 2010; "Data integration to evaluate nanomaterial-biological interactions" to the National Nanomanufacturing Network Nanoinformatics" on January 15, 2010; "Integrative Approaches to Greener Nanotechnologies" to the Northwest Hazardous Materials Conference for Household and Small Business Programs, NAHMMA in 2008; "Data Integration to Support the Development of Environmentally-Benign Nanomaterials," at the iNANO meeting in Denmark in 2008; and "Data Integration Strategies to Define Nanomaterial-Biological Interactions" for Intel, OR in 2007.

We are currently in the process of final reviews of the new NBI that was remodeled by collaborators at The Northwest Alliance for Computational Science and Engineering (NACSE) at OSU (Figure 4). The NBI has been migrated to the NACSE's computing facilities and is being maintained by NACSE director and her staff. The new domain name is

Approved for public release; distribution is unlimited.

www.nbi.oregonstate.edu and the system has been upgraded from Drupal due to interoperability constraints. It is now hosted on a NACSE server and maintained by NACSE staff. The redesigned NBI infrastructure and data structure is to better harmonize with ISA-TAB-Nano.
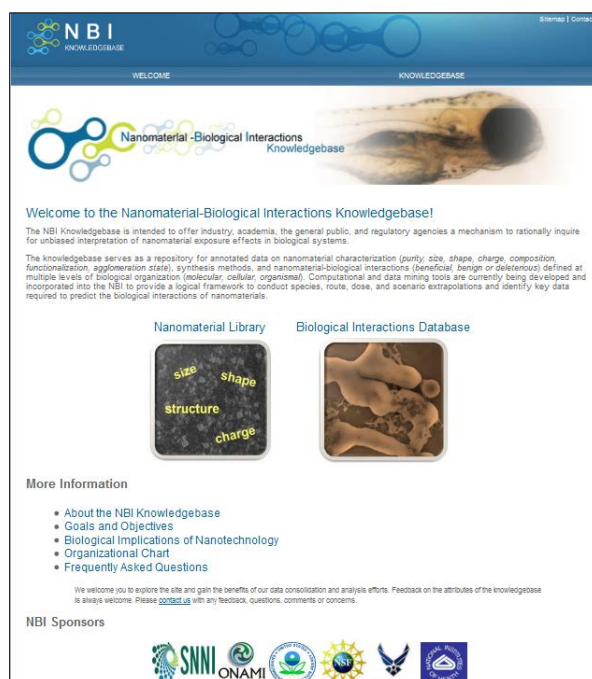
Figure 44. New website for the NBI knowledgebase, www.nbi.oregonstate.edu.

We have extended the platform to include multiple experimental records for a given material file, experimental data can be exported in spreadsheet format using an easy to use 3-tab system that includes: 1) Material File 2) Assay File and 3) Experimental Data. Restructuring will allow us to facilitate the exchange of data among resources. We have revised the graphing package to include scalable features and the ability to soon in on specific data points, select individual lines to display or turn on/off graphing and heat mapping as needed. Finally, we have provided a mechanism to enable use of the NanoParticle Ontology, our input spreadsheet is supported by drop-down menus that guide ontology reference selection. We are currently in the process of QA/QC evaluation of all of our data files, filling in data gaps where possible. The NBI launched the new site on April 4, 2012.

The fields of nanomedicine and nanotoxicology face many challenges in the development of standards to support meaningful data submission and information exchange. Numerous physico-chemical, *in vitro*, and *in vivo* assays must be addressed, with measurements currently dependent on non-standardized protocols and diverse technology types. Representing Structure-Activity-Relationships (SARs), in particular, is critical to understanding the effects of nanomaterial structure on biological activity. Unfortunately, information describing the nanomaterial including functionalizing entities and 3D structure is often represented in an undisciplined fashion. This lack of standardization has been a significant deterrent to meaningful data sharing across the nanotechnology community; few publications contain sufficient information to enable adequate interpretation of results and successful achievement of experimental reproducibility. The ISA-TAB-Nano effort aims to address data sharing challenges in nanotechnology by

53

providing a standard means for identifying nanomaterials and characterizations in a tab-delimited format. ISA-TAB-Nano is based on existing standards developed by the European Bioinformatics Institute (EBI) and the Investigation/Study/Assay (ISA-TAB) file format, which represents a variety of assays and technology types. The ISA-TAB-Nano specification leverages ISA-TAB files describing investigations, study-samples, and assays and provides extensions to support nanomaterial structural information and assay measurements from the Washington University NanoParticle Ontology (NPO). The ISA-TAB-Nano standard specification will enable the submission and exchange of nanomaterials to/from nanotechnology resources like the NCI's caNanoLab nanotechnology portal and the OSU Nanomaterial-Biological Interactions (NBI) knowledgebase; empower organizations to adopt standards for representing data in nanotechnology publications; and provide researchers with guidelines for representing nanomaterials and characterizations to achieve cross-material comparison. The ISA-TAB-Nano effort is a collaboration between a variety of organizations including the NCI, Washington University, OSU, ONAMI, NIOSH, Stanford, and ISA-TAB. ISA-TAB-Nano is registered as an ASTM Work Item, which facilitates a broad community outreach and input to the development of ISA-TAB-Nano and other standards needed to support nanomedicine. Dr. Harper was recently invited to present to the EU NanoSafety Cluster Databases Team on "ISA-TAB-Nano: Standardizing a file format to enable nanotechnology data sharing".

In collaboration with Intertox (Seattle, WA), we have developed the beta version of a Multi-Criteria Decision Analysis tool that will support end-user specification of data selection in the NBI knowledgebase. We have taken a community-based approach to refine the selection criteria (Figure 45) and have evaluated 15 primary papers with the current MCDA tool. We are trying to cover the spectrum of papers from really good to very poor so we have an indication based on the score as to how well the paper/dataset conforms to the MCDA criteria. Thus far, the modifications that have been made have improved the precision of the tool for distinguishing solid papers from those that do not have vital information.

Data Quality	Characterization of Particle Physical/ Chemical Properties		Exposure & Toxicity Study Protocol
Inter-laboratory testing	Manufacturer/ Source	Size distribution	Test subjects/ system
Instrument calibration	Method of production	Functional groups/ ligands	Measurement/ testing apparatus
Replicates	Timing of particle characterization	Purity	Materials/ reagents/ solutions
Controls	Core composition	Aggregate/ agglomerate	Dosage/ route/ duration
Error/ variability	Shape	Solubility	Data collection
Data transformation	Image	Surface chemistry	Statistical processes
			Validation

Figure 45. Categories of the criteria judged to be most important for capturing and filtering information around.

Thrust Group 2: Greener Nanomanufacturing
The overarching goal within this thrust group is to develop methods of manufacturing nanoparticles using a process that is efficient and minimizes waste, while optimizing and maintaining the properties needed for high-performance applications. The lessons that emerge from the research conducted during the initial SNNI funding cycle are the importance of developing (i) a mechanistic understanding of the reactions developed for use in microscale reactors, (ii) real-time, in situ, as well as ex situ, characterization methods to guide research and production decisions, and (iii) strong integration and project coordination between the chemistry and engineering in order to develop reactors and methods capable of continuous, high-rate production of highly functionalized nanoparticles. *Three tasks under this research thrust are:*

Task 4: Studies to guide high-rate, continuous flow nanoparticle production: in situ spectroscopy in microcapillary reactors (S. Kevan, J. Hutchison): This task provided synthetic strategies, mechanistic investigation, development of in situ spectroscopic probes and overall project coordination between Tasks 4 and 5. The goal within the Thrust Group was to develop continuous flow production of nanoparticles that increases production rate and decreases waste compared to the batch processes.

Task 5 and 6: Microsystem development for metal nanoparticle production (V. Remcho, C-H. Chang, B. Paul, D. Palo, S. Ramprasad, T. Miller, Sundar Atre, Shoichi Kimura, Goran Jovanovic, Vinod Narayanan): This task aimed to develop engineering approaches to separations, mixing and reactor development to support the Thrust Group's efforts to significantly reduce processing time and greatly improves product purity.

Mechanistic studies and in situ spectroscopy toward high-rate, continuous flow nanoparticle production in microchannel reactors
Jim Hutchison, Steve Kevan* (University of Oregon)
* Dr. Kevan is now Deputy Director of Science at Lawrence Berkeley National Laboratory
The overarching goals of the research in this task have been to develop new syntheses and in-line analysis tools that allow us to enhance material quality, increase production rates and decrease waste for nanoparticle production. Given the sensitivity of nanoparticle formation reactions to process conditions, particularly reagent mixing, we examined the use of continuous flow reactors and compared their performance with standard batch conditions. A considerable emphasis is placed on developing new methods to gain this mechanistic insight, including the development of in situ spectroscopic probes.

The key findings from this research derive from studies that integrate the use of small angle x-ray scattering (SAXS) studies of nanoparticles in continuous flow environments and the development of continuous flow reaction chemistry to produce (i) undecagold and then (ii) a range of gold nanoparticle sizes based upon nanoparticle production in the presence of Bunte salts.

We developed an in situ multitechnique approach that permits the real-time measurement of the sizes of nanoparticles in flowing solutions.[17] A series of ligand-stabilized Au nanoparticle standards (d_{CORE} = 0.8 – 5 nm) was analyzed by simultaneous small angle X-ray scattering (SAXS) and UV-visible spectroscopy in a microscale flow system. A specially designed

observation cell provided access to both measurements at an identical location in the flow system and allowed for the correlation of SAXS and TEM analyses. Comparison of flow-based UV-vis data to those obtained ex situ provided a bridge between in situ SAXS and ex situ TEM measurements. Average core size from both techniques matched closely for each sample, while polydispersity values from SAXS measurements were smaller than those from TEM. By correlating in situ and ex situ measurements for well-defined nanoparticle standards, these experiments form the basis of a powerful approach to assess nanoparticle core size within flowing microscale systems.

Our aim was to employ the SAXS/UV-vis measurement system to observe nanoparticle growth in a flow reactor setting. To isolate nanoparticle nucleation from growth, we planned to produce monodisperse Au_{11} as seeds and monitor growth of these nanoparticles upon addition of more gold salt and reducing agent. The next task was to develop a synthesis of the Au_{11} clusters in a simple microscale flow system. We developed an optimized synthetic process to provide rapid, reproducible, direct access to large quantities of a single atomically precise product, $Au_{11}(PPh_3)_7Cl_3$. In addition, direct experimental observation of the reaction pathways indicated that the key to monodispersity in the synthesis was the remarkable stability of $Au_{11}(PPh_3)_7Cl_3$ under the identified reaction conditions. Unfortunately, the stability of this core material prevented its use as a seed for bigger particles.

Although we were able to produce Au_{11} in high yield and with high purity, its lack of reactivity prevented its use as a seed for controlled growth. A wide range of reducing agent and gold precursor concentrations were examined, but no conditions were found that showed growth from the Au_{11} seeds (although nucleation of new particles occurred under certain conditions). We turned our attention to the use of Bunte salts to see whether this might be a more viable approach to study nanoparticle growth and develop scalable methods for functionalized gold nanoparticle production.

Inspired by previous reports on the use of alkyl thiosulfates (Bunte salts) as ligand precursors, we anticipated that the slower passivation kinetics of these masked thiols would provide a method to directly synthesize large functionalized AuNPs. We found that Bunte salts produce larger AuNPs under the same synthetic conditions than thiols. We investigated the effect of ligand:gold ratio, temperature, and reducing agent concentration on the particle diameter and dispersity to better understand how to control particle size.[56] The AuNP core size can be systematically controlled by varying the ratio of ligand precursor:gold (L:Au) and the temperature of the reaction. The synthesis produces functionalized AuNPs ranging from 1.5-20.0 nm in diameter. The use of Bunte salts provides a convenient synthetic platform for the synthesis of AuNPs across this size range that possess a variety of surface functionalities, including positive, negative, and neutral functional groups.[56]

With this new synthesis developed, we turned our attention back to the use of SAXS to monitor nanoparticle size evolution in the continuous flow system. We measured these dynamic systems wherein the nanoparticles are formed by mixing reagents in a microfluidic flow reactor and have measured the growth of nanoparticles in a flow cell. Our hypothesis was that this type of flow system would provide steady-state populations of nanoparticles that could be analyzed by SAXS and UV-vis at specific reaction times. We have shown that this is indeed the case. We were able

to examine the sizes at different residence times and observed showed that nanoparticle formation occurs all within the first few seconds after mixing.   We have also shown that it is possible to control the rates of the reaction and the final particle size by varying the ratio of reagents (gold salt, reducing agent and ligand).

We had hoped to extract quantitative kinetic information from the size vs. residence time plots, however, we found that the rates of these reactions are sensitive to mixing, order of reagent addition, concentration, age of the reducing agent solution and pH of the solution. Given the strong dependence on these parameters we have been trying to determine whether it is possible to adequately control these variables in the flow system we developed. Research to isolate and control these variables continues and we working to utilize the lab-based SAXS system for flow studies so that our progress will not be limited by access to the beamline at ALS.

Microreactor Development for Microreactor-Assisted Nanomanufacturing
Brian Paul, Chih-Hung Chang (Oregon State University)
The long-term objective of the research within this task was to develop microchannel reactor technology in support of safer and greener nanomaterial synthesis. The first part of this section summarizes efforts to scale the production of various nanomaterials. The second part of this section summarizes the evolution of microreactor development through this research including advances in interdigital mixing, reverse oscillatory flow mixing and segmented flow reactor mechanisms. The program objective was to develop a system that significantly reduces processing time and greatly improves nanomaterial product purity through the application of microreaction technology.

Scale-up of a Microreactor System for the Production of Au Nanoclusters
Microreactors are normally operated at relatively small flow rates (1~ 100 µL/min). While claims have been made for the ease of scaling-up nanoparticle synthesis within microreactors, the technical literature does not provide any scale-up demonstrations for the microchannel processing of nanomaterials. We have synthesized triphenylphosphine (PPh$_3$)-stabilized gold nanoclusters made by the reduction of mononuclear gold phosphine compounds using a continuous flow microreactor at high rate. The microreactor system features a newly developed multilayered micromixer. This micromixer design offers the ability to scale-up simply by increasing the numbers of laminae while maintaining the same microscale diffusional distances for fast mixing.

The device was produced from 75 µm thick stainless steel 316L laminae using a microlamination approach involving photochemical machining and diffusion bonding. The chemical etching and diffusion bonding processes used to fabricate the micromixer define lamina design constraints. Chemical etching defines a minimum feature size while diffusion bonding imposes an upper limit on span between structural supports. Channel depth was etched to approximately one half of the lamina thickness. It is well known that improper stress distribution within diffusion bonding can lead to warpage and leakage phenomena within microlamination architectures.[57, 58] Consequently, because of the thickness of the shimstock, efforts were made to provide adequate structural support. Bonding conditions were found to cause warpage in microchannel fin with spans greater than 300 µm.

Three-dimensional computational fluid dynamic (CFD) analyses were used to investigate various lamina designs. Two-dimensional analyses were determined to be grossly inaccurate because the fluid volume is sandwiched between upper and lower walls that influence flow dispersion. The commercial CFD software package CFD-ACE+ (ESI Software, Huntsville, AL) was used to model the lamina design. Two-dimensional hybrid (Figure 46a) and triangular meshes were generated then extruded to match the etch depth of the features in the lamina. Water was specified at a constant velocity at the inlet boundaries and zero gage pressure assigned at the outlets. The Reynolds number, based on inlet dimensions and velocity, was 35. The fluid was constrained by top and bottom walls until exiting the header. Downstream of the header, the top and bottom were defined as symmetry boundaries to simulate joining with flow from adjacent laminae. Pressure-velocity coupling was achieved via the SIMPLEC pressure correction algorithm, using the algebraic multigrid solver with second order discretization for all variables. Pre- and post-processing were performed using CFD-ACE+ on Windows XP while the solver was run on a 64-bit Linux machine.
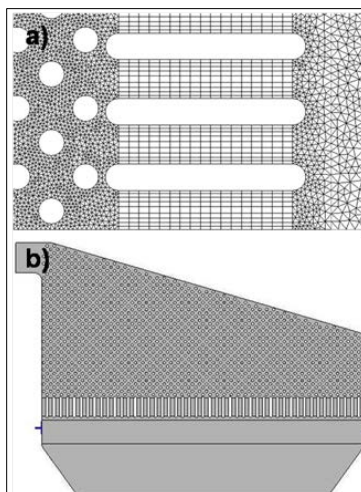
Figure 46. a) Section of two-dimensional hybrid mesh extruded to create three-dimensional CFD model. b) Lamina design showing inlet flow from left with 270 mm diameter cylindrical pillars within the header.

The resulting lamina design is shown in Figure 46b. In this particular lamina, the inlet is shown on the left followed by a header region with cylindrical support pillars and finally a triangular mixing region at the bottom of the figure. The mixing region is through-etched. All other gray areas were blind etched. To make the device, 20 of these laminae were interspersed between 20 laminae having a mirror image of Figure 46b. This allowed for two inlets (one on the left and one on the right) that both fed a combined mixing region leading to a single outlet.

Phosphine-stabilized nanoclusters are a good building block material because the phosphine ligand used to stabilize the particle can be exchanged with other functionalized groups to become either organic or water soluble using ligand exchange methods. The traditional batch protocol for the synthesis of phosphine-stabilized undecagold nanoclusters was not ideal for a continuous flow system because of the required addition of a solid reducing agent, $NaBH_4$, to a suspension of the precursor compound $Au(PPh_3)Cl$ in EtOH[59]. A novel synthesis route was designed by McKenzie and Hutchison in collaboration with our group[60] that enabled the facile synthesis of

Approved for public release; distribution is unlimited.

phosphine-stabilized undecagold gold nanoparticles via a continuous flow microreactor. In this system, the Au precursor was dissolved in THF, and the reducing agent was introduced through the EtOH solution.[60] Undecagold clusters were synthesized from $Au(PPh_3)Cl$ in THF and NaBH in pure EtOH. 40.5mM of $Au(PPh_3)Cl$ dissolved with THF and 40.5mM of $NaBH_4$ dissolved with EtOH were pumped into the multilayered micromixer at room temperature. The mixture passed through a microcapillary tube with a desired length to control the mean residence time for reaction. The reaction was carried out at room temperature. The mixture was collected into pentane to quench the reaction and to separate out the products through precipitation. Dichloromethane (CH_2Cl_2) was used for filtering product.

The phosphine-stabilized undecagold nanoparticles were characterized by ^{31}P and ^{1}H NMR spectroscopy, UV-vis absorption spectroscopy, thermogravimetric analysis (TGA), X-ray photoelectron spectroscopy, transmission electron microscopy and mass spectrometry. In order to demonstrate the scale up capability using our layer-up approach, phosphine-stabilized undecagold nanoparticles were synthesized using flowrates of 20 ml/min and 100 ml/min via 20-layer and 40-layer interdigital micromixers, respectively. The results are presented in Figure 47. The resulting yield is 71% from the 20-layer micromixer operating at a flow rate of 20ml/min with a production rate of 2.4 mg/s. The yield is also 71% from the 40-layer micromixer operating at a flow rate of 100ml/min with a production rate of 11.8 mg/s. The results demonstrate the synthesis can be scaled up to higher production rate using a microlamination strategy without sacrificing the overall yield.
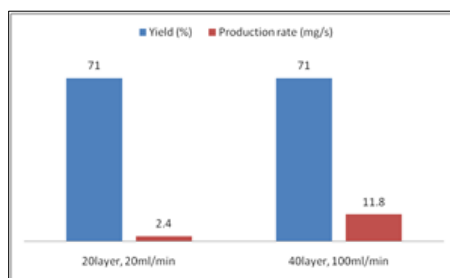
Figure 47. Yield and production rate comparison of a 20 layer vs. a 40 layer micromixer running at a different flow rate.

Continuous Synthesis of SnTe Nanorods
We have demonstrated the first continuous synthesis of high quality rod shaped SnTe NCs. The size and shape of these NCs could be tuned simply by adjusting the reaction time and temperature of the microreactor. The microreactor has a simple design which uses all readily available low cost components. It uses an inner microtube to precisely control the injection of TOPTe into the $SnCl_2$ solution as shown in Figure 48.
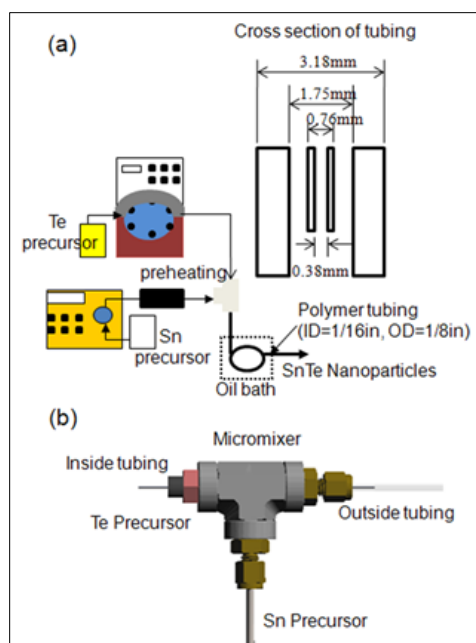
Figure 48. Schematic illustration of (a) setup (inset figure is cross section of tubing) and (b) the continuous hot-injection microreactor.

Rapid injection plays an important role in dividing the nucleation and growth process which is crucial in producing a narrow size distribution.[61] The design of this microreactor also has the advantages of alleviating sticking of nanoparticles on the growth channel wall since QDs are formed from the center of tubing. The flowrates of the two precursors are 0.25 ml/min (tin precursor) and 0.1 ml/min (Te precursor). This reaction temperature was held constantly using an oil bath that was maintained between 170 and 190°C to drive the SnTe nanocrystal formation reaction. The SnTe NCs were isolated and purified using centrifugation. No additional size selection process was employed.

Transmission Electron Microscopy (TEM) images of the as-synthesized SnTe nanorods are given in Figure 49. Figure 49a shows rod shaped SnTe NCs with dimensions of 20 x 5 nm wide and 60 x 10 nm long at a temperature range between 180°C and 190°C with a 5 min reaction time. The aspect ratio of the rods is around 3. The lattice fringes related to the (200) planes can be visualized clearly from the HRTEM image. Spherical shaped NCs were synthesized at a temperature range between 170°C and 180°C. The mean particle size was 3.04 nm ($\sigma = 0.7$, N = 305). X-ray diffraction (XRD) spectra indicate the SnTe NCs have good crystallinity with a cubic rock-salt structure identical to that of bulk SnTe (space group Fm3m, a = 6.327 Å) (Figure 50a-c). The major diffraction peaks of a cubic rock-salt structure observed at 28.19 (200), 40.28 (220), 49.89 (222), and 65.98 (420).
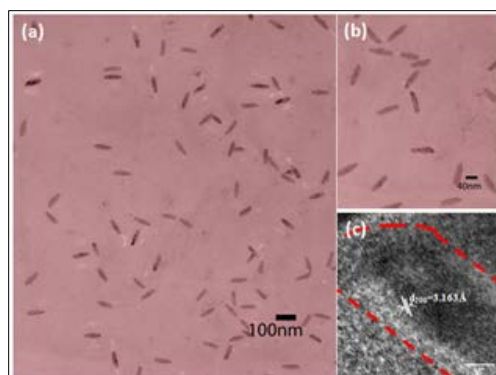
Figure 49. TEM images of rod shaped SnTe nanocrystals with a 5 min residence time (a) scale bar of 100 nm (b) scale bar of 40 nm and (c) high resolution TEM image with a scale bar of 5 nm.
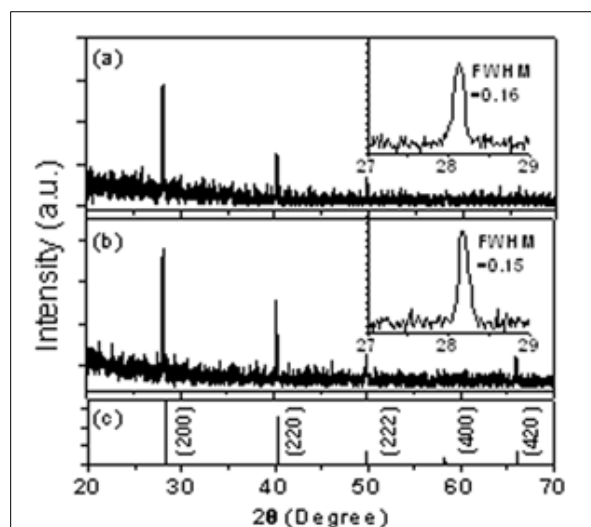
Figure 50. Experimental and reference XRD patterns of SnTe (a) spherical shaped NCs, (b) rod shaped and spherical shaped NCs with a residence time of 7 min, (c) JCPDS 46-1210, TEM images of SnTe.

It is known that the electrical and optical properties of NCs depend strongly on both size and shape.[62] The rod shaped NCs exhibit some potential technological advantages over spherical shaped NCs such as larger Stokes shift of the emission band and provides a favored path for enhanced electronic transport.[63] Solar cells require sufficient thickness for the absorption of all incident light, however film thickness increment also increase the probability of carrier trapping at defect and recombination sites.[64] Formation of the nanocrystals with anisotropic shapes requires the kinetic growth control other than the thermodynamic control. In the kinetically controlled growth regime, high-energy surface grow more quickly than low-energy surface. Shape control can also be achieved by using surface selective surfactants to alter the relative growth rates of different crystal facets.

Ning et al.[65] reported that the length of the fatty chain in amine control the shape and size of SnTe nanocrystals. An oriented attachment mechanism is proposed for the formation of SnTe nanowires driven by the reduction of surface free energy. The SnTe nanowires appear to have

more irregular shape as a result of oriented attachments. In this work, microreactor was used to offer a unique opportunity in creating kinetically controlled growth by precise control over temperature, concentration and reaction time. The shape and size of SnTe NCs can be tuned by controlling the reaction conditions. The use of both TOP and OA affects the nucleation and growth process significantly. TOP binds more strongly to SnTe NCs than OA does. Thus, a high TOP concentration can suppress the nucleation process due to its bonding strength and steric hindrance effects. NC nuclei in an extremely high chemical potential environment have a higher probability of forming anisotropic nanocrystals. The suppression led to a lower number of nuclei during the nucleation step. The suppression also resulted in a higher concentration of monomers that were available in the growth step. We believe that the high concentration of TOP along with the higher temperature promoted the formation of rod-shaped NCs. Slightly longer reaction time created a lower chemical potential environment and spherical shaped NCs were observed in addition to larger nanorods. Ostwald ripening is likely the cause for the broader and more skewed size and shape distribution.

In summary, we demonstrate the first continuous synthesis of SnTe nanorods using a continuous hot-injection microreactor. $SnCl_2$, and TOPTe were used as reactants successfully in coordinating OA and TOP solvents. No glovebox and Schlenk line are required for this work. Both rod shaped and spherical shaped SnTe nanocrystals with uniform size distributions could be obtained. A blue shift was observed from these SnTe nanocrystals. Production rate at about 5mg/min (300mg/hr) was achieved using a microreactor with a size of $1.78cm^3$.

Continuous Synthesis of CuInSe$_2$ Nanocrystals
We have elucidated the formation mechanism of CuInSe$_2$ nanocrystals for the development of a continuous flow process for their synthesis. CuInSe$_2$ nanocrystals were synthesized with good size control ranging from 2.6 nm to 4.1 nm using a continuous hot-injection microreactor (Figure 51). The continuous-flow microreactor could overcome the drawbacks of conventional batch synthesis such as a low production rate, long heating, cooling and reaction times, the need for a Schlenk line and/or a glove box, and most importantly the challenge for scale up. It was found that copper-rich CuInSe$_2$ with a sphalerite structure was formed initially followed by the formation of more ordered CuInSe$_2$ at longer reaction times, along with the formation of Cu_2Se and In_2Se_3. It was found that Cu_2Se was formed at a much faster rate than In_2Se_3 under the same reaction conditions. By adjusting the Cu/In precursor ratio, we were able to develop a very rapid and simple synthesis of CuInSe$_2$ nanocrystals. The different bonding strength and steric effect of the coordinating solvents, OA and TOP, offer a good opportunity to tailor the size, size distribution and production yield. The metal halide precursor was less reactive when high TOP concentration was used. High production rates were achieved up to 11 mg/min (or 660 mg/hr) using a microreactor with a size of only $3.2 cm^3$.
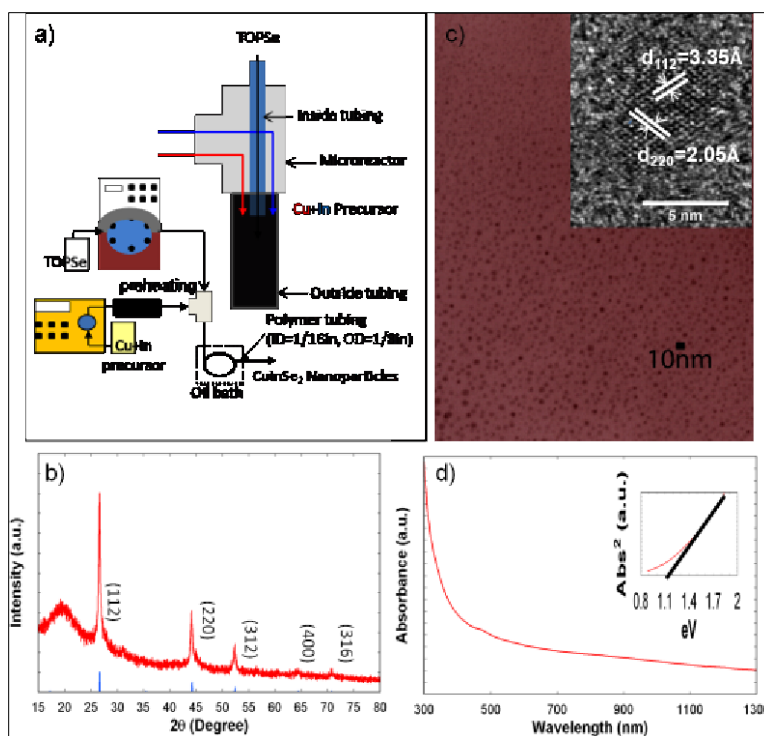
Figure 51. a) Schematic of the microreactor and reactants supplying. Inset is detailed microreactor, b) Reference XRD (vertical line: JCPDS 40-1487) and experimental patterns of continuous process at 8min reaction time. Surfactant ratio OA and TOP is 4:1, c) TEM images of CIS QDs (N=566) and d) UV-Vis-NIR absorbance spectrum of CuInSe₂ QDs in chloroform.

UV-Vis-NIR absorbance spectra showed that bandgaps of as-synthesized $CuInSe_2$ nanocrystals of different sizes can be adjusted between 1.1 eV and 1.3 eV simply by changing the OA to TOP ratios. The combination of this facile synthesis with the scalable continuous flow microreator process could open up opportunity for the fabrication of solar cells using $CuInSe_2$ nanocrystals synthesized from this size tunable process for optimum solar energy harvesting.

Reverse Oscillatory Flow for the Synthesis of Uniformly-Sized Nanoparticles
Microchannel mixers enable faster mixing times compared with batch stir mixing leading to the promise of higher throughput, better yields and less solvent usage for the solution-phase reactive precipitation of inorganic nanoparticles. However, reliance on diffusive transport for subsecond mixing requires channel dimensions in the tens of micrometers. These channel dimensions make diffusive micromixers vulnerable to clogging. An oscillatory flow mixing strategy has been explored to increase the contact area between reagents within larger microchannels (Figure 52). Forward and reverse oscillatory signals were designed to pump reactants through a 450 µm high serpentine microchannel to increase advection within the flow. Computational fluid dynamics simulations were performed to provide insight into flow behavior and nanoparticle morphology. Quantification of mixing performance has been proposed using mixing quality and particle residence time metrics.
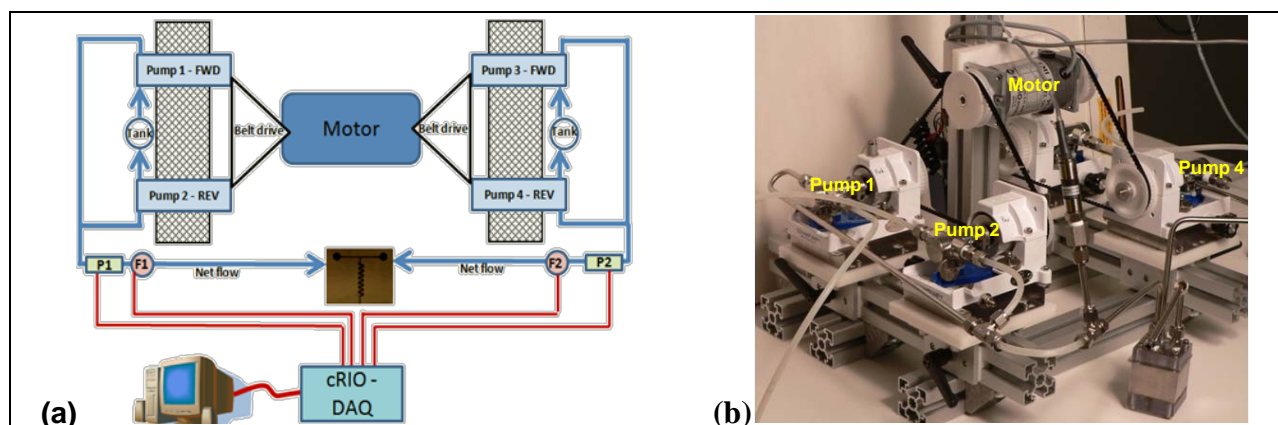
Figure 52. a) schematic of the oscillatory flow experimental setup; and b) a photograph showing the physical apparatus.

TEM micrographs (Figure 53) yielded interesting results for the reactive precipitation of CdS QDs using different mixing conditions. Reactant concentrations of 0.0004 M resulted in well-dispersed particles with a narrow size distribution in the size range of 11.3±2.1 nm. This compares favorably with other size distributions reported in the literature for this particle size. In particular, these results are in the same size range of 3.2 – 12 nm reported in Edel et al[66] for the same chemistry under identical concentrations and at 0.5X the Reynolds number. However, it should be noted that the flow rate demonstrated in the present work is nearly 415X (125 ml/min vs. 0.3 ml/min) higher than that reported by Edel et al[66]. The shapes of the QDs in case B are not perfectly spherical. This may suggest non-uniform growth conditions and the need for better mixing quality over shorter mixing times. Finally, some QDs have greater contrast suggesting higher crystallinity.
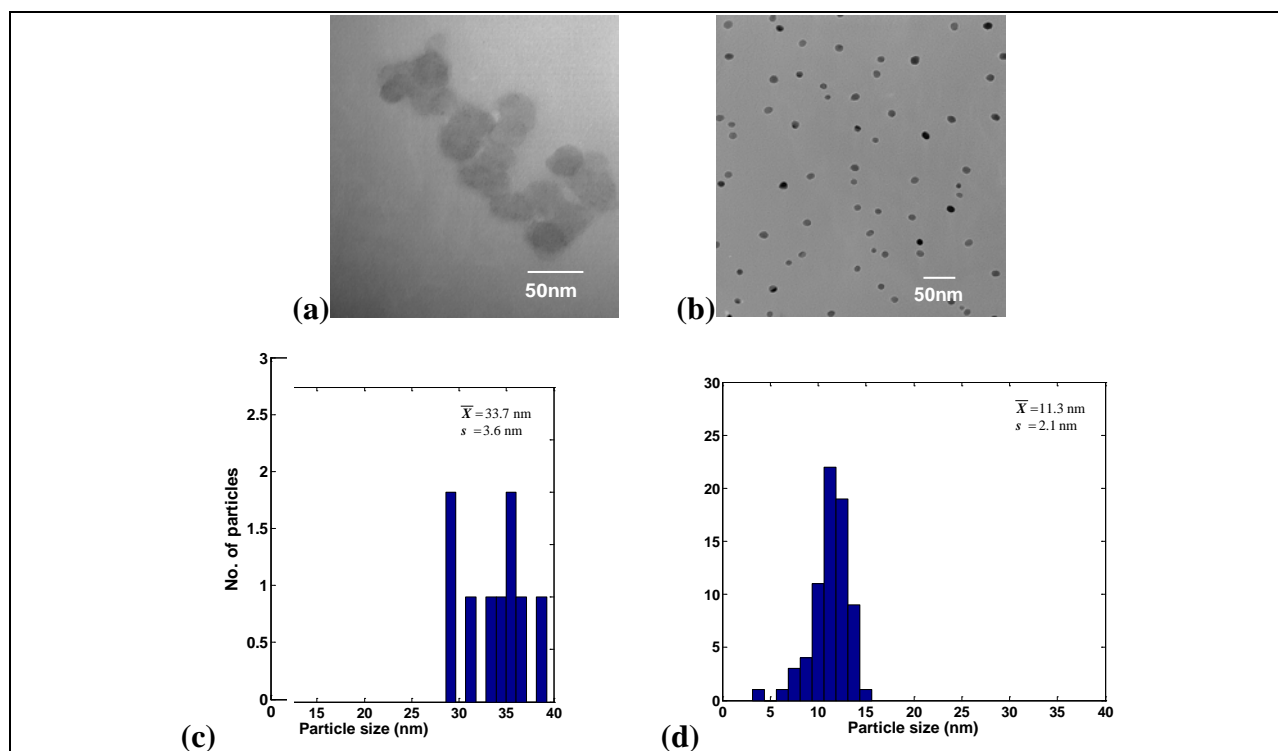
Figure 53. TEM images showing CdS NPs formed using the same oscillatory flow mixer but under different residence times: (a) 0.42 sec.; and (b) 1.66 sec. Histograms showing the nanoparticle size distribution for: (c) case a with an average nanoparticle size of 33.7±3.6 nm; and (d) case b with an average nanoparticle size of 11.3±2.1 nm.

Flow Segmentation via High Pressure Hermetic Compression Seals
The application of elastomeric membrane microvalves with polymeric microfluidic devices is currently impeded by bonding methods which limit operating pressures. A novel compression sealing approach was presented for embedding elastomeric membranes between polymeric microchannel laminae through the use of sealing bosses. Sealing bosses are used effectively to concentrate clamping forces producing compression seals with higher operating pressures. The technique is capable of integrating elastomeric membrane microvalves within a wider variety of materials. Further, compression seals allow devices to be disassembled allowing for cleaning and analysis. Finite element methods were used to investigate the effects of sealing boss size and location on valve deformation as a function of clamping pressure (Figure 54). Experimental results were found to be in good agreement with the model and show that the device can be configured to withstand operating pressure beyond 689 kPa.
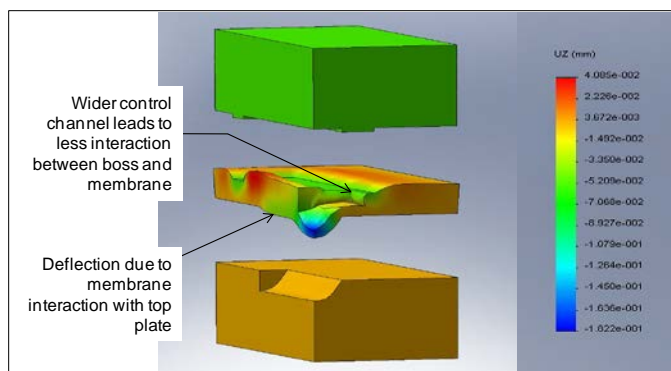
Figure 54. Exploded view of FEA results from the third parametric study (CR = 18:1; Tv = 30 µm; Lc = 500 µm) showing z-axis strain when clamping, flow and pneumatic pressure are applied.

Purification of high-value nanoparticles
Vincent Remcho (Oregon State University)

Nanofiltration membrane media have become attractive for the separation and purification of mixtures of macromolecules and nanoparticles. A large majority of the research effort in the field of nanofiltration to date has focused on aqueous nanofiltration systems for food and water purification.[67] More recently, organic solvent resistant nanofiltration (OSN) membranes have been developed and applied in pharmaceutical and petrochemical studies.[68-72] Our studies have extended the range of applicability of OSN membranes to include purification of high-value nanoparticles in process streams. We have also explored the use of OSN membranes for reclamation and recycling of waste reactants.

The unique optical and electronic properties of nanoparticles have inspired their application in medical imaging and in the production of high-performance electronics. To capitalize on these unique properties, which are generally size-dependent[73, 74], both high-selectivity synthetic approaches and high-selectivity purification processes are required to limit polydispersity and enhance purity. To achieve greater product stability and shelf life, which are adversely affected by variability in ligand shell composition and the presence of residual monomers[59, 60], others have used separation methods including centrifugation[75], size-exclusion chromatography[75], and flow-field fractionation[76] to purify nanoparticles. These techniques are inherently slow, discontinuous ("batch" mode), and require copious volumes of wash solutions. Membrane filtration, by comparison, is an inherently "greener" process, requiring less solvent and time than other methods. Furthermore, prediction of membrane performance is possible based on membrane characteristics, and scale-up for industrial applications promises to be much easier than for many other methods.

For 1-5 nm gold nanoparticles, a narrow size distribution was achieved by ultrafiltration of a post-synthetic mixture using commercial ultrafiltration membranes in the diafiltration mode.[77, 78] However, the method is limited to particle sizes of 1 nm and larger. In the novel work described here, the nanofiltration of sub-nanometer sized, tetrahydrofuran soluble, $Au_{11}(PPh_3)_8Cl_3$ (Au_{11}), with emphasis on interfacing to an upstream microreactor, was demonstrated. The ligand properties and small size of Au_{11} make it attractive as a catalyst for the oxidation of alcohols by H_2O_2,[79] and as a labeling agent for stoichiometric conjugation with proteins.[80] Au_{11} has also been

Approved for public release; distribution is unlimited.

reported to be a precursor whose phosphine ligands can be replaced by thiolates or glutathione, which results in larger nanoparticles for other applications.[59, 81]

In these studies, two different nanofiltration membranes were used; ceramic (Inopor®nano), and polymeric (DuraMem500) materials. Ceramic membranes offer unique advantages relative to their organic polymer membrane counterparts. They are stable over a wide pH range (2-14), are resistant to most polar and non-polar solvents, and are stable even at extremely high temperatures (~ 350˚C).[71, 82, 83] The ceramic membranes were acceptable for aprotic solvent environments, such as tetrahydrofuran -soluble Au_{11}. Ceramic membrane media are expensive, and a thick support layer is needed to protect the fragile, active thin layer. Polymeric membranes have the limitation of modest operating temperature, but their advantages include their flexible shape and relatively low price. Solvent options are limited by the composition material of the polymeric membrane and swelling is a common problem.[67, 71] Tetra-hydrofuran, however, is compatible with the DuraMem series membranes.[68] Both membranes showed the retention of Au_{11} "standard" and removal of byproducts such as triphenylphonsphine (PPh_3) and chloro(triphenylphonsphine)gold (I) ($AuClPPh_3$).

Au_{11} rejection values were calculated by UV absorbance at 420 nm for the retentate and permeate solutions following the dead-end flow filtration of Au_{11} "standard" and post-synthetic Au_{11} using the Macroscale test fixture (MTF, Table 2, Figure 55).
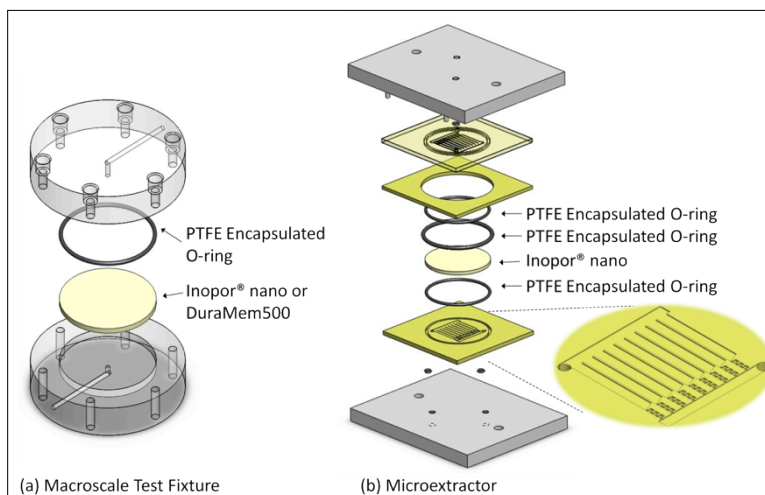
Figure 55. Diagram of (a) the macroscale test fixture (MTF)[2] and (b) micro-extractor

Table 2. Rejection data for an Au_{11} standard and post-synthetic Au_{11}

	Macroscale test fixture (MTF) Rejection (%)				In-line filtration with a microreactor
	0.04 g/L Au_{11} Standard	10x diluted post-synthetic Au_{11}	0.1 g/L PPh_3	0.1 g/L $AuClPPh_3$	10x diluted post-synthetic Au_{11}
Inopor®nano[1]	93 ± 3 %	65 %	12 ± 2 %	17 ± 2 %	67 %
DuraMem500[2]	82 ± 8 %	88 %[3]	~0 %	4 ± 2 %	n/a

1) 5 mL of feed volume 2) 10 mL of feed volume 3) post-synthetic Au_{11} without dilution, The observed rejection of the membrane was calculated as: Rejection, R=$((1-C_{Permeate}/C_{retentate}) \times 100\%)$, where $C_{permeate}$ and $C_{retentate}$ are the final concentrations in the permeate and retentate, respectively.

The "standard" and post-synthetic Au_{11} samples yielded rejection values of 93% and 65%, respectively, on the Inopor®nano membrane, and 82% and 88%, respectively, on the DuraMem500 membrane. In addition, the anticipated low rejection values of PPh_3 and $AuClPPh_3$ (R = 12% and 17%, respectively, on the Inopor®nano membrane and, R= ~0% and 4%, respectively, on the DuraMem500 membrane) had molecular weights lower than each stated membrane's MWCO. Both membranes were shown to concentrate Au_{11} particles and remove PPh_3 and $AuClPPh_3$ from the post-synthetic Au_{11} solution.

The rejection of post-synthetic Au_{11} (R=65%) was shown to be lower than that of the Au_{11} standard solution (R=93%) on the Inopor®nano membrane using MTF (dead-end flow filtration). However, post-synthetic Au_{11} was filtered using the micro-extractor (cross-flow filtration) at 1.4 bar (Figure 56). A rejection of 97% was calculated from the UV-Vis data (Figure 57). The rejection values demonstrated an enhancement in rejection performance (with continuous flow) relative to the dead-end flow filtration approach. In the dead-end flow filtration, the samples caked on the membrane, which caused membrane fouling (active filtration layer erosion and chemistry change).[71] However, cross-flow swept away the buildup of material on the membrane surface and decreased the incidence of membrane fouling. Fouling membrane could be a factor in the decrease of membrane performance.

(a) Diafiltration step 1 of 10x diluted post-synthetic Au_{11}

(b) Diafiltration step 2 of 10x diluted post-synthetic Au_{11}
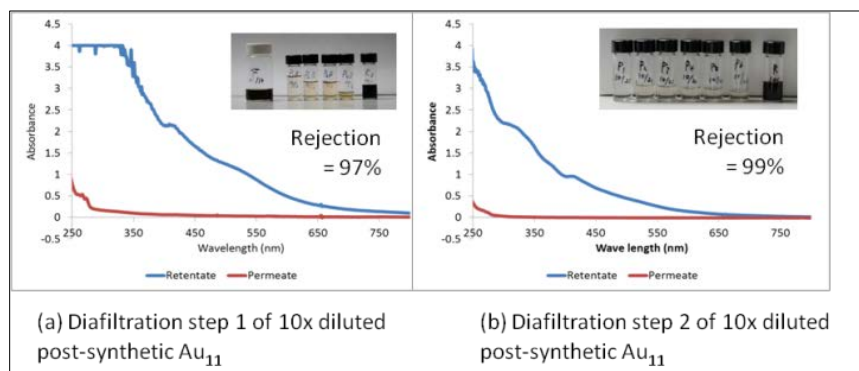
Figure 56. UV-Vis spectrums of 10x diluted post-synthetic Au_{11} of each step in the microextractor using the Inopor®nano membrane. All samples were diluted by 10x to allow absorbance measurements. The photos of undiluted feed (F), permeate (P), and retentate (R) are inserted.
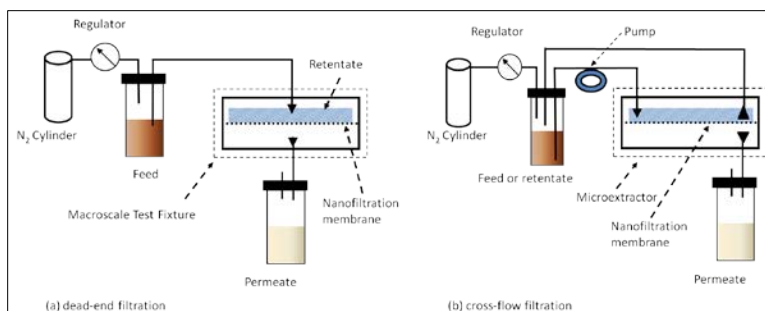
Figure 57. Fluidic schemes for dead-end flow filtration in the MTF (a) and for cross-flow filtration in the microextractor (b)

The UV-Vis and NMR data for diafiltration of post-synthetic Au_{11} in the microextractor provided for continuous removal of byproducts from the post-synthetic Au_{11} (Figure 57 and 59). The UV-Vis data of each diafiltration step provided 97% rejection of Au_{11}. The permeate UV-Vis spectrums showed the free ligand peak (PPh_3 at 255 ~ 280 nm) and the intensity of these peaks decreased with each subsequent step.

In ^{31}P-NMR data of diafiltration of post-synthetic Au_{11} using the inopor®nano media, the permeate fractions showed only byproducts, and the retentate fraction contained the Au_{11} concentrated from the feed solution. (Figure 58) The extra ligand peak found at 29 ppm corresponded to a significant amount of free ligand in the feed solution. After the first filtration of the post-synthetic Au_{11} solution, the peak area ratio (0.89:1) of the ligand over the Au_{11} peak in retentate solution after the first step diafiltration decreased dramatically compared to the initial ratio (2.58:1) in feed solution. This retentate, diluted with a mixture of 50:50% (v/v) tetrahydrofuran:ethanol (50% THF), was used as the feed of the second diafiltration step and had the peak ratio 0.23:1 = free ligand: Au_{11}. The precursor ($AuClPPh_3$), unreacted or dissociated from the Au_{11}, was seen at 33 ppm. The relative amount of retentate in step 1 was also decreased by about 50%, but retentate in step 2 showed a similar ratio between Au_{11} and $AuClPPh_3$ because the purification time was extended in the second step; it is possible that some of the Au_{11} could have decomposed into $AuClPPh_3$. It was previously reported that byproducts of the Au_{11} reactions (and an impurity in many reaction mixtures of larger PPh_3-stabilized Au nanoparticles) led to the decomposition of Au_{11}.[60, 84] Transmission electron microscopy (TEM) revealed a 1.4 ± 1.0 nm particle size. (Figure 58) The particle size can be overestimated by the poor contrast between the smallest metal nanoparticles (below 1nm) and the support films used for the electron microscopy based on the bias microscopic measurements.[85]
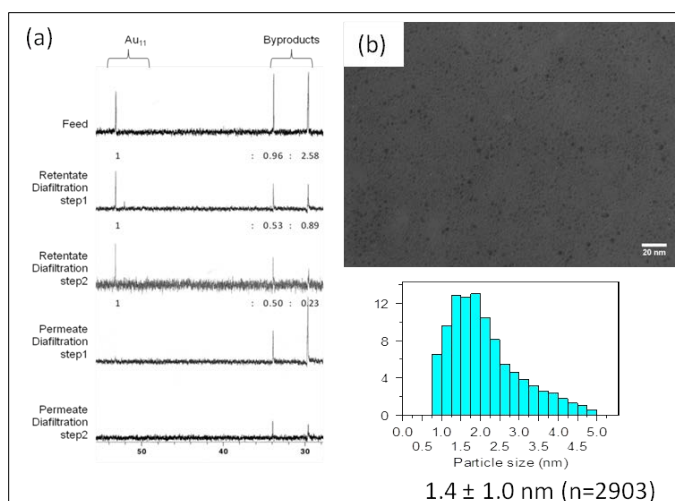
Figure 58. (a) ^{31}P NMR spectroscopy (^{31}P, 161.98 MHz) of diafiltration, retentate and permeate from the microextractor. The feed was diluted 10x in 50% THF. Step 1 retentate was used as the feed for the diafiltration step 2. The numbers below each peak represent the area ratio of each peak of Au$_{11}$ and byproducts. The ^{31}P NMR spectrum showed the free ligand (29 ppm) and the precursor (33 ppm) of the permeate, and concentrated Au$_{11}$ peak (53.2 ppm) of the retentate. A decreased ratio of the peak area of Au$_{11}$ and byproducts was noted in each successive filtration step. (b) TEM image of retentate from step 2 and particle size distribution. The particle diameter was 1.4 ± 1.0 nm (n=2903)

The rejection percentage of the in-line nanofiltration system was 67%. The high yield and high production rate of Au$_{11}$ synthesis using a microreactor[60] suggests that it might be advantages to directly interface the nanofiltration system (for the post-synthetic Au$_{11}$ purification) to upstream reactor, which would reduce the total production time (Figure 59).
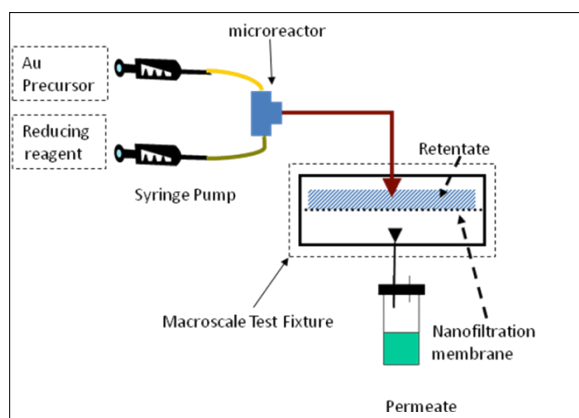
Figure 59. Fluidic control schematic for in-line microreactor and nanofiltration. The output flow (total flow rate: 0.08 mL/min) of the microreactor was introduced directly to the MTF equipped with a membrane.

A post-synthetic Au$_{11}$ rejection value of 88% on the DuraMem^{TM}500 membrane showed that the polymeric membrane had a comparable rejection performance to the 83% rejection value of "standard" Au$_{11}$. The DuraMem^{TM}500 membrane was less affected by the post-synth etic Au$_{11}$ filtration from the Inopor®nano membrane.[86] Three consequent diafiltration experiments were

70

also conducted with post-synthetic Au_{11} on the DuraMem[TM]500 membrane using the MTF (dead-end flow filtration). The ^{31}P-NMR data confirmed the collection of Au_{11} in the retentate reservoir and the removal of PPh_3 and other byproducts in each permeate reservoir following diafiltration with the DuraMem[TM]500 membrane (Figure 60).
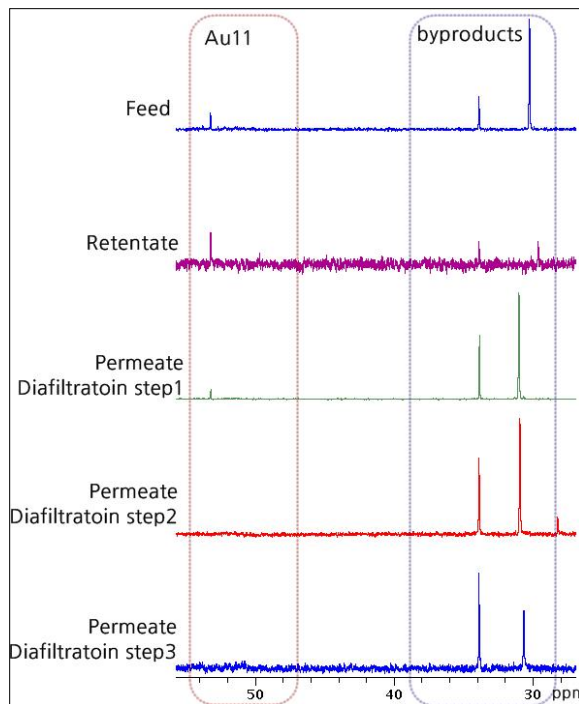
Figure 60. ^{31}P-NMR (^{31}P, 161.98 MHz) of feed, retentate, and permeate from diafiltration using DuraMem[TM]500.

The feed was post-synthetic Au_{11}. Permeate solution was collected and analyzed after each filtration, but the retentate solution was analyzed after the final filtration.

The continuous synthesis process, coupled with the nano-filtration system, resulted in a significant reduction in synthesis time while delivering a higher apparent yield than could be achieved in batch experiments. Filter cake formation was noted, and largely attributed to concentration polarization on the membrane surface, filtration speed, and electrostatic interaction between the filter and NPs. Tangential flow filtration, also called cross-flow filtration or diafiltration, is capable of reducing clogging, concentration polarization and other problems attributable to the dead-end flow geometry. The in-house built microextractor was designed to generate even cross-flow on commercial disk-filters[87], and achieved high-purity preparation of nanoparticles of low polydispersity. We suspect that inopor®nano membrane degradation, seen during the dead-end filtration experiments, may be compensated by use of a tangential flow filtration approach in a microextractor. The computational dynamic model of the microextractor improved the flow and pressure balance and made the distribution more uniform, which increased system performance as evidenced by an increase in throughput and simplified maintenance of the membrane.[87]

The MTF and microextractor were run at a 1.4 bar pressure drop, below the maximum differential pressure (1.5 bar) of the peristaltic pump. The solvent flux of the microextractor had a higher value than that for the MTF, thus the microextractor was capable of purifying higher amounts of solution per unit time (Table 3).

Table 3. Average flux (L m^{-2} h^{-1}) of 50:50 v/v THF:EtOH solvent in the MTF and the microextractor before and after post-synthetic Au$_{11}$ filtration using the Inopor® nano membrane

	MTF (Dead-end flow)	Microextractor (Cross-flow)
J_w (L m^{-2} h^{-1})	8.74 ± 0.22	33.32 ± 1.32
J_a (L m^{-2} h^{-1})	2.26 ± 0.05	16.06 ± 0.63
J_a/J_w (%)	25.87 ± 0.83	48.21 ± 2.68
J_w – the pure solvent flux of the clean membrane J_a- the permeate solvent flux after the filtration		

The ratio of J_a/J_w was correlated to the permeate flux loss due to the interaction between the post-synthetic Au$_{11}$ and the membrane material, indicating membrane fouling. The J_a/J_w value measured for the microextractor was higher than those observed for the MTF, which suggested that lower permeate flux loss occurred when using the microextractor than was the case for the MTF; other have made similar observations for this class of membrane in other applications.[86]

Both the ceramic and polymeric membranes endured extended use in the non-aqueous solvent environments required for Au$_{11}$ nanoparticle synthesis. We identified media appropriate to the task of retaining nanoparticles while freely passing byproducts, such as free-ligands and unreacted starting materials. The chemical and thermal robustness of the ceramic membranes facilitated their reuse after cleaning with dilute acids or bases.

The membrane-based microextractor developed in the course of this research enabled the use of membrane discs having a wide variety of physical dimensions and molecular weight cut-offs. The microextractor was coupled to an upstream microreactor, and we demonstrated continuous diafiltration as a possible path to commercial scale-up.

Continuous Production of Metal Nanoparticles in Microstructured Devices
D. R. Palo, S. Ramprasad, (PNNL), R. T. Miller, V. T. Remcho (OSU)
Copper nanoparticle suspensions are increasingly attractive to inkjet printing applications because they offer a low cost alternative to noble metal nanoparticles.[88] However, the high susceptibility of copper to oxidation has necessitated synthesis by novel techniques such as the polyol process, which enables synthesis of nanoparticles in ambient atmosphere using various ligands to protect the metal core from oxidation.[89-91]

Mixing of reagents in the polyol process can be challenging because it normally involves a highly viscous solution of high molecular weight ligand. Conventional polyol synthesis by batch process employs vigorous stirring to ensure uniform mixing of reagent mixtures, which leads to additional non-uniformities and other logistical issues in scale-up. The continuous synthesis of copper nanoparticles can overcome many of these batch-based shortcomings and offer a pathway

to scale-up in nanomanufacturing. The significance of the synthesis of nanoparticles by continuous process using microchannel devices has been described by other research groups.[92]

Continuous flow synthesis of nanoparticles is non-trivial. Reagent concentration, reaction temperature, and optimum reaction time are a few of the key parameters that are critical for synthesizing monodisperse nanoparticles in flow synthesis. It is interesting to note that the majority of the literature on metal nanoparticles synthesized by flow systems has utilized a very low metal pre-cursor concentration <10mM which is not viable for large scale production since the maximum yield of copper nanoparticles would be less than two grams per liter of reaction mixture. Researchers have reported the challenges of irreversible nanoparticle aggregation at higher reagent concentrations leading to a bottleneck for large scale production.[93] Flow synthesis of metal nanoparticles has received considerable attention in recent years.[94] However, there is limited literature on a synthesis route that has utilized flow rates >10 ml/min. We report a higher throughput continuous flow synthesis along with significantly higher metal pre-cursor concentrations that are more suitable for nanomanufacturing.

A schematic of the experimental set up is shown in Figure 61. Positive displacement pumps (Acuflow Series III) were used to circulate each stream of reagents at a constant flow rate of 20 ml/min. The reagents were introduced in a 2:1 mole ratio of reductant to copper. Stream A consisted of copper sulfate (0.3 M) in ethylene glycol with up to a 5% water addition necessary to eliminate supersaturation of the ethylene glycol solution, which would otherwise cause some recrystallization of the copper sulfate. Stream B consisted of sodium hypophosphite monohydrate (0.6 M) as the reducing agent, and polyvinyl pyrrolidone (PVP, MW=10kD) in ethylene glycol used as a capping agent. Both streams were introduced to the mixer at room temperature by separate metering pumps set at 10 ml/min each. All reagents used in this study were of analytical grade. The reagents from the two streams were passed through a mixer before entering the heat exchanger. Two micromixers were used in this study an Upchurch PEEK Y-connector used as a micromixer (ID : 500 um, swept volume ~2 ml) or a purpose-built stainless steel dual-inlet micromixer designed and fabricated at the Microproducts Breakthrough Institute (MBI). The MBI mixer is designed for efficient mixing at and above 20 ml/min. An image of the MBI micromixer used is shown in Figure 62.
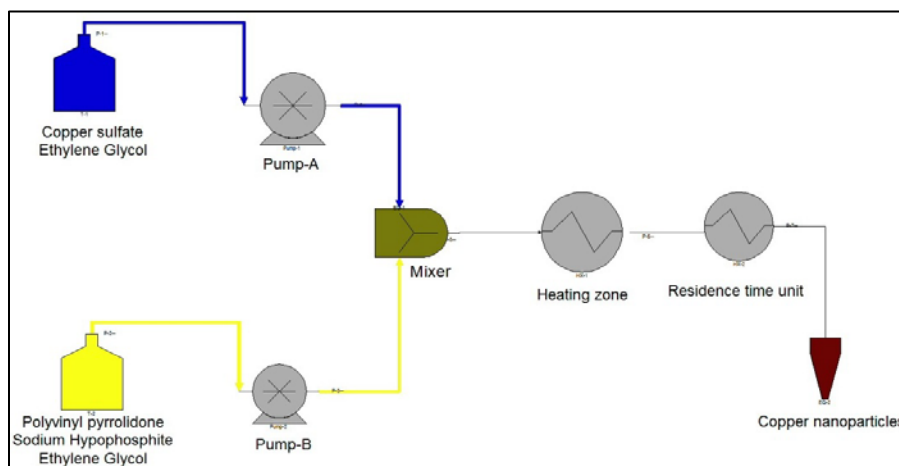
Figure 61. A schematic of continuous flow synthesis of copper nanoparticles by polyol process.

73

Figure 62. Picture of a SS micromixer produced by diffusion bonding of thin laminae and micro-welding of inlet and outlet tubing.

The two reagent streams are mixed in the mixer and circulated through the heating zone to initiate the nucleation and the reaction is completed in the optimized residence time unit to synthesize copper nanoparticles.

The heat exchanger consisted of two sections, namely a rapid heating zone (HZ) and an adjustable residence time (RT) section. The HZ is the initial section of the stainless steel (SS) tubing with a 1/16" inner diameter (ID) and 10 feet (~300 cm) in length in which the mixed reagents enter at room temperature and are heated rapidly to an exit temperature that depends on the wall temperature, flow rate and heat transfer characteristics of the mixture. The heating zone was immersed in a glycol bath maintained at 90 °C; therefore the wall temperature was at this temperature. The heated fluid exiting from the heating zone entered a well-insulated RT unit which comprises a coiled section of ¼" ID silicone tubing and 4 feet (~122 cm) long. The function of the RT unit was to maintain a constant fluid temperature during transit while providing additional residence time to complete the reaction. The residence time in the RT unit is contingent on the length of silicone tubing that was used. Thermocouples at the inlet and outlet of the residence time unit recorded the average temperature of the fluid, which was ~70°C. The measured entrance and exit temperatures varied by only 1-2°C for the duration of the experimental runs, showing that the reaction mixture temperature was essentially constant. All tests were performed in duplicate. The temperature triggers the nucleation of copper nanoparticles and the exiting stream contains copper nanoparticles which are collected. The product was then washed with DI water and acetone and suspended in ethanol.

The copper nanoparticles synthesized in flow synthesis while using the Y-mixer exhibited a size distribution of 20 to 30 nm as shown in the transmission electron microscopy (TEM) images in Figure 63a. On the other hand the copper nanoparticles synthesized in flow synthesis while using the micro-mixer demonstrated a size distribution of 2 to 10 nm as shown in the TEM images in Figure 64a. The selected area electron diffraction (SAED) patterns confirm the face-centered cubic crystalline structure for the copper nanoparticles synthesized using both mixer types. The SAED are shown in Figure 63b and Figure 64b respectively. X-Ray Diffraction analysis (Bruker, D8 Discover, Cu Kα) shown in Figure 65 for the copper nanoparticle indicated the presence of both copper oxide and copper. It can be hypothesized that formation of copper oxide could be due to the low ratio of PVP capping agent to copper salt precursor.
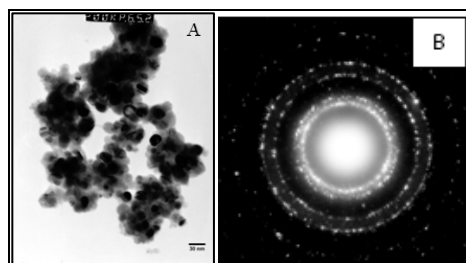
Figure 63. (a) Transmission electron microscope images of copper nanoparticles synthesized by a continuous polyol process using a Y-mixer. The copper nanoparticles are ~ 20 to 30 nm in size. The scale bar is 30nm. (b) SAED of copper nanoparticles indicates a face-centered cubic structure.
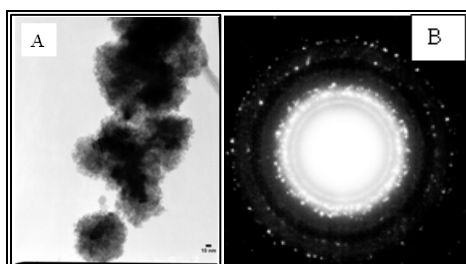
Figure 64. (a) Transmission electron microscope images of copper nanoparticles synthesized by a continuous polyol process using a micro-mixer. The copper nanoparticles are ~ 2 to 10 nm in size. The scale bar is 10nm. (b) SAED of copper nanoparticles indicates a face-centered cubic structure.
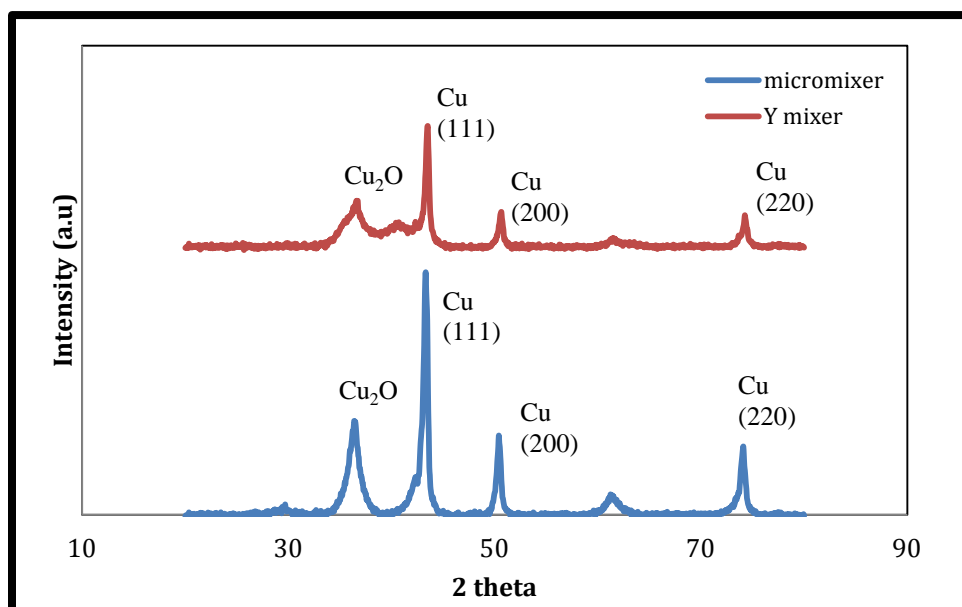
Figure 65. X-Ray diffraction indicating the crystalline phases of the copper nanoparticles synthesized by continuous polyol process using (a) Y- mixer and (b) micro- mixer.

It has been reported that the higher reaction temperatures have facilitated synthesis of smaller size and narrower size distribution.[93] To synthesize nanoparticles by flow synthesis it is critical to maintain a constant wall temperature. It has been observed during the continuous polyol

Approved for public release; distribution is unlimited.

synthesis of copper nanoparticles, if the wall temperature is very hot (>100°C) instantaneous localized nucleation of nanoparticles occurs that consequently causes plating of nanoparticles in the thermal boundary layer, reducing the overall flow cross- section in the flow system and potentially clogging the channel. With appropriate heat exchanger design, we have demonstrated synthesis of copper nanoparticles with an average size of ~ 15 nm at a low temperature of 70°C.

In summary, this project reports several salient features that contribute towards significant progress in the nanomanufacturing of copper nanoparticles. Improvements to the flow process over previous work reported in the literature have been made during the course of this project. Firstly, we report a relatively high flow rate (20 ml/min) continuous flow synthesis using the MBI micromixer designed to enable rapid and complete mixing of reagents involved in the polyol process. Secondly, we have utilized a high precursor concentration (0.3M) that enables generation of 50g of nanoparticles in one hour at 20 ml/min from a single reactor unit. Finally, by utilizing an adjustable residence time unit for the heat exchanger a low solution temperature of 70°C has been developed for synthesizing copper nanoparticles of controlled size. TEM analysis have indicated that the copper nanoparticles synthesized in flow synthesis while using the Y-mixer exhibited a size distribution of 20 to 30 nm and those synthesized with the Micromixer have a size distribution of 2 to 10nm. XRD and SAED analysis have demonstrated that the copper nanoparticles synthesized are crystalline. The characterization results compare the micromixers' performance in the overall process, and indicate that a well-designed micromixer tailored to the flow conditions may be one of the key factors in obtaining high quality nanoparticles in flow synthesis.

Future work will include development of a low Reynolds number plug flow microreactor system to eliminate radial temperature gradients and promote uniform bulk fluid temperatures that enable tighter control of size distribution. In addition, the future work envisioned will systematically delineate and optimize appropriate conditions for nanoparticle synthesis and scaling to higher flow rates, possibly higher precursor concentrations. It is evident from the process developed in this project that the continuous flow synthesis is a viable approach for large-scale production of nanomaterials. However, further optimization of reaction parameters and flow conditions is necessary to successfully scale the process to enable a viable nanomanufacturing process.

Safer production and processing of ceramic nanoparticles: an integrated approach
Sundar V. Atre, Shoichi Kimura, Goran Jovanovic and Vinod Narayanan
To fabricate high temperature microchannel reactors for the controlled synthesis of silicon nitride nanoparticles[95].
An alumina microreactor (Figure 66) was designed and fabricated to study the synthesis of nanosized silicon nitride powder via the ammonolysis of SiO vapor at temperatures ranging from 1300°C to 1400°C.
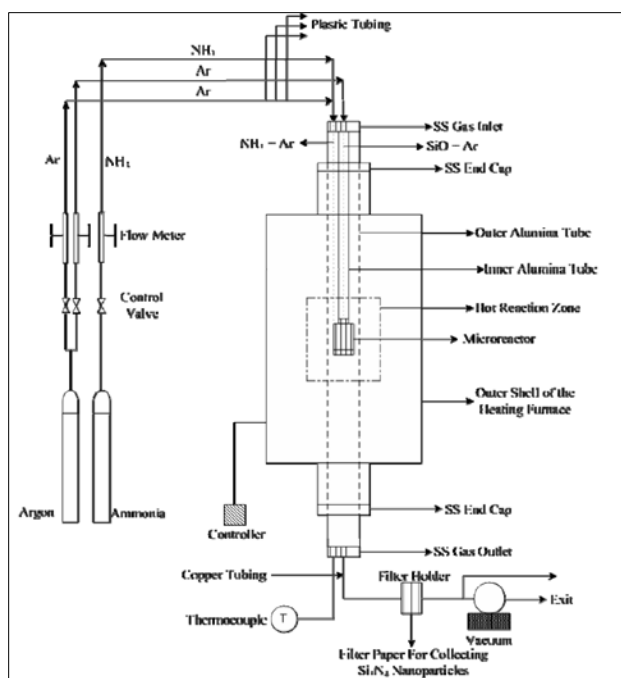
Figure 66. Alumina microreactor.

It is the first high temperature ceramic microreactor capable of operating at temperatures up to 1600°C. A CO_2 laser was used for fabricating the top and bottom plates, while the extruded body of the microreactor was fabricated using highly porous alumina (50-60% porosity). These porous microchannel walls simplify the use of multiple flows in the microreactor, because it facilitates the reactant gas stream to enter into the microreactor through the pores.[96] The microreactor was finally tested in a horizontal tube-heating furnace to synthesize silicon nitride nanoparticles by performing gas-phase reactions between SiO and ammonia. The SiO vapor generation was controlled by the flow of argon gas. The ammonia dissociation at high temperatures was taken into account by maintaining flow rate of ammonia at least 5 times higher than the flow rate of SiO. Due to its portability, and hence reduced reaction volume this microreactor provides a better control over the residence time and diffusion length of the reactants in the hot reaction zone, resulting in a better control over the particle morphology and size distribution.

The reaction between SiO and ammonia was carried out by varying the flow rates of ammonia ranging between 1000-4000 cc/min, while the flow rate of argon was kept constant at 240 cc/min. The reaction was carried out at a constant temperature of 1350°C for a cycle time of 1hr. The reaction yielded silicon nitride nanoparticles were then collected on different filter papers at the exit of the microreactor. The results (Figure 67) showed that particle size decreased with increasing flow rate (mean residence time). Different powder characterization techniques such as transmission electron microscopy (TEM) and x-ray diffraction (XRD) were used to determine the particle size, particle size distribution, and chemical composition of the nano-sized particles. XRD analysis indicated peaks of silicon oxy-nitride (Si_2N_2O) in all the samples except the sample obtained after the first run. This is because Si_3N_4 nanoparticles on exposure to atmosphere were oxidized to form Si_2N_2O.
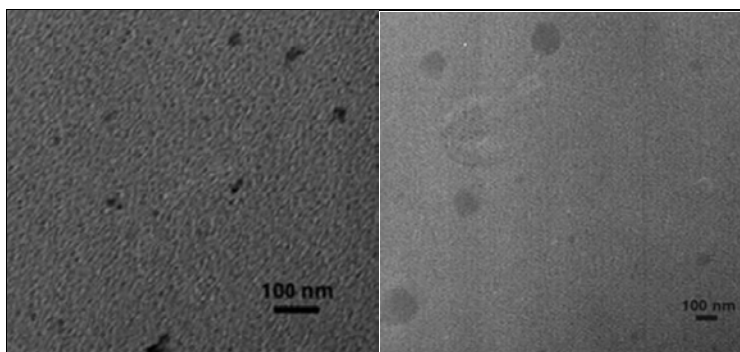
Figure 67. Silicon nitride nanoparticles collected on filter paper from the microreactor.

To understand reaction conditions that determine product yields and silicon nitride nanoparticle characteristics.

Concentrically arranged multiple-tube reactors with different dimensions were built for synthesizing nano-sized silicon nitride powder via the ammonolysis of SiO vapor. The reaction was operated at temperatures ranging from 1350 to 1400°C and pressure slightly above atmospheric pressure. Silicon monoxide (SiO) vapor was generated by charging argon gas through a bed of SiO particles packed in the innermost feeding tube and reacted with ammonia gas introduced through a separate feeding tube into the concentrical arrangement. Additional argon was fed into the annular space between SiO feeder and ammonia feeder to prevent the two-reactant gases from reacting instantly at the feeder outlets and forming whiskers. None of the reactors with micro-scale dimensions (less than 1 mm) could be operated stably due to whisker formation at the SiO feeders. On the other hand, a meso-scale reactor with a 3.25 mm ID innermost tube for feeding SiO vapor was successfully operated for synthesizing nano-sized powder at measurable quantities.
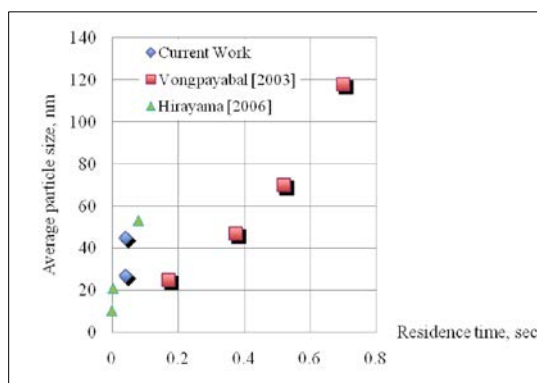
Figure 68. Comparison of particle size and residence times with other studies.

The velocity feed ratio of argon through a bed of SiO particles/NH3 was maintained at 8.5 for effective production, maximizing nano-sized powder production and minimizing whisker formation. The arrangement of the feeding tubes of reactor was one of the most important parameters that have a direct influence on nano-sized powder formation. When a SiO generating tube was extended out of the annular Ar feeder, the highest efficiency of nano-sized powder production was obtained. The mean residence time of the reactants in the reacting zone was

Approved for public release; distribution is unlimited.

adjusted by the length of product collection tube placed in the uniform temperature zone and set to be about 0.04 seconds.
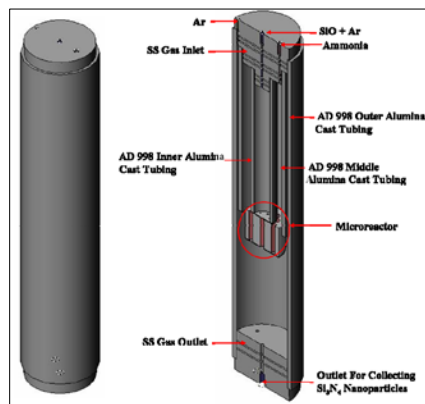
Figure 69. Reactor design.

High reaction temperature promoted the SiO utilization, leading to more nanosized Si_3N_4 powder as well as Si_3N_4 whiskers at the outlet of the SiO generator. The apparent activation energy for the formation of nano-sized powder was 211 kJ/mol,based on an assumption of first-order with respect to the SiO concentration. The average particle size of nano-sized powder decreased with an increase in the reaction temperature, lying in the same range as obtained in the preceding work.
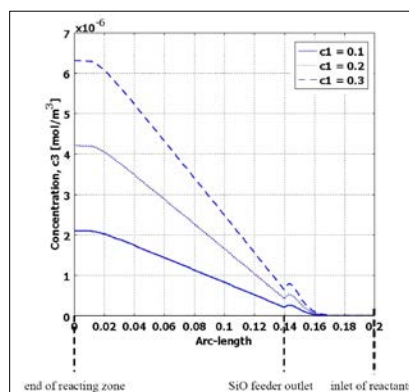
Figure 70. Simulation of reactor.

To develop methodologies for microchannel reactor design and process integration
The microreactor was designed using 3D CAD software SolidWorks and AutoCAD. This entirely new design of the microreactor simplifies the lamination and bonding techniques by using just 3 plates instead of stacking a number of plates together. This design simplification was made feasible by using a combination of advanced processing techniques such as laser machining, extrusion, and tape casting.

The flow of a gaseous mixture in the reactor was simulated with a math software as an effective aid for identifying a reactor structure and operating variables suitable for synthesizing nano-sized silicon nitride powders. The simulated results suggested the optimal configuration of reactor and

operating conditions to be employed in the experimental runs. It also revealed that locations where whiskers form corresponded to those appeared in the experimental runs.

Toxicology tests were also conducted in order to determine the toxicity effects of Si_3N_4 nanoparticles on different body parts of zebra fish. The data obtained was then further used to discuss the advantages of the microreactor in synthesis of Si3N4 nanoparticles and its integration to a post processing system such as compaction press, injection molding, and extrusion.[97]
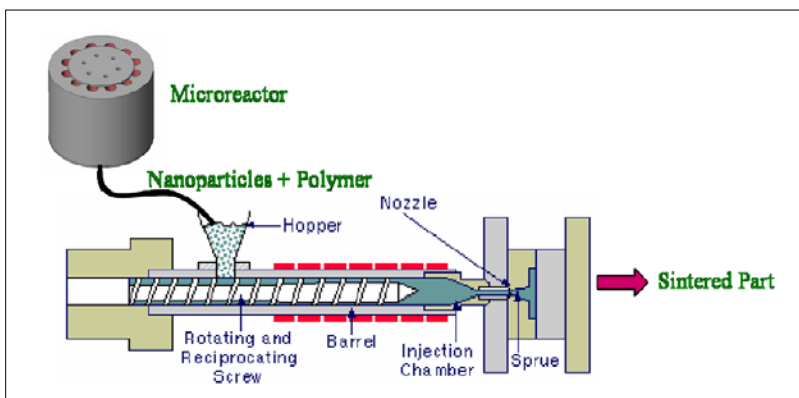
Figure 71. Post processing system.

Approved for public release; distribution is unlimited.

Thrust Group 3: Interfacing Nanoparticles to Nano- and Macro-Structures for Device Applications

Nanomaterials are driving innovation in optical and electronic devices with potential applications in areas such as sensing, computation, energy storage and conversion, adaptive behavior, and communications. Realizing the full potential of nanoscale matter in device technologies requires the development and understanding of superstructures based on nanoscale building blocks. The first two tasks of this thrust group (7 and 8) focus on nanoparticle assemblies involving greener manufacturing approaches. The third task extends the overall focus of the proposal on nanoparticles to include important work on nanostructured assemblies based on nanolaminates that interface nanometer-scale thin films into macroscopic materials. These nanostructured assemblies provide important precursors in the low-cost and greener manufacture of more traditional microscale devices and materials and discovery of exotic new materials. *Three tasks under this research thrust to meet this goal are:*

Task 7: Develop efficient, inexpensive and environmentally benign routes for the synthesis, functionalization, transport, handling, and deposition of nanoparticles (and hierarchical structures composed of integrated nanomaterials) using supercritical fluids (ScFs) and near critical fluids (NcFs) as solvents. (S. Addleman, G. Fryxell, J. Hutchison): Methods to direct formation of 1, 2, and 3D assemblies of metal nanoparticles were developed based upon biopolymer templating and surface modification reactions. The approach offers greener methods of construction of nanostructured assemblies useful for sensing, nanoelectronic or optical applications.

Task 8: Develop nanomaterials for photonic devices (G. Rorrer, M. Jones, M. Lonergan,): Two types of synthetic routes to developing nanomaterials for photonic devices were employed; (1) environmentally-benign, bio-based routes were developed for the green synthesis of nanoscale photonic crystals designed to enhance solar energy conversion of dye-sensitized solar cells and (2) photonic device structures based on synthetic routes of ionically functionalized nanoparticles were investigated. The ionically functionalized nanoparticles fed into the studies of the biological impacts of nanomaterials by expanding the library of nanoparticles available for study.

Task 9: Develop the chemistry of nanostructured matter: low-temperature and solution-based processing of nanostructured inorganic materials (D. Johnson, D. Keszler, M. Subramanian): Our work in the initial support period yielded an understanding of the formation of amorphous films, their transformation to the crystalline states and the potential formation of nanostructured products. We extended these techniques to produce more complex oxides and other material types, and to control the doping levels of these materials to separate effects of different nanostructure from effects caused by different carrier concentrations. We developed a mechanistic understanding of the evolution of solution-derived films and the formation of nanostructured solids from nanostructured precursors prepared by using both solution and vapor phase deposition techniques.

Exploring environmentally benign routes for transport, purification and functionalization of nanoparticles and nanoparticle structures
Shane Addleman and Marvin Warner (Pacific Northwest National Laboratory)
Supercritical fluids (ScFs) and near-critical fluids (NcFs) are nontoxic compressed gasses (such as CO_2 or propane) that behave like organic solvents whose properties can be tuned by

Approved for public release; distribution is unlimited.

temperature and pressure adjustments. The use of ScFs and NcFs in the manufacturing of these materials will bring several important advantages over conventional solvents. Some of the more important benefits from ScFs/NcFs for nanomaterial processing are:

- Environmentally benign:
- Dramatic reduction in volumes of organic solvents
- No residual solvent
- Nontoxic
- Inexpensive, self-purifying, and may be readily reused
- Gas-like mass transport enabler faster diffusion-limited reactions
- Tunable conditions with modest changes in pressure and temperature
- Low viscosity, good mass transport facilitate access to high surface-area and high aspect-ratio materials
- Access to high (anaerobic) synthetic temperatures (typically needed for nanoparticle synthesis)
- ScFs eliminate issues associated with surface wetting and liquid-phase boundary forces.

Recent articles and a DOE-supported study identifies ScFs as a key enabling technology for nanomanufacturing.[98-103] In general, ScFs/NcFs offer industrial processes faster kinetics with dynamic control and significant waste reduction. Industrial scale up of ScFs/NcFs processes has been shown to be economically viable and valuable for bulk extractions (coffee decaffeination, solvent-free dry cleaning, and pharma product purification) and ScF technology is beginning to be used in the microtechnology sector. Consequently, supercritical fluid methods should provide improvements for nanomaterial manufacturing that are industrially scalable and environmentally benign. The steel fabricated microchannel reactors explored in other portions of the SNNI program are low volume and strong enough to enable pressurization making them ideally suited for ScF, or better NcF, conditions eliminating typical concerns with operating under pressurized conditions. The ScF and NcF methods developed in this effort provide the tools and understanding to enable cost-effective, industrially scalable, environmentally benign nanomaterial processing.

In this program, we focused upon exploring ScFs/NcFs applicability to better nanomaterial manufacturing in general. We explored end-to-end processing of nanoparticles (NPs) manufacturing using ScFs (or NcFs) that could synthesize, modify, purify, transport, manipulate, and deposit the NP onto device surfaces. This process would take advantage of NcF and ScF "dry" characteristics in order to exploit the phase change of the fluid to a gas, by virtue of the pressure being lowered during device removal from the system. As a result, this will lead to a final finished product that would be free of processing solvents and ultimately will decrease processing time by removing the traditional solvent "drying step." In doing this, the formed device should be immediately ready for additional down-stream assembly into the final product or package. The diagram in Figure 72 illustrates a conceptual process flow. This program/task explored novel, greener methods for the processing of nanoparticles with ScFs and NcFs.
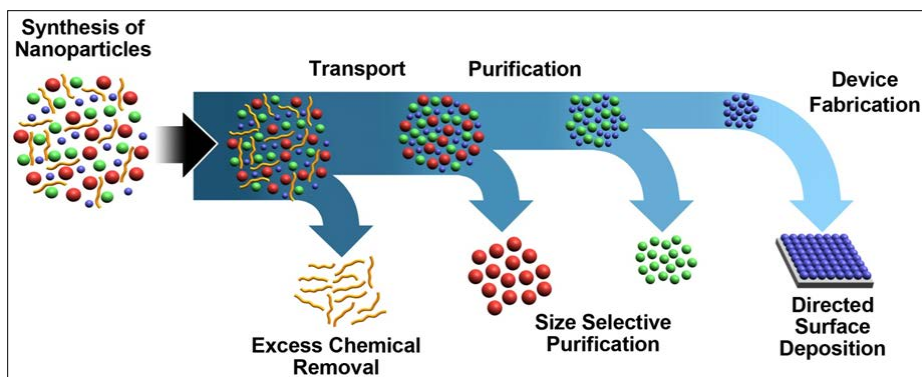
Figure 72. General Process Flow for Compressed Fluid (supercritical or near critical phase) Explored for Nanoparticle (NP) Processing.

We have mapped the ScF and NcFs conditions enabling modification, facial transport, purification, and deposition of nanoparticles. We have explored ScF and NcFs manipulation of Au, Fe_3O_4, and PbS nanoparticles (stabilized with organic ligand shells). The results of this effort quantitatively demonstrate that NcFs can offer pressure-tunable, size-selective control of NP solvation and transport at room temperature and easily obtainable relatively low-pressure conditions. These capabilities provide clear advantages over conventional solvents and direct application to various nanomaterial manufacturing processes. In summary, we found:

- We could use NcFs and ScFs to remove excess organic reactants, byproducts, and solvents from batches of produced NPs without loss of nanomaterial or generation of chemical waste—a substantial improvement over conventional nanomaterials processing methods.

- We could change the NP surface chemistry using ScF and NcFs. This method can be operated at room temperature and generates no organic waste products—a substantial improvement over conventional nanomaterials processing methods.

- ScFs and NcFs media were found to be ineffective solvent systems for many nanoparticles synthesis methods.

- We can transport NPs (with organic surface chemistry) with liphophilic ScFs and NcFs media such as ethane, propane, and noble gasses. The commonly used ScF, CO2, is not effective for most NP solvation and transport but is very effective for the removal of excess ligands or ligand exchange reactions.

- NcF ethane was found to provide a low temperature but very tunable processing solution for organic functionalized NPs.

- NcF propane was found to provide good solubility at low temperatures and pressures but lacks tunability.

- NP solubility was dependant upon ligand shell composition, core material, and core size. ~10 nm appeared to be around the upper limit of size that could be solvated for the NPs and fluids tested.

- ScFs and NcFs can be used to purify NPs and narrow the size distribution of a production batch without waste generation.

- By varying the pressure (i.e., density) of the fluid (NcF or ScF), we could control the deposition and the separation of NPs from a mixture.

83

Synthesis and Clean Up of Nanoparticles with Supercritical and Near-critical Fluids

Many of the reactants required for synthesis of most NPs are polar, that is, metal salts and oxides, and consequently the ScFs and NcFs media (that are nonpolar) were found to be ineffective solvents for present nanoparticles synthesis methods. However, the ScFs and NcFs media were found to be very effective for post-synthesis cleanup of nanoparticles. This is significant and valuable because the manufacturing of nanoparticles requires the removal of residual reagents and side products from the post-synthetic production stream before the material can be used. A method to remove excess organics from the nanomaterials post production as well as change the surface chemistry of NPs using ScF and NcFs was been developed.[104-106] For fluids such as ethane and propane surface chemistry modifications are carried out at pressures high enough to solvate the organics involved in the synthesis but insufficient to mobilize the NPs. Alternatively CO_2, is not effective for solvation and transport of most NPs but is a very effective solvent for the removal of excess ligands or ligand exchange reactions. Regardless of solvent, this method operates at lower pressures and room temperature, and generates no organic wastes—a substantial improvement over conventional nanomaterials processing methods.

Methods for synthesis of new NP surface chemistries were developed that provide improved separations for environmental and industrial processes. Specifically the focus was upon the modification of the superparamagnetic Fe_3O_4 NPs for the recovery of heavy metals and radioactive materials.[107-113] When correctly modified and handled, the Fe_3O_4 NPs provided efficient and rapid separation.

Transport of NPs in Near-critical and Supercritical Fluids

We explored the fundamental solubility and dispersibility of NPs of different core sizes and different surface chemistries in selected near-critical and supercritical fluids.[98, 100, 104-106, 114] Typical NcFs and ScFs are usually lipophilic solvent systems with low dielectrics and polarity but they can have good polarizability. CO_2 can provide good densities, tenability, and accessible critical points values. Further, CO_2 is inexpensive, non-flammable, nontoxic, and typically an effective widely used NcF/ScF CO_2—but has been found to ineffective solvents for NPs.[115] The heavier noble gasses (i.e., Xe and Kr) were found to be good solvents for NPs. They have good polarizability, are chemically inert, and are optically clear over a wide spectroscopic range. This makes these fluids very useful for fundamental studies, but they are likely cost-prohibitive for any large-scale utilization. However, recycle of the compressed solvent in a closed process could significantly mitigate cost issues. As previously reported for other nanoparticles and subsequently shown herein, NPs (specifically demonstrated with PbS QDs, Au NPs and Fe_2O_3 NPs) stabilized with nonpolar ligand shells (i.e., alkanes) formed stable dispersions in NcF and ScF ethane and propane, and their dispersibility transport are a function of fluid density and pressure.[98-100, 104, 114] The higher the density of the fluid, the better solvent it becomes for the NPs. Compressed ethane and propane were found to provide good solubility over a wide range of fluid conditions. Both of these solvents enable green chemical processing and transport of NPs due to their nominal toxicity, high degree of tunability, and reduction of solvent waste. NP dispersibility was found to be strongly dependent upon nanoparticle size, surface chemistry, and solvent density. The data showed that the NPs follow the Chrastil model[116] for solubility in compressed gas systems. This is an interesting observation since the Chrastil model is thermodynamically derived for molecular solvation interactions—yet it still applies for the much more massive nanoscale structures.

If other properties are correct, the higher the density of the fluid the better solvent it becomes for the NPs. As can been seen in Figure 73, propane provides high densities, even at relatively low pressures but is not tunable at lower temperatures due to a higher critical temperature. Propane provides good solvation of alkane-functionalized NPs due to its relatively high densities at even modest pressures but the critical temperature is high, and as shown Figure 73, changes in density are not easily achievable for modest temperatures even with large changes in pressure. Consequently, for solvation of alkane-functionalized NPs, propane is a good solvent but is not effective if tunable processes are desired.
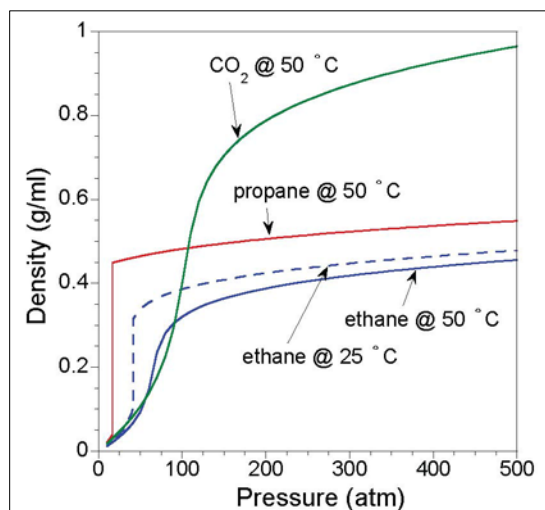
Figure 73. For selected fluids, the change in density with pressure (values from National Institute of Standards & Technology). CO2 and propane provide higher densities (resulting in better solvation strength) but ethane shows better tunability over the pressure ranges achievable with conventional reactors.

Compressed NcF and ScF ethane was found to provide good solubility of NPs and excellent pressure-controlled NP solvation and transport. Ethane provides less density, and hence less solvation strength, than propane for any given set of conditions but as shown in Figure 3, even at room temperature the changes in NcF density with pressure are dynamic. Despite the lower densities, compressed ethane has been found to be effective at solvation of alkane-functionalized NPs, particularly the smaller particles under 5 nm. Further, as shown in Figure 74, the dynamic changes in density allow for simple pressure tuning of the solvation process making this a very interesting fluid system to exploit for the solvation, transport and manipulation of NPs in general. The properties and capabilities of ethane as a solvent are demonstrated in Figure 74. Both near-critical (25°C) and supercritical ethane (50 ^{o}C) provides solubility for varying PbS QD core sizes (with oleate ligand shells). Clearly, the solubility of the QDs is strongly dependent upon fluid pressure/density and QD size.

We have mapped the conditions enabling solubility and facial-transport of QDs, Fe_3O_4 and Au nanoparticles (with alkane ligand shells) with ScF and NcFs. The results of this study quantitatively demonstrate that NcFs can offer pressure-tunable, size-selective control of NPs solvation and transport at room temperature and easily obtainable pressure conditions. These capabilities provide clear advantages over conventional solvents and have direct application to

Approved for public release; distribution is unlimited.

various nanomaterials processes such as separation, transport purification, and selective deposition of nanocrystals.
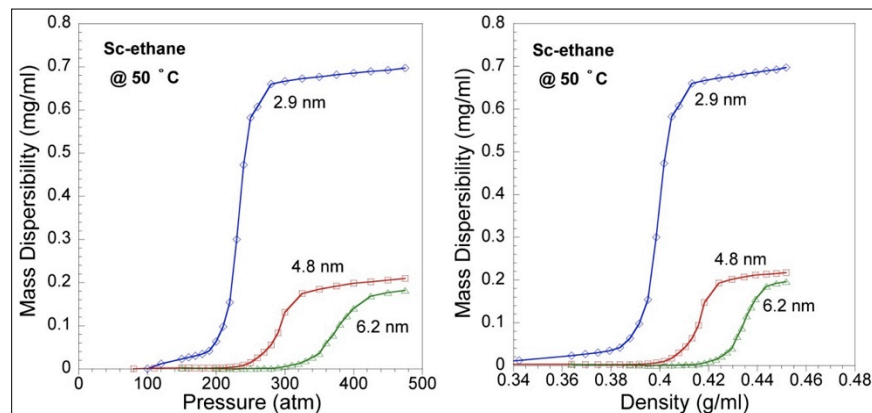
Figure 74. Plots of Maximum Possible Concentration of PbS QDs (oleate ligand shells) with Respect to Pressure and Density for Supercritical Ethane (50°C).

Clearly the solubility of the QDs is strongly dependent upon fluid pressure/density and QD size. The flat regions at upper pressure/density regions indicate all of the QDs from the sample are in solution (subsaturated condition).

NP Size Purification with Compressed Fluids

Since the functioning properties of the nanoparticles are frequently size-dependent (i.e., emission wavelength of quantum dots) size purification and selective sorting is a desired capability for the production of nanoparticles with uniform characteristics. Very limited alternative size-selective deposition and purification methods are available for NPs; and they are typically inefficient (with very expensive material) and generate significant volumes of waste. We explored a range of methods for NP size purification with compressed fluids. After evaluating a number of methods, we found that by varying the pressure (i.e., density) of the solvent fluid, we could control solvation and enable separation of NP into various size fractions.

Room-temperature purification of as-synthesized NPs has been demonstrated by simply increasing the pressure. Figures 75 and 76 show the QD size distributions lifted in each higher pressure fraction from a mixture of PbS (oleate) QDs with sizes ranging from approximately 1– 10 nanometers. The larger components of the mixture enter the NcF ethane solution as pressure increases. This enables selective and controlled separation and purification of NPs with sequential ethane rinses at increasing pressure. The size distribution and separation can be controlled by the number of pressure steps used to wash the sample. The insoluble portion can be observed (see Figure 75) to be mostly larger, chunky components. The few smaller remaining components may be strongly bound to large particles or have incomplete ligand shells that prevent them from interacting with the solvent strong enough to be solvated and transported. These incomplete ligand shells may also result in unstable nanostructures that subsequently result in agglomeration. Clearly using pressure adjustments enables size purification and selective solution transport.
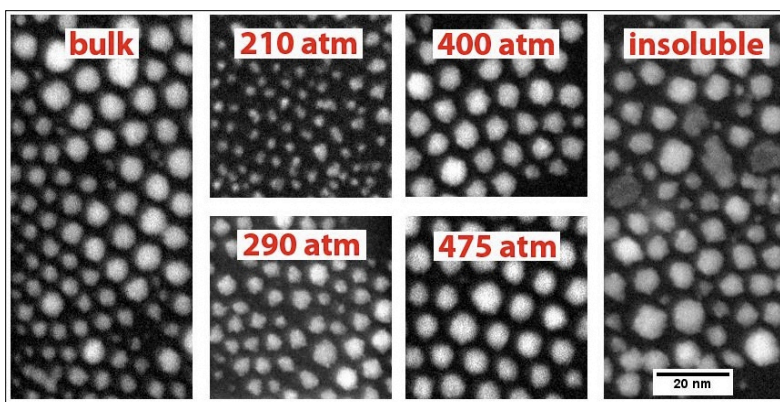
Figure 75. STEM Images Showing the PbS (oleate ligand shell) Nanoparticle Fractions Collected After Washing in Compressed Ethane at the Respective Pressures.

Size purification was conducted while increasing pressure. Lower pressures solvated smaller particles. As pressure increased, the size of the particle transported increased. The insoluble fraction can be seen to be mostly very large irregular particles that ethane could not be soluabilized and transport. All images are shown at the same size scale so they can be visually compared to each other easily, where the 20-nm scale bar is applicable in all cases.
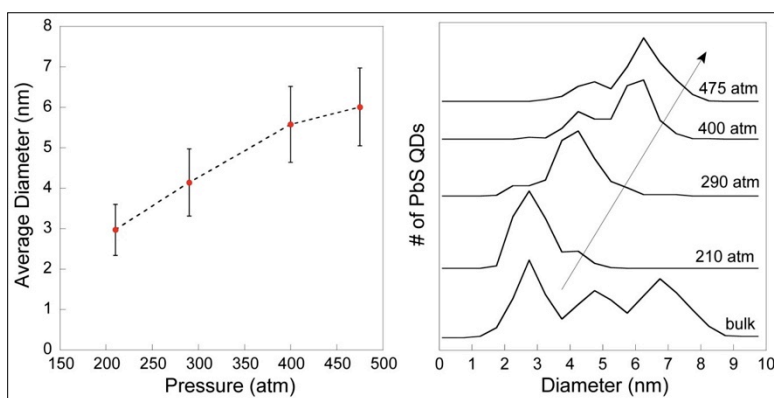
Figure 76. PbS (oleate) QD Fractions Lifted with Selective Solution and Transport.

Each nanoparticle fraction had a minimum of 350 particles counted, where error bars show one standard deviation (on left graph). Note insoluble residual fraction contains mostly particles greater than 8 nm. The arrow in the graphic on the right indicates increasing pressure. The QD size distribution collected at increasing pressures show the ability to separate size fractions from the bulk sample with a large size distribution.

We have mapped the conditions enabling facial purification and size separation of QDs (and other nanoparticles) with ScF and NcFs. We demonstrated controlled size separation of NPs from mixtures with large distributions. The ability to achieve particle separation is crucial because the performance of the nanomaterials correlates directly to their size. The ability of easily separating size fractions from a batch of nanoparticles reduces demands upon the production process and enables greater (useful) yield from a given reaction batch. The approach also separates the polar byproducts, residual reactants, and incompletely surface-stabilized

Approved for public release; distribution is unlimited.

nanomaterials in a single step. We have demonstrated a simple method for general size fractionation and cleanup of lipophilic NPs.

NP Deposition Upon Surfaces

Selective NP surface deposition from ScFs and NcFs was explored with a PbS (oleate) QD mixture (~1–10 nm). It was found that by varying the pressure (i.e., density) of the solvent fluid, we could control surface deposition. Again the low-temperature tunablility of ethane made it the solvent of choice. As shown in Figure 77, we demonstrated controlled deposition of QDs (PbS oleate) with room-temperature ethane by varying the pressure (i.e., density) of the solvent fluid. The dashed-line histogram fraction at 475 atm shows the full size distribution of the solubilized QDs within the NcF ethane fluid before deposition. The PbS (oleate) nanoparticle size distribution was a trimodal *mixture* with an average size distribution of 4.9 nm but clearly has a broad distribution (1–10 nm) of core sizes. The mixture was created from combination of 3, 5, and 7-nm (mean size) PbS materials. The solid-line histogram fractions show the deposited QD sizes with decreasing pressure. Clearly decreasing pressure drops the larger particles out first and can be used to dictate when, and what size of particles, are deposited upon the surface. Because the performance of the QDs (and other nanomaterials) correlates directly to their size, the ability to achieve controlled particle deposition is valuable. It provides the ability to assemble specific sized NPs upon surfaces for PV, catalysis, sensing and other applications needing NPs deposited upon surfaces. It should be noted that the ability of compressed gas solvents to effectively permeate high aspect ratio devices, porous materials, and other challenging supports makes such controlled deposition from compressed fluids a valuable method with a range of applications.
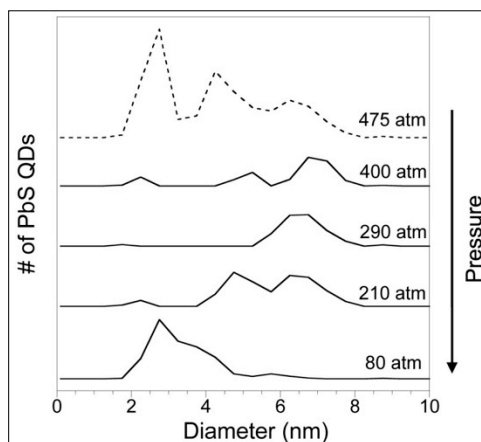
Figure 77. The Calculated and Demonstrated Deposition of PbS (oleate) QDs while Decreasing (ethane) Pressure.

The dashed-line histogram fraction at 475 atm showing the full size distribution of the solubilized QDs within the fluid before deposition. The solid-line histogram fractions show the deposited QD sizes with decreasing pressure. A decrease from 475 to 400 atm desposits mostly larger particles above 5 nm. The decrease from 210 to 80 atm deposits mostly the smaller particles below 5 nm. Clearly decreasing pressure can be used to dictate when, and what size of particles, are deposited from the solution upon a surface.

Future Efforts for Controlled NP Film Deposition
We will continue to explore methods to direct thin NP film formation from ScF/NcF solutions. Solvation of NPs is a dynamic tension between solvation forces from the fluid and attractive forces from the surfaces. Adjusting chemistry and solvent conditions should enable controlled NP film formation from compressible fluids without waste generation or inefficient use of precious NPs.

Thin film deposition in porous materials or over large surface areas is best accomplished by a simple reduction in pressure/density of the ScF. We continue to explore methods that utilize controlled ScF pressure/density as means for generating NP films over larger surface areas (planar or porous). Optimal conditions and methods to evenly dispersed NPs across a surface and/or provide dense NP monolayers on a surface remain to be developed.

We will continue to explore fluid conditions that allow selective deposition of NPs onto chemically functionalized surfaces while minimizing unwanted nonspecific binding of the NPs to the unfunctionalized surfaces. This will enable efficient directed and patterned deposition of very expensive materials. The patterned thin films of NPs will provide a tailored localized interface and enable device applications. Various classes of surface chemistries will be explored for binding, including alkane and thiol terminated moieties (that are known to have high affinities for functionalized NPs) that can be installed on a variety of surfaces using established techniques (i.e. silanization or photolithography). Ligand exchange on the particles in films could adjust them for improved structural stability, enhanced charge transfer or sensitize them to specific analytes.

Characterize electron transport in 1D arrays of Au nanoparticles assembled on DNA
Richard Taylor (University of Oregon)
This task focused on the detection and characterization of phase coherence and chaotic electron dynamics in mesoscopic semiconductor arrays and Au nanoparticle arrays on DNA scaffolds. We aimed to chart these phenomena as a function of the coupling strength between individual array elements. Potential applications centered primarily on the ability to control the devices' chaotic sensitivity, which is a desirable property for high-speed switches and novel electromagnetic sensors. Here we detail the progress of our project toward these goals over the course of our two-year AFRL grant.

Mesoscopic Semiconductor Arrays
These devices are based on an InGaAs/InP semiconductor heterostructure in which donor electrons are confined to a narrow (9nm) layer of InGaAs between two layers of InP (see Fig.78a). The confinement occurs because of a band mismatch between the two semiconductor species. This forms a quantum well in the InGaAs layer that is $< \lambda_F$ (Fermi wavelength of the electron) in width, which is seen as 2-D by the confined electrons. This layer of mobile electrons is well-separated from the donor atoms, which results in high mobilities and long mean free paths. It is referred to as a 2-D electron gas or 2DEG.
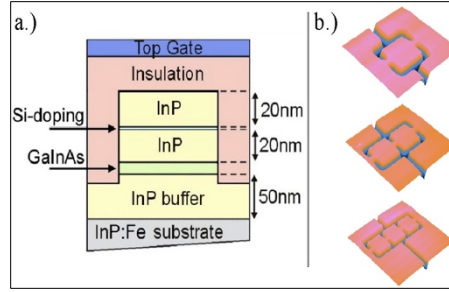
Figure 78. A schematic of the etched heterostructure (a), and AFM images of the arrays (b). The 2DEG is confined in the GaInAs (9nm thickness) indicated in (a).

Our arrays are formed by chemically etching the heterostructure so that we are left with ~1 μm square islands connected by quantum point contacts (QPCs). This structure is then covered by a layer of insulating polymer and a metal top gate is used to tune the Fermi energy in the underlying 2DEG. In order to carefully study the transition from a single element to an array, we fabricated our three devices (Fig. 78b) on a single Hall bar. This allows simultaneous measurements of all three devices in identical experimental conditions.

During the term of this grant, we conducted experiments to explore electron dynamics in the arrays in both the 'open' regime, where electrons freely move through the QPCs, and the 'closed' regime, where electrons must tunnel through the QPCs into the array.

The analogy between the nanoparticle arrays, in which each element is a metal particle surrounded by an insulating molecular shell, and the closed dot arrays is the most literal one. However, our experiments with closed arrays showed that the magnetoconductance fluctuations (MCF) that we use to chart the evolution of chaotic electron dynamics occur on a much larger field scale than the open arrays. This made further study of the closed arrays impractical for the near term, and we proceeded instead with our analysis of the open arrays. We can use the open array MCF (Figure 79) to extract the average time between phase-breaking events (τ_φ), examine the distribution of electron trajectories within the array, and make inferences about the extent to which the elements of the array are coupled. For example, we can calculate τ_φ from the variance of these fluctuations and standard device parameters.[117]
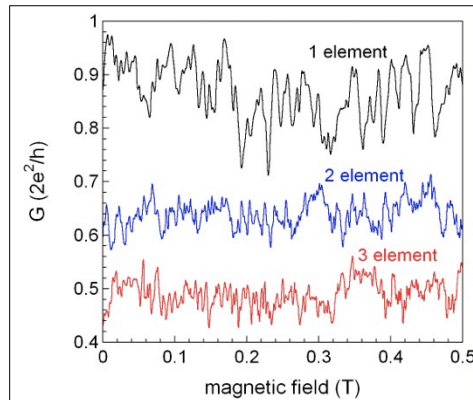
Figure 79. MCF for a single conducting mode in each of the three devices.

Approved for public release; distribution is unlimited.

The single element array trace is offset upward by 0.2 x $2e^2$/h for clarity.

Figure 80 shows that while τ_φ is the same (within error) for each of the three arrays (Fig. 80a), we see a significant decrease in the average energy level spacing (ΔE_s) in the two and three element arrays (Fig. 80b) compared to the one. We believe this is clear evidence of coupling between each array element via a hybridization of their energy level spectra. This novel analysis technique and supporting analyses is described in Martin, 2009.[118]
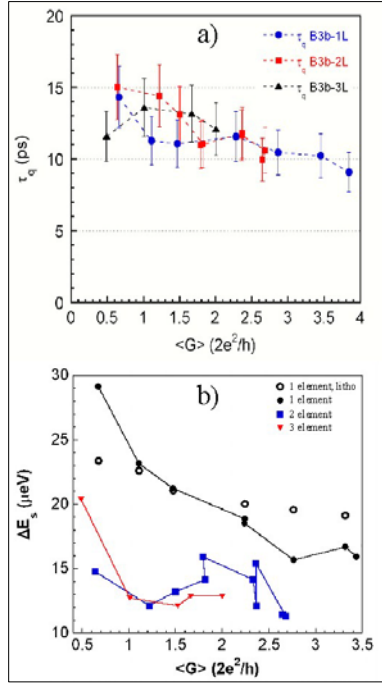
Figure 80. Phase-breaking times for the one, two, and three element arrays based on high field correlations (a), and the average energy level spacing in each device (b). The open circles in (b) represent a baseline calculated from the device's lithographic dimensions.

Nanoparticle Arrays
Near the start of the project, we realized that the ideal device architecture, both for physical specificity and for analogy to the semiconductor arrays, was a single strand of DNA stretched between two electrical contacts. Once the nanoparticles were deposited on to this single strand, we would have a single 1-D tunneling array. The existing devices were fabricated such that many thousands of nanoparticle arrays lay between the contacts, removing the ability to address single array behavior.

However, moving to the proposed single array device architecture required a complete re-thinking of the fabrication process, from chemistry to lithography. This process was undertaken by our collaborator in the Hutchison Lab, Greg Kearns, and was successfully completed near the end of this grant's term.

Once devices (for an example, see Fig. 81a (inset)) were available, we integrated them into our measurement setup. For this experiment, the apparatus consisted of a high-sensitivity dc

91

measurement circuit connected to a variable temperature He3 cryostat. All of this was computer-controlled via a GPIB connection.
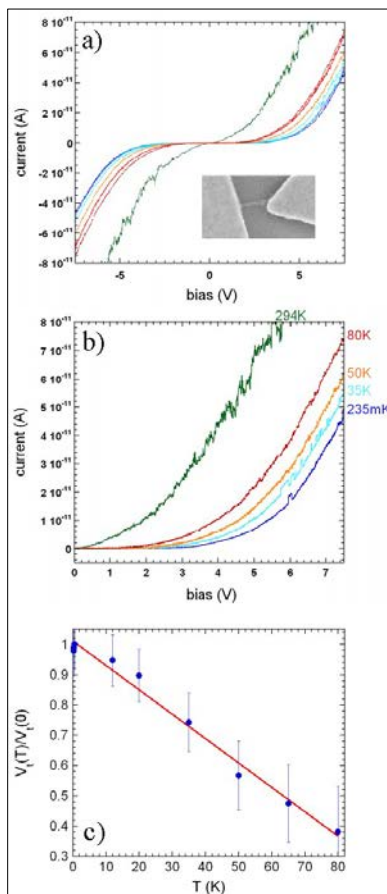
Figure 81. Nonlinear, antisymmetric I-V curves (a) show Coulomb blockade in our devices (example, inset(a)). The threshold for current flow is temperature dependent (b), and is shown (c) to be linear, consistent with theoretical treatment.

Unlike a previous experiment showing dc I-V characteristics of nanoparticle arrays on DNA scaffolding, we see a set of clear, nonlinear I-V curves (Fig. 81a). The flat region at the center that is symmetric in voltage indicates a phenomenon known as Coulomb blockade, which blocks current below a threshold voltage. The threshold voltage is related to the classical charging energy for a single element of the array and is temperature dependent (Fig. 81b).
Current theory[119] predicts that the threshold voltage will have a linear dependence on temperature, which we observe in our device (Figure 81c). Extrapolation of the linear trend suggests that Coulomb blockade in this device would disappear at ~120K, though this varies between devices. It is possible that using smaller nanoparticles, which have a correspondingly larger individual charging energy, would increase the maximum temperature for Coulomb blockade.

Self-Assembled Fractal Nanocircuits: A Green Approach To Nanoscale Energy Transport
Richard Taylor (University of Oregon)
The goal of this project was the investigation of the electronic properties of self-assembled fractal circuits. In addition to capitalizing on the material efficiency of the 'bottom-up' approach, the resulting circuits exploit the favorable electrical properties associated with conduction through fractal patterns with the aim of developing novel circuit functionality. The investigation focused on the degree to which the fractal characteristics (quantified by a fractal analysis of electron microscope images of the circuits) provide an enhanced performance of the circuits. During the period of the project, three applications of fractal circuits were considered: 1) non-linear gated circuits, 2) circuits that interface retinal implants to retinal neurons, 3) circuits that form the electrode of novel solar devices.

Simulations of the electronic conduction properties of the circuits
The initial investigations focused on simulations of the electrical conduction properties of fractal circuits. We examined how electrostatic gates could be employed to transfer the inherent nonlinearity of the fractal's spatial geometry into novel nonlinear features in the circuit's gate characteristics. To explore a wide variety of possible circuit architectures, we developed a simple circuit simulation program based on the modified nodal analysis technique. Figure 82 shows simulation results for the '2 iteration' Sierpinski circuit, where we calculated the differential resistance of the circuit as a function of the electrostatic depletion from the side gates.[120] The cross-section of the pattern depleted by each gate position is shown in the corresponding color above the differential resistance plot, and the cross-section is aligned with the x-axis such that, for instance, the third pixel aligns with a 3-pixel gate depletion. Depleting the current-carrying channels (colored pixels) causes a series of differential resistance responses whose amplitudes are dominated by the width of the remaining conducting channels, but whose frequency (in x space) is dictated by the fractal geometry of the circuit. These simulations were repeated on the equivalent Sierpinski circuit featuring 4 iterations also shown in Figure 82. The narrow gates have the same positions as before, although now they deplete over cross-sections 81 pixels in length (as shown above the plot). The two additional iterations give this circuit 9 times the area of the 2 iteration circuit and feature sizes ranging from one pixel (the same as before) to 81 pixels. This corresponds to an additional ~ 1 order of magnitude in fractal scaling over the previous simulation. The frequency (in x space) of the features is once again dictated by the fractal geometry of the circuit. However, the increase in iterations leads to a far more complex differential resistance response (Figure 82). These simulations demonstrate that novel, non-linear conduction behavior can be generated from the underlying fractal geometry of the circuits. Furthermore, increasing the fractal scaling range of the circuit drastically increases this non-linearity.
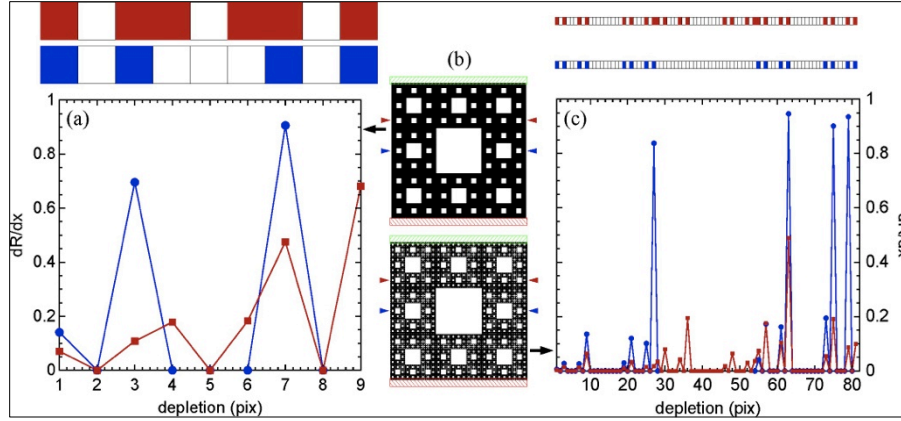
Figure 82. Plots of the differential resistance (a, c) for Sierpinski circuits featuring 2 (b, top) and 4 (b, bottom) iterations of the square pattern.

The differential resistance (dR/dx) is calculated as a function of depletion x, measured in pixels from the edge of the circuit to the edge of the large central square (corresponding to 9 pixels for the '2 iteration' circuit and 81 pixels for the '4 iteration' circuit). The gates are modeled as being one pixel in width. The depletion pattern along the width of the circuit is shown above each plot in colors corresponding to the data points. In (b), the positions of the gates are shown with red and blue triangles. The source (red) and drain (green) electrodes are shown as striped boxes.

Simulations of the self-assembly growth process

The above simulations were conducted on simple, so-called 'exact' fractals, which can be fabricated suing conventional fabrication techniques such as optical and electron-beam lithography. However, self-assembly fabrication techniques will generate branched fractals where the statistical qualities of the branch patterns recur at increasingly fine magnifications. In order to confirm that these self-assembled circuits also generate the same novel non-linear performance as the exact fractals, we created a program that simulates the fractal patterns generated from self-assembly. Examples, showing the results of three differing growth conditions, are shown in Figure 83. When these patterns form the basis of the electrical simulations, the results confirm that they exhibit similar non-linear properties to those shown in Figure 82 for the exact fractal circuits.
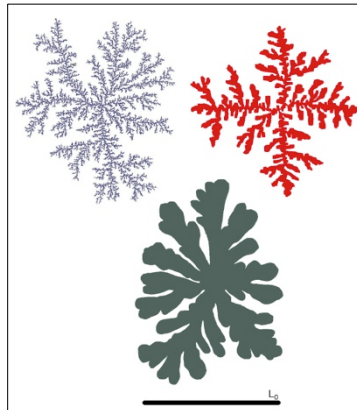
Figure 83. Three examples of simulated self-assembled fractal circuits [1]. The size bar L represents 5 microns.

Fabrication of the self-assembly growth process.
Figure 84 is a schematic of the self-assembly process.[120] In this process, metallic nanoclusters are carried on an inert flow of gas until they impinge on a smooth substrate (left). The fractal patterns then assemble according to the dynamics of diffusion-limited aggregation (DLA).[120] Figure 85 shows an image of a fabricated self-assembled circuit composed of antimony. Whereas these fabricated circuits will exhibit the novel-nonlinear conduction properties of the simulations, in the final year of the project we have been investigating their potential use as 1) interconnects for retinal implants[121] and solar devices. The former concept exploits the fractals ability to maximize electrical connection to neurons while concurrently maximizing light transmission to the implant. A patent application is pending.[122]
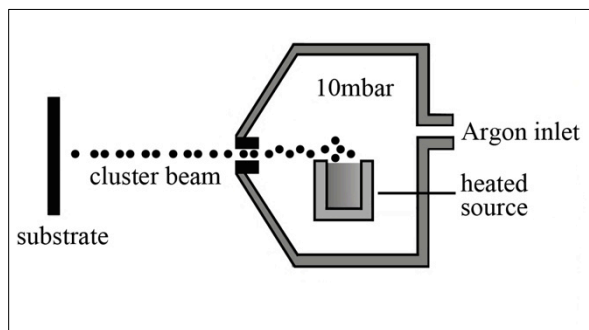
Figure 84. The self-assembly fabrication process.

Figure 85. An atomic force microscope image of a self-assembly electrical circuit. The diameter of the circuit is 5 microns.

Development of nanomaterials for energy storage
Biological Fabrication of Nanostructured Thin Films for Photovoltaic and Energy Storage Applications
Greg Rorrer (Oregon State University), Jun Jiao, Bin Jiang (Portland State University), Mark Jones (Pacific Northwest National Laboratory)
Preparation of semiconductor thin films containing periodic nanostructures isolated from photosynthetic marine microorganisms
Efforts focused on the preparation of diatom thin films, and the deposition of nanoscale TiO_2 onto the diatom biosilica thin films.

Approved for public release; distribution is unlimited.

Diatom thin film preparation. Two approaches were developed to deposit diatom frustules onto glass substrates. In the first approach, nanostructured diatom biosilica thin films were prepared by growing a monolayer of *Pinnularia* diatom cells on a glass substrate, followed by removal of the organic material via ethanol extraction and UV/ozone cleaning. This process left behind a dense monolayer of diatom biosilica (SiO_2) frustules on the glass substrate (*Figure86a*). In the second approach, diatom frustules were isolated from hydrogen peroxide treatment of cultured diatom cells. The frustules were suspended in methanol, and the slurry was drop deposited onto the glass substrate (*Figure 86b*).
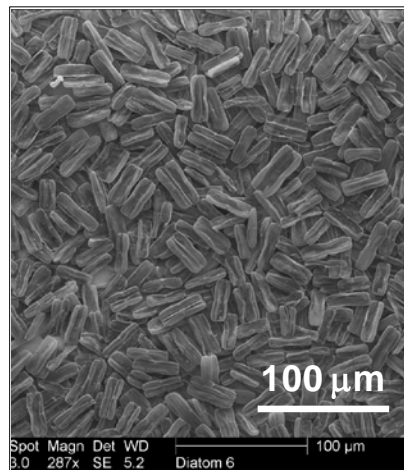
Figure 86a. Diatom cells grown on glass substrate, followed removal of organic matter to prepare diatom frustule monolayer.
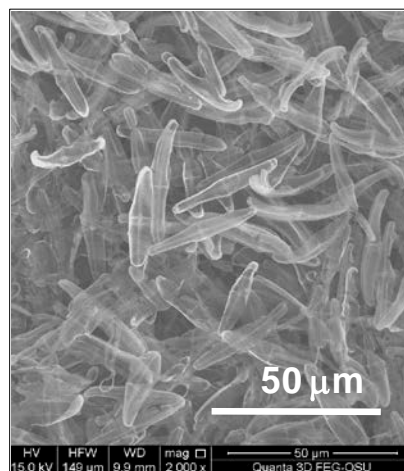
Figure 86b. Diatom layer on glass substrate prepared by deposition of diatom frustules in MeOH slurry.
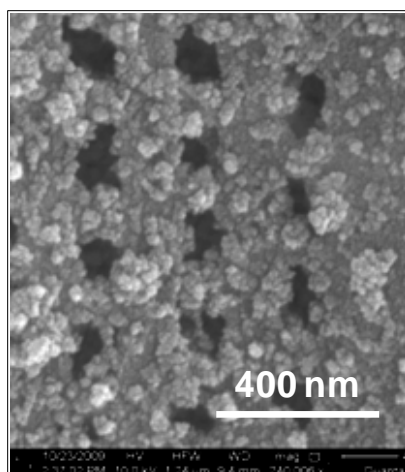
Figure 86c. Partial filling of frustule pore array with TiO₂ nanoparticles deposited by Ti-BALDH condensation on PLL-adsorbed diatom biosilica.

Deposition of nanoscale TiO₂ on the diatom thin film. The diatom frustule thin film was coated with nanoscale TiO_2 by a peptide-mediated deposition process using soluble titanium in the form of Ti-BALDH. First, the polypeptide poly-L-lysine (PLL) was conformally adsorbed onto the nanostructured diatom biosilica by immersing a coupon of the diatom thin film with an aqueous solution of PLL. The PLL-adsorbed diatom thin film was then immersed in TiBALDH solution. *Figure 86c* shows the presence of TiO_2 nanoparticles deposited on the diatom biosilica pore structure. Thermal annealing in air at 450 ^{o}C for 1.0 hr converted the amorphous TiO_2 to the anatase crystalline form. A microscopic image of a FITC-labled PLL-adsorbed diatom biosilica thin film confirms that PLL is adsorbed only on the diatom biosilica, and not on the underlying glass substrate (*Figure 87a*).

The addition of a co-solvent (ethanol, EtOH) in the buffered solutions used for PLL adsorption and TiO_2 deposition significantly increased both the extent of PLL adsorbed on the diatom biosilica and the amount of TiO_2 deposited on the PLL-adsorbed diatom biosilica. Adsorption isotherms for PLL solution on diatom biosilica in phosphate buffer (PBS, pH 7.9), TRIS buffer (pH 9.1), and TRIS buffer with 70 vol% EtOH (pH 9.1) are compared in *Figure 87b*. Although the addition of the EtOH co-solvent only modestly improved PLL adsorption, it increased the extent of TiO_2 deposition by a factor of three (*Figure 87c*). Obviously, solution and solvation parameters play a significant role in moderating peptide-mediated conformal TiO_2 deposition onto diatom biosilica, and merit more detailed investigations in the future.

Figure 87a. Epi-fluorescent microscopy of FITC-labeled PLL adsorbed on diatom thin film.

97
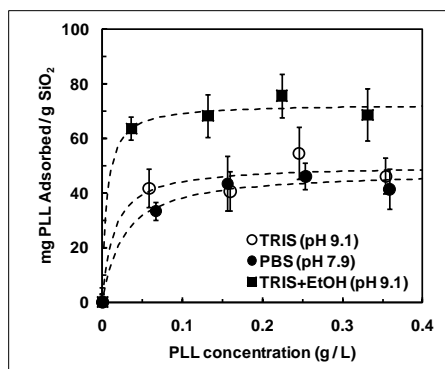
Figure 87b. PLL adsorption isotherm at 25 ^{o}C in different buffers and co-solvents.
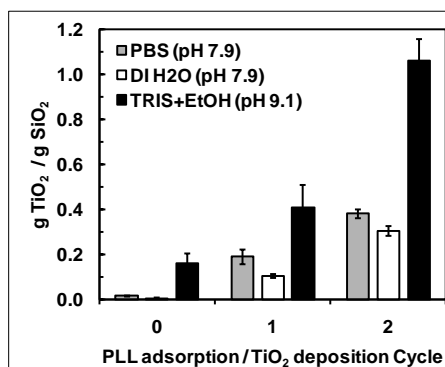
Figure 87c. Comparison of the extent of TiO$_2$ deposited on diatom biosilica frustule thin films at 25 ^{o}C.

Imaging and characterization of biologically fabricated, nanostructured semiconductor thin films for photovoltaic and energy storage applications

Efforts focused on the integration of diatom thin films into a dye-sensitized solar cell (DSSC) thin film photovoltaic device. The fundamentals of DSSC operation are described by Hamann et al.[123]

Device Fabrication.   The base photoanode consisted of a ~15 μm thick mesoporous layer of anatase TiO$_2$ nanocrystals (25 nm) on a fluorine-doped SnO$_2$ transparent conducting (FTO) glass substrate. The loading of TiO$_2$ on the mesoporous TiO$_2$ layer was approximately 3 mg TiO$_2$/cm^2. The diatom-TiO$_2$ layer was added to the top of the mesoporous TiO$_2$ layer (*Figure 88*). Specifically, biosilica frustules isolated from cultured cells of the pennate diatom *Pinnularia* were coated with TiO$_2$ nanoparticles by a peptide-mediated deposition process described in Jeffyres et al. (2008)[124]. This diatom-TiO$_2$ material was suspended in methanol to ~ 1 mg/mL, and the slurry was evenly pipetted onto the surface of mesoporous anatase TiO$_2$ nanocrystal layer to provide a "monolayer" of diatom frustules. This material was then thermally annealed in air at 450 ^{o}C to for 1 hr to convert the biogenic (amorphous) TiO$_2$ to anatase TiO$_2$. The amount of TiO$_2$ loaded on the diatom frustule was 1.1g TiO$_2$ / g SiO$_2$, and surface coverage of the diatom-TiO$_2$ was 62 μg/cm^2 (33 μg TiO$_2$/cm^2), or about 1% of the total TiO$_2$ in the device.   The "control device" did not contain the diatom-TiO$_2$ layer. Images of the mesoporous TiO$_2$ layer and the diatom-TiO$_2$ layer deposited on top of the mesoporous TiO$_2$ layer are presented in *Figures 89a & 89b.*

98

Approved for public release; distribution is unlimited.
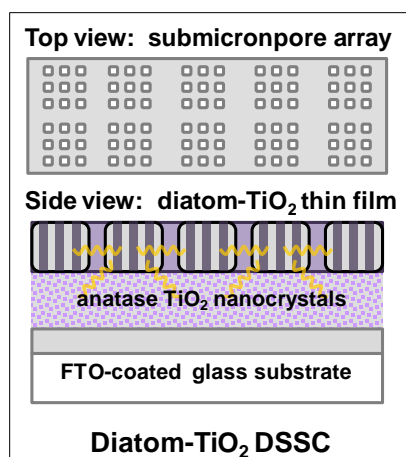
Figure 88. Schematic of diatom-TiO$_2$ layer integration into DSSC device stack.
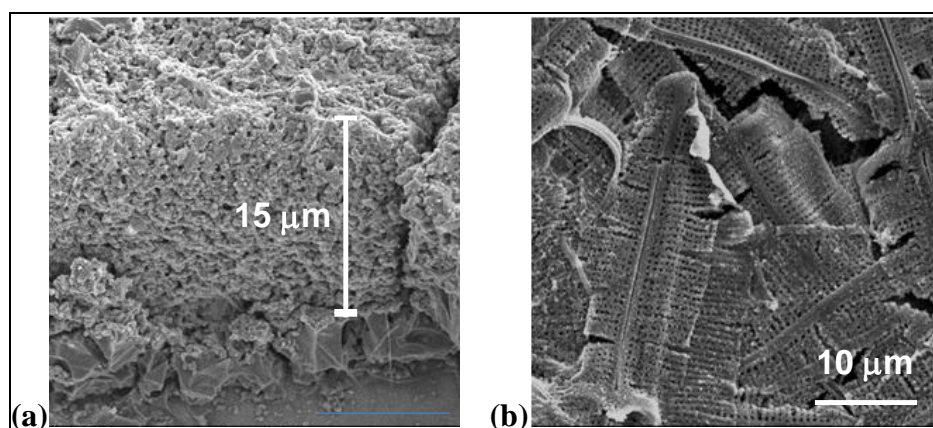
Figure 89. SEM images of the photoanode. (a) ~15 μm thick mesoporous layer of anatase TiO$_2$ nanocrystals (25 nm); (b) top view of diatom-TiO$_2$ layer and underlying mesoporous TiO$_2$ layer.

To complete the device fabrication, the annealed photoanode was soaked in 0.5 mM of N719 photosensitizing dye in ethanol solution for 24 hr. The photoanodes were washed once using ethanol. A 50-um thick plastic spacer and counter electrode of Pt-coated FTO glass were assembled on top of the photoanode. Redox electrolyte (0.1 M 1-aminopyridinium iodide (97%, Aldrich) in 0.1 M KI and 0.05 M I$_2$ dissolved in acetonitrile) was wicked into the space between the photoanode and counter electrode. The device was clamped to prevent evaporation or leakage of the electrolyte.

Device Testing Procedures. Device performance was characterized by photocurrent vs. applied voltage (bias) measurements under simulated solar irradiance normalized to AM 1.5 G sunlight (100 mW/cm^2, Oriel model 96000 150 W light source). The active surface area of the measurement was 0.12 cm^2 (0.4 x 0.3 cm). The efficiency of the device (η)) was estimated by

$$\eta = \frac{harvested\ energy}{incident\ solar\ energy} = \frac{P_{max}}{P_o} = \frac{I_{SC} \cdot V_{OC} \cdot FF}{P_O} \qquad (2)$$

where I_{SC} is the short-circuit current (mA), V_{OC} is the open-circuit voltage (V), FF is the fill factor, and P_o is the incident irradiance (100 mW/cm^2). The maximum power output (P_{max}) is determined from the maxima of the power curve ($P = I \cdot V$ *vs. V*), and FF is backed out from η, I_{SC}, and V_{OC}.

DSSC with diatom-TiO$_2$ layer.   The device architecture for the DSSC with Diatom-TiO$_2$ Layer integrated into the photo-anode is shown in *Figure 90a.* A comparison of the typical performance curve for the control DSSC device vs. the diatom-TiO$_2$ device is shown in *Figure 89b*, and the device parameters are compared in *Table 4.* Average results (and associated 1.0 standard deviation) from 3 measurements on separate locations of 3 independently-fabricated devices (n = 9) are reported. The data provided in *Table 4* and *Figure 90b* clearly show that the diatom-TiO$_2$ layer increased the photocurrent generated by the device, which in turn increased the device efficiency by over a factor of 2. Our working hypothesis is that the diatom-TiO$_2$ layer acts an enhanced scattering layer to direct light into the device, as envisioned in *Figure 88*. This light molding process would be directed by the ordered pore arrays within the diatom frustule, which have pore diameters that are approximately one-half the wavelength of visible light. It is speculated that the diatom frustule acts as a photonic crystal to capture light within the device, thus improving photon absorption.
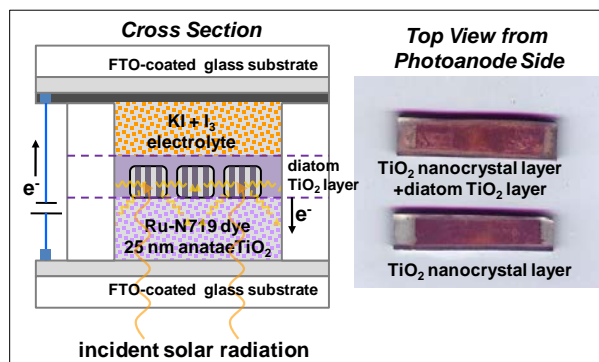
Figure 90a. Cross-section of DSSC device architecture containing diatom-TiO$_2$ layer on top of the mesoporous TiO2 photoanode.
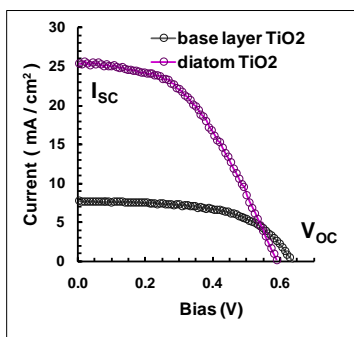
Figure 90b. Representative current-voltage profile for DSSC with diatom-TiO2 layer (1.1 g TiO$_2$/g SiO$_2$) on 15 μm thick mesoporous TiO$_2$ photoanode.

Table 4. Comparison of device performance parameters for the DSSC device containing a 15 μm thick mesoporous TiO$_2$ layer vs. the diatom-TiO$_2$ device containing a diatom-TiO$_2$ monolayer deposited on top of the mesoporous TiO$_2$ layer.

Device	Open Circuit Voltage, VOC (V)	Short Circuit Current, ISC (mA/cm2)	Fill Factor (FF)	Efficiency (η) (%)
control DSSC	0.64 ± 0.03	7.8 ± 2.4	0.58 ± 0.05	2.9 ± 1.1
diatom-TiO2 DSSC	0.61 ± 0.03	23.0 ± 4.7	0.48 ± 0.07	6.7 ± 1.4

DSSC with diatom layer. DSSC devices were fabricated where diatom biosilica frustules containing no nanoscale TiO$_2$ layer were added to the top of the mesoporous TiO$_2$ photoanode. The device performance results are presented in *Figure 91*. The addition of the diatom layer alone modestly increased the device efficiency, but there was significant variance is the open-circuit voltage of the fabricated devices. Consequently, device performance was compared only in devices with comparable open-circuit voltage. These experiments, when in interpreted in the context of *Figure 90b*, suggest that the addition of the nanoscale TiO$_2$ layer onto the diatom biosilica is needed to impart enhanced performance to the DSSC.
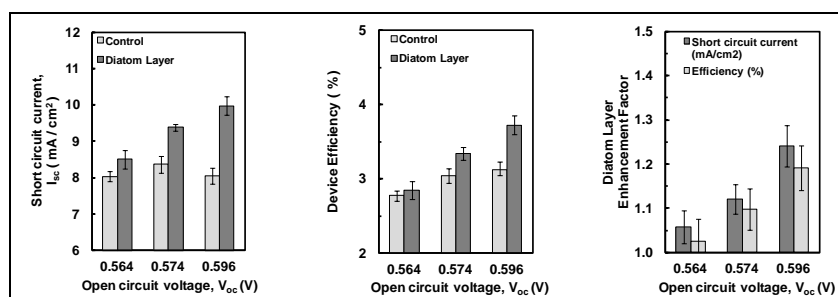
Figure 91. Modest enhancement of DSSC device performance with diatom biosilica light scattering layer deposited on top of mesoporous TiO$_2$ photoanode of ~6 μm thickness. In this device configuration, no TiO$_2$ was deposited on the diatom biosilica.

Ligand exchange provides a facile route to PbS Nanoparticles with short chain ionic ligands
Mark Lonergan (University of Oregon)
We developed a two-phase ligand exchange route to PbS nanoparticles with short-chain ionic ligands. Figure 92 shows the two ligands. One has a monothiol head group binding to the nanoparticle core and is termed MT, and the other has a chelating dithiol head group binding to the core and is termed DT. Figure 92 also shows the ligand exchange process highlighting its two-phase nature. As detailed below, the PbS-MT and PbS-DT nanoparticles were used to demonstrate the ability of short-chain ionic ligands to stabilize metal chalcogenide nanoparticles, the greater photochemical stability of nanoparticles based on 1,2 dithiol head groups relative to monothiol or 1,3 dithiol head groups, the ability of short-chain ligands to promote interparticle charge transport, the impact of mobile ions on the photoconductivity of semiconductor nanoparticles, and the role of ligand and photochemical decomposition in the toxicity of PbS nanoparticles using the Zebrafish model. The two-phase ligand exchange used oleic acid capped PbS nanoparticles as a starting point.[125] The oleic acid in these particles was successfully exchanged for the MT and DT ligands, as depicted in Figure 92.[37] The ligand exchange process proceeded with very little change to the nanoparticle core. This was evidenced by a minimal shift

in the position of the first exciton absorption and transmission electron microscopy (TEM) data (see Figure 93). The PbS-MT and PbS-DT nanoparticles were observed to be indefinitely stable in air-free aqueous solutions.
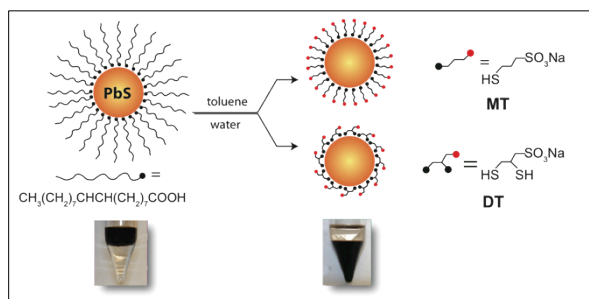
Figure 92. Schematic showing the ligand exchange synthesis of short-chain ionically functionalized nanoparticles based on a dithiol (DT) and monothiol (MT) ligand. The photographs show the migration of the nanoparticles from the organic phase to the aqueous phase during ligand exchange.
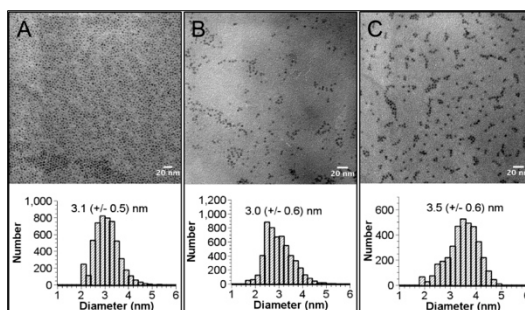
Figure 93. Light-field TEM images of (a) PbS-OLA (OLA=oleic acid), (b) PbS-MT, and (c) PbS-DT nanocrystals with corresponding histograms showing typical particle size distributions (bottom).

1,2 dithiol ligands improve photochemical stability of PbS nanoparticles

As in other semiconductor nanoparticle systems, the ligands and ultimately nanoparticle cores were observed to undergo photochemical decomposition in the presence air. The PbS-MT and PbS-DT particles decomposed at very different rates, with the PbS-DT exhibiting greater solution stability under photoxidative conditions.[37] This result was initially somewhat surprising because previous reports in the literature had indicated that chelating dithiol ligands are photochemically less stable than monothiols.[126] These previous reports on the relative instability were with 1,3 dithiols, which are readily oxidized to cyclic disulfides. We demonstrated that 1,2 dithiols are in fact more stable than 1,3 dithiols and monothiols because of the ring strain that would be involved in forming a cyclic disulfide. The photochemical formation of disulfides must occur intermolecularly, and it was hypothesized that this process leads to polymerization of the 1,2 dithiols on the surface of the nanoparticle thereby promoting stability.
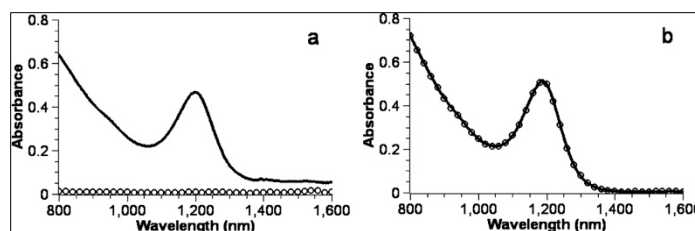
Figure 94. Comparison of the stability of PbS-MT and PbS-DT, under air-free conditions.

Absorption spectra were measured fresh (solid line) and after 108 h (squares) for (a) PbS-MT and (b) PbS-DT. Both samples were stored under 16 mW/cm^2 illumination with a tungsten-halogen lamp.

Ligands strongly affects toxicity of PbS nanoparticles in the zebrafish model due to differences in particle decomposition

The relative stability of the PbS-MT and PbS-DT particles made them interesting candidates to study the toxicity of PbS nanoparticles and the influence of ligand shell. In collaboration with the Tanguay group at Oregon state, we characterized the toxicity of PbS-MT and PbS-DT nanoparticles relative to Pb(NO$_3$)$_2$ in the zebrafish system.[28] Figure 95 shows the results of the toxicity studies. Neither the MT or DT ligand exhibited substantial toxicity over the exposure range studies. There was a substantial difference in the toxicity observed between the PbS-MT and PbS-DT nanoparticles. The PbS-DT nanoparticles were observed to be less toxic, on a per mass basis, than both Pb(NO$_3$)$_2$ and the PbS-MT nanoparticles. The differential stability was argued to be due to the differences in the rates of decomposition of the nanoparticles and its relation to the rate of lead leaching from the nanoparticle core.
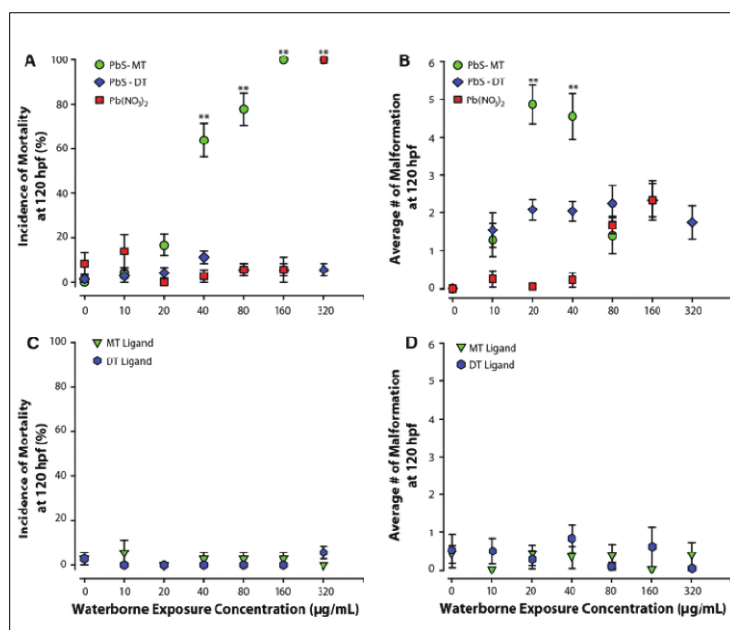
Figure 95. Mortality and malformation curves for embryos exposed to PbS-MT, PbS-DT, Pb(NO$_3$)$_2$, and MT and DT ligands.

Embryos were exposed to PbS-MT, PbS-DT, or $Pb(NO_3)_2$ at 6 hpf and were evaluated for malformations and mortality at 120 hpf. Mortality (a) was statistically significant for PbS-MT (40–320 µg/ml) and $Pb(NO_3)_2$ (only at 320 µg/ml). All surviving embryos exposed to PbS-MT had malformations (average of 5 at 20 µg/ml) (b). $Pb(NO_3)_2$-exposed embryos had little to no malformations (<0.25) up until 40 µg/ml, where a steady increase in malformations was observed at 80 and 160 µg/ml. MT and DT ligands did not induce mortality (c) or malformations (d) in exposed embryos.

Short-chain ionic ligands promote electron transfer between nanoparticles
One of the motivating factors for synthesizing the MT- and DT-ligated nanoparticles was the desire to develop solution processable nanoparticles with very short-chain ligands so as to promote interparticle coupling and thereby enhance charge transport. The repulsion between the ionic ligands helps to prevent aggregation and hence promote solubility. To evaluate the performance of the shot-chain ligands, solid films of the PbS-MT and PbS-DT nanoparticles were evaluated in photodetector geometries in comparison to oleic acid capped particles.[2] Specifically, thin films were cast on interdigitated electrodes (IDEs), and the photoconductive characteristics of the resulting structures were evaluated. This geometry follows closely from other work on PbS nanoparticle photodetectors.[5] Figure 96 compares the ratio of photocurrent to dark current ratio for IDEs coated with either PbS-DT or PbS-OLA. As can been seen, the response of the PbS-DT sample is much greater. In the PbS-DT detectors values of the responsivity exceeding 1 A /W were achieved in the NIR range of the spectrum.
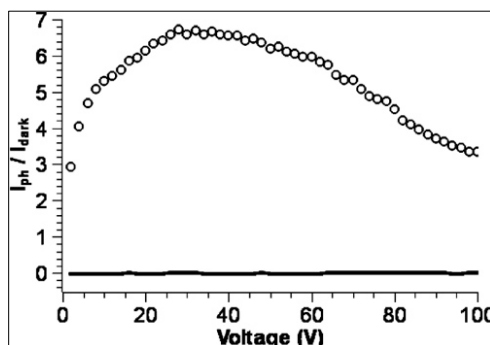
Figure 96. Ratio of photocurrent (I_{ph}) under 100 µW illumination at 900 nm to dark current (I_{dark}) for PbS-OLA (line) and PbS-DT (open circles) thin films.

The IDE used to measure the photoresponse of the PbS-OLA sample had half the electrode spacing of the PbS-DT sample and still no measurable photocurrent was observed.

The presence of ions results in time-dependent enhancements of the dark and photocurrent in PbS nanoparticle arrays.
The presence of ionic ligands opens the possibility for ion migration upon application of bias. Such migration could substantially affect charge injection and consequently photoresponse. Indeed, the responsivity of PbS-DT films (Na^+ counterion) on IDEs is time dependent due to the slow redistribution of ions. For instance, Figure 97 shows the responsivity of a Pb-DT (Na^+ counterion) photodetector subjected to constant bias of 10V and intermittent exposure to light at 1190nm.[127] The responsivity increases with time. Further, after application of bias, the system retains a memory of the ion polarization for hundreds of seconds. This makes possible the

Approved for public release; distribution is unlimited.

operation of the photodetector in photovoltaic mode because the initial redistribution of ions leads to an asymmetry that can split excitons without an externally applied electric field.
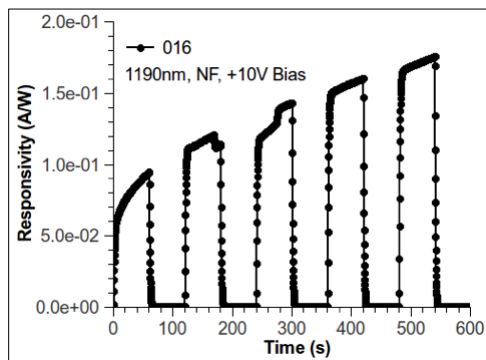
Figure 97. Time dependent response of a PbS-DT (Na$^+$ counterion) nanoparticle film on an interdigitated electrode.

The light was cycled on and off in an approximately 50 s interval. The responsivity increases with time.

The nature of the counterions in ionically functionalized nanoparticle arrays can be used to control the photocurrent response.

The presence of counter-ions in the Pb-DT and Pb-MT nanoparticles provide another opportunity for tailoring the response of the nanoparticles. For instance, the time dependence of the responsivity reported in Figure 97 is due to the redistribution of Na$^+$ ions. It was hypothesized that exchanging the Na$^+$ ions for the divalent Ca^{2+} ion would greatly reduce ion mobility and perhaps improve interparticle charge transport. To test this, a solid film of PbS-DT, with Na$^+$ counterions, was exchange for Ca^{2+}. Figure 99 compares the spectral response of PbS IDE photodetectors with Na$^+$ and Ca^{2+} counterions as a function of time after application of 10V bias.[6] Consistent with the data of Figure 97, the responsivity of the Na$^+$ sample increases with time. The Ca^{2+} sample, however, exhibits very little time dependence. Further, the responsivity of the Ca^{2+} sample at all times is near the highest responsivity achieved in the Na$^+$ sample after biasing for 5 hours.
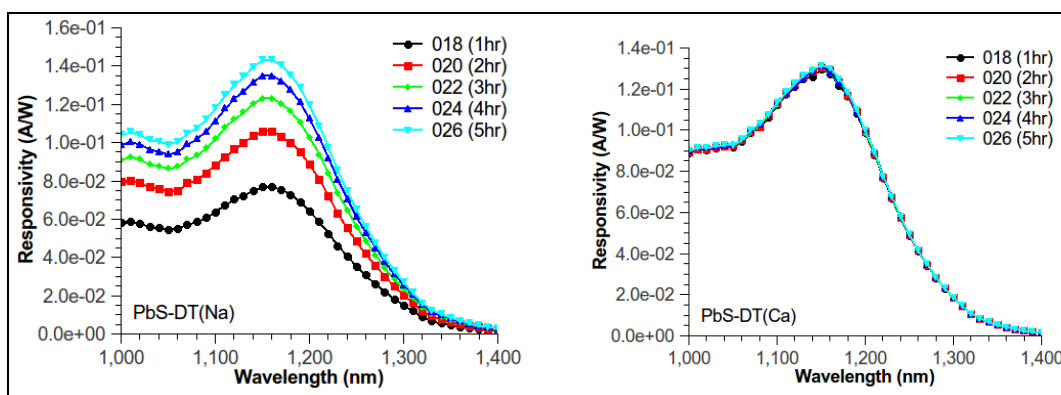
Figure 98. Comparison of the time-dependent spectral response of PbS-DT films on IDEs with Na$^+$ (left) and Ca^{2+} (right) counterions.

The legend shows the time following initial application of 10V bias.

Gold nanoparticle arrays provide tunable work function contacts that can be used to fabricate a semiconductor diode with tunable characteristics.
In the area of metal nanoparticle arrays, we collaborated with the Stucky group at Santa Barbara on tunable contacts to semiconductors. A solid film of gold nanoparticles can be readily oxidized and reduced to change the overall redox state of the film. This is equivalent to changing the work function or Fermi level of electrons. The result is a tunable work function contact, which in principle can then be used to actively tune the current-voltage characteristics of a semiconductor interface. Figure 99 shows the realization of this concept.[128] The family of current-voltage curves shown were all collected at a single n-InP/gold nanoparticle interface. By performing *in situ* electrochemical oxidation or reduction of the nanoparticle film, its work function can be tuned along with the current-voltage behavior of the underlying interface leading to the family of curves shown.   The level of control achieved at this single interface is greater than has been achieved at all know n-InP/metal interfaces and in our earlier work using tunable conjugated polymer contacts.[129] Although not directly supported by this project, the collaboration initiated with the Stucky group led to further study on the use of ionic ligands to control the electrochemistry and charging of gold nanoparticle arrays.[128, 130]
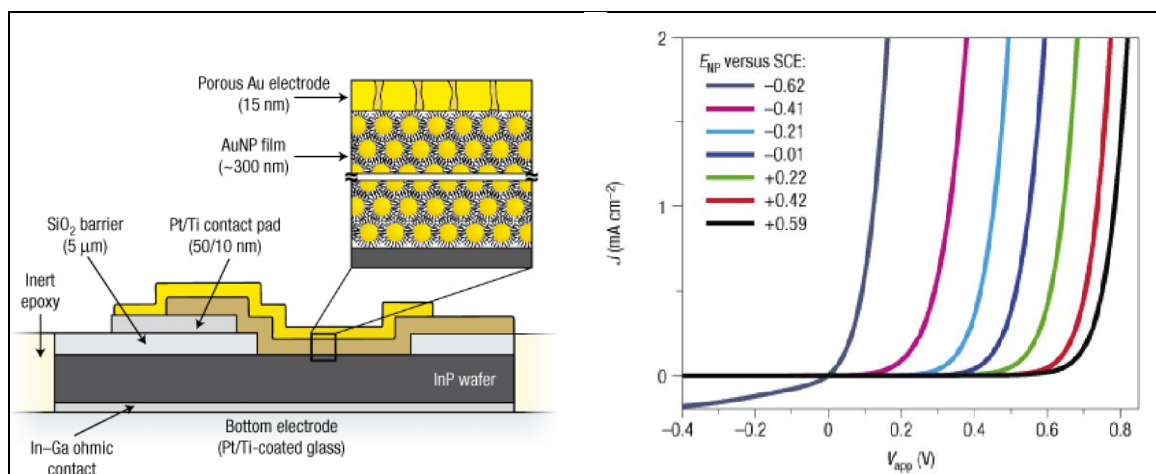
Figure 99. Left: Schematic of a gold nanoparticle array contacted to an n-InP wafer. The top electrode contact is porous and contacted with a liquid electrolyte to enable active electrochemical manipulation of the electrode potential (Fermi level) of the nanoparticle array. Right: current density-voltage curves collected at a single InP-gold nanoparticle interface as a function of the electrode potential E_{NP} of the gold nanoparticle array.

Nanofibrous conductive polymers integrated with nanostructured semiconductors for inverse dye-sensitized solar cells
Carl C. Wamser (PSU-Chemistry), Rolf Koenenkamp (PSU-Physics), Glen E. Fryxell (PNNL)
Research activities and results have focused in four main areas: 1) incorporation of n-type semiconductors into poly-TAPP nanofibers for inverse dye-sensitized solar cells (iDSSCs), 2) development of new dyes for attachment to poly-TAPP or for use in standard DSSCs, 3) computational methods to help understand the mechanisms of electronic conductivity in poly-TAPP, 4) exploration of photocatalytic applications of poly-TAPP and related pyridyl porphyrin and metalloporphyrin derivatives.

Inverse DSSCs

In collaboration with Dr. Glen Fryxell's group at Pacific Northwest National Laboratory (PNNL), we have developed ways to incorporate TiO_2 into the pores of nanofibrous poly-TAPP in order to create a novel inverse dye-sensitized solar cell (iDSSC). Using nanofibers of polyaniline as a template, TiO_2 was grown by sol-gel processing from a Tyzor LA solution (pH 1.7, 70°C). Good growth was observed, but the TiO_2 was amorphous rather than crystalline. Similar studies with nanofibrous poly-TAPP are underway, as are methods to develop mild conditions to convert amorphous TiO_2 to anatase.[131]

In collaboration with Professor Rolf Koenenkamp's group, we have developed ways to incorporate ZnO into the pores of nanofibrous poly-TAPP. Spray pyrolysis of a zinc acetate solution followed by PCBM spin coating is relatively effective, and cells made in this way show external quantum efficiencies up to 0.5% that track with the absorption spectrum of the porphyrin (see Figures 100 and 101). Beginning with novel ZnO nanowires or nanorods, we have generated an overlayer of poly-TAPP followed by pore filling with P3HT; these solar cells gave similar results of up to 0.5% external quantum efficiency. Sensitization with CdSe quantum dots followed by P3HT pore filling has also been studied.
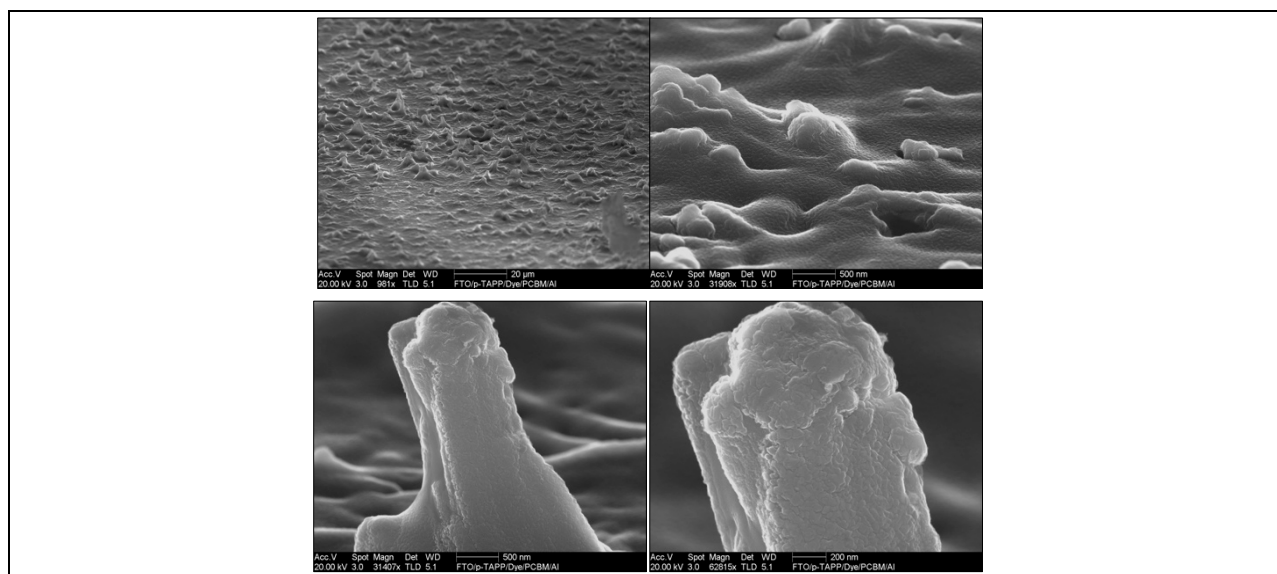
Figure 100. Scanning Electron Micrographs of a poly-TAPP/TCPP/ZnO/PCBM Electrode

Approved for public release; distribution is unlimited.
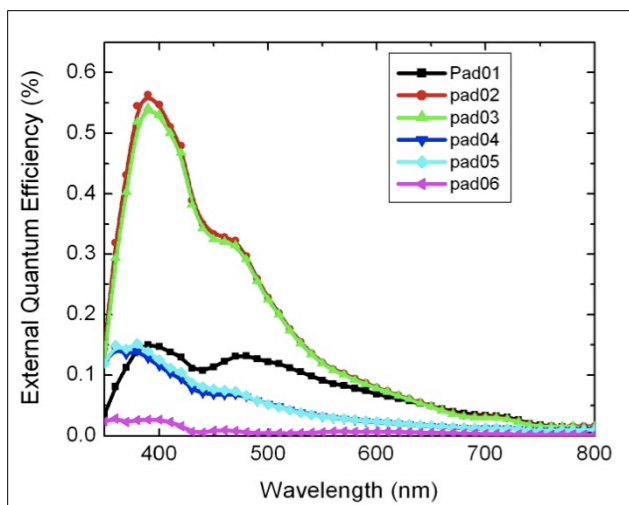
Figure 101. Action Spectrum of a poly-TAPP/TCPP /ZnO/PCBM/Al Solar Cell.

Novel porphyrin dyes and co-adsorbents
Because phosphonate groups show better binding to TiO_2 than carboxylate groups, we have developed ways to attach phosphonate groups to poly-TAPP (using $POCl_3$) and to synthesize new porphyrins with phosphonate groups. Treatment of aryl amines with $POCl_3$ followed by an aqueous ammonia workup generates the corresponding phosphonic acid/amide. We have synthesized tetra(4-bromophenyl)porphyrin and used Pd coupling to attach one or more phosphonate groups. We are studying the strength of binding on TiO_2 compared to carboxylate derivatives as well as means of covalent attachment of these phosphonate derivatives to poly-TAPP.

We have a full set of spectra representing acid-base titrations of tetraphenylporphyrins with one to four aminophenyl substituents. We observe hyperporphyrin spectra for all of them, with strong and broad far-red absorption peaks, which may make them desirable solar dyes. Particularly unusual is the detection of a mono-protonated state for the monoaminoporphyrin, which we believe is the first case in which a porphyrin has been observed with only one (as opposed to two) additional protons on the central pyrrole nitrogens.[132] We have also studied each of these with and without Zn metallation (TA_xC_yPP and $ZnTA_xC_yPP$ series) as potential DSSC dyes as well as potential polyporphyrin precursors.

Novel dyes are being synthesized in which the porphyrin and one or more phenyl substituents are held substantially coplanar by covalent linkages. Spectra show a distinct broadening and red shift, which would make these improved solar dyes.

Computational chemistry
We have initiated a collaboration with Dr. Niri Govind at PNNL. We are applying the NWCHEM computational program to study both the new porphyrin dyes under construction as well as the structure and properties of poly-TAPP. Also while on sabbatical this past spring, Professor Wamser spent one week at the University of Tromso Centre for Theoretical and Computational Chemistry. In collaboration with Professor Abhik Ghosh there, studies were initiated on the molecular structure and electronic properties of TAPP monomer in neutral, protonated, and oxidized (-2e) forms. Preliminary results indicate a distinct tendency towards

increased planarization of the phenyl groups upon oxidation. The studies will be extended to include dimers and larger oligomers, focusing on the effect of structural features on electronic delocalization and conductivity.

We have installed NWCHEM and Gaussian 09 in our lab and are using these programs to study the structure and electronic distributions in TAPP, poly-TAPP, and model compounds.

Photocatalysis
We have initiated studies that explore possible photocatalytic water-splitting activity of poly-TAPP and various metallated derivatives using the approach of the SHArK Project.[133]

Based on reports of photocatalytic reduction of CO_2 by pyridine derivatives,[134] we have begun investigating the use of pyridyl porphyrins as photocatalysts. We have synthesized and characterized the spectroscopy and electrochemistry of the complete set of porphyrins that have one to four pyridyl groups (the remaining substituents are either phenyl, aminophenyl, or carbomethoxyphenyl). These are being investigated as potential photocatalysts for solar fuel production. Since cobalt porphyrins have also been cited as potential photocatalysts for CO_2 reduction,[135] we have initiated studies with metalloporphyrins incorporated in poly-TAPP. In particular, cobalt porphyrins are effective at reduction of CO_2 to formate but relatively ineffective at further reductions. In contrast, pyridyl photoreduction carries out reduction of CO_2 all the way to methanol, with the first stage of reduction rate-limiting. Future work will include surface groups on poly-TAPP that include both pyridyl and cobalt groups to create a high surface area photocatalyst with multiple active sites.

Future directions
The research on inverse DSSCs will continue to emphasize the synthesis and characterization of the conductive porphyrin polymers and exploring new ways of generating conformal coatings of n-type semiconductors. New grant proposals are being prepared for submission to NSF (novel conductive organic frameworks) and to DOE (photocatalysis with conductive porphyrin polymers).

Nanostructured solids for high-efficiency energy production and storage
Dave Johnson (University of Oregon), Doug Keszler and Mas Subramanian (Oregon State University)
The results of these studies have led to a $20M, National Science Foundation, Phase II Center for Chemical Innovation, The Center for Sustainable Materials Chemistry.

Synthesis of Compounds with Designed Nanoarchitectures
Dave Johnson (University of Oregon)
Significant progress was made in four main areas during the current fiscal year.

1. The preparation of new ferecrystalline compounds containing new structure types.

2. Further elucidation of the mechanism of ferecrystal formation resulting in the ability to prepare structural isomers at each composition.

3. Additional structural characterization of ferecrystals and the discovery of systematic structural changes with thickness of constituents.

4.   The discovery of systematic changes in physical properties as a function of nanoarchitecture and unusual temperature dependence of electrical transport properties resulting from turbostratic disorder inherent to ferecrystals.

In the following pages we will elaborate on the progress that has been made and provide rational for the focus of our efforts.

New Constituent Structures Incorporated Into Ferecrystals
While organic chemists can predict an extraordinary number of potential new compounds based on local bonding rules that predict potential metastable synthetic targets, the corresponding ability to either predict or prepare new compounds did not exist for inorganic structures with extended crystal structures prior to our early work resulting from SNNI support. We have shown that it is possible to prepare many new metastable compounds based on intergrowths of rock salt compounds and transition metal diselenides – $[(MSe)_{1+y}]_m(TSe_2)_n$ – where M can be Pb, Bi, or Ce, T can be Mo, W, V, Nb, Ta, or Ti, and y represents the difference in the area per metal atom in the constituent structures. By determining the relative thicknesses needed to deposit a precursor that results in the formation of $[(MSe)_{1+d}]_1(TSe_2)_1$, Figure 102, we have shown that we can prepare any specific m and n member of this family of compounds by depositing the appropriate precursor.[136] A key objective this period was to determine if this synthesis approach worked with other constituent structures and orthorhombic SnSe, FeSe with the PbO structure type and the ternary spinel $CuCr_2Se_4$ were chosen as probe structures with increasing structural complexity.
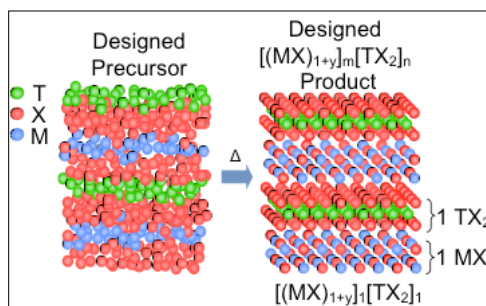
Figure102: A schematic of a precursor designed to form $[(MSe)_{1+y}]_1(TSe_2)_1$.

By changing the number of deposited MX layers in the precursor to n and TX layers to m, the compound $[(MSe)_{1+y}]_m(TSe_2)_n$ can be prepared.

We have explored and been able to prepare new ferecrystals, $[(SnSe)_{1+d}]_m(TSe_2)_n$ – where T can be Mo, V, Ta, or Ti.[137, 138] A representative STEM image of $[(SnSe)_{1.04}]_1(MoSe_2)_1$ is shown in Figure 103. The lateral size of the SnSe domains increased as m and n were increased. During the calibration of SnSe containing compounds, we were surprised that sharp 00l diffraction patterns could be prepared for a range of compositions as long as the total thickness of the repeating unit of the precursor remained constant. STEM investigation of these samples revealed that if there was extra SnSe and a deficiency of TSe_2, SnSe replaced a small region of the TSe_2 layers maintaining the long-range coherency of the structure as shown in the STEM image in Figure 104.[139] The layers of SnSe joined by this substitution maintained their crystalline

orientation. The frequency and size of this substitution was proportional to the deviation from ideal stoichiometry. This mechanism provides an additional avenue to control these structures.
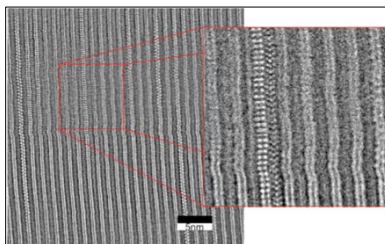
Figure 103: A STEM image of a $[(SnSe)_{1.04}]_1(MoSe_2)_1$ ferecrystal is presented, where the inset image contains an example of the rotational disorder between layers.
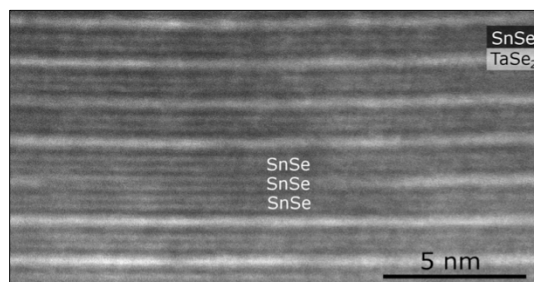
Figure 104: STEM image of a coherent replacement of a portion of a $TaSe_2$ layer by SnSe.

We have also been able to prepare new ferecrystals containing $CuCr_2Se_4$ and FeSe, but we are still optimizing their synthesis. As can be seen below in Figure 4, the samples are compositionally and structurally modulated. The interfaces in the $CuCr_2Se_4$ containing ferecrystal appear asymmetric. Surprisingly, these constituents, as well as SnSe discussed above, always form with a specific crystallographic orientation with the dichalcogenide.
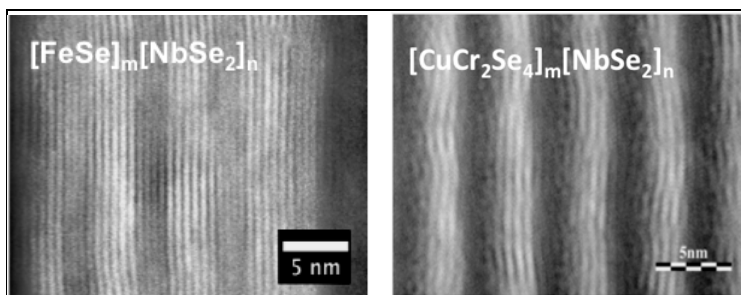
Figure 105: STEM images of representative ferecrystals containing FeSe and $CuCr_2Se_4$.

These exploratory studies suggest that it will be possible to prepare many new ferecrystalline compounds with precise control over the number of atomic planes and orientation of the constituents. Satisfying the local coordination of the atoms within the constituent structures appears to be sufficient to obtain a metastable state that can be accessed at low temperatures. Preliminary studies suggest that three components can be interwoven as well, greatly increasing the potential ability to tune properties with designed nanostructure. All of the selenide misfits that we have prepared are stable to 300C in an inert atmosphere.

Diversity Through Structural Isomers

During this period we also explored the synthesis of structural isomers - compounds containing the same number of constituent units but arranged in different sequences. Figure 106 contains STEM images of 3 of the 6 possible 4:4 isomers. We have calculated the expected number of isomers as m and n is varied, and Figure 107 contains the results of these calculations. Then number of isomers increases rapidly as m and n is increased, resulting in over 20,000 compounds where m and n are ten or less.
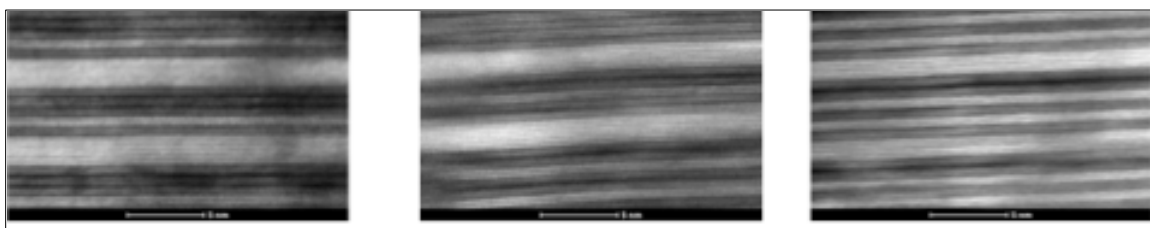
Figure 106: STEM images of three of the six possible isomers of $[(PbSe)]_4(NbSe_2)_4$. From right to left, $[(PbSe)]_3(NbSe_2)_3[(PbSe)]_1(NbSe_2)_1$, $[(PbSe)]_2(NbSe_2)_3[(PbSe)]_2(NbSe_2)_1$, and $[(PbSe)]_4(NbSe_2)_4[(PbSe)]_4(NbSe_2)_4[(PbSe)]_4(NbSe_2)_4$. Not shown are $[(PbSe)]_4(NbSe_2)_4$, $[(PbSe)_3(NbSe_2)_2[(PbSe)]_1(NbSe_2)_2$ and $[(PbSe)]_2(NbSe_2)_1[(PbSe)]_1(NbSe_2)_2[(PbSe)]_1(NbSe_2)_1$.
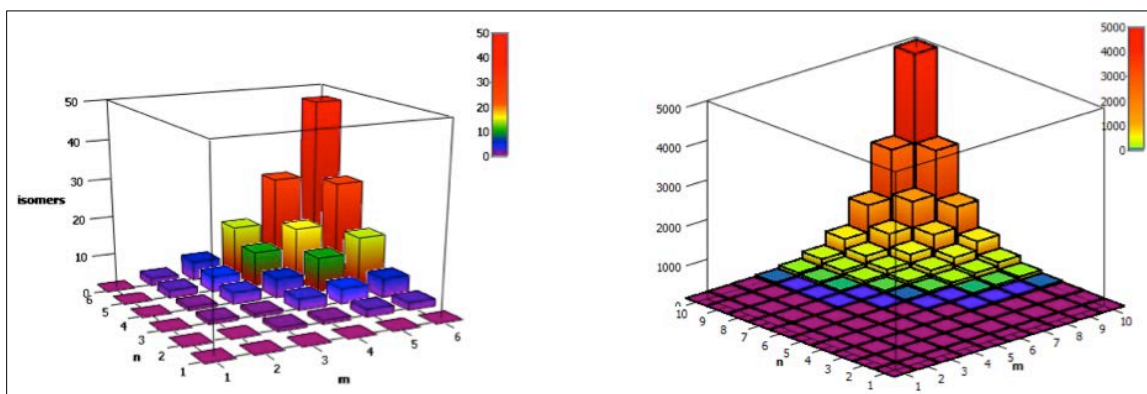
Figure 107: The calculated number of isomers for each value of m and n in a ferecrystal containing two distinct structural constituents. Two graphs are shown, the one of the left for n and m less than or equal to six and the one of the right for m and n ten or less, because the number of isomers increase very rapidly as n is increased.

Structural changes with constituent layer thickness

Conceptually, the free energy of a ferecrystal consists of a free energy per unit volume for each of the constituents and an interface free energy. For the m=n=1 compound, the interface energy is a maximum while as m and n increase, the importance of the free energy per unit volume increase. The crystal structure reflects the relative importance of these energy terms. The orthorhombic structure of SnSe provided a simple way to follow structural changes as the value of m was varied. Figure 108a contains a selection of hk0 diffraction patterns, which show the splitting of the 200 and 020 Bragg reflections as m is increased. Figure 108b shows the a and b lattice parameters a function of increasing the value of m. For m=1, the a and b lattice parameters are equal. As m is increased, a and b approach the values obtained for bulk SnSe. STEM investigations have shown that each of the SnSe layers is a single domain for the entire

thickness and that the in-plane domain size increases as m increases. For $[(SnSe)_{1.16}]_m(TaSe_2)_4$, the in plane domain size increases from 13 to 16 to 31 nm as m increases from 1 to 3 to 6 respectively.
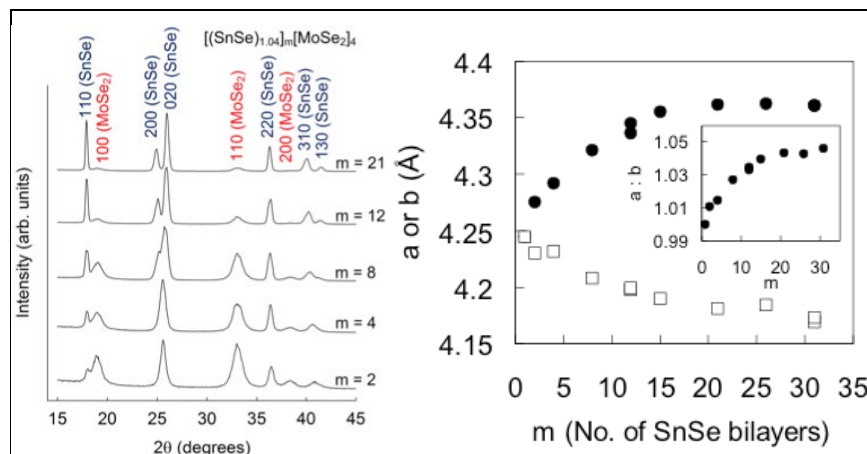
Figure 108: The figure on the left contains representative hk0 diffraction patterns for [(SnSe)1.04]m(MoSe2)4 compounds. The figure on the right plots the variation of the lattice parameters as a function of m.

We have also observed unusual diffraction phenomena due to coherent diffraction between ferecrystalline domains separated by extra layers. If the extra layer thickness is one half of the unit cell size, all odd order diffraction peaks are split because the ferecrystalline domains are exactly out of phase. The even order peaks are not split, as the extra distance traveled through the extra layer is an integer wavelength. Figure 109 contains diffraction patterns obtained that show the magnitude of this phenomena as a function of the domain size of the ferecrystal.
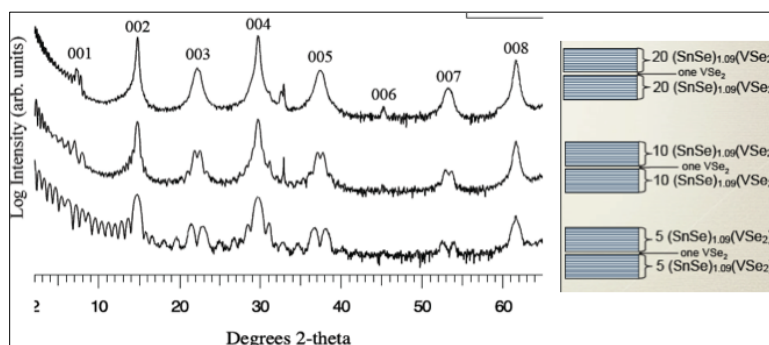
Figure 109: Diffraction patterns obtained from films with two ferecrystal domains separated by an extra layer of VSe$_2$. Since this distance is half of the c lattice parameter of the ferecrystal, all odd order peaks are split.

Thermal and Electronic Properties of Ferecrystals
The observed turbostratic disorder between constituent layers has a profound effect on the physical properties of ferecrystals. We have discovered that the thermal and electrical properties of ferecrystals are very different than what is observed in their crystalline misfit analogs. For example, the misfit compound $[(PbSe)_{1.16}]_1(TiSe_2)_2$ was found by Cava to be a superconducting metal with a room temperature resistivity of 2×10^4 Ωm and a Seebeck coefficient of -50 μVK^{-1}.

113
Approved for public release; distribution is unlimited.

The ferecrystalline $[(PbSe)_{1.16}]_1(TiSe_2)_2$ has an order of magnitude higher lower resistivity, 3.7×10^{-5} Ωm and a Seebeck coefficient of -92 μVK^{-1}. The resistivity of the ferecrystal is almost temperature independent. These properties, and the low lattice thermal conductivity discussed next, make $TiSe_2$ containing ferecrystals promising thermoelectric materials.

The lack of long-range structural order, discussed above, results in extraordinarily small thermal conductivities parallel to the layering direction, on the order of 0.1 $Wm^{-1}K^{-1}$. Perpendicular to the layering direction, thermal conductivities are small, 0.4 - 0.6 W $m^{-1}K^{-1}$. Parallel to the layering direction, ferecrystals are amorphous and hence do not have phonons. Perpendicular to the layering direction, the phonon mean free path is limited by the grain size.[140] The unusual lattice thermal conductivity of ferecrystals suggests exploring phenomena that depend on electron –phonon interactions, such as thermoelectric properties, charge density waves and superconducting behavior.

We are exploring thermoelectric properties within the $[(PbSe)_{1.16}]_m(TiSe_2)_n$ family and we have found that the electrical resistivity and the Seebeck coefficient do not change significantly as m is varied. As n is increased, the electrical resistivity *decreases* while the Seebeck coefficient increases (Figure 110). This behavior is very unusual, as the Seebeck coefficient typically increases as carrier concentration decreases, resulting in an *increase* in electrical resistivity. One explanation is that the mobility of the carriers is increasing enough to decrease the resistance even though the carrier concentration is decreasing. Efforts to measure the carrier concentration via Hall measurements are currently underway.

We have also found that the onset temperature of charge density waves in $[(SnSe)_{1.16}]_m(TaSe_2)n$ compounds systematically change with m and n. Efforts to measure Hall effect as a function of temperature are underway to confirm that the reversible increase in resistance as temperature in lowered results from a decrease in carrier concentration.
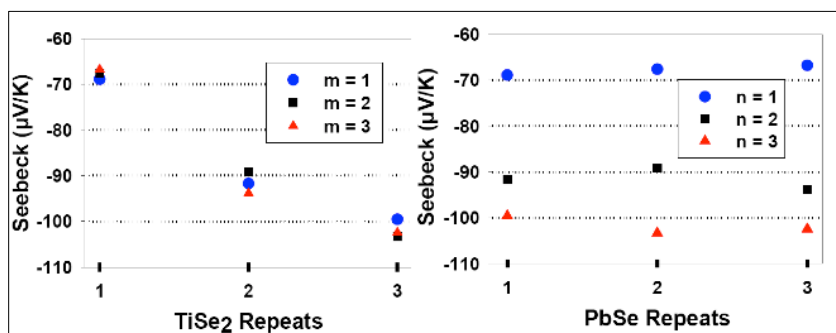
Figure 110: Dependence of the Seebeck coefficient on the values of m and n for $[(PbSe)_{1.16}]_m(TiSe_2)_n$ compounds.

Greener methods for depositing high-quality oxide thin films and development of high-performance transparent thin-film transistors (TFTs)
Douglas Keszler, Oregon State University
In the initial phase of the project, work was directed to understanding and developing new methods for depositing high-quality oxide thin films from water. Two binary materials, ZnO and TiO_2, were selected as case studies.

In recent years, the material has garnered additional attention as a channel material for high-performance transparent thin-film transistors (TFTs). Part of a large class of semiconducting oxides, the facile thin-film processing of ZnO has enabled physical vapor deposition fabrication of ZnO TFTs with a wide variety of gate dielectrics, even extending to flexible substrates. Since the beginning of this ZnO TFT renaissance (the first ZnO TFT was proposed in 1968), a coincident effort has been made to develop solution-based methods for large-area, low-cost, and low-temperature printing of ZnO films for macroelectronic applications. These efforts, however, have been hampered by a lack of solution precursors appropriate for a high-speed, low-temperature printing process. The defect and solution chemistries of ZnO, vital to electrical performance and film quality, have been too often ignored in favor of the ready application of conventional metal-organic preparative routes common to ceramic synthesis. In this work, we demonstrated a simple aqueous precursor specifically designed to take advantage of the unique solution chemistry of Zn.

Our approach for preparing an aqueous precursor ink for deposition of ZnO involved a simple two-step process:

(1) $Zn(NO_3)_2(aq) + 2\ NaOH(aq) \rightarrow Zn(OH)_2(s) + 2\ NaNO_3(aq)$
(2) $Zn(OH)_2(s)+ x\ NH_3(aq) \rightarrow Zn(OH)_2(NH_3)_x(aq) + ZnO(s) + xNH_3(g) + H_2O(g)$
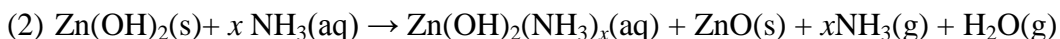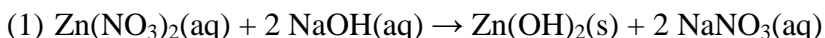
Following precipitation and filtration, $Zn(OH)_2$ was dissolved in $NH_3(aq)$. After spin coating this precursor on a suitable substrate, heat was applied to expel $NH_3(g)$ and $H_2O(g)$ to produce ZnO. We found that temperatures as low as 150 ^{o}C could be used to produce high-quality films suitable for demonstration as channel layers in TFTs.
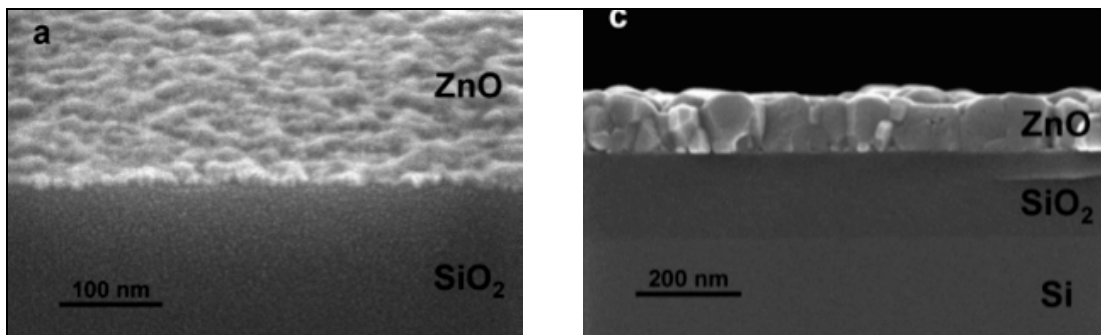
Figure 111. ZnO Thin Films Prepared from Aqueous Precursor

Electrical analyses of ZnO films were performed by using bottom-gate TFT structures. Device performance was assessed through an analysis of the turn-on voltage (V_{on}), drain current on-to-off ratio (I_{on}/I_{off}), and incremental channel mobility (μ_{inc}). Qualitatively ideal transistor performance was realized in I-V characteristics, even for devices that were processed at only 150 ^{o}C. For devices processed between 150 and 300 ^{o}C, V_{on} was found to vary from 1-3 V, μ_{inc} ranged between 2 and 3 cm^2/V·s, and I_{on}/I_{off} was consistently greater than 10^6. Despite numerous efforts around the world directed to improving on these results, they still set the performance benchmark for solution-processed ZnO TFTs.
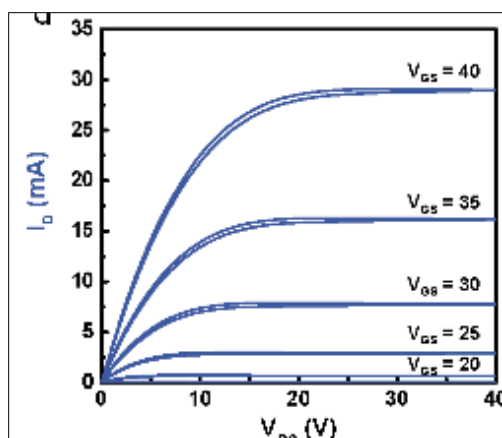
Figure 112. I-V Characteristics for ZnO Transistor Processed at 150 $^{\circ}$C

We extended our work on ZnO to TiO_2 by realizing that extended Ti–(OH)$_x$–Ti frameworks could be formed through the hydrolysis-condensation reactions of titanium peroxo species. These condensation reactions, coupled with ready decomposition of the small-volume peroxo group, provided a path to low-temperature crystallization and densification. A few approaches have been described for the deposition of TiO_2 films from peroxo sol–gels via dip and spin coating. In these previous studies, however, the aged precursors consisted of large colloids, or the precursor solutions contained undesirable counterions or organics, impeding low-temperature processing and the production of smooth, dense films. By carefully limiting colloid growth, we were able to produce dense, high-quality films with atomically smooth surfaces. We then employed the qualities of these films to examine the chemistry and physical properties of nanolaminates containing TiO_2. In one set of experiments, we designed and fabricated a series of laminated optical elements, using solution-processing for the first time to fabricate an inorganic dielectric mirror at low temperatures (T = 300 $^{\circ}$C).
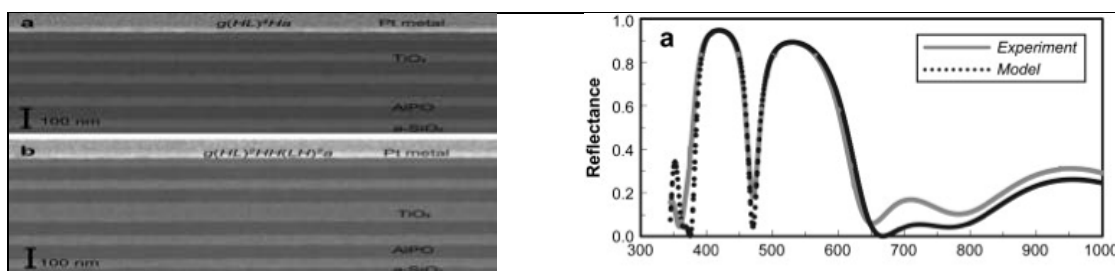
Figure 113. TiO_2/AlPO (aluminum phosphate) Dielectric Mirror

In the second phase of the project, we shifted our emphasis to the synthesis of sulfide thin films via aqueous solution chemistry. We initially focused on approaches for deposition of FeOOH and Fe_2O_3, as these oxides could readily be transformed to FeS_2, iron pyrite, via treatment under H_2S(g). Unique precursors could be formed by dissolving freshly precipitated FeOOH(s) in a minimum quantity of aqueous oxalic acid or by dissolving Fe metal in a methanolic solution of $Fe(NO_3)_3 \cdot xH_2O$. Subsequent sulfurization of these films resulted in stoichiometric FeS_2 with grain sizes approaching the thickness of the film. The films were characterized by resistivities = 0.2 Ω cm, Seebeck coefficients = +55 μV/K, and carrier concentrations near 10^{19} cm^{-3}, which were nearly identical to those measured for an FeS_2 film deposited by physical vapor deposition

(PVD). Like the PVD films, a very large absorption with $\alpha \sim 10^5$ cm^{-1} was observed at energies below the band gap. We used these results as part of a larger effort in the Center for Inverse Design, a DOE-sponsored Energy Frontier Research Center, to unravel the mysteries of why FeS_2 pyrite has never functioned as a useful photovoltaic material. We learned from the experimental results and supporting theoretical calculations that FeS_2 undergoes a very low temperature decomposition that results in the precipitation of phases related to FeS. These phases are metallic, giving rise the high carrier concentrations, p-type behavior, and optical sub-band-gap absorption observed in FeS_2 films.

On the basis of the FeS_2 results, we formulated design rules for identifying new Fe-based chalcogenide absorbers. These rules led us to the new family of Fe_2MX_4 (M = Si, Ge; X = X, Se), which exhibit the desirable optical and electrical properties of FeS_2 without the limitations. Work is ongoing to fully understand the properties of these new materials and examine them as photovoltaic absorbers in thin-film form.
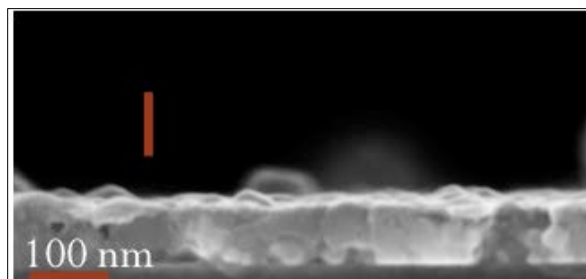
Figure 114. FeS$_2$ Thin Film from Solution Precursor

Our second target for sulfide synthesis was $CuInS_2$ and its substitutional derivatives. This sulfide is used as the absorber layer in thin-film solar cells. As a *p*-type semiconductor, it can also be used as the active channel layer in a thin-film transistor. Solution-based deposition of $CuInS_2$ has previously been accomplished by spray-pyrolysis and hydrazine-based methods. Spray methods have generally resulted in films having very poor morphological characteristics. In addition, they are known to contain high concentrations of impurities. Hydrazine-based methods provide a means to produce very high-quality films, but hydrazine is extremely toxic and difficult to handle.

Our approach has relied on the use of a aqueous-based precursor. We have established the crystal structures of the molecular species in these solutions. The copper and sulfur sources are represented by the thiourea dimer $[Cu_2(SC(NH_2)_2)_6]^{2+}$, while indium is derived from the formate hydroxide $In(HCOO)_2(OH)$. We have found that the indium formate can be synthesized simply by oxidizing In metal with hydrogen peroxide in the presence of formic acid. Ga can be substituted into the precursors and subsequently employed for the deposition of thin films. For these materials, the resulting band gaps can be tuned between 1.1 and 1.5 eV. Initial results from EPMA indicate that O impurity concentrations in the films are near 1 at%. Films with stoichiometries deficient in Cu have also been deposited.

Approved for public release; distribution is unlimited.
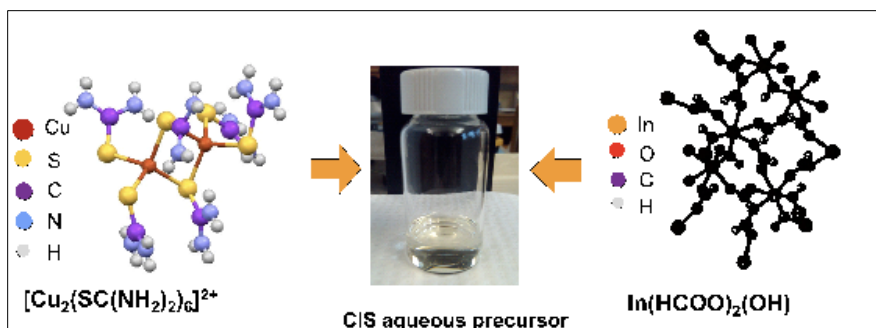
Figure 115. Aqueous Precursor for Production of Cu(In,Ga)S$_2$
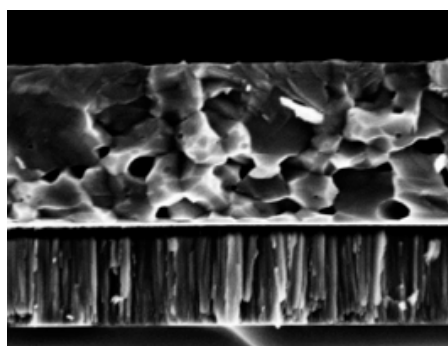
Figure 116. 1-µm Thick CuInS$_2$ Film from Aqueous Precursor

Low temperature and solution-based processing of nanostructured inorganic materials
Mas Subramanian, Oregon State University
Our task in the project focused on the chemistry of nanostructured matter, which includes low temperature and solution based processing of nanostructured inorganic materials.   Particularly, we focused on environmentally benign colossal dielectric materials and films fabricated through solution chemistry leading to high energy storage capacitors.

High Dielectric Constant Nanostructures
The overall goal of this work is focused towards the development of a solution method using benign precursors for thin film deposition by spin-coating of high K dielectrics based on CaCu$_3$Ti$_4$O$_{12}$. CaCu$_3$Ti$_4$O$_{12}$ crystallizes in perovskite related structure (Figure 117a) and show dielectric constant of ~10,000 which is nearly frequency and of temperature independence (Figure 117b).[141]
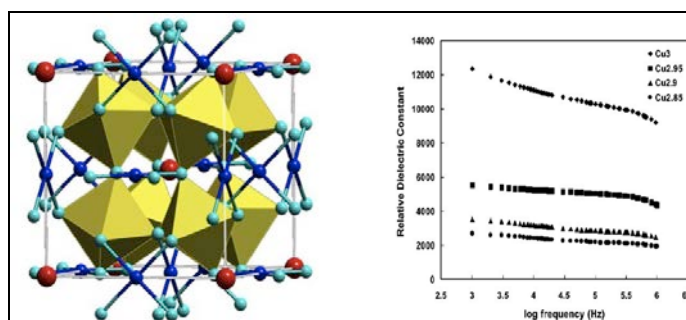
Figure 117. a (left) Crystal Structure of CaCu3Ti4O12, b (right) Dielectric properties of CaCu$_3$Ti$_4$O$_{12}$ related bulk compositions.

Our work was focused primarily on the formulation of a single precursor solution (tri-solution) in which Ti^{4+}, Ca^{2+} and Cu^{2+} cations are stable. The Tri-solution was achieved by dissolving each of the precursors separately and mixing at decreased temperatures to suppress a side reaction fueled by the exothermic reaction of the addition of TiO_2 in a basic mixture of NH_4OH and H_2O_2 to the acidic mixture of $Ca(OH)_2$ and CuO in dilute HNO_3. As mentioned in the last report, pH modifications resulted in a reddish brown Tri-solution that is very stable and precipitate free. Figure 118 shows the flow chart with details on synthesis and methods.

Spin coating of the Tri-solution was a roadblock in our research due to the low adhesion of the solution to the substrate (200nm of insulating thermal oxide on non-conductive silicon. The deposition on glass, thermal oxide wafers, and high density alumina and have obtained mild success. Initial films showed obvious pinholes and islands.
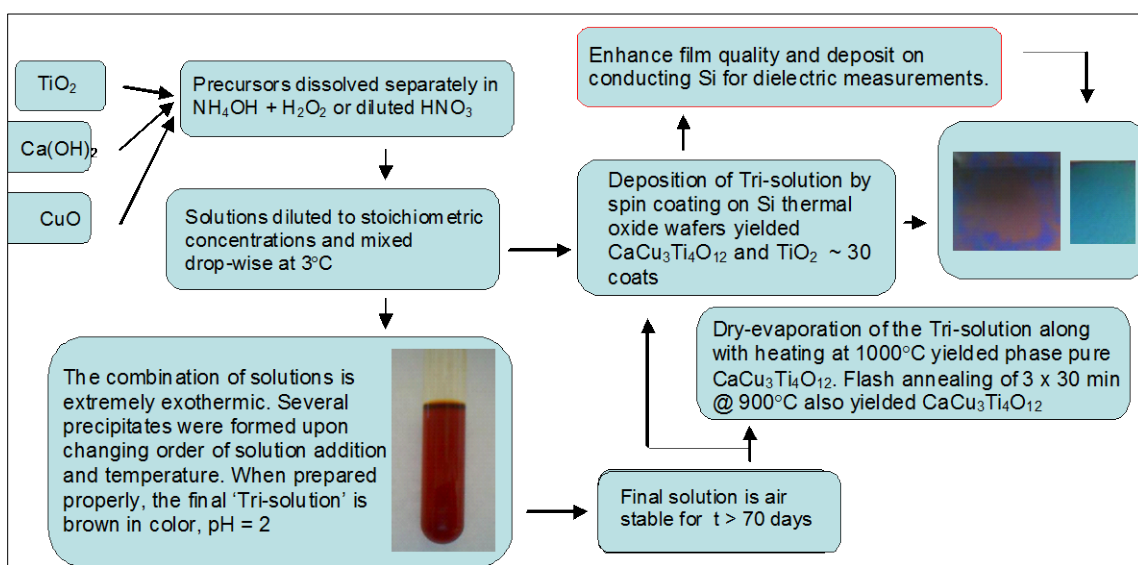
Figure 118. Flow chart showing the details on synthesis of CaCu3Ti412 thin film

By modifying the pH of the Tri-solution slightly and have obtained better quality films after approximately 20 coatings. X-ray analysis of these films has yielded what appear to be an amorphous $CaCu_3Ti_4O_{12}$ The dielectric measurements at 100 KHz frequency are of the order of 200-1300 depending on the thickness and porosity of films and annealing conditions. Future directions should include the modification of the Ti^{4+} precursor solution to allow for a higher concentration of the tri-solution.

Fluorine doped $CaCu_3Ti_4O_{12}$
Unfortunately, the $CaCu_3Ti_4O_{12}$ loss tangent of ~0.15 is high for present electronics application requirements. The best known high- κ dielectric material is barium titanate, $BaTiO_3$, which has a dielectric constant and loss favorable for application, $\kappa = $ ~1,500 and tan $\delta = $ ~0.01. There are several reports of cation substitution in $CaCu_3Ti_4O_{12}$. Substitution has included Co, Fe, Ni, Zr, Sc and Nb on the Ti site, and La or Na on the Ca site. Some reports indicate success in lowering the dielectric loss. For example, a loss of 0.015 was reported for $Ca_{0.8}La_{0.2}Cu_3Ti_4O_{12}$; however, the dielectric constant was also suppressed to 3,000.[142] Some compounds with the $CaCu_3Ti_4O_{12}$

structure show a low loss tangent but not a giant dielectric constant.[143] In this task, we discovered a novel route for decreasing the tan δ of $CaCu_3Ti_4O_{12}$ by anion substitution.

Analysis of powder XRD patterns indicated that the substitution of fluorine for oxygen was successful for doping levels of x = 0.05 – 1.3. Attempted doping levels above x = 1.3 resulted in secondary phases, mainly CaF_2 and TiO_2.
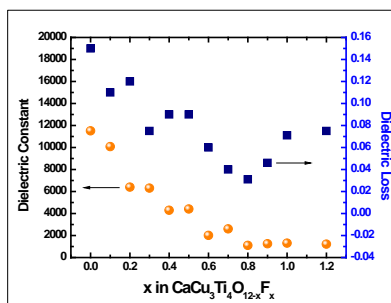
Figure 119: Result of fluorine substitution on the dielectric constant (κ) and dielectric loss (loss tangent, tan δ) for pure and F-doped $CaCu_3Ti_4O_{12-x}F_x$ where x = 0-1.2 at 25°C at a frequency of 100 kHz.

Figure 119 shows the dielectric constant and the dielectric loss as a function of fluorine content in $CaCu_3Ti_4O_{12}$ at 25°C and 100 kHz. As fluorine doping increases, the dielectric constant and loss tangent decrease. As the fluorine doping increases from x = 0.1 to 0.5, a large dielectric constant is still observed but is decreased from **κ** = 10,080 to 4,404, and tan δ is decreased from 0.11 to 0.075. Taking into consideration both the constant and loss, an optimal fluorine content is x = 0.3 where the dielectric constant is **κ** = 6,310 and tan δ is 0.075

The temperature dependence of the dielectric constant and loss tangent relationships for select fluorine doped levels in $CaCu_3Ti_4O_{12-x}F_x$ is presented in Figure 120 and 121 respectively. The dielectric constants remain essentially temperature independent for the various doping levels from 25° to 175°C. This is an improvement over pure $CaCu_3Ti_4O_{12}$ at 100 kHz where the dielectric constant increases steadily with tan δ throughout the full temperature range.

There is a consensus that the giant dielectric constant in $CaCu_3Ti_4O_{12}$ is due to an internal barrier layer mechanism (IBLM). This mechanism normally applies to materials with conducting grains and insulating grain boundaries. However, in $CaCu_3Ti_4O_{12}$ it has been shown that the giant dielectric constant is obtained within grains[143-145]. Thus, there must be insulating planar defects in these grains. Despite much effort, there is still no good definition of these defects. Dopants frequently concentrate at lattice defects. The F, thus, may be concentrating on the important planar defects in $CaCu_3Ti_4O_{12}$. This could increase the electrical resistivity of the internal barrier and decrease the dielectric loss. Movement of electrons from cation to cation through F is much more difficult than through O.
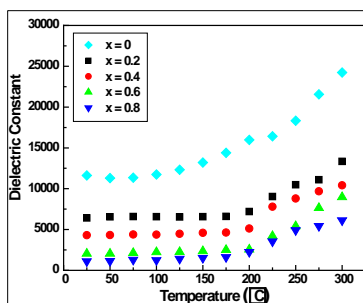
Figure 120. Temperature dependence of the dielectric constant (κ) for pure and F-doped CaCu$_3$Ti$_4$O$_{12-x}$F$_x$ at a frequency of 100 kHz.
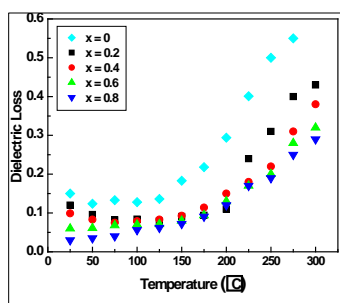
Figure 121. Temperature dependence of the dielectric loss (loss tangent, tan δ) for pure and F-doped CaCu$_3$Ti$_4$O$_{12-x}$F$_x$ at a frequency of 100 kHz.

It has been shown in this study that anion substitution by fluorine in CaCu$_3$Ti$_4$O$_{12-x}$F$_x$ was successful, and that single phase samples were prepared for fluorine doping levels of x < 1.3. A lower dielectric loss tangent, tan δ = 0.075, and a giant dielectric constant, κ = 6310, was obtained for a fluorine doped level of x = 0.3.

A solution-based synthesis is attempted to fabricate thin-films as shown in Figure 118. The films were not very dense and the observed dielectric constants for the films are of the order of 500-900 but the losses were low. Further work is necessary to fine tune the thin-film procedure to make more dense films.

Discovery of New Dielectric Materials based on InMCu$_{1-x}$Mg$_x$O$_4$ (M = Ga^{3+}, Al^{3+})
New oxides of the type InMCu$_{1-x}$Mg$_x$O$_4$ (M = Ga^{3+}, Al^{3+}) have been synthesized. The compounds crystallize in YbFe$_2$O$_4$-type structure (Figure 122) and characterized by X-ray diffraction and dielectric measurements. These oxides contain no heavy elements (e.g. Ba, Sr) and are non-toxic. Dielectric constant values as high as 10,000 were observed at low frequencies. The insulating behavior of Mg^{2+} in the InMCuO$_4$ (M = Ga^{3+}, Al^{3+}) lattice resulted in a decrease of the dielectric constant for each solid solution, but the dielectric loss was not affected until the concentration of Mg^{2+} was above x = 0.50. Although the dielectric constant decreased with the addition of Mg^{2+}, it was observed that for small amounts of Mg^{2+}, the dielectric loss was fairly constant over the observed temperature range. The comparison of Ga^{3+} and Al^{3+} illustrated that the aluminum compounds were much less polarizable than the gallium compounds, as a result of the smaller ionic radii of Al^{3+}.
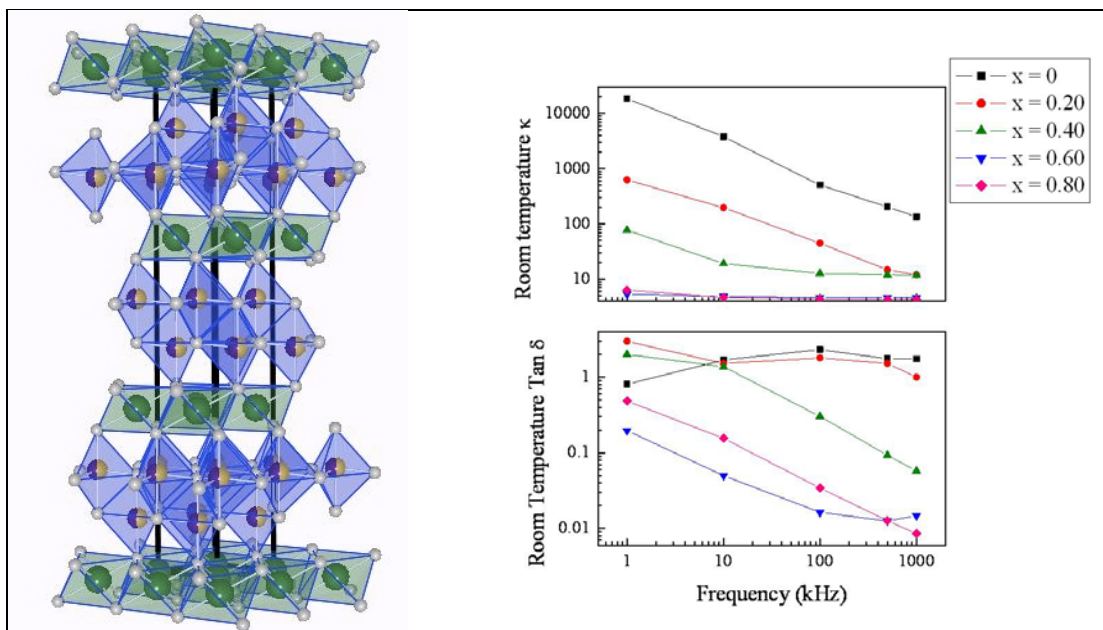
Figure 122. Crystal Structure (left) of InGaCuO₄ (Ga and Cu in Trigonal bipyramidal Coordination and In atoms in trigoanl prismatic sites) and dielectric properties (right) for InGaCu₁₋ₓMgₓO₄

References

1.   Mihai, C.; Xie, Y.; Tolic, A.; Chrisler, W.; Tan, R.; Zangar, R.; Orr, G. In *Mechanism of aerosolized zinc oxide nanoparticle toxicity in alveolar epithelial cells at the air-liquid interface*, 51st Society of Toxicology Annual Meeting, San Francisco, March 11-15, 2012; SOT: San Francisco, **2012**.

2.   Rundel, J. T.; Paul, B. K.; Remcho, V. T., Organic solvent nanofiltration for microfluidic purification of poly(amidoamine) dendrimers. *Journal of Chromatography A* **2007,** *1162* (2), 167-174.

3.   Xie, Y.; Williams, N. G.; Tolic, A.; Chrisler, W. B.; Teeguarden, J. G.; Maddux, B. L. S.; Pounds, J. G.; Laskin, A.; Orr, G., Aerosolized ZnO nanoparticles impose toxicity in alveolar type II epithelial cells at the air-liquid interface. *Toxicological Sciences* **2012,** *125* (2), 450-461.

4.   Oregon Nanoscience and Microtechnologies Institute. http://www.onami.us/.

5.   The Safer Nanomaterials and Nanomanufacturing Initiative. http://www.greennano.org/.

6.   NNI. Environmental, Health, and Safety Research Strategy 2011. http://www.nano.gov/node/681 (accessed 26 March 2012).

7.   Center for Sustainable Materials Chemistry. http://sustainablematerialschemistry.org.

8.   Committee to Develop a Research Strategy for Environmental, H.; Nanomaterials, S. A. o. E.; Council, N. R., *A Research Strategy for Environmental, Health, and Safety Aspects of Engineered Nanomaterials*. The National Academies Press: 2012.

9.   Nanosafety Consortium for Carbon. http://www.nanosafetyconsortium.com/.

10.   THE PATH AHEAD: Creating a Green Chemistry Roadmap for Washington State. http://www.pprc.org/gcr/ (accessed 30 March **2012**).

11.   Waddell, D. *Laboratory Waste Management Guide*; Local Hazardous Waste Management Program in King County: Seattle, WA, **2012**.

12.   The 21st Century Nanotechnology Research and Development Act. 111th CONGRESS, 1st Session ed.; **2009**; Vol. 15 U.S.C. 7501 et seq.

13.   Rung, R. D. NNI Reauthorization, "Nanomanufacturing" and U.S. Competitiveness **2008**. http://www.nanotech-now.com/columns/?article=201 .

14.   de la Iglesia, D.; Harper, S.; Hoover, M. D.; Klaessig, F.; Lippell, P.; Maddux, B.; Morse, J.; Nel, A.; Rajan, K.; Reznik-Zellen, R.; Tuominen, M. T. Nanoinformatics 2020 Roadmap 2011. http://eprints.internano.org/607/ http://nanotechinformatics.org/nanoinformatics/index.php/Nanoinformatics:Roadmap_2020

15.   Richman, E. K.; Hutchison, J. E., The Nanomaterial Characterization Bottleneck. *ACS Nano* **2009,** *3* (9), 2441-2446.

16.   Matus, K. J.; Hutchison, J. E.; Peoples, R.; Rung, S.; Tanguay, R. L. Green Nanotechnology Challenges And Opportunities 2011. http://www.acs.org/greenreport, http://www.greennano.org/roadmap (accessed 15 August 2011).

17.   McKenzie, L. C.; Haben, P. M.; Kevan, S. D.; Hutchison, J. E., Determining Nanoparticle Size in Real Time by Small-Angle X-ray Scattering in a Microscale Flow System. *The Journal of Physical Chemistry C* **2010,** *114* (50), 22055-22063.

18.   Oliveri, A. F.; Carnes, M. E.; Baseman, M. M.; Richman, E. K.; Hutchison, J. E.; Johnson, D. W.; "Single Nanoscale Cluster Species Revealed by 1H NMR Diffusion-Ordered Spectroscopy and Small-Angle X-ray Scattering". *Ang. Chem.* **2012,** 51:10992-10996.

Approved for public release; distribution is unlimited.

19.   EPA, Process design manual: Nitrogen control. Agency, U. S. E. P., Ed. Washington, DC, **1993**.

20.   Kowalchuk, G. A.; Stephen, J. R., Ammonia-oxidizing bacteria: a model for molecular microbial ecology. *Annu Rev Microbiol* **2001,** *55*, 485-529.

21.   Wijnhoven, S. W. P.; Peijnenburg, W. J. G. M.; Herberts, C. A.; Hagens, W. I.; Oomen, A. G.; Heugens, E. H. W.; Roszek, B.; Bisschops, J.; Gosens, I.; Van De Meent, D.; Dekkers, S.; De Jong, W. H.; van Zijverden, M.; Sips, A. J. A. M.; Geertsma, R. E., Nano-silver, A review of available data and knowledge gaps in human and environmental risk assessment. *Nanotoxicology* **2009,** *3* (2), 109-138.

22.   Harper, S.; Usenko, C.; Hutchison, J. E.; Maddux, B. L. S.; Tanguay, R. L., In vivo biodistribution and toxicity depends on nanomaterial composition, size, surface functionalisation and route of exposure. *Journal of Experimental Nanoscience* **2008,** *3* (3), 195 - 206.

23.   Raffi, M.; Hussain, F.; Bhatti, T. M.; Akhter, J. I.; Hameed, A.; Hasan, M. M., Antibacterial characterization of silver nanoparticles against E. coli ATCC-15224. *J Mater Sci Technol* **2008,** *24* (2), 192-196.

24.   Martínez-Castañón, G.; Niño-Martínez, N.; Martínez-Gutierrez, F.; Martínez-Mendoza, J.; Ruiz, F., Synthesis and antibacterial activity of silver nanoparticles with different sizes. *Journal of Nanoparticle Research* **2008,** *10* (8), 1343-1348.

25.   Jin, X.; Li, M.; Wang, J.; Marambio-Jones, C.; Peng, F.; Huang, X.; Damoiseaux, R.; Hoek, E. M., High-throughput screening of silver nanoparticle stability and bacterial inactivation in aquatic media: influence of specific ions. *Environmental Science & Technology* **2010,** *44* (19), 7321-8.

26.   Radniecki, T. S.; Semprini, L.; Dolan, M. E., Expression of merA, amoA and hao in continuously cultured Nitrosomonas europaea cells exposed to zinc chloride additions. *Biotechnology and Bioengineering* **2009,** *102* (2), 546-553.

27.   Radniecki, T. S.; Stankus, D. P.; Neigh, A.; Nason, J. A.; Semprini, L., Influence of liberated silver from silver nanoparticles on nitrification inhibition of Nitrosomonas europaea. *Chemosphere* **2011,** *85*, 43-49.

28.   Truong, L.; Moody, I.; Stankus, D.; Nason, J.; Lonergan, M.; Tanguay, R., Differential stability of lead sulfide nanoparticles influences biological responses in embryonic zebrafish. *Archives of Toxicology* **2011,** *85* (7), 787-798.

29.   Troung, L.; Harper, S. L.; Tanguay, R. L., Evaluation of embryotoxicity using the zebrafish model. In *Methods in Molecular Biology*, Gautier, J.-C., Ed. Springer: Totowa, NJ, 2011; Vol. 691, pp 271-279.

30.   Mandrell, D.; Truong, L.; Jephson, C.; Sarker, M. R.; Moore, A.; Lang, C.; Simonich, M. T.; Tanguay, R. L., Automated zebrafish chorion removal and single embryo placement: optimizing throughput of zebrafish developmental toxicity screens. *J Lab Autom* **2012,** *17* (1), 66-74.

31.   Truong, L.; Saili, K. S.; Miller, J. M.; Hutchison, J. E.; Tanguay, R. L., Persistent adult zebrafish behavioral deficits results from acute embryonic exposure to gold nanoparticles. *Comparative Biochemistry and Physiology Part C: Toxicology & Pharmacology* **2012,** *155* (2), 269-274.

32.   Harper, S. L.; Carriere, J. L.; Miller, J. M.; Hutchison, J. E.; Maddux, B. L. S.; Tanguay, R. L., Systematic Evaluation of Nanomaterial Toxicity: Utility of Standardized Materials and Rapid Assays. *ACS Nano* **2011,** *5* (6), 4688–4697.

33.   Truong, L.; Tilton, S. C.; Zaikova, T.; Richman, E.; Waters, K. M.; Hutchison, J. E.; Tanguay, R. L., Surface functionalities of gold nanoparticles impact embryonic gene expression responses. *Nanotoxicology* **2012**.

34.   Stankus, D. P.; Lohse, S. E.; Hutchison, J. E.; Nason, J. A., Interactions between natural organic matter and gold nanoparticles stabilized with different organic capping agents. . *Environmental Science and Technology* **2011,** *45* (8), 3238-3244.

35.   Truong, L.; Zaikova, T.; Hutchison, J. E.; Tanguay, R. L., Media ionic strength impacts embryonic responses to engineered nanoparticle exposure. *Nanotoxicology* **2011,** (In press).

36.   Glover, R. D.; Miller, J. M.; Hutchison, J. E., Generation of Metal Nanoparticles from Silver and Copper Objects: Nanoparticle Dynamics on Surfaces and Potential Sources of Nanoparticles in the Environment. *ACS Nano* **2011**.

37.   Moody, I. S.; Stonas, A. R.; Lonergan, M. C., PbS Nanocrystals Functionalized with a Short-Chain, Ionic, Dithiol Ligand. *J Phys Chem C* **2008,** *112* (49), 19383-19389.

38.   Mackiewicz, M.; Ayres, B.; Reed, S., Reversible, reagentless solubility changes in phosphatidylcholine-stabilized gold nanoparticles. *Nanotechnology* **2008,** *19* (11), 115607.

39.   Sitaula, S.; Mackiewicz, M. R.; Reed, S. M., Gold nanoparticles become stable to cyanide etch when coated with hybrid lipid bilayers. *Chem Commun (Camb)* **2008,** (26), 3013-5.

40.   Mackiewicz, M. R.; Hodges, H. L.; Reed, S. M., C-Reactive Protein Induced Rearrangement of Phosphatidylcholine on Nanoparticle Mimics of Lipoprotein Particles. *The Journal of Physical Chemistry B* **2010,** *114* (16), 5556-5562.

41.   Norris, C. B.; Joseph, P. R.; Mackiewicz, M. R.; Reed, S. M., Minimizing Formaldehyde Use in the Synthesis of Gold,Silver Core, Shell Nanoparticles. *Chemistry of Materials* **2010,** *22* (12), 3637-3645.

42.   Ostblom, M.; Liedberg, B.; Demers, L. M.; Mirkin, C. A., On the structure and desorption dynamics of DNA bases adsorbed on gold: A temperature-programmed study. *Journal of Physical Chemistry B* **2005,** *109* (31), 15150-15160.

43.   Nutiu, R.; Li, Y. F., Structure-switching signaling aptamers. *Journal of the American Chemical Society* **2003,** *125* (16), 4771-4778.

44.   Liu, J.; Lu, Y., Colorimetric Biosensors Based on DNAzyme-Assembled Gold Nanoparticles. *Journal of Fluorescence* **2004,** *14* (4), 343-354.

45.   Li; Rothberg, L. J., Label-Free Colorimetric Detection of Specific Sequences in Genomic DNA Amplified by the Polymerase Chain Reaction. *Journal of the American Chemical Society* **2004,** *126* (35), 10958-10961.

46.   Nam, J. M.; Thaxton, C. S.; Mirkin, C. A., Nanoparticle-based bio-bar codes for the ultrasensitive detection of proteins. *Science* **2003,** *301* (5641), 1884-6.

47.   Li, W.; Nie, Z.; Xu, X.; Shen, Q.; Deng, C.; Chen, J.; Yao, S., A sensitive, label free electrochemical aptasensor for ATP detection. *Talanta* **2009,** *78* (3), 954-8.

48.   Liu, J.; Lu, Y., Preparation of aptamer-linked gold nanoparticle purple aggregates for colorimetric sensing of analytes. *Nature Protocols* **2006,** *1*, 246-252.

49.   Liu, J.; Mazumdar, D.; Lu, Y., A simple and sensitive "dipstick" test in serum based on lateral flow separation of aptamer-linked nanostructures. *Angew Chem Int Ed Engl* **2006,** *45* (47), 7955-9.

50.   Huizenga, D. E.; Szostak, J. W., A DNA aptamer that binds adenosine and ATP. *Biochemistry* **1995,** *34* (2), 656-65.

51.   Deussen, A.; Stappert, M.; Schafer, S.; Kelm, M., Quantification of extracellular and intracellular adenosine production: understanding the transmembranous concentration gradient. *Circulation* **1999,** *99* (15), 2041-7.

52.   Jin, R.; Wu, G.; Li, Z.; Mirkin, C. A.; Schatz, G. C., What controls the melting properties of DNA-linked gold nanoparticle assemblies? *J Am Chem Soc* **2003,** *125* (6), 1643-54.

53.   Gann, J. P.; Yan, M., A versatile method for grafting polymers on nanoparticles. *Langmuir* **2008,** *24* (10), 5319-23.

54.   Fleer, G. J.; Stuart, M. A. C.; Scheutjens, J. M. H. M., *Polymers at Interfaces*. Springer: **1993**.

55.   Schmid, D.; Handge, U. A.; Gann, J. P.; Yan, M.; Caseri, W., Melt Elongation of Polymer Nanocomposites: A Method for the Controlled Production of Dichroic Films. *Macromolecular Materials and Engineering* **2008,** *293* (6), 471-478.

56.   Lohse, S. E.; Dahl, J. A.; Hutchison, J. E., Direct Synthesis of Large Water-Soluble Functionalized Gold Nanoparticles Using Bunte Salts as Ligand Precursors. *Langmuir* **2010,** *26* (10), 7504-7511.

57.   Paul, B. K.; Kwon, P.; Subramanian, R., Understanding Limits on Fin Aspect Ratios in Counterflow Microchannel Arrays Produced by Diffusion Bonding. *Journal of Manufacturing Science and Engineering* **2006,** *128* (4), 977-983.

58.   Wattanutchariya, W.; Paul, B. K., Bonding fixture tolerances for high-volume metal microlamination based on fin buckling and laminae misalignment behavior. *Precision Engineering* **2004,** *28* (2), 117-128.

59.   Woehrle, G. H.; Warner, M. G.; Hutchison, J. E., Ligand exchange reactions yield subnanometer, thiol-stabilized gold particles with defined optical transitions. *Journal of Physical Chemistry B* **2002,** *106* (39), 9979-9981.

60.   McKenzie, L. Mechanistic insights on nanoparticle formation: Investigation of reaction pathways and development of controlled syntheses for triphenylphosphine-stabilized undecagold. University of Oregon, Eugene, 2009.

61.   Milliron, D. J.; Hughes, S. M.; Cui, Y.; Manna, L.; Li, J. B.; Wang, L. W.; Alivisatos, A. P., Colloidal nanocrystal heterostructures with linear and branched topology. *Nature* **2004,** *430* (6996), 190-195.

62.   Kan, S.; Mokari, T.; Rothenberg, E.; Banin, U., Synthesis and size-dependent properties of zinc-blende semiconductor quantum rods. *Nature Materials* **2003,** *2* (3), 155-158.

63.   Peng, X. G.; Manna, L.; Yang, W. D.; Wickham, J.; Scher, E.; Kadavanich, A.; Alivisatos, A. P., Shape control of CdSe nanocrystals. *Nature* **2000,** *404* (6773), 59-61.

64.   Ahrenkiel, S. P.; Micic, O. I.; Miedaner, A.; Curtis, C. J.; Nedeljkovic, J. M.; Nozik, A. J., Synthesis and characterization of colloidal InP quantum rods. *Nano Letters* **2003,** *3* (6), 833-837.

65.   Ning, J.; Men, K.; Xiao, G.; Zou, B.; Wang, L.; Dai, Q.; Liu, B.; Zou, G., Synthesis of narrow band gap SnTe nanocrystals: nanoparticles and single crystal nanowires via oriented attachment. *CrystEngComm* **2010,** *12* (12), 4275-4279.

66.   Edel, J. B.; Fortt, R.; deMello, J. C.; deMello, A. J., Microfluidic routes to the controlled production of nanoparticles. *Chem Commun* **2002,** (10), 1136-1137.

67.   Schäfer, A. I.; Fane, A. G.; Waite, T. D., *Nanofiltration : Principles and Applications* Oxford, Inglaterra : Elsevier: **2005**.

68.   Sereewatthanawut, I.; Lim, F. W.; Bhole, Y. S.; Ormerod, D.; Horvath, A.; Boam, A. T.; Livingston, A. G., Demonstration of Molecular Purification in Polar Aprotic Solvents by Organic Solvent Nanofiltration. *Org Process Res Dev* **2010,** *14* (3), 600-611.

69.   So, S. U.; Peeva, L. G.; Tate, E. W.; Leatherbarrow, R. J.; Livingston, A. G., Organic Solvent Nanofiltration: A New Paradigm in Peptide Synthesis. *Org Process Res Dev* **2010,** *14* (6), 1313-1325.

70.   Van Doorslaer, C.; Glas, D.; Peeters, A.; Odena, A. C.; Vankelecom, I.; Binnemans, K.; Mertens, P.; De Vos, D., Product recovery from ionic liquids by solvent-resistant nanofiltration: application to ozonation of acetals and methyl oleate. *Green Chem* **2010,** *12* (10), 1726-1733.

71.   Vandezande, P.; Gevers, L. E. M.; Vankelecom, I. F. J., Solvent resistant nanofiltration: separating on a molecular level. *Chem Soc Rev* **2008,** *37* (2), 365-405.

72.   Sheth, J. P.; Qin, Y. J.; Sirkar, K. K.; Baltzis, B. C., Nanofiltration-based diafiltration process for solvent exchange in pharmaceutical manufacturing. *J Membrane Sci* **2003,** *211* (2), 251-261.

73.   Woehrle, G. H.; Hutchison, J. E., Thiol-functionalized undecagold clusters by ligand exchange: Synthesis, mechanism, and properties. *Inorganic Chemistry* **2005,** *44* (18), 6149-6158.

74.   Woehrle, G. H.; Warner, M. G.; Hutchison, J. E., Molecular-level control of feature separation in one-dimensional nanostructure assemblies formed by biomolecular nanolithography. *Langmuir* **2004,** *20* (14), 5982-5988.

75.   Novak, J. P.; Nickerson, C.; Franzen, S.; Feldheim, D. L., Purification of molecularly bridged metal nanoparticle arrays by centrifugation and size exclusion chromatography. *Analytical Chemistry* **2001,** *73* (23), 5758-5761.

76.   Contado, C.; Argazzi, R., Size sorting of citrate reduced gold nanoparticles by sedimentation field-flow fractionation. *Journal of Chromatography A* **2009,** *1216* (52), 9088-9098.

77.   Akthakul, A.; Hochbaum, A. I.; Stellacci, F.; Mayes, A. M., Size fractionation of metal nanoparticles by membrane filtration. *Advanced Materials* **2005,** *17* (5), 532-+.

78.   Sweeney, S. F.; Woehrle, G. H.; Hutchison, J. E., Rapid Purification and Size Separation of Gold Nanoparticles via Diafiltration. *Journal of the American Chemical Society* **2006,** *128* (10), 3190-3197.

79.   Liu, Y. M.; Tsunoyama, H.; Akita, T.; Tsukuda, T., Preparation of similar to 1 nm Gold Clusters Confined within Mesoporous Silica and Microwave-Assisted Catalytic Application for Alcohol Oxidation. *J Phys Chem C* **2009,** *113* (31), 13457-13461.

80.   Ariyasu, S.; Onoda, A.; Sakamoto, R.; Yamamura, T., Conjugation of Au11 cluster with Cys-rich peptides containing the alpha-domain of metallothionein. *Dalton T* **2009,** (19), 3742-3747.

81.   Shichibu, Y.; Negishi, Y.; Tsukuda, T.; Teranishi, T., Large-scale synthesis of thiolated Au-25 clusters via ligand exchange reactions of phosphine-stabilized Au-11 clusters. *Journal of the American Chemical Society* **2005,** *127* (39), 13464-13465.

82.   Buekenhoudt, A., Stability of Porous Ceramic Membranes. In *Membrane Science and Technology*, Mallada, R.; Menéndez, M., Eds. Elsevier: **2008**; Vol. Volume 13, pp 1-31.

83.   Li, K., *Ceramic membranes for separation and reaction*. John Wiley and Sons: 2007.

84.   Woehrle, G. H.; Brown, L. O.; Hutchison, J. E., Thiol-Functionalized, 1.5-nm Gold Nanoparticles through Ligand Exchange Reactions: Scope and Mechanism of Ligand Exchange. *Journal of the American Chemical Society* **2005,** *127* (7), 2172-2183.

85.   Wilcoxon, J. P.; Martin, J. E.; Provencio, P., Size distributions of gold nanoclusters studied by liquid chromatography. *Langmuir* **2000,** *16* (25), 9912-9920.

86.   Koschuh, W.; Thang, V. H.; Krasteva, S.; Novalin, S.; Kulbe, K. D., Flux and retention behaviour of nanofiltration and fine ultrafiltration membranes in filtrating juice from a green biorefinery: A membrane screening. *J Membrane Sci* **2005,** *261* (1-2), 121-128.

87.   Kim, T.; Lingam, G. K.; Paul, B. K.; Remcho, V. T. In *On-line, continuous nanofiltration of gold eleven nanoparticles (au11) produced synthetically in a microreactor*, Micro Total Analysis Systems Conference, Jeju, South Korea, The Chemical and Biological Microsystems Society: Jeju, South Korea, **2009**; pp 1210-1212.

88.   Kang, J. S.; Kim, H. S.; Ryu, J.; Hahn, H. T.; Jang, S.; Joung, J. W., Inkjet printed electronics using copper nanoparticle ink. *J Mater Sci-Mater El* **2010,** *21* (11), 1213-1220.

89.   Cha, S. I.; Mo, C. B.; Kim, K. T.; Jeong, Y. J.; Hong, S. H., Mechanism for controlling the shape of Cu nanocrystals prepared by the polyol process. *Focus Issue on Biomimetic and Bio-Enabled Materials Science and Engineering* **2006,** *21* (9), 2371-2378.

90.   Jeong, S.; Woo, K.; Kim, D.; Lim, S.; Kim, J. S.; Shin, H.; Xia, Y. N.; Moon, J., Controlling the thickness of the surface oxide layer on Cu nanoparticles for the fabrication of conductive structures by ink-jet printing. *Advanced Functional Materials* **2008,** *18* (5), 679-686.

91.   Lee, Y.; Choi, J. R.; Lee, K. J.; Stott, N. E.; Kim, D., Large-scale synthesis of copper nanoparticles by chemically controlled reduction for applications of inkjet-printed electronics. *Nanotechnology* **2008,** *19* (41).

92.   Kumar, D. V. R.; Kasture, M.; Prabhune, A. A.; Ramana, C. V.; Prasad, B. L. V.; Kulkarni, A. A., Continuous flow synthesis of functionalized silver nanoparticles using bifunctional biosurfactants. *Green Chem* **2010,** *12* (4), 609-615.

93.   Kasture, M. B.; Patel, P.; Prabhune, A. A.; Ramana, C. V.; Kulkarni, A. A.; Prasad, B. L. V., Synthesis of silver nanoparticles by sophorolipids: Effect of temperature and sophorolipid structure on the size of particles. *J Chem Sci* **2008,** *120* (6), 515-520.

94.   Luo, G. S.; Du, L.; Wang, Y. J.; Lu, Y. C.; Xu, J. H., Controllable preparation of particles with microfluidics. *Particuology* **2011,** *9* (6), 545-558.

95.   Nagasawa, H.; Mae, K., Development of a New Microreactor Based on Annular Microsegments for Fine Particle Production. *Ind Eng Chem Res* **2006,** *45* (7), 2179-2186.

96.   Knitter, R.; Liauw, M. A., Ceramic microreactors for heterogeneously catalysed gas-phase reactions. *Lab on a Chip* **2004,** *4* (4), 378-383.

97.   Dahl, J. A.; Maddux, B. L.; Hutchison, J. E., Toward greener nanosynthesis. *Chemical reviews* **2007,** *107* (6), 2228-69.

98.   Fernandez, C. A.; Bekhazi, J. G.; Hoppes, E. M.; Fryxell, G. E.; Wang, C.; Bays, J. T.; Warner, M. G.; Wiacek, R. J.; Addleman, R. S., Effect of the Ligand Shell Composition on the Dispersibility and Transport of Gold Nanocrystals in Near-Critical Solvents. *Langmuir* **2009,** *25* (9), 4900-4906.

99.   Fernandez, C. A.; Bekhazi, J. G.; Hoppes, E. M.; Wiacek, R. J.; Fryxell, G. E.; Bays, J. T.; Warner, M. G.; Wang, C.; Hutchison, J. E.; Addleman, R. S., Advancements Toward the Greener Processing of Engineered Nanomaterials - Effect of Core Size on the Dispersibility and Transport of Gold Nanocrystals in Near-Critical Solvents. *Small* **2009,** *5* (8), 961-969.

100.   Fernandez, C. A.; Hoppes, E. M.; Bekhazi, J. G.; Wang, C.; Wiacek, R. J.; Warner, M. G.; Fryxell, G. E.; Bays, J. T.; Addleman, R. S., Tuning and quantifying the dispersibility of gold nanocrystals in liquid and supercritical solvents. *J Phys Chem C* **2008,** *112* (36), 13947-13957.

101.   Marre, S.; Jensen, K. F., Synthesis of micro and nanostructures in microfluidic systems. *Chem Soc Rev* **2010,** *39* (3), 1183-1202.

102.   Pekarskaya, E. *Nanomanufacturing for Energy Efficiency Market Assessment*; Lux Research: 2008.

103.   Romang, A. H.; Watkins, J. J., Supercritical Fluids for the Fabrication of Semiconductor Devices: Emerging or Missed Opportunities? *Chemical reviews* **2010,** *110* (1), 459-478.

104.   Busche, B. J.; Clubb, D. C.; Roberts, J. G.; Warner, M. G.; Addleman, R. S., Environmentally Benign Processing of PbS Quantum Dots with Near Critical and Supercritical Ethane *Green Chem* **in preparation**.

105.   Busche, B. J.; Clubb, D. C.; Roberts, J. G.; Warner, M. G.; Addleman, R. S., Quantum Dot Solubility and Dispersibility in Near Critical and Supercritical Fluids. *J Phys Chem C* **in preparation**.

106.   Clubb, D. C.; Busche, B. J.; Roberts, J. G.; Warner, M. G.; R.S., A., Functionalization and Manipulation of Superparamagnetic FeO NPs in Supercritical and Near Critical Fluids. *Green Chem* **in preparation**.

107.   Addleman, R. S.; Warner, C. L.; Chouyyok, W.; O'Hara, M. D.; Warner, M. G., Mn-doping of magnetic iron oxide nanoparticles: Modified magnetic iron oxide nanoparticles for the rapid collection and separation of radionuclides. . *Analyst* **in preparation**.

108.   Chouyyok, W.; Warner, C. L.; Pittman, J. W.; Mackie, K. E.; Addleman, R. S., Aqueous Collection and Recovery of Rare Earths with Nanostructured Sorbents. *Applied Material and Interfaces* **in preparation**.

109.   Chouyyok, W.; Warner, C. L.; Pittman, J. W.; Mackie, K. E.; Addleman, R. S., Recovery and Recycling of toxic and vital metals from electronic waste with nanostructured sorbents. *Environmental Science & Technology* **in preparation**.

110.   Warner, C. L.; Warner, M. G.; Mackie, K. M.; Neiner, D.; Clubb, D. C.; Addleman, R. S., Green Chemical Production of Low Toxicity Quantum Dots. *Green Chem* **in preparation**.

111.   Rutledge, R. D.; Warner, C. L.; Pittman, J. W.; Addleman, R. S.; Engelhard, M.; Chouyyok, W.; Warner, M. G., Thiol-Ene Induced Diphosphonic Acid Functionalization of Superparamagnetic Iron Oxide Nanoparticles. *Langmuir* **2010,** *26* (14), 12285-12292.

112.   Warner, C. L.; Addleman, R. S.; Cinson, A. D.; Droubay, T. C.; Engelhard, M. H.; Nash, M. A.; Yantasee, W.; Warner, M. G., High-Performance, Superparamagnetic, Nanoparticle-

Based Heavy Metal Sorbents for Removal of Contaminants from Natural Waters. *Chemsuschem* **2010,** *3* (6), 749-757.

113.   Carter, T. G.; Yantasee, W.; Sangvanich, T.; Fryxell, G. E.; Johnson, D. W.; Addleman, R. S., New functional materials for heavy metal sorption: "Supramolecular" attachment of thiols to mesoporous silica substrates. *Chem Commun* **2008,** (43), 5583-5585.

114.   Fernandez, C. A.; Wiacek, R. J.; Nachimuthu, P.; Fryxell, G. E.; Pierson, A. M.; Warner, C. L.; Warner, M. G.; Addleman, R. S., A Simple Method for the Prevention of Non-Specific Adsorption by Nanocrystals onto Surfaces. *Journal of Nanoscience and Nanotechnology* **2008,** *8*, 5781-5786.

115.   Sun, L.; Yang, X. N.; Wu, B.; Tang, L. J., Molecular Simulation of Interaction between Passivated Gold Nanoparticles in Supercritical CO(2). *J Chem Phys* **2011,** *135* (20).

116.   Chrastil, J., Solubility of Solids and Liquids in Supercritical Gases. *J Phys Chem-Us* **1982,** *86* (15), 3016-3021.

117.   Hackens, B.; Delfosse, F.; Faniel, S.; Gustin, C.; Boutry, H.; Wallart, X.; Bollaert, S.; Cappy, A.; Bayot, V., Long dephasing time and high-temperature conductance fluctuations in an open InGaAs quantum dot. *Physical Review B* **2002,** *66* (24), 241305.

118.   Martin, T. P.; Fairbanks, M. S.; Scannell, B. C.; Marlow, C. A.; Linke, H.; Taylor, R. P., Investigation of electron wave function hybridization in Ga(0.25)In(0.75)As/InP arrays. *Applied Physics Letters* **2009,** *95* (18).

119.   Elteto, K.; Antonyan, E. G.; Nguyen, T. T.; Jaeger, H. M., Model for the onset of transport in systems with distributed thresholds for conduction. *Physical Review B* **2005,** *71* (6).

120.   Fairbanks, M. S.; McCarthy, D. N.; Scott, S. A.; Brown, S. A.; Taylor, R. P., Fractal electronic devices: simulation and implementation. *NANOTECHNOLOGY* **2011,** *22* (36).

121.   Taylor, R. P., Artificial Vision. *Physics World* 2011, pp 22-27.

122.   Taylor, R.; Brown, S.; Montgomery, R. Fractal Interconnects for Neuroelectronic Interfaces and Implants using the Same (patent application filed). 2011.

123.   Hamann, T. W.; Jensen, R. A.; Martinson, A. B. F.; Van Ryswyk, H.; Hupp, J. T., Advancing beyond current generation dye-sensitized solar cells. *Energy & Environmental Science* **2008,** *1* (1), 66-78.

124.   Jeffryes, C.; Gutu, T.; Jiao, J.; Rorrer, G. L., Peptide-mediated deposition of nanostructured TiO2 into the periodic structure of diatom biosilica. *J. Mat. Res.* **2008,** *23* (12), 3255-3262.

125.   Hines, M. A.; Scholes, G. D., Colloidal PbS nanocrystals with size-tunable near-infrared emission: Observation of post-synthesis self-narrowing of the particle size distribution. *Advanced Materials* **2003,** *15* (21), 1844-1849.

126.   Aldana, J.; Wang, Y. A.; Peng, X. G., Photochemical instability of CdSe nanocrystals coated by hydrophilic thiols. *Journal of the American Chemical Society* **2001,** *123* (36), 8844-8850.

127.   Moody, I. S.; Lonergan, M. C., Photoconductivity of PbS nanocrystals functionalized with ionic ligands. **in preparation**.

128.   Boettcher, S. W.; Berg, S. A.; Schierhorn, M.; Strandwitz, N. C.; Lonergan, M. C.; Stucky, G. D., Ionic ligand mediated electrochemical charging of gold nanoparticle assemblies. *Nano Lett* **2008,** *8* (10), 3404-8.

129.   Lonergan, M. C., A tunable diode based on an inorganic semiconductor vertical bar conjugated polymer interface. *Science* **1997,** *278* (5346), 2103-2106.

130.   Boettcher, S. W.; Schierhorn, M.; Strandwitz, N. C.; Lonergan, M. C.; Stucky, G. D., Ionic-Ligand-Mediated Electrochemical Charging of Anionic Gold Nanoparticle Films and Anionic-Cationic Gold Nanoparticle Bilayers. *J Phys Chem C* **2010,** *114* (9), 4168-4178.

131.   Walter, M. G.; Rudine, A. B.; Wamser, C. C., Porphyrins and Phthalocyanines in Solar Cells. *J. Porphyrins Phthalocyanines* **2010,** *14* (9), 759-792.

132.   Rudine, A. B.; DelFatti, B. D.; Wamser, C. C., Spectroscopy of Protonated Tetraphenylporphyrins with Amino/Carbomethoxy Substituents: Evidence for a Monoprotonated Porphyrin. *J. Phys. Chem. A* **submitted March 2012**.

133.   Parkinson, B. The SHArK Project (Solar Hydrogen Activity Research Kit). http://www.thesharkproject.org (accessed 28 March 2012).

134.   Morris, A. J.; Meyer, G. J.; Fujita, E., Molecular Approaches to the Photocatalytic Reduction of Carbon Dioxide for Solar Fuels. *Accounts Chem Res* **2009,** *42* (12), 1983-1994.

135.   Cole, E. B.; Lakkaraju, P. S.; Rampulla, D. M.; Morris, A. J.; Abelev, E.; Bocarsly, A. B., Using a One-Electron Shuttle for the Multielectron Reduction of CO(2) to Methanol: Kinetic, Mechanistic, and Structural Insights. *Journal of the American Chemical Society* **2010,** *132* (33), 11539-11551.

136.   Beekman, M.; Heideman, C.; Anderson, M.; Smeller, M.; Atkins, R.; Lin, Q.; Nguyen, N.; Johnson, D. C., Design and realization of nanostructured inorganic intergrowths. In *CRC Handbook "Thermoelectrics and its Energy Harvesting"*, accepted.

137.   Atkins, R.; Johnsom, D., Synthesis of New Ferecrystals [(SnSe)y]m(TSe2)n where T= V and Ta. In *2011 11th IEEE International Conference on Nanotechnology*, IEEE Xplore: Portland, OR, 2011; pp 1230-1234.

138.   Moore, D. B.; Beekman, M.; Johnson, D., Synthesis of Four New Members of the (PbSe)1.16(TiSe2)n (n = 1, 2, 3, and 4) Family of Ferecrystals. In *2011 11th IEEE International Conference on Nanotechnology*, IEEE Xplore: Portland, OR, 2011; pp 1363-1366.

139.   Rouvimov, S.; Beekman, M.; Atkins, R.; Grosse, C.; Kirmse, H.; Johnson, D.; Neumann, W., Structural investigations of ferecrystals [(SnSe)1+x]m[TSe2]n (T = Mo, Ta) by means of transmission electron microscopy. In *2011 11th IEEE International Conference on Nanotechnology*, IEEE Xplore: Portland, OR, 2011; pp 398-403.

140.   Mortensen, C.; Beekman, M.; Johnson, D. C., Probing the Effects of Alloying, Grain Size, and Turbostratic Disorder on Thermal Conductivity. *Science of Advanced Materials* **2011,** *3* (4), 639-645.

141.   Subramanian, M. A.; Li, D.; Duan, N.; Reisner, B. A.; Sleight, A. W., High dielectric constant in ACu(3)Ti(4)O(12) and ACu(3)Ti(3)FeO(12) phases. *Journal of Solid State Chemistry* **2000,** *151* (2), 323-325.

142.   Chiodelli, G.; Massarotti, V.; Capsoni, D.; Bini, M.; Azzoni, C. B.; Mozzati, M. C.; Lupotto, P., Electric and dielectric properties of pure and doped CaCu3Ti4O12 perovskite materials. *Solid State Communications* **2004,** *132* (3-4), 241-246.

143.   Parkash, O.; Kumar, D.; Goyal, A.; Agrawal, A.; Mukherjee, A.; Singh, S.; Singh, P., Electrical behaviour of zirconium doped calcium copper titanium oxide. *J Phys D Appl Phys* **2008,** *41* (3), 1-8.

144.   Chung, S. Y.; Lee, S. I.; Choi, J. H.; Choi, S. Y., Initial cation stoichiometry and current-voltage behavior in Sc-doped calcium copper titanate. *Applied Physics Letters* **2006,** *89* (19), 1-3.

145.   Grubbs, R. K.; Venturini, E. L.; Clem, P. G.; Richardson, J. J.; Tuttle, B. A.; Samara, G. A., Dielectric and magnetic properties of Fe- and Nb-doped CaCu3Ti4O12. *Physical Review B* **2005,** *72* (10), 1-11.

Appendix I. Project Investigators

University of Oregon	Oregon State University	Portland State University	Pacific Northwest National Laboratory
Chemistry	**Chemistry**	**Chemistry**	**Energy and Efficiency Directorate**
Jim Hutchison	Vince Remcho	Mingdi Yan	Glen Fryxell
Mark Lonergan	Doug Keszler	Scott Reed**	Dan Palo***
Dave Johnson	Mas Subramanian	Gertrude Rempfer	Sudhir Ramprasad
Andy Berglund		Jun Jiao	Marvin Warner
Ken Doxsee	**Chemical, Biological, Environmental Engineering**	Carl Wamser	
	Jeff Nason		**National Security Directorate**
Institute of Molecular Biology	Lew Semprini	**Mathematics**	Marvin Warner
Eric Johnson	Tyler Radniecki*	Bin Jiang	Shane Addleman
Karen Guillemin	Greg Rorrer	**Physics**	
John Postlethwait	Stacey Harper	Rolf Koenenkamp	**EMSL**
Andy Berglund			Galya Orr
	Mechanical, Industrial, Manufacturing Engineering		
Physics	Todd Miller		**Marine Science Laboratory**
Steve Kevan	Chih-Hung Chang		Mark Jones
Richard Taylor	Brian Paul		
	Sundar Atre		
	Shoichi Kimura		
	Goran Jovanovic		
	Vinod Narayanan		
	Environmental Molecular Toxicology		
	Robert Tanguay		
	Stacey Harper		

*Now at San Diego State University
**Now at University of Colorado, Denver
***Now at Barr Engineering

Appendix II. Manuscripts published through this work
Publications that list the AFRL grant

1.   Baker, N.A., J.D. Klemm, S.L. Harper, S. Gaheen, M. Heiskanen, P. Rocca-Serra, S.A. Sansone. 201X. Supporting reproducible and reusable research with nanotechnology data standards. Nature Nanotechnology. *Submitted*

2.   Park, K.*,* G. Tuttle, F. Sinche, and S.L. Harper. Stability of citrate-capped nanoparticles in exposure media and their effects on the development of embryonic zebrafish (*Danio rerio*). Archives of Pharmacol Research. *Submitted*

3.   Kim, K.-T.; Zaikova, T.; Hutchison, J. E.; Tanguay, R. L. Subtle Surface Ligand Variations Influence Biological Compatibility of Gold Nanoparticles. ACS Nano 2013, *Submitted.*

4.   Oliveri, A.F.; Elliot, E.W.; Carnes, M.E.; Hutchison, J.E.; Johnson, D.W. Elucidating Inorganic Nanoscale Species in Solution: Complementary and Corroborative Approaches. ChemPhysChem, 2013, *in press*.

5.   Kim, K.T., Zaikova, T., Hutchison, J.E., Tanguay, R.L., 2013. Gold Nanoparticles Disrupt Zebrafish Eye Development and Pigmentation. Toxicol. Sci. *in press.*

6.   Smith, M. R.; Boenzli, M. G.; Hindagolla, V.; Ding, J.; Miller, J. M.; Hutchison, J. E.; Greenwood, J. A.; Abeliovich, H.; Bakalinsky, A. T., Identification of gold nanoparticle-resistant mutants of *Saccharomyces cerevisiae* suggests a role for respiratory metabolism in mediating toxicity. *Appl Env. Micro.* 2013, 79, 728-33.

7.   Thomas, D. G.; Gaheen, S.; Harper, S. L.; Fritts, M.; Klaessig, F.; Hoover, M. D.; Hahn-Dantona, E.; Paik, D. S.; Pan, S.; Stafford, G.; Freund, E. T.; Klemm, J. D.; Baker., N. A., nano-TAB: A specification for sharing nanomaterial research data in spreadsheet-based format. BMC Biotechnology, 2013, 12. 1-15.

8.   Truong, L.; Tilton, S. C.; Zaikova, T.; Richman, E.; Waters, K. M.; Hutchison, J. E.; Tanguay, R. L., Surface functionalities of gold nanoparticles impact embryonic gene expression responses. *Nanotox.* 2013, 7, 192-201.

9.   Oliveri, A. F.; Carnes, M. E.; Baseman, M. M.; Richman, E. K.; Hutchison, J. E.; Johnson, D. W., Single Nanoscale Cluster Species Revealed by 1H NMR Diffusion-Ordered Spectroscopy and Small-Angle X-ray Scattering. *Ang. Chem. Int. Ed.* 2012, 51, 10992-10996.

10.   Truong, L.; Zaikova, T.; Richman, E. K.; Hutchison, J. E.; Tanguay, R. L., Media ionic strength impacts embryonic responses to engineered nanoparticle exposure. Nanotoxicology 2012, 6 (7), 691-699.

11.   Truong, L.; Saili, K. S.; Miller, J. M.; Hutchison, J. E.; Tanguay, R. L., Persistent adult zebrafish behavioral deficits results from acute embryonic exposure to gold nanoparticles. Comparative Biochemistry and Physiology Part C: Toxicology & Pharmacology 2012, 155 (2), 269-274.

12.   Warner, C. L.; Chouyyok, W.; Mackie, K. E.; Neiner, D.; Saraf, L. V.; Droubay, T. C.; Warner, M. G.; Addleman, R. S., Manganese Doping of Magnetic Iron Oxide Nanoparticles: Tailoring Surface Reactivity for a Regenerable Heavy Metal Sorbent. Langmuir 2012, 28 (8), 3931-3937.

13.   Xie, Y.; Williams, N. G.; Tolic, A.; Chrisler, W. B.; Teeguarden, J. G.; Maddux, B. L. S.; Pounds, J. G.; Laskin, A.; Orr, G., Aerosolized ZnO nanoparticles impose toxicity in alveolar type II epithelial cells at the air-liquid interface. Toxicological Sciences 2012, 125 (2), 450-461.

14. Fairbanks, M. S.; McCarthy, D. N.; Scott, S. A.; Brown, S. A.; Taylor, R. P., Fractal electronic devices: simulation and implementation. *Nanotech*. 2011, 22 (36).

15. Glover, R. D.; Miller, J. M.; Hutchison, J. E., Generation of Metal Nanoparticles from Silver and Copper Objects: Nanoparticle Dynamics on Surfaces and Potential Sources of Nanoparticles in the Environment. ACS Nano, 2011.

16. Harper, S. L.; Carriere, J. L.; Miller, J. M.; Hutchison, J. E.; Maddux, B. L. S.; Tanguay, R. L., Systematic Evaluation of Nanomaterial Toxicity: Utility of Standardized Materials and Rapid Assays. ACS Nano, 2011, 5 (6), 4688–4697.

17. Jeffryes, C.; Campbell, J.; Li, H.; Jiao, J.; Rorer, G., The potential of diatom nanobiotechnology for applications in solar cells, batteries, and electroluminescent devices. Energy & Environmental Science 2011, 4 (10).

18. Jin, H. D.; Chang, C.-H., Continuous synthesis of SnTe nanorods. J Mater Chem, 2011, 21 (33), 12218-12220.

19. Koretsky, M. D.; Yokochi, A.; Harper, S., Development of an Option in Nanotechnology: Elements of Student Learning. In 2011 11th IEEE International Conference on Nanotechnology, IEEE Xplore: Portland OR, 2011; pp 948-952.

20. Matus, K. J.; Hutchison, J. E.; Peoples, R.; Rung, S.; Tanguay, R. L. Green Nanotechnology Challenges And Opportunities 2011. http://www.acs.org/greenreport, http://www.greennano.org/roadmap (accessed 15 August 2011).

21. Miller, J. M.; Glover, R.; Hutchison, J., New characterization strategies for streamlining the commercialization of nanomaterials. In 2011 11th IEEE International Conference on Nanotechnology, IEEE Xplore: Portland, OR, 2011; pp 1499-1503.

22. Mortensen, C.; Beekman, M.; Johnson, D. C., Probing the Effects of Alloying, Grain Size, and Turbostratic Disorder on Thermal Conductivity. Science of Advanced Materials 2011, 3 (4), 639-645.

23. Nadarajah, A.; Rouvimov, S.; Koenenkamp, R., Improved Transport with 1,2-Ethanedithiol Treatment in the Preparation of Quantum-Dot-Nanowire Solar Cells. In 2011 11th IEEE International Conference on Nanotechnology, IEEE Xplore: Portland, OR, 2011; pp 675-679.

24. Palanisamy, B.; Paul, B., Continuous synthesis of ceria nanoparticles using a micromixer. In 2011 11th IEEE International Conference on Nanotechnology, IEEE Xplore: Portland, OR, 2011; pp 328-331.

25. Paul, B. K.; Abhinkar, B. S.; Lee, S., High pressure hermetic compression seals for embedding elastomeric membrane microvalves in polymer microfluidic devices. Precision Engineering 2011, 35 (2), 348-354.

26. Peterson, D. A.; Chandran, P.; Paul, B. K., A Reverse Oscillatory Flow Microreactor System for the Synthesis of Uniformly-Size CdS Nanoparticles. In 2011 11th IEEE International Conference on Nanotechnology, IEEE Xplore: Portland, OR, 2011; pp 666-670.

27. Peterson, D. A.; Garrison, A.; Paul, B. K. In Evaluation of a Reverse Oscillatory Flow Microreactor Design for the Synthesis of Uniformly-Sized Nanoparticles, ASME 2011 Manufacturing Science and Engineering Conference, Corvallis, OR, 13-17 June 2011; ASME: Corvallis, OR, 2011; pp MSEC2011-50246.

28.   Radniecki, T. S.; Stankus, D. P.; Neigh, A.; Nason, J. A.; Semprini, L., Influence of liberated silver from silver nanoparticles on nitrification inhibition of Nitrosomonas europaea. Chemosphere 2011, 85, 43-49.

29.   Ramprasad, S.; Ramsing, P.; Rundel, J.; Miller, T.; Remcho, V.; Palo, D., Copper nanoparticle synthesis in continuous mode by the polyol method –Progress towards nanomanufacturing. In 2011 11th IEEE International Conference on Nanotechnology, IEEE Xplore: Portland, OR, 2011; pp 323-327.

30.   Rouvimov, S.; Beekman, M.; Atkins, R.; Grosse, C.; Kirmse, H.; Johnson, D.; Neumann, W., Structural investigations of ferecrystals [(SnSe)1+x]m[TSe2]n (T = Mo, Ta) by means of transmission electron microscopy. In 2011 11th IEEE International Conference on Nanotechnology, IEEE Xplore: Portland, OR, 2011; pp 398-403.

31.   Shinagawa, T.; Nadarajah, A.; Könenkamp, R., All-Solution-Processed CIS Solar Cells Based on Electrodeposited ZnO Nanopillars. In 2011 11th IEEE International Conference on Nanotechnology, IEEE Xplore: Portland, OR, 2011; pp 343-346.

32.   Stankus, D. P.; Lohse, S. E.; Hutchison, J. E.; Nason, J. A., Interactions between natural organic matter and gold nanoparticles stabilized with different organic capping agents. . Environmental Science and Technology 2011, 45 (8), 3238-3244.

33.   Tanguay, R., A fresh look at nanomaterials. International Innovation 2011, Healthcare (2), 92-94.

34.   Thomas, D. G.; Klaessig, F.; Harper, S. L.; Fritts, M.; Hoover, M. D.; Gaheen, S.; Stokes, T. H.; Reznik-Zellen, R.; Freund, E. T.; Klemm, J. D.; Paik, D. S.; Baker, N. A., Informatics and standards for nanomedicine technology. Wiley Interdisciplinary Reviews: Nanomedicine and Nanobiotechnology 2011, 3 (5), 511-532.

35.   Thompson, J. O.; Anderson, M. D.; Ngai, T.; Allen, T.; Johnson, D. C., Nucleation and growth kinetics of co-deposited copper and selenium precursors to form metastable copper selenides. Journal of Alloys and Compounds 2011, 509 (40), 9631-9637.

36.   Truong, L.; Moody, I.; Stankus, D.; Nason, J.; Lonergan, M.; Tanguay, R., Differential stability of lead sulfide nanoparticles influences biological responses in embryonic zebrafish. Archives of Toxicology 2011, 85 (7), 787-798.

37.   Boettcher, S. W.; Schierhorn, M.; Strandwitz, N. C.; Lonergan, M. C.; Stucky, G. D., Ionic-Ligand-Mediated Electrochemical Charging of Anionic Gold Nanoparticle Films and Anionic-Cationic Gold Nanoparticle Bilayers. J Phys Chem C 2010, 114 (9), 4168-4178.

38.   Harper, S. L.; Hutchison, J.; Maddux, B. L. S.; Tanguay, R. L. In Integrative Strategies to Understand Nanomaterial-Biological Interactions, International Environmental Nanotechnology Conference: Applications and Implications, Chicago, IL, October 7-9, 2008; Environmental Protection Agency: Chicago, IL, 2010; pp 51-56.

39.   Mackiewicz, M. R.; Hodges, H. L.; Reed, S. M., C-Reactive Protein Induced Rearrangement of Phosphatidylcholine on Nanoparticle Mimics of Lipoprotein Particles. The Journal of Physical Chemistry B 2010, 114 (16), 5556-5562.

40.   Norris, C. B.; Joseph, P. R.; Mackiewicz, M. R.; Reed, S. M., Minimizing Formaldehyde Use in the Synthesis of Gold,Silver Core, Shell Nanoparticles. Chemistry of Materials 2010, 22 (12), 3637-3645.

41. Orr, G., Organelle-Specific Pharmaceutical Nanotechnology: Active Cellular Transport of Submicro- and Nanoscale Particles. In Organelle-Specific Pharmaceutical Nanotechnology, John Wiley & Sons, Inc.: 2010; pp 337-356.

42. Orr, G. A.; Chrisler, W. B.; Cassens, K. J.; Tan, R.; Tarasevich, B. J.; Markillie, L. M.; Zangar, R. C.; Thrall, B. D., Cellular recognition and trafficking of amorphous silica nanoparticles by macrophage scavenger receptor A. Nanotoxicology 2010, Sept 17, 1-16.

43. Stone, D. L.; Harper, B. J.; Lynch, I.; Dawson, K.; Harper, S. L., Exposure assessment: Recommendations for nanotechnology-based pesticides. . International Journal of Occupational and Environmental Health 2010, 16 (4), 467-474.

44. Bothara, M. G.; Vijay, P.; Atre, S. V.; Park, S. J.; German, R. M.; Sudarshan, T. S.; Radhakrishnan, R., Design of Experiment Approach for Sintering Study of Nanocrystalline SiC Fabricated Using Plasma Pressure Compaction. Sci Sinter 2009, 41 (2), 125-133.

45. Jain, K.; Wu, C.; Atre, S. V.; Jovanovic, G.; Narayanan, V.; Kimura, S.; Sprenkle, V.; Canfield, N.; Roy, S., Synthesis of Nanoparticles in High Temperature Ceramic Microreactors: Design, Fabrication and Testing. Int J Appl Ceram Tec 2009, 6 (3), 410-419.

46. Orr, G.; Panther, D. J.; Cassens, K. J.; Phillips, J. L.; Tarasevich, B. J.; Pounds, J. G., Syndecan-1 mediates the coupling of positively charged submicrometer amorphous silica particles with actin filaments across the alveolar epithelial cell membrane. Toxicology and Applied Pharmacology 2009, 236 (2), 210-220.

47. Chang, C.; Paul, B.; Remcho, V.; Atre, S.; Hutchison, J., Synthesis and post-processing of nanomaterials using microreaction technology. Journal of Nanoparticle Research 2008, 10 (6), 965-980.

48. Gann, J. P.; Yan, M., A versatile method for grafting polymers on nanoparticles. Langmuir 2008, 24 (10), 5319-23.

49. Garrison, A.; Paul, B. K., Design of an Interdigital Micromixer for Nanoparticle Manufacturing Using Computational Fluid Dynamics. In International Conference on Micromanufacturing, University of Illinois, Urbana-Champaign, 2008; pp 260-264.

50. Harper, S.; Dahl, J.; Maddux, B.; Tanguay, R., Proactively designing nanomaterials to enhance performance and minimise hazard. International Journal of Nanotechnology 2008, 5 (1), 124-142.

51. Harper, S.; Usenko, C.; Hutchison, J. E.; Maddux, B. L. S.; Tanguay, R. L., In vivo biodistribution and toxicity depends on nanomaterial composition, size, surface functionalisation and route of exposure. Journal of Experimental Nanoscience 2008, 3 (3), 195 - 206.

52. Laddha, S. The Effect of Feedstock Composition on Defect Evolution in Powder Injection Molded Ceramic Microarrays using Simulations and Experiments. Oregon State University Corvallis, OR, 2008.

53. Mackiewicz, M.; Ayres, B.; Reed, S., Reversible, reagentless solubility changes in phosphatidylcholine-stabilized gold nanoparticles. Nanotechnology 2008, 19 (11), 115607.

54. Rung, R. D. Nanomaterials-Biological Systems Interactions - Addressing the Complexity 2008. http://www.nanotech-now.com/columns/?article=247 (accessed 10/22/08).

55. Schmid, D.; Handge, U. A.; Gann, J. P.; Yan, M.; Caseri, W., Melt Elongation of Polymer Nanocomposites: A Method for the Controlled Production of Dichroic Films. Macromolecular Materials and Engineering 2008, 293 (6), 471-478.

56.   Sitaula, S.; Mackiewicz, M. R.; Reed, S. M., Gold nanoparticles become stable to cyanide etch when coated with hybrid lipid bilayers. Chem Commun (Camb) 2008, (26), 3013-5.

57.   Usenko, C. Y.; Harper, S. L.; Tanguay, R. L., Fullerene C60 exposure elicits an oxidative stress response in embryonic zebrafish. Toxicol Appl Pharmacol 2008, 229 (1), 44-55.

58.   Wu, C. L.; Laddha, S. G.; Atre, S. V.; Lee, S.; Simmonds, K.; Park, S. J.; German, R. M.; Whychell, D., Microscale Heterogeneity in Powder Injection Molded Ceramic Microarrays. Powder Injection Molding International 2008, 2 (2), 68-73.

59.   Abhinkar, B. S.; Lee, S.; Paul, B. K. In A Conformal Membrane Microvalve for the Plug-Flow Reaction of Nanomaterials, Industrial Engineering Research Conference, Nashville, Tennessee, Nashville, Tennessee, 2007.

60.   Boettcher, S. W.; Strandwitz, N. C.; Schierhorn, M.; Lock, N.; Lonergan, M. C.; Stucky, G. D., Tunable electronic interfaces between bulk semiconductors and ligand-stabilized nanoparticle assemblies. Nature Materials 2007, 6 (8), 592-6.

61.   Dahl, J. A.; Maddux, B. L.; Hutchison, J. E., Toward greener nanosynthesis. Chemical reviews 2007, 107 (6), 2228-69.

62.   Maddux, B.; Rung, R.; Hutchison, J., Developing Green Nanotechnology: Challenges and Opportunities Through Innovation. NSTI-NanoTech 2007, 1, 612-615.

63.   Maddux, B. L. S.; Hutchison, J. E. ONAMI - Safer Nanomaterials & Nanomanufacturing Initiative [SNNI] statement on EHS research needs for engineered nanomaterials; National Nanotechnology Initiative: Arlington, VA, 4 January, 2007.

64.   Miller, J. M.; Kearns, G. J.; Hutchison, J. E., Windows of Opportunity: A New Platform to Understand Structure-Property Relationships in Nanotechnology. In Technical Proceedings of the 2007 NSTI Nanotechnology Conference and Trade Show, NanoScience and Technology Institute: Santa Clara, CA, 2007; Vol. 1, pp 305-308.

65.   Rundel, J. T.; Paul, B. K.; Remcho, V. T., Organic solvent nanofiltration for microfluidic purification of poly(amidoamine) dendrimers. Journal of Chromatography A 2007, 1162 (2), 167-174.

66.   Tanguay, R., An interview with Robert Tanguay, Ph.D. Interviewed by Vicki Glaser. Zebrafish 2007, 4 (3), 163-8.

67.   The Safer Nanomaterials and Nanomanufacturing Initiative. http://www.greennano.org/

Publications strengthened by AFRL seed funding to project investigators or impacted/supported by the seed award.

1.   Kim, K.-T.; Truong, L.; Wehmas, L.; Tanguay, R. L., Silver nanoparticle toxicity in the embryonic zebrafish is governed by particle dispersion and ionic environment. *Nanotechnol* 2013, 24, 115101.

2.   Kim, K.T., Tanguay, R.L., 2013. Integrating zebrafish toxicology and green nanoscience for safer product development. Green Chemistry 15, 872-880.

3.   Beekman, M.; Heideman, C.; Anderson, M.; Smeller, M.; Atkins, R.; Lin, Q.; Nguyen, N.; Johnson, D. C., Design and realization of nanostructured inorganic intergrowths. In *Modules, Systems, and Applications in Thermoelectrics*, Rowe, D. M., Ed. CRC Press: 2012; Vol. 2. pp 1-12.

4.	A Research Strategy for Environmental, Health, and Safety Aspects of Engineered Nanomaterials, Committee to Develop a Research Strategy for Environmental, Health, Safety Aspects of Engineered Nanomaterials National Research Council [Online], 2012. http://www.nap.edu/openbook.php?record_id=13347.

5.	Karakoti, A. S.; Munusamy, P.; Hostetler, K.; Kodali, V.; Kuchibhatla, S.; G. Orr, J. G. P.; Teeguarden, J. G.; Thrall, B. D.; Baer, D. R., Preparation and Characterization Challenges to Understanding Environmental and Biological Impacts of Nanoparticles. *Surf Interface Anal* 2012, 44, 882-889.

6.	Imahori, H.; Kurotobi, K.; Walter, M. G.; Rudine, A. B.; Wamser, C. C., Porphyrin and Phthalocyanine-Based Solar Cells. In Handbook of Porphyrin Science, Kadish, K. M.; Smith, K. M.; Guilard, R., Eds. World Scientific Press: 2012; Vol. 18.

7.	Mandrell, D.; Truong, L.; Jephson, C.; Sarker, M. R.; Moore, A.; Lang, C.; Simonich, M. T.; Tanguay, R. L., Automated zebrafish chorion removal and single embryo placement: optimizing throughput of zebrafish developmental toxicity screens. J Lab Autom 2012, 17 (1), 66-74.

8.	Mihai, C.; Xie, Y.; Tolic, A.; Chrisler, W.; Tan, R.; Zangar, R.; Orr, G. In Mechanism of aerosolized zinc oxide nanoparticle toxicity in alveolar epithelial cells at the air-liquid interface, 51st Society of Toxicology Annual Meeting, San Francisco, March 11-15, 2012; SOT: San Francisco, 2012.

9.	Atkins, R.; Johnson, D., Synthesis of New Ferecrystals $[(SnSe)_y]m(TSe2)_n$ where T= V and Ta. In 2011 11th IEEE International Conference on Nanotechnology, IEEE Xplore: Portland, OR, 2011; pp 1230-1234.

10.	Baer, D. R.; Karakoti, A. S.; Munusamy, P.; Thrall, B. D.; Pounds, J. G.; G., J.; Teeguarden; Amonette, J. E.; Orr, G., Testing in EHS: What is the Current Status of Experimentation? In 2011 11th IEEE International Conference on Nanotechnology, IEEE Xplore: Portland, OR, 2011; pp 18-19.

11.	de la Iglesia, D.; Harper, S.; Hoover, M. D.; Klaessig, F.; Lippell, P.; Maddux, B.; Morse, J.; Nel, A.; Rajan, K.; Reznik-Zellen, R.; Tuominen, M. T. Nanoinformatics 2020 Roadmap 2011. http://eprints.internano.org/607/

12.	Donovan, J.; Johnson, D., A Transmission Electron Probe Nano Analyzer for Improved High Accuracy Elemental Analysis. In 2011 11th IEEE International Conference on Nanotechnology, IEEE Xplore: Portland, OR, 2011; pp 392-397.

13.	Gale, D. K.; Jeffryes, C.; Gutu, T.; Jiao, J.; Chang, C.-h.; Rorrer, G. L., Thermal annealing activates amplified photoluminescence of germanium metabolically doped in diatom biosilica. J Mater Chem 2011, 21 (29), 10658-10665.

14.	Kernan, F.; Nadarajah, A.; Higgins, J. A.; Pejcinovic, B.; Koenenkamp, R., Terahertz Characterization of Zinc Oxide Nanowires Using Parallel-Plate Waveguides. In 2011 11th IEEE International Conference on Nanotechnology, IEEE Xplore: Portland, OR, 2011; pp 404-408.

15.	Mishra, A.; Harper, S.; Yun, S.-I., Interaction of biosynthesized gold nanoparticles with genomic DNA isolated from E. coli and S. aureus. In 2011 11th IEEE International Conference on Nanotechnology, IEEE Xplore: Portland, OR, 2011; pp 1745-1750.

16.	Mochel, A.; Sergueev, I.; Nguyen, N.; Long, G. J.; Grandjean, F.; Johnson, D. C.; Hermann, R. P., Lattice dynamics in the FeSb_{3} skutterudite. Physical Review B 2011, 84 (6), 064302.

17.   Moore, D. B.; Beekman, M.; Johnson, D., Synthesis of Four New Members of the (PbSe)1.16(TiSe2)n (n = 1, 2, 3, and 4) Family of Ferecrystals. In 2011 11th IEEE International Conference on Nanotechnology, IEEE Xplore: Portland, OR, 2011; pp 1363-1366.

18.   Nadarajah, A.; Koenenkamp, R., Laser annealing of photoluminescent ZnO nanorods grown at low temperature. Nanotechnology 2011, 22 (2), 025205.

19.   Nadarajah, A.; Rouvimov, S.; Könenkamp, R., Effect of Annealing on ZnO Nanowires grown at Low Temperature. In 2011 11th IEEE International Conference on Nanotechnology, IEEE Xplore: Portland, OR, 2011; pp 1006-1010.

20.   Nammoonnoy, J.; Fuchs, B. K.; Koesdjojo, M. T.; Remcho, V. T., Development of Photoactivable Nanofiber Membranes for Efficient Metal Ion Extraction. In 2011 11th IEEE International Conference on Nanotechnology, IEEE Xplore: Portland, OR, 2011; pp 920-925.

21.   Pleus, R. C., Guidance on physicochemical characterization for manufacture nano-objects submitted for toxicological testing. In 2011 11th IEEE International Conference on Nanotechnology, IEEE Xplore: Portland, OR, 2011; pp 20-21.

22.   Qiyin Lin; Tepfer, S.; Heideman, C.; Mortensen, C.; Nguyen, N.; Zschack, P.; Beekman, M.; Johnson, D. C., Influence of selenium vapor postannealing on the electrical transport properties of PbSe–WSe2 nanolaminates. Journal of Materials Research 2011, 26, 1866-1871.

23.   Schaeublin, N. M.; Braydich-Stolle, L. K.; Schrand, A. M.; Miller, J. M.; Hutchison, J.; Schlager, J. J.; Hussain, S. M., Surface charge of gold nanoparticles mediates mechanism of toxicity. Nanoscale 2011, 3 (2), 410-420.

24.   Smith, A. E.; Sleight, A. W.; Subramanian, M. A., Synthesis and properties of solid solutions of hexagonal YCu0.5Ti0.5O3 with YMO3 (M=Mn, Cr, Fe, Al, Ga, and In). Mat. Res. Bul. 2011, 46 (1), 1-5.

25.   Taylor, R. P., Artificial Vision. Physics World 2011, pp 22-27.

26.   Troung, L.; Harper, S. L.; Tanguay, R. L., Evaluation of embryotoxicity using the zebrafish model. In Methods in Molecular Biology, Gautier, J.-C., Ed. Springer: Totowa, NJ, 2011; Vol. 691, pp 271-279.

27.   Wang, M. S.; Reed, S. M., Electrophoretic Mobility of Lipoprotein Nanoparticle Mimics. In 2011 11th IEEE International Conference on Nanotechnology, IEEE Xplore: Portland, OR, 2011; pp 1652-1656.

28.   Wang, W.; Wentz, K. M.; Hayes, S. E.; Johnson, D. W.; Keszler, D. A., Synthesis of the Hydroxide Cluster $[Al_{13}(Œ^o_3\text{-OH})6(Œ^o\text{-OH})_{18}(H2O)_{24}]_{15+}$ from an Aqueous Solution. Inorganic Chemistry 2011, 50 (11), 4683–4685.

29.   Word, R. C.; Fitzgerald, J.; Könenkamp, R., S- and P-polarization dependence of localized surface plasmon enhanced photoelectron emission from fractal gold/ITO nanostructures. In 2011 11th IEEE International Conference on Nanotechnology, IEEE Xplore: Portland, OR, 2011; pp 1271-1273.

30.   Yu, L.; Lany, S.; Kykyneshi, R.; Jieratum, V.; Ravichandran, R.; Pelatt, B.; Altschul, E.; Platt, H. A. S.; Wager, J. F.; Keszler, D. A.; Zunger, A., Iron Chalcogenide Photovoltaic Absorbers. Advanced Energy Materials 2011, 1 (5), 748-753.

31.   Cowell, E. W.; Knutson, C. C.; Wager, J. F.; Keszler, D. A., Amorphous Metal/Oxide Nanolaminate. ACS Applied Materials & Interfaces 2010, 2 (7), 1811–1813.

32. Dixit, A.; Smith, A. E.; Subramanian, M. A.; Lawes, G., Suppression of multiferroic order in hexagonal ceramics. Solid State Communications 2010, 150 (15-16), 746-750.

33. Fairbanks, M. S.; Martin, T. P.; Scannell, B. C.; Marlow, C. A.; Linke, H.; Taylor, R. P., Measuring hybridization in GaInAs/InP electron billiard arrays. Physica E 2010, 42 (4), 1205-1207.

34. Heideman, C.; Rostek, R.; Anderson, M.; Herzing, A.; Anderson, I.; Johnson, D., Synthesis and Electronic Properties of the Misfit Layer Compound. J. Elec. Mat. 2010, 39 (9), 1476-1481.

35. Hinderliter, P.; Minard, K.; Orr, G.; Chrisler, W.; Pounds, J.; Thrall, B.; Teeguarden, J., ISDD: A Computational Model of Nano and Micro Particle Sedimentation, Diffusion and Target Cell Dosimetry for In Vitro Toxicity Studies. Particle and Fiber Toxicology 2010, 7, 36.

36. Johnson, D. C.; Johnson, D.; Wager, J. F.; Keszler, D. In Green Semiconductor Manufacturing - Potential New Routes Using Aqueous Solultion Chemistry, The International Conference on Compound Semiconductor Manufacturing Technology, Portland, OR, 17-20 May 2010; CS MANTECH Conference: Portland, OR, 2010; pp 3-6.

37. Kim, J. Y.; Choi, Y.-J.; Park, H.-H.; Golledge, S.; Johnson, D. C., Effective atomic layer deposition procedure for Al-dopant distribution in ZnO thin films. Journal of Vacuum Science & Technology A: Vacuum, Surfaces, and Films 2010, 28 (5), 1111-1114.

38. Lin, Q.; Smeller, M.; Heideman, C. L.; Zschack, P.; Koyano, M.; Anderson, M. D.; Kykyneshi, R.; Keszler, D. A.; Anderson, I. M.; Johnson, D. C., Rational Synthesis and Characterization of a New Family of Low Thermal Conductivity Misfit Layer Compounds $[(PbSe)_{0.99}]m(WSe_2)_n$. Chem Mat. 2010, 22 (3), 1002-1009.

39. Lohse, S. E.; Dahl, J. A.; Hutchison, J. E., Direct Synthesis of Large Water-Soluble Functionalized Gold Nanoparticles Using Bunte Salts as Ligand Precursors. Langmuir 2010, 26 (10), 7504-7511.

40. Mavrokefalos, A.; Lin, Q.; Beekman, M.; Seol, J. H.; Lee, Y. J.; Kong, H.; Pettes, M. T.; Johnson, D. C.; Shi, L., In-plane thermal and thermoelectric properties of misfit-layered $[(PbSe)_{0.99}]_x(WSe_2)_x$ superlattice thin films. Appl. Phys. Lett. 2010, 96 (18), 181908-3.

41. McKenzie, L. C.; Haben, P. M.; Kevan, S. D.; Hutchison, J. E., Determining Nanoparticle Size in Real Time by Small-Angle X-ray Scattering in a Microscale Flow System. J. Phys. Chem. C 2010, 114 (50), 22055-22063.

42. Mortensen, C.; Zschack, P.; Johnson, D. C., The Evaluation of TiTe2 as a Diffusion Barrier in the Formation of Low Thermal Conductivity Nanolaminates with Bi2Te3 and Sb2Te3. Advances in Science and Technology 2010, 74, 38-47.

43. Nguyen, N. T.; Berseth, P. A.; Lin, Q.; Chiritescu, C.; Cahill, D. G.; Mavrokefalos, A.; Shi, L.; Zschack, P.; Anderson, M. D.; Anderson, I. M.; Johnson, D. C., Synthesis and Properties of Turbostratically Disordered, Ultrathin WSe2 Films. Chemistry of Materials 2010, 22 (9), 2750-2756.

44. Radniecki, T. S. In Silver nanoparticle inhibition of the ammonia oxidizing bacterium, Nitrosomonas europaea: Influence of aquatic chemistry on bioavailability and exposure., 2010 American Institute of Chemical Engineers Annual Meeting, Salt Lake City, 7-12 November 2010; Salt Lake City, 2010.

45. Radniecki, T. S.; Anderson, J. W.; Schneider, M. C.; Stankus, D. P.; Nason, J. A.; Semprini, L. In Influence of biological macromolecules and aquatic chemistries on the inhibition of

nitrifying bacteria by silver nanoparticles, American Geophysical Union, San Francisco, CA, 13-17 December 2010; San Francisco, CA, 2010; pp H42C-02.

46.   Rudine, A. B.; Walter, M. G.; Wamser, C. C., Reaction of Dichloromethane with Pyridine Derivatives under Ambient Conditions. The Journal of Organic Chemistry 2010, 75 (12), 4292-4295.

47.   Rutledge, R. D.; Warner, C. L.; Pittman, J. W.; Addleman, R. S.; Engelhard, M.; Chouyyok, W.; Warner, M. G., Thiol-Ene Induced Diphosphonic Acid Functionalization of Superparamagnetic Iron Oxide Nanoparticles. Langmuir 2010, 26 (14), 12285-12292.

48.   Taylor, A.; Mortensen, C.; Rostek, R.; Nguyen, N.; Johnson, D., Vapor Annealing as a Post-Processing Technique to Control Carrier Concentrations of Bi2Te3 thin films. Journal of Electronic Materials 2010, 39 (9), 1981-1986.

49.   Tennico, Y. H.; Hutanu, D.; Koesdjojo, M. T.; Bartel, C. M.; Remcho, V. T., On-Chip Aptamer-Based Sandwich Assay for Thrombin Detection Employing Magnetic Beads and Quantum Dots. Analytical Chemistry 2010, 82 (13), 5591-5597.

50.   Truong, L.; Moody, I.; Stankus, D.; Nason, J.; Lonergan, M.; Tanguay, R., Differential stability of lead sulfide nanoparticles influences biological responses in embryonic zebrafish. Arch. Tox. 2010, 1-12.

51.   Usenko, C. Y.; Harper, S. L.; Simonich, M. T.; Tanguay, R. L., Fullerene C60 Toxicology. *In Nanophysics*: Nanomedicine and Nanorobotics., 1st ed.; Sattler, K. D., Ed. Taylor and Francis: London, England, 2010; pp 17.1-17.8.

52.   Walter, M. G.; Rudine, A. B.; Wamser, C. C., Porphyrins and Phthalocyanines in Solar Cells. J. Porphyrins Phthalocyanines 2010, 14 (9), 759-792.

53.   Walter, M. G.; Wamser, C. C., Synthesis and Characterization of Electropolymerized Nanostructured Aminophenylporphyrin Films. J. Phys. Chem. C 2010, 114 (17), 7563-7574.

54.   Warner, C. L.; Addleman, R. S.; Cinson, A. D.; Droubay, T. C.; Engelhard, M. H.; Nash, M. A.; Yantasee, W.; Warner, M. G., High-Performance, Superparamagnetic, Nanoparticle-Based Heavy Metal Sorbents for Removal of Contaminants from Natural Waters. Chemsuschem 2010, 3 (6), 749-757.

55.   Yantasee, W.; Rutledge, R. D.; Chouyyok, W.; Sukwarotwat, V.; Orr, G.; Warner, C. L.; Warner, M. G.; Fryxell, G. E.; Wiacek, R. J.; Timchalk, C.; Addleman, R. S., Functionalized Nanoporous Silica for the Removal of Heavy Metals from Biological Systems: Adsorption and Application. ACS Applied Mat. & Interfaces 2010, 2 (10), 2749-2758.

56.   The 21st Century Nanotechnology Research and Development Act. 111th CONGRESS, 1st Session ed.; 2009; Vol. 15 U.S.C. 7501 et seq.

57.   Nanotoxicology Research Gives Clues to Impact of Inhaling Particles. http://www.pnl.gov/science/highlights/highlight.asp?id=593 (accessed 8 June 2010).

58.   Ayres, B. R.; Reed, S. M.; Garrick, W.; Murthy, S.; Sanghvi, N.; Kulkarni, A., Chem Map: A Geographic Information System Web Page for Chemical Education. Journal of Chemical Education 2009, 86 (2), 255.

59.   Busche, B.; Wiacek, R.; Davidson, J.; Koonsiripaiboon, V.; Yantasee, W.; Addleman, R. S.; Fryxell, G. E., Synthesis of nanoporous iminodiacetic acid sorbents for binding transition metals. Inorg Chem Commun 2009, 12 (4), 312-315.

60.   Chiritescu, C.; Mortensen, C.; Cahill, D. G.; Johnson, D.; Zschack, P., Lower limit to the lattice thermal conductivity of nanostructured Bi[sub 2]Te[sub 3]-based materials. Journal of Applied Physics 2009, 106 (7), 073503-5.

61.   Fernandez, C. A.; Bekhazi, J. G.; Hoppes, E. M.; Fryxell, G. E.; Wang, C.; Bays, J. T.; Warner, M. G.; Wiacek, R. J.; Addleman, R. S., Effect of the Ligand Shell Composition on the Dispersibility and Transport of Gold Nanocrystals in Near-Critical Solvents. Langmuir 2009, 25 (9), 4900-4906.

62.   Fernandez, C. A.; Bekhazi, J. G.; Hoppes, E. M.; Wiacek, R. J.; Fryxell, G. E.; Bays, J. T.; Warner, M. G.; Wang, C.; Hutchison, J. E.; Addleman, R. S., Advancements Toward the Greener Processing of Engineered Nanomaterials - Effect of Core Size on the Dispersibility and Transport of Gold Nanocrystals in Near-Critical Solvents. Small 2009, 5 (8), 961-969.

63.   Harper, S. L. Activites to meet NanoEHS needs; National Nanotechnology Initiative: Oklahoma City, Ok, 1-3 April 2009, 2009.

64.   Lisowski, C. E.; Hutchison, J. E., Malonamide-Functionalized Gold Nanoparticles for Selective, Colorimetric Sensing of Trivalent Lanthanide Ions. Analytical Chemistry 2009, 81 (24), 10246-10253.

65.   Maddux, B. L. S. Review of the "Strategic Research Agenda, Vision Paper from the European Technology Platform on NanoMedicine"; ANSI TAG Meeting: Washington, DC, 2-3 April 2009, 2009.

66.   Martin, T. P.; Fairbanks, M. S.; Scannell, B. C.; Marlow, C. A.; Linke, H.; Taylor, R. P., Investigation of electron wave function hybridization in Ga(0.25)In(0.75)As/InP arrays. Applied Physics Letters 2009, 95 (18).

67.   Martin, T. P.; Marlow, C. A.; Scannell, B. C.; Fairbanks, M. S.; Linke, H.; Brown, S. A.; Taylor, R. P., Chaotic scattering in nano-electronic systems: from billiards to clusters. International Journal of Nanotechnology 2009, 6 (3-4), 408-417.

68.   Matar, S. F.; Baraille, I.; Subramanian, M. A., First principles studies of SnTiO3 perovskite as potential environmentally benign ferroelectric material. Chemical Physics 2009, 355 (1), 43-49.

69.   Mizoguchi, H.; Sleight, A. W.; Subramanian, M. A., Low temperature synthesis and characterization of SnTa2O6. Materials Research Bulletin 2009, 44 (5), 1022-1024.

70.   Radniecki, T. S.; Semprini, L.; Dolan, M. E., Expression of merA, amoA and hao in continuously cultured Nitrosomonas europaea cells exposed to zinc chloride additions. Biotechnology and Bioengineering 2009, 102 (2), 546-553.

71.   Richman, E. K.; Hutchison, J. E., The Nanomaterial Characterization Bottleneck. ACS Nano 2009, 3 (9), 2441-2446.

72.   Rorrer, G.; Li, H.; Jeffryes, C.; Gutu, T.; Jiao, J., Peptide-mediated deposition of nanostructured TiO_2 into the periodic structure of diatom biosilica and its integration into the fabrication of a dye-sensitized solar cell device. *In Synthesis of Bioinspired Hierarchical Soft and Hybrid Materials*, Meldrum, F.; Yang, S.; Kotov, N.; Li, C., Eds. Mater. Res. Soc. Symp. Proc. San Francisco, CA, 2009; 1189E: MM02-05, 1-8.

73.   Smith, A. E.; Calvarese, T. G.; Sleight, A. W.; Subramanian, M. A., An anion substitution route to low loss colossal dielectric CaCu3Ti4O12. Journal of Solid State Chemistry 2009, 182 (2), 409-411.

74.   Smith, A. E.; Mizoguchi, H.; Delaney, K.; Spaldin, N. A.; Sleight, A. W.; Subramanian, M. A., Mn3+ in Trigonal Bipyramidal Coordination: A New Blue Chromophore. Journal of the American Chemical Society 2009, 131 (47), 17084-17086.

75.   Sweeney, S. F.; Hutchison, J. E.; Tanguay, R.; Maddux, B. L. S. SNNI's Proactive Approach to Healthier and Safer of Nanomaterials Nanotechnology Thought Leaders [Online], 2009. http://www.azonano.com/details.asp?ArticleId=2469 (accessed 22 December 2009).

76.   Taylor, R. P. Fractals in Nanodevices The Nano-Experts Series, The On-Line Journal of Nanotechnology [Online], 2009. http://www.azonano.com/details.asp?ArticleId=2413 (accessed 06/08/2010).

77.   Wang, J. S.; Sheaff, C. N.; Yoon, B.; Addleman, R. S.; Wai, C. M., Extraction of Uranium from Aqueous Solutions by Using Ionic Liquid and Supercritical Carbon Dioxide in Conjunction. Chem-Eur J 2009, 15 (17), 4458-4463.

78.   Wang, W.; Gutu, T.; Gale, D. K.; Jiao, J.; Rorrer, G. L.; Chang, C.-h., Self-Assembly of Nanostructured Diatom Microshells into Patterned Arrays Assisted by Polyelectrolyte Multilayer Deposition and Inkjet Printing. Journal of the American Chemical Society 2009, 131 (12), 4178-4179.

79.   Warner, M. G.; Warner, C. L.; Addleman, R. S.; Yantasee, W., Magnetic Nanomaterials for Environmental Applications. In Magnetic Nanomaterials, Kumar, C. S. S. R., Ed. Wiley-VCH: 2009; pp 311-345.

80.   Zepps, J., Sustainable Technology. In Brink, Episode 23 ed.; Williams, D., Ed. The Science Channel: US, 2009.

81.   Zhao, J.-H.; Gupta, V.; Mortensen, C. D.; Lu, K.-H.; Edwards, D. R.; Johnson, D. C.; Ho, P. S. In Thermomechanical Property Characterization of Ultra Low-k Materials, Austin (Texas), Ho, P. S.; Zschech, E.; Ogawa, S., Eds. AIP: Austin (Texas), 2009; pp 87-96.

82.   Boettcher, S. W.; Berg, S. A.; Schierhorn, M.; Strandwitz, N. C.; Lonergan, M. C.; Stucky, G. D., Ionic ligand mediated electrochemical charging of gold nanoparticle assemblies. Nano Lett 2008, 8 (10), 3404-8.

83.   Bothara, M.; Atre, S. V.; Sudarshan, T.; Radhakrishnan, R.; S.J. Park; German, R. M. In Taguchi Method for Sintering Study of Nanoscale Silicon Carbide Fabricated Using Plasma Pressure Compaction, 2008 World Congress on Powder Metallurgy & Particulate Materials, Washington, D.C., June 8-12; Metal Powder Industries Federation: Washington, D.C., 2008.

84.   Carter, T. G.; Yantasee, W.; Sangvanich, T.; Fryxell, G. E.; Johnson, D. W.; Addleman, R. S., New functional materials for heavy metal sorption: "Supramolecular" attachment of thiols to mesoporous silica substrates. Chem Commun 2008, (43), 5583-5585.

85.   Cascade, U. Hutchinson Advocates for Green Nano UO Cascade [Online], 2008. http://cascade.uoregon.edu/fall2008/natural-sciences/hutchinson-advocates-for-green/ (accessed 27 July 2009).

86.   Chase, S., Green Nanotechnology. ScienCentral, Ed. ScienCentral: 2008.

87.   Chiritescu, C.; Cahill, D. G.; Heideman, C.; Lin, Q.; Mortensen, C.; Nguyen, N. T.; Johnson, D.; Rostek, R.; Bottner, H., Low thermal conductivity in nanoscale layered materials synthesized by the method of modulated elemental reactants. Journal of Applied Physics 2008, 104 (3), 033533.

88.   Fairbanks, M. S.; Marlow, C. A.; Taylor, R. P.; Linke, H., Nonlinear characteristics in the magnetoconductance of electron billiards. Current Applied Physics 2008, 8 (3-4), 340-342.

89.   Fernandez, C. A.; Hoppes, E. M.; Bekhazi, J. G.; Wang, C.; Wiacek, R. J.; Warner, M. G.; Fryxell, G. E.; Bays, J. T.; Addleman, R. S., Tuning and quantifying the dispersibility of gold nanocrystals in liquid and supercritical solvents. J Phys Chem C 2008, 112 (36), 13947-13957.

90.   Fernandez, C. A.; Wiacek, R. J.; Nachimuthu, P.; Fryxell, G. E.; Pierson, A. M.; Warner, C. L.; Warner, M. G.; Addleman, R. S., A Simple Method for the Prevention of Non-Specific Adsorption by Nanocrystals onto Surfaces. Journal of Nanoscience and Nanotechnology 2008, 8, 5781-5786.

91.   Harper, S. L., Review of Nanotoxicology: Characterization, Dosing and Health Effects. Doody's Review Service (on-line). 2008.

92.   Heideman, C.; Nyugen, N.; Hanni, J.; Lin, Q.; Duncombe, S.; Johnson, D. C.; Zschack, P., The synthesis and characterization of new [(BiSe)1.10]m[NbSe2]n, [(PbSe)1.10]m[NbSe2]n, [(CeSe)1.14]m[NbSe2]n and [(PbSe)1.12]m[TaSe2]n misfit layered compounds. Journal of Solid State Chemistry 2008, 181 (7), 1701-1706.

93.   Hutchison, J. E., Greener Nanoscience: A Proactive Approach to Advancing Applications and Reducing Implications of Nanotechnology. ACS Nano 2008, 2 (3), 395-402.

94.   Ito, D.; Jespersen, M. L.; Hutchison, J. E., Selective Growth of Vertical ZnO Nanowire Arrays Using Chemically Anchored Gold Nanoparticles. ACS Nano 2008, 2 (10), 2001-2006.

95.   Jeffryes, C.; Gutu, T.; Jiao, J.; Rorrer, G. L., Peptide-mediated deposition of nanostructured TiO2 into the periodic structure of diatom biosilica. J. Mat. Res. 2008, 23 (12), 3255-3262.

96.   Jeffryes, C.; Gutu, T.; Jiao, J.; Rorrer, G. L., Metabolic Insertion of Nanostructured TiO2 into the Patterned Biosilica of the Diatom Pinnularia sp. by a Two-Stage Bioreactor Cultivation Process. ACS Nano 2008, 2 (10), 2103-2112.

97.   Johnson, D. C.; Lin, Q.; Smeller, M.; Heideman, C.; Smalley, A. L. E., Synthesis and thermoelectric properties of the pseudo-binary skutterudites CoGe1.5Se1.5 and CoSn1.5Te1.5. In Solid-State Chemistry of Inorganic Materials VII [Online] P.M. Woodward, J. F. M., S.L. Brock, J.S.O. Evans, Ed. Mater. Res. Soc. Symp. Proc. Volume 1148E: Warrendale, PA, 2008. http://www.mrs.org/s_mrs/sec_subscribe.asp?CID=16658&DID=250610&action=detail (accessed 11 November 2009).

98.   Kim, S.; Zuo, J. M.; Nguyen, N. T.; Johnson, D. C.; Cahill, D. G., Structure of layered WSe2 thin films with ultralow thermal conductivity. Focus Issue on Biomimetic and Bio-Enabled Materials Science and Engineering 2008, 23 (4), 1064-1067.

99.   Ladha, S. G.; Wu, C. L.; Atre, S. V.; Lee, S.; Simmons, K.; Park, S. J.; German, R. M. In The Effect of Feedstock Composition on Defect Evolution in Powder Injection Molded Ceramic Microarrays, 2008 World Congress on Powder Metallurgy & Particulate Materials, Princeton, NJ, Metal Powder Industries Federation: Princeton, NJ, 2008.

100. Lin, F.; Wang, Y.; Lonergan, M., Ion transport in polyacetylene ionomers. Journal of Applied Physics 2008, 104 (10), 103517-8.

101. Lin, Q.; Heideman, C. L.; Nguyen, N.; Zschack, P.; Chiritescu, C.; Cahill, D. G.; Johnson, D. C., Designed Synthesis of Families of Misfit-Layered Compounds. European Journal of Inorganic Chemistry 2008, 2008 (15), 2382-2385.

102. Liu, S.; Chang, C. h.; Paul, B. K.; Remcho, V. T., Convergent synthesis of polyamide dendrimer using a continuous flow microreactor. Chemical engineering journal 2008, 135, S333-S337.

103. Maglione, M.; Subramanian, M. A., Dielectric and polarization experiments in high loss dielectrics: A word of caution. Applied Physics Letters 2008, 93 (3), 032902-3.

104. Mizoguchi, H.; Wattiaux, A.; Kykyneshi, R.; Tate, J.; Sleight, A. W.; Subramanian, M. A., Synthesis and characterization of Sn^{2+} oxides with the pyrochlore structure. Materials Research Bulletin 2008, 43 (8-9), 1943-1948.

105. Moody, I. S.; Stonas, A. R.; Lonergan, M. C., PbS Nanocrystals Functionalized with a Short-Chain, Ionic, Dithiol Ligand. J Phys Chem C 2008, 112 (49), 19383-19389.

106. Reed, S. M.; Do, M. T.; Masta, S. E., Parallel factor analysis of spider fluorophores. J Photochem Photobiol B 2008, 93 (3), 149-54.

107. Rung, R. D. NNI Reauthorization, "Nanomanufacturing" and U.S. Competitiveness 2008. http://www.nanotech-now.com/columns/?article=201.

108. Tran M. Phung; Jacob M. Jensen; David C. Johnson; John J. Donovan; Brian G. McBurnett, Determination of the composition of Ultra-thin Ni-Si films on Si: constrained modeling of electron probe microanalysis and x-ray reflectivity data. X-Ray Spectrometry 2008, 37 (6), 608-614.

109. Urval, R.; Lee, S.; Atre, S. V.; Park, S. J.; German, R. M., Optimisation of process conditions in powder injection moulding of microsystem components using a robust design method: part I. primary design parameters. Powder Metallurgy 2008, 51 (2), 133-142.

110. Vercruysse, K. P.; Harper, S. L.; Ivory, D. M.; Whalen, M. M.; Saili, K. S.; Tanguay, R. L. In Potential anti-inflammatory properties of biologically-synthesized nanoparticles of gold or silver, NSTI-Nanotech, 2008; pp 501-504.

111. Chiritescu, C.; Cahill, D. G.; Nguyen, N.; Johnson, D.; Bodapati, A.; Keblinski, P.; Zschack, P., Ultralow Thermal Conductivity in Disordered, Layered WSe2 Crystals. Science 2007, 315 (5810), 351-353.

112. Fryxell, G. E.; Mattigod, S. V.; Lin, Y. H.; Wu, H.; Fiskum, S.; Parker, K.; Zheng, F.; Yantasee, W.; Zemanian, T. S.; Addleman, R. S.; Liu, J.; Kemner, K.; Kelly, S.; Feng, X. D., Design and synthesis of self-assembled monolayers on mesoporous supports (SAMMS): The importance of ligand posture in functional nanomaterials. J Mater Chem 2007, 17 (28), 2863-2874.

113. Harper, S.; Maddux, B. L. S.; Hutchison, J. E.; Usenko, C.; Tanguay, R., Biodistribution and toxicity of nanomaterials in vivo: effects of composition, size, surface functionalization and route of exposure. NSTI-Nano Tech 2007, 1, 666-669.

114. Isaacson, C. W.; Usenko, C. Y.; Tanguay, R. L.; Field, J. A., Quantification of Fullerenes by LC/ESI-MS and Its Application to in Vivo Toxicity Assays. Analytical Chemistry 2007, 79 (23), 9091-9097.

115. J. T. Anderson; C. L. Munsee; C. M. Hung; T. M. Phung; G. S. Herman; D. C. Johnson; J. F. Wager; D. A. Keszler, Solution-Processed HafSOx and ZircSOx Inorganic Thin-Film Dielectrics and Nanolaminates. Advanced Functional Materials 2007, 17 (13), 2117-2124.

116. Lin, Q.; Smalley, A. L. E.; Johnson, D. C.; Martin, J.; Nolas, G. S., Synthesis and Properties of CexCo4Ge6Se6. Chemistry of Materials 2007, 19 (26), 6615-6620.

117. Mavrokefalos, A.; Nguyen, N. T.; Pettes, M. T.; Johnson, D. C.; Shi, L., In-plane thermal conductivity of disordered layered WSe[sub 2] and (W)[sub x](WSe[sub 2])[sub y] superlattice films. Applied Physics Letters 2007, 91 (17), 171912-3.

118. Nguyen, N. T.; Howe, B.; Hash, J. R.; Liebrecht, N.; Zschack, P.; Johnson, D. C., Synthesis of a Family of {[(VSe2)n]1.06(TaSe2)m}z Compounds. Chemistry of Materials 2007, 19 (8), 1923-1930.

119. Orr, G.; Panther, D. J.; Phillips, J. L.; Tarasevich, B. J.; Dohnalkova, A.; Hu, D.; Teeguarden, J. G.; Pounds, J. G., Submicrometer and Nanoscale Inorganic Particles Exploit the Actin Machinery To Be Propelled along Microvilli-like Structures into Alveolar Cells. ACS Nano 2007, 1 (5), 463-475.

120. Teeguarden, J. G.; Hinderliter, P. M.; Orr, G.; Thrall, B. D.; Pounds, J. G., Particokinetics in vitro: dosimetry considerations for in vitro nanoparticle toxicity assessments. Toxicol Sci 2007, 95 (2), 300-12.

121. Usenko, C. Y.; Harper, S. L.; Tanguay, R. L., In vivo evaluation of carbon fullerene toxicity using embryonic zebrafish. Carbon N Y 2007, 45 (9), 1891-1898.

122. Yantasee, W.; Warner, C. L.; Sangvanich, T.; Addleman, R. S.; Carter, T. G.; Wiacek, R. J.; Fryxell, G. E.; Timchalk, C.; Warner, M. G., Removal of Heavy Metals from Aqueous Systems with Thiol Functionalized Superparamagnetic Nanoparticles. Environmental Science & Technology 2007, 41 (14), 5114-5119.

123. Harper, S. L.; Usenko, C.; Tanguay, R. L. In Differential distribution and toxicity of nanomaterials in vivo, AIChE Annual Meeting, San Francisco Hilton, November 12th-17th, 2006; OmniPress: San Francisco Hilton, 2006.

124. Kearns, G. J.; Foster, E. W.; Hutchison, J. E., Substrates for direct imaging of chemically functionalized SiO2 surfaces by transmission electron microscopy. Analytical Chemistry 2006, 78 (1), 298-303.

125. Kearns, G. J.; Hutchison, J. E. In Biomolecular nanolithography: Using DNA to direct nanoparticle assemblies, Abstr Pap Am Chem S, Mar 26; 2006.

126. N. T. Nguyen; B. Howe; J. R. Hash; N. Liebrecht; D. C. Johnson, Synthesis of [(VSe2)n]1.06[(TaSe2)n] Superlattices Using a Hybrid Approach: Self-Assembly of Amorphous Nanostructured Reactant. Advanced Materials 2006, 18 (1), 118-122.

127. Parks, B. W.; Gilbertson, R. D.; Hutchison, J. E.; Healey, E. R.; Weakley, T. J.; Rapko, B. M.; Hay, B. P.; Sinkov, S. I.; Broker, G. A.; Rogers, R. D., Solution and structural investigations of ligand preorganization in trivalent lanthanide complexes of bicyclic malonamides. Inorg Chem 2006, 45 (4), 1498-507.

128. Sweeney, S. F.; Woehrle, G. H.; Hutchison, J. E., Rapid Purification and Size Separation of Gold Nanoparticles via Diafiltration. Journal of the American Chemical Society 2006, 128 (10), 3190-3197.

129. Antonelli, S. B.; Allen, T. L.; Johnson, D. C.; Dubin, V. M., Crystallization Behavior of Ni–P Alloy Films on Co and Cu Seed Layers. Journal of The Electrochemical Society 2005, 152 (9), J120–J124.

130. Li, S. L.; Johnson, D. C. In Evaluation of TiTe2 as a Diffusion Barrier in the Synthesis of (Bi2Te3)5(SnTe)5 Misfit Layer Compound, Materials Research Symposium, Society, M. R., Ed. MRS Publications: 2005; pp F03-12.

131. Mortensen, C.; Matelich, B.; Rostek, R.; Schmid, B.; Johnson, D. C. In Preparation of (TiTe2)3(Sb2Te3)y(TiTe2)3(Bi2Te3)z using the Modulated Elemental Reactants (MER) Technique, Materials Research Symposium, Society, M. R., Ed. MRS Publications: 2005; pp F03-14.

132. Smeller, M. M.; Harris, F. R.; Johnson, D. C. In Synthesis of (Bi2Te3)x(TiTe2)x and (Bi2Te3)x(TiTe2)3 Superlattices, Materials Research Symposium, Society, M. R., Ed. MRS Publications: 2005; pp F03-07.

133. Woehrle, G. H.; Brown, L. O.; Hutchison, J. E., Thiol-Functionalized, 1.5-nm Gold Nanoparticles through Ligand Exchange Reactions: Scope and Mechanism of Ligand Exchange. Journal of the American Chemical Society 2005, 127 (7), 2172-2183.

134. McKenzie, L. C.; Hutchison, J. E., Green nanoscience: An integrated approach to greener products, processes, and applications. Chemistry Today 2004, pp 25-28.

135. Weare, W. W.; Reed, S. M.; Warner, M. G.; Hutchison, J. E., Improved Synthesis of Small (dCORE, 1.5 nm) Phosphine-Stabilized Gold Nanoparticles. Journal of the American Chemical Society 2000, 122 (51), 12890-12891.

136. Center for Sustainable Materials Chemistry. http://sustainablematerialschemistry.org

Appendix III. Research to Innovation Enterprises

SNNI Faculty has independently employed the principles of green chemistry in their research for many years. By 1997, UO Chemistry faculty developed innovative course content incorporating the principles and practice of green chemistry into undergraduate lecture and laboratory classes. Many of these UO researchers, along with researchers from OSU, PSU, and the PNNL, formed unique collaborations. Working together, they ensure that the emerging field of nanotechnology develops responsibly, providing new technologies that are inherently safer (greener) by design, in order to protect health, the environment, and the workforce.

SNNI offer several avenues for collaborations and services for industry, government laboratories, and academia through Affiliated Services including the Nanomaterials Interactions Knowledgebase (NBI), the Greener Nano Conference series, Research to Innovation Enterprises, and Research Centers of excellence.

Affiliated Services

Center For Advanced Materials Characterization in Oregon (CAMCOR)
http://camcor.uoregon.edu/
A full-service, comprehensive materials characterization center located at the University of Oregon in Eugene is open to outside clients. Its core capabilities include capital-intensive equipment for microanalysis, surface analysis, electron microscopy, semiconductor device fabrication, as well as traditional chemical characterization. Remote access allows clients to interface directly with the experts and the instrument in real-time. The staff members who run the facilities are expertly trained and highly experienced in sample preparation, data collection, and data analysis. In addition, they periodically offer workshops to provide hands-on training for users of the facility.

Center for Electron Microscopy and Nanofabrication (CEMN) http://www.emc.pdx.edu/
The Center for Electron Microscopy and Nanofabrication (CEMN) at PSU is a major research resource for the Northwest that features a state-of-the-art FEI Tecnai transmission electron microscope, an FEI Sirion scanning electron microscope, a JEOL 100CX TEM, an FEI-focused ion beam microscope, and a dual-beam FEI microscope for sample patterning and extraction. Full sample preparation facilities are available.   Facilities also available for nanofabrication include carbon nanotube and semiconductor nanowire deposition reactors, plasma etching , and lithography tools. A semiconductor analyzer and probe station are available for testing specimen electrical properties.

Microproducts Breakthrough Institute (MBI) http://mbi-online.org/
The Microproducts Breakthrough Institute, a joint venture between OSU College of Engineering and PNNL, helps both small and large businesses develop and commercialize ONAMI-related technologies into new products. MBI's state-of-the-art Nano-Micro fabrication facility brings together research teams with business representatives within the ONAMI community to solve real-world problems by researching and applying microchannel device manufacturing techniques.

Nanomaterial-Biological Interactions Knowledgebase (NBI) http://nbi.oregonstate.edu/
A knowledgebase of Nanomaterial-Biological Interactions has been established at Oregon State University to provide information on the environmental, health, and safety aspects of

nanomaterials. NBI serves as an open-source repository for data on nanomaterial characterization, synthesis methods, and biological responses.

Sinnhuber Aquatic Research Facility (SARL) http://ehsc.science.oregonstate.edu/SARL
A full-service state-of-the-art aquatic biomedical research facility located just off the OSU campus. Core capabilities include a specific pathogen free zebrafish facility equipped to produce thousands of quality fertilized eggs per day, histopathology, advanced microscopy, high content imaging, and automated behavioral assessment instrumentation.

Conference Series
Greener Nano Conference Series http://www.greennano.org
SNNI's Greener Nano conference series was funded by this grant. It focused on cutting edge research in greener nanomaterials design and production, and brought together academics, industrialists, and policymakers to discuss approaches to developing economically viable, environmentally benign, methods to advance nanotechnology.

Collaborators
Intertox http://www.intertox.com/
Intertox is actively engaged in managing Environmental Health and Safety (EHS) risks from nanomaterials on a number of levels. Their projects and partnerships in nano-EHS have involved first tier nanomaterial laboratories, small and large industries, and the U.S. government. They have assisted with the development of science-based guidelines and standards for nanomaterials through the American National Standards Institute (ANSI) Technical Advisory Group (TAG) 229 to the International Organization for Standardization (ISO). They have developed several application-specific multi-criteria decision analysis (MCDA) tools for government and private users. Intertox is working with SNNI to develop metrics for nanomaterials commonality and expanding the scientific content of the NBI data repository.

Center for the Environmental Implications of NanoTechnology (CEINT) http://www.ceint.duke.edu/
Created in 2008 with funding from the National Science Foundation and the US Environmental Protection Agency, the CEINT performs fundamental research on the behavior of nano-scale materials in laboratory and complex ecosystems.

Research to Innovation Enterprises
Dune Sciences http://www.dunesciences.com/
Dune Sciences, Inc., is a provider of innovative tools and techniques for molecular scale engineering. Our patented and patent-pending technologies are enhancing materials and devices in medicine, bionanotechnology, alternative energy, and nanoscience.

Floragenex http://www.floragenex.com/
Floragenex and the University of Oregon are partnering to revolutionize a gene sequencing process with the development of an automated system for preparing DNA samples for analysis by next-generation DNA sequencing systems. Utilizing microreactor technology in partnership with the Microproducts Breakthrough Institute at Oregon State University, the team is working

to develop sample preparation methods which provide higher throughput, lower cost, and greater repeatability than existing methods of DNA sample preparation.

Inpria Corporation http://www.inpria.com/
Inpria and Oregon State University are demonstrating application of a new technology that provides highly efficient deposition and patterning of functional materials for device applications at all length scales. The most promising application of the platform is to enable printed electronics via inorganic materials, which are expected to have much higher performance at far lower cost than organic approaches. The Inpria / OSU team is working with a leading thin-film display partner to assess the feasibility of applying their unique technology through fabrication of a liquid-crystal display, thin-film transistor backplane test vehicle.

Research Centers spin-off as a result of seed funding
Center for Sustainable Materials Chemistry http://sustainablematerialschemistry.org
The Center for Sustainable Materials Chemistry (CSMC) is a $20M, Phase II Center for Chemical Innovation funded by NSF. The mission is to conduct curiosity-driven and use-inspired research to enhance the sustainable chemistry toolbox with new methods and new techniques that will advance the scientific enterprise and transform the next generation of products, while preparing student to become the next generation of green chemists.

Center for Inverse Design http://www.centerforinversedesign.org/
The Center for Inverse Design, a collaboration among NREL, Northwestern University, Oregon State University, and the SLAC National Accelerator Laboratory is one of the DOE's 46 newly established Energy Frontier Research Center, a $777 million initiative to create breakthrough technology for a 21st-century energy economy. The Center's innovative concept focuses on theory and computation along with other experimental methods to more rapidly identify the advanced materials that can make solar power less costly and more efficient.

Approved for public release; distribution is unlimited.

Appendix IV.
Project report from no cost extension period April 2012 – April 2013
In April 2012, we filed an interim report (pp 1-132) on all of the tasks funded to date, including draft final reports for all of projects that have completed and interim reports for those projects that remained ongoing during the no-cost extension period. As demonstrated in the interim report (above), the project team made excellent progress toward the milestones set forth in the statements of work (SOWs) submitted throughout the project period 2005 – 2012.

The extension made it possible to capitalize on discoveries within Thrust Groups 1 and 2 that unveiled toward the end of the grant period. These discoveries are important to AFRL and ONAMI and deepen the partnership between SNNI and AFRL researchers. During the extension period researchers furthered their investigations of these new discoveries. The key research activities conducted during the extension period include:

- i. Mechanistic investigations of the formation of daughter silver nanoparticles from larger particles that adds to the complexity of nanosilver (eco)toxicology,
- ii. Development and toxicological testing of libraries of ligand-coated nanoparticles to investigate the role ligand mixtures and nanoparticle core sizes over the range of 1-5 nm
- iii. Investigation of the influence of ionic strength of the exposure medium on gold nanoparticle toxicity and
- iv. Development and toxicological testing of larger, functionalized gold and metal oxide nanoparticle sizes with significantly reduced polydispersities.

These discoveries significantly enhanced the impact of the research within the two thrust areas. The completion of this project provides AFRL critical information about the health and safety of engineered nanoparticles.

Expanded libraries of precision-engineered nanoparticles
James Hutchison, Chemistry, University of Oregon
The goals of the work under this objective were (i) to develop syntheses and produce materials for biological screening in the zebrafish assays and (ii) to investigation the formation of daughter silver nanoparticles from larger particles. The final period of the project was very productive. The key accomplishments are described below:

•   Supplied well-characterized AuNPs to the Tanguay group for systematic evaluation of the effects of test medium on the toxicity of these particles. Stability studies were conducted to evaluate the NP stability in test media before transferring to the Tanguay group. We found that nanoparticles with ionizable functionality (for example, carboxylic acids) can precipitate in media. In the case of the carboxylic acid terminated NPs, divalent ions cause precipitation. We developed a spectroscopic assay that could be used by the toxicology group to monitor NP stability during exposures. They, in turn, found exposure conditions that ensured that the NPs remained soluble throughout the exposure timeframe. The results of these studies have been reported in *Nanotoxicology*.

•   Supplied well-characterized AuNPs to the Tanguay group to evaluate the influence of surface chemistry on the incidence of eye pigmentation defects in zebrafish. These results are being published in *Toxicological Sciences*.

- Produced and supplied precisely characterized, mixed-ligand shell AuNPs to the Tanguay group so that they could investigate how subtle changes in the ligand shell lead to significant changes in toxicity. In these cases, the presence of a small number of triphenylphosphine ligands in the shell significantly increased the toxicity and/or increased the incidence of developmental defects relative to the AuNPs containing none of the triphenylphosphine. A manuscript describing these results has been submitted to *ACS Nano.*

- Developed syntheses for water-soluble AuNPs with a series of nanoparticle sizes, ranging from 0.8-5 nm, all with the same ligand shell, in this case trimethylammoniumethanethiol, to investigate the influence of NP core size on toxicity. This series of NPs has been produced and supplied to the Tanguay group for analysis.

- Supplied AuNPs to the Bakalinsky group at Oregon State University so that they could evaluate the influence of surface functional groups on the respiratory metabolism of yeast. The work has been published in *Applied and Environmental Microbiology.*

- Supplied well-characterized AuNPs to the Tanguay group for evaluation of the impacts of nanoparticle surface chemistry on gene expression. This work has been published in *Nanotoxicology.*

- Continued to develop rapid size analysis approaches using small angle X-ray scattering (SAXS). This technique was used to support the characterization most of our recent production runs of AuNPs. We demonstrated the key advantages of SAXS for small particle analysis by comparing the results from SAXS analysis to solid-state crystallography and diffusion ordered spectroscopy (DOSY) NMR for a 1-nm cluster. SAXS confirmed the core size in solution is the same as in the solid-state structure. The diffusion coefficient determined from DOSY is larger. The combined use of DOSY and SAXS revealed new information about the degree of solvent ordering around the nanocluster. These results were published in *Angewandte Chemie, International Edition in English.*

- Based upon the publication comparing SAXS and DOSY NMR, we were invited to prepare a perspective article describing the use of corroborative and complementary techniques to determine nanoparticle size in solution. This perspective article has just been accepted for publication in *ChemPhysChem.*

- We conducted a detailed study to follow up our initial findings that larger silver nanoparticles (and macroscopic silver objects) generate "daughter" silver nanoparticles on surfaces. We confirmed our original findings that the production of daughter particles occurs only under humid conditions and deepened our understanding of humidity's influence. Below 50% RH, surface oxidation of the AgNPs takes place, but lateral diffusion of the silver ions are hindered. As the humidity is increased above 50%, the extent of lateral diffusion increases with increasing humidity. As oxidation of the parent particles continues, one would expect that the local pH would increase to the point where oxidation would cease. However, at higher pH, the deposition of silver oxide is favored and that deposition once again lowers the pH. We detected Ag_2O nanoparticles and showed that they are an intermediate that are ultimately converted to the silver daughter nanoparticles. These results have been written up for publication and will be submitted soon.

- Throughout the project, we established and refined a comprehensive nano/bio research strategy based upon precision-engineered nanoparticles and high-content, high throughput screening using embryonic zebrafish. This strategy exemplifies the interdisciplinary approach

that is necessary to advance safer nanotechnology and safe, effective medical applications of nanomaterials. (Hutchison, J. E. "Greener Nanoscience: A Proactive Approach to Advancing Applications and Reducing Implications of Nanotechnology," *ACSNano* 2008**, 2**, 395-402. 53 citations to date). The type of approach is being widely adopted throughout the research community. The initial blueprint for this strategy, a Chemical Reviews article published during the early stages of this project, has been cited more than 400 times since 2007. Key components of the strategy include precision synthesis, comprehensive characterization, in vitro assay, and in situ measurement. Our approaches to characterization and in situ measurement (Richman, E.K.; Hutchison, J.E. "The Nanomaterial Characterization Bottleneck," *ACS Nano* 2009, *3*, 2441-2446.) have also influenced how research teams are approaching the challenge of nanoparticle structural and compositional analysis. This research strategy, developed through AFRL support, helped inform a new federal research strategy on nanotechnology health and safety. (*A Research Strategy for Environmental, Health, and Safety Aspects of Engineered Nanomaterials*, Committee to Develop a Research Strategy for Environmental Health and Safety Aspects of Engineered Nanomaterials, National Research Council, The National Academies Press: 2012)

Rapid Throughput Whole Animal Platform To Define Nanoparticle/Biological Interactions: A Path To Safer Nanomaterial Design
Robert Tanguay, Environmental & Molecular Toxicology, Oregon State University
The purpose of our project is to exploit our integrated *in vivo* zebrafish toxicity assay to define the nanomaterial properties that influence biological interactions and responses. The principal materials under investigation are the series of gold functionalized nanomaterials produced by the Hutchison group.

Key Accomplishments
- We have automated all of the nanomaterial bioactivity assessments steps

- We have built tested and implemented the shuttle boxes to assess adult behavioral responses to NP exposure

- Partially functionalized 1.3 nM gold nanoparticles specifically produce eye development defects

- We developed a robust human cancer cell xenograft model to asses nanomaterial chemotherapeutic effects

- We have utilized laser ablation ICP-MS to detect gold NP distribution in situ

- We have completed a comprehensive RNA-seq study following exposure to two differentially toxic gold NPs

- We have evaluated a series of silver nanomaterials coated with PVP and citrate and determined that the media ionic strength greatly affects bioavailability and subsequent toxicity.

- We have completed a number of studies demonstrating that surface defects play a major role in biocompatibility.

Major findings are detailed below:
To investigate if subtle ligand variations on the surface of gold nanoparticles (AuNPs) would dictate hazard potential, Jim Hutchison provided four well-defined AuNPs ligand stabilized 1.3

Approved for public release; distribution is unlimited.

nm particles with: (1) anionic 2-mercaptoethanesulfonic acid (MES) (MES AuNPs), (2) a mixture of MES and a small amount of triphenylphosphine (TPP) (MES/TPP AuNPs), (3) cationic N,N,N trimethylammoniumethanethiol (TMAT) (TMAT AuNPs) and (4) a mixture of TMAT and a small amount of TPP (TMAT/TPP AuNPs) Small-angle X-ray scattering (SAXS) confirmed that the core sizes of AuNPs were maintained without agglomeration in the embryonic test medium. MES/TPP and TMAT/TPP AuNPs contained higher phosphorus content than MES and TMAT AuNPs as determined by XPS and NMR analysis, indicating that the phosphorus in the form of TPP remained on the surface of MES/TPP and TMAT/TPP AuNPs. Whne these particles were assessed in the embryonic zebrafish assay, we found that MES/TPP AuNPs caused significantly more embryonic mortality and malformation than MES AuNPs, and that TMAT/TPP AuNPs elicited a similar amount of mortality as TMAT AuNPs, but a higher incidence of eye defects was observed. The developmental toxicity was consistent with gene expression. Both mixed ligand particles significantly disrupted genes regulating apoptosis (p53 and bax), eye development (pax6a, otx2 and rx1) and pigmentation (sox10 and mitfa) in a concentration-dependent manner. We also used laser ablation ICP-MS analysisand determined that the uptake of the mixed ligand AuNPs was more pronounced. These findings provide new insights into the understanding of ligand mediated toxicity mechanism, and further emphasize the importance of precise synthetic engineering and characterization for assessing nanoparticle toxicity. These findings have been submitted to ACS Nano.

Awards and Presentations

- Society of Toxicology Roundtable Discussion: "A Decade of Nanotoxicology: Where Do We Stand Now?" San Antonio, Texas, March 10, 2013

- ASME 2013 2nd Global Congress on NanoEngineering for Medicine and Biology (NEMB2013),
"Rapid In Vivo Assessment Of The Nano/Bio Interface": Boston, Massachusetts, February 4, 2013

- Department of Pharmaceutical Sciences, University of New Mexico: "Rapid In Vivo Assessment of Chemical and Biological Interactions: High Content Data for the 21st Century." Albuquerque, New Mexico, March 29, 2013

- National Toxicology Program Sponsored The Future of Models and Methods to Predict Metabolism and Toxicity Workshop: "Rapid In Vivo Assessment of Bioactivity in Zebrafish: High Content Data for Predictive Toxicology." RTP, North Carolina, February 29, 2013.

- National Research Council, Workshop to Develop a Research Strategy for Environmental, Health, and Safety Aspects of Engineered Nanomaterials: "Nano EHS – Gaps, Progress and Needs" Washington D.C., November 7, 2012.

- Safe Nano Design Workshop: "High throughput assessments of the nano/bio interface to proactively guide safer nanomaterial design", Albany NY, August 15, 2012.

- SETAC 6th World Congress/SETAC Europe 22nd Annual Meeting: "Rapid in vivo assessment of the nano/bio interface to guide safer nanomaterial design." Berlin, Germany, May 2012

Computational and analytic tools to support the development of environmentally-benign nanomaterials
Stacey Harper, Chemical, Biological, and Environmental Engineering and Environmental & Molecular Toxicology, Oregon State University

SNNI supported a workshop on nanoinformatics in July 2012. The goals of the GreenerNano 2012: Nanoinformatics Tools and Resources Workshop were to establish a better understanding of current nanoinformatics applications and to clearly define immediate and projected informatics infrastructure needs of the nanotechnology community. The theme of nanotechnology environmental health and safety (nanoEHS) was used to provide real-world, concrete examples on how informatics can be utilized to advance our knowledge and guide nanoscience. In preparation for the workshop, two preliminary webinars were held to ensure participant engagement and maximize the outputs of a one-day workshop. The first webinar provided 15 minute overviews of current nanoinformatics tools with detailed information on our current state-of-the-science. The following webinar recordings are available at http://nanoinformatics.org/2012/webinar. The second webinar aimed to provide live interactions with the developers of those nanoinformatics tools and resources prior to the workshop. The webinar allowed for preliminary discussions on the workshop topics and an overview of the day's events.

Key Accomplishments
The workshop brought in over 70 participants nationally and internationally, which were representative of academics (US and abroad), government bodies (NNCO, NIESH, NIOSH, State Agencies, military), national laboratories, and industry. A publication highlighting the meeting outcomes has been drafted and will be published in Computational Science and Discovery.
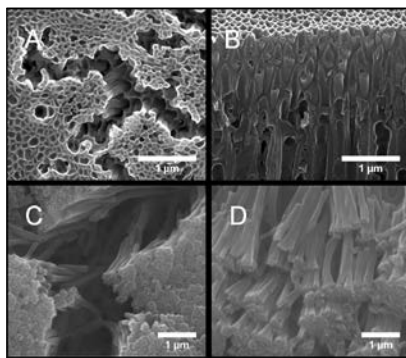
Separation and purification of nanoparticles using a novel templated silsesquioxane membrane
Vincent T. Remcho, Chemistry, Oregon State University

A templated silsesquioxane (ssq) membrane was synthesized on a porous alumina support and used for the separation and purification of nano-sized materials, such as nanoparticles and macromolecules. The ssq membrane was fabricated by polycondensation of a silsesquioxane monomer solution in the presence of a surfactant within the macroporous space of an alumina membrane. The ssq membrane was annealed at 120˚C and subsequently washed with ethanol to remove the surfactant template from the membrane matrix. The ssq membrane was evaluated using 5-8 nm gold nanoparticles (protected with dodecanethiol) in chloroform. Following filtration, it was determined by transmission electron microscopy that the average particle size of the permeate was 4.4 ±0.6 nm, indicating the separation efficacy of the membrane. Myoglobin (~3.2 nm; 17 kDa) and bovine serum albumin (~7.2 nm, 66 kDa), prepared in 2-(N-morpholino)ethanesulfonic acid buffer solution, were also used to determine the membrane performance. Rejection values of 31.8% and 97.a% were determined for these test probes by UV-Vis assays of the permeate and the retentate, respectively. These results indicate that the ssq membrane has the desired size cut-off of 5 nm.

Morphology of the ssq membrane

The SEM images show bundles of ssq channels inside the anodisc alumina membrane (AAM) pores. (Figure 123 A, B) The ssq nanotubes are aligned vertically on the membrane surface. Also, space was observed between the ssq nanotubes and the AAM membrane wall attributed to contraction during the drying and calcination process. This space is similar to that observed for silica nanotubes on AAMs. After complete removal of the AAM, the ssq nanotubes were observed to be in regular and continuous alignment along the vertical axis. (Figure 123 C, D)


Figure 123. The SEM images show bundles of ssq channels inside the anodisc alumina membrane (AAM) pores

Separation and purification of gold nanoparticles using the ssq membrane

The ssq membrane was evaluated using 5-8 nm gold nanoparticles protected with dodecanethiol. A 5 mL aliquoof a gold nanoparticle solution in chloroform was applied to the ssq membrane and filtered under gentle vacuum.

Each feed and permeate solution was studied by monitoring the change in particle size distribution using transmission electron microscopy (TEM) following filtration. The feed solution histogram (3A') shows a wide particle size distribution (between 5 and 8 nm) for an unfiltered initial sample, while the permeate (3B') exhibits a particle size of 4.4 ± 0.6 nm, which is an impressively narrow particle size distribution. (Figure 124) PbS (oleic acid) nanoparticles (3.5 ± 0.8 nm, λmax = 1200 nm, plus aggregates) were also filtered using the ssq membrane. After filtration, a particle size of 3.5 ± 0.7 nm was determined by TEM analysis, which confirmed that the smaller particles (< 5 nm) were passing through the ssq membrane while the larger aggregates were being retained. These results indicate that the ssq membrane possessed the desired 5 nm cut-off.
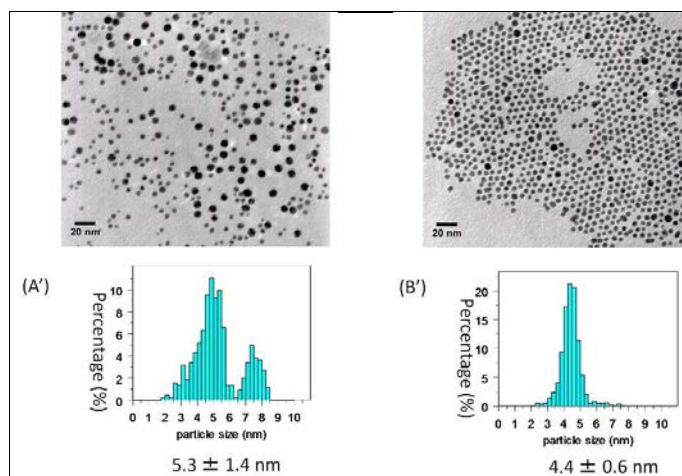
Figure 124. TEM images and particle size histograms of the feed solution (A) and the permeate solution (B) of gold nanoparticle mixtures filtered using the ssq membrane.

Ssq membrane performance metrics for macromolecules

A feed volume of 20 mL of each solution (0.2 mM myoglobin and 0.05 mM bovine serum albumin in 100 mM 2-(N-morpholino)ethanesulfonic buffer) was subjected to filtration separately on a similarly prepared ssq membrane at 40 psi by dead-end flow filtration. The hydrodynamic size of BSA and myoglobin are ~7.2 nm and ~3.2 nm, respectively. An untreated AAM showed no separation of BSA or myoglobin. Rejection values for myoglobin and BSA on the ssq membrane were experimentally determined to be 31.8% and 97.4%, respectively. (Figure 125) These results agree with the results previously obtained using gold nanoparticles on similarly 76 prepared ssq membranes, where separation of nanoparticles smaller than 5 nm was successfully accomplished. BSA (larger particles larger than the 5 nm size of the ssq pores) was retained, while myoglobin being smaller than 5 nm, demonstrated the expected low rejection and passed through the ssq membrane.
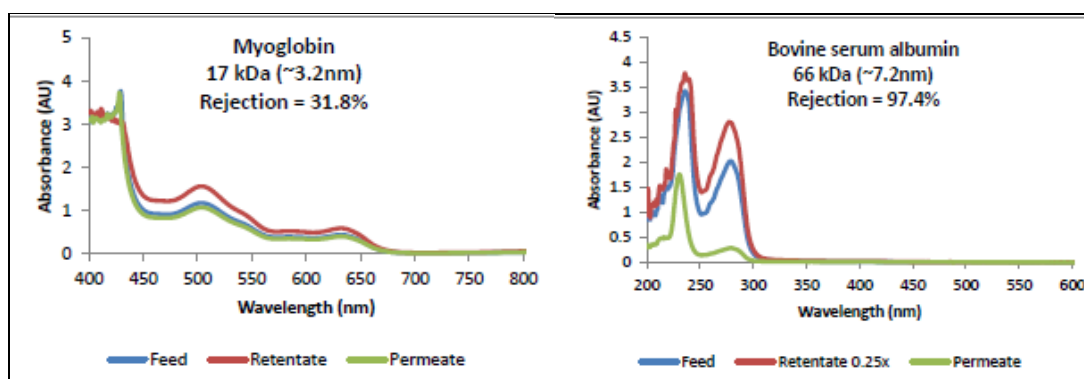

Figure 125. UV-Vis absorbance spectra of the feed, retentate, and permeate solutions of each Myoglobin and bovine serum albumin solution after filtration. Each macromolecular solution was subjected to the ssq membrane at 40 psi of N2 gas pressure and ambient conditions.

Future work - Enhanced lateral flow immunoassay using gold nanoparticles.
In our future work, we will utilize gold nanoparticles as labeling carriers to achieve improved optical lateral flow immunoassay performance. Lateral-flow assays are rapid, simple, paper-based assays that employ chemistries "embedded" in test strips. We have developed several new lateral-flow approaches for determination of adulterated pharmaceuticals, and have determined that enhanced detection sensitivity is a critical need if these inexpensive, promising assays are to become mainstays of field analysis. We are in the early experimental stages of using gold nanoparticles as signal enhancing agents in paper-based immunochemical sandwich assays.   The gold nanoparticles are functionalized or coated with analyte-binding antibodies, then exposed to a sample. The resulting analyte-nanoparticle complex flows laterally through a series of overlapping membranes and is captured on an antigen capture line. A visual result can be achieved in a few minutes, allowing rapid interpretation without the need for complex or expensive instrumentation.
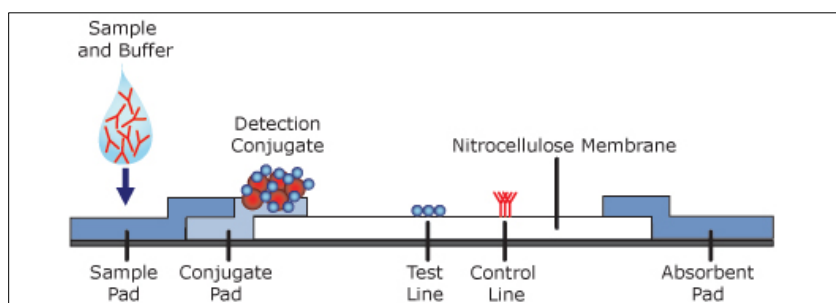
Figure 126. Lateral Flow Approach

Approved for public release; distribution is unlimited.

LIST OF ACRONYMS, ABBREVIATIONS AND SYMBOLS

Acronym	Description
ONAMI	Oregon Nanoscience and Microtechnologies Institute
SNNI	Safer Nanomaterials and Nanomanufacturing Initiative
OSU	Oregon State University
PSU	Portland State University
PNNL	Pacific Northwest National Laboratory
NNI	National Nanotechnology Initiative
GN	Greener Nano
NT4D	Nanotechnology for Defense
OECD	Organisation for Economic Co-operation and Development
CSMC	Center for Sustainable Materials Chemistry
PCAST	President's Council of Advisors on Science and Technology
EHS	Environmental, Health, and Safety
Au	Gold
NP	Nanoparticles
NBI	Nanomaterial-Biological Interactions
AuNPs	Gold Nanoparticles
AOB	Ammonia Oxidizing Bacteria
Ag-NP	Silver Nanoparticles
NH_3	Ammonia
NO_2^-	Nitrite
AMO	Ammonia Monooxygenase
HAO	Hydroxylamine Oxidoreductase
SRHA	Suwanne River Humic Acid
DLS	Dynamic Light Scattering
TEM	Transmission Electron Microscopy
AuNPs	Gold Nanoparticles
TMAT	Trimethylammoniumethanethiol
MES	Mercaptoethanesulfonic Acid
MEEE	Mercaptoethoxy)ethoxy)ethanol
INAA	Instrument Neutron Activation Analysis
ICP-MS	Inductively Coupled Plasma – Mass Spectrometry
ALI	Air-Liquid Interface
LDL	Low-Density Lipoprotein
CRP	C-Reactive Protein
GNR	Gold Nanorod

Acronym	Description
AuNRs	Gold Nanorods
SAXS	Small Angle X-Ray Scattering
XPS	X-Ray Spectroscopy
GSH	Glutathione
PFPA	Perfluorophenyl Azido
ODTMS	Octadecyltrimethoxysilane
PC	Phytochelatin
NCC	Nanocrystalline Cellulose
AO	Anti-Oxidants
AAPH	2'-Azobis-2-methyl-propanimidamide Dihydrochloride
AO	Alpha-Lipoic Acid
NEHI	Nanotechnology Environmental Health Implications
NACSE	Northwest Alliance for Computational Science and Engineering
EBI	European Bioinformatics Institute
ISA-TAB	Investigation/Study/Assay
NPO	NanoParticle Ontology
CFD	Computational Fluid Dynamic
CH_2Cl_2	Dichloromethane
TGA	Thermogravimetric Analysis
OSN	Organic Solvent Resistant Nanofiltration
PPh_3	Triphenylphonsphine
$AuClPPh_3$	Chloro(triphenylphonsphine)gold
RT	Residence Time
ID	Inner Diameter
SAED	Selected Area Electron Diffraction
SiO	Silicon Monoxide
ScFs	Supercritical Fluids
NcFs	Near Critical Fluids
QPCs	Quantum Point Contacts
DLA	Diffusion-Limited Aggregation
IDEs	Interdigitated Electrodes
TFTs	Thin-film Transistors
V_{on}	Turn-On Voltage
I_{on}/I_{off}	Current On-to-Off Ratio
μ_{inc}	Incremental Channel Mobility
IBLM	Internal Barrier Layer Mechanism
ANSI	American National Standards Institute

Acronym	Description
TAG	Technical Advisory Group
MCDA	Multi-Criteria Decision Analysis
CEINT	Center for the Environmental Implications of NanoTechnology
SOWs	Statements of Work
DOSY	Diffusion Ordered Spectroscopy
TPP	Triphenylphosphine
SSQ	Silsesquioxane
AAM	Anodisc Alumina Membrane